Regge-plus-resonance approach to strangeness production from the deuteron

Pieter Vancraeyveld

Promotor: Prof. Dr. Jan Ryckebusch

Proefschrift ingediend tot het behalen van de academische graad van
Doctor in de Wetenschappen: Fysica

Universiteit Gent
Faculteit Wetenschappen
Vakgroep Fysica en Sterrenkunde
Academiejaar 2010-2011

Begin at the beginning [...] and go on till you come to the end: then stop.
— Lewis Carroll

Preface

Op de kaft staat dat dit proefschrift wordt ingediend tot het behalen van de graad van doctor in de wetenschappen. Maar zoals Michaelis, de *ticket-of-leave apostle*, zegt in Joseph Conrad's *The Secret Agent*: "*All idealization makes life poorer. To beautify it is to take away its character of complexity – it is to destroy it.*" Dit proefschrift betekent dan ook veel meer dan twee letters en een puntje voor mijn naam. Het staat symbool voor vele uren peinzen, wroeten, prutsen en herbeginnen, briljante ideeën die even later doorprikt worden, dagenlang zoeken naar *off-by-one errors*, maar ook bergen chocola uit Nancy's kolenschophanden, ping-pongpartijtjes, wetenschappelijke (?!) discussies tijdens de koffiepauze, happy hours, ... Zonder de hulp, raad en vriendschap van de mensen om mij heen zou dit boekje nu niet voor u liggen.

Jan, bedankt om me destijds de kans te geven bij u te mogen thesissen en vervolgens te doctoreren. Uw begeestering voor fysica en de boeiende gesprekken over vreemdheid, complexiteit en meer wereldse zaken waren een verrijking. Lesley, jarenlang hebben we samengehokt, de één zwetend, de ander rillend, samen gevloekt op *strangecalc*, samen gejuicht bij grote en minder grote successen. Het was mij een waar genoegen. Nu *lua* de top-20 van meest gebruikte programmeertalen is binnengedrongen, heb ik niets meer te zeggen behalve merci! Tamara, dankzij jou heb ik een vliegende start kunnen maken. In dat eerste jaar, terwijl je zelf je thesis aan het schrijven was, heb je je ontelbare keren moeten omdraaien, omdat dat koorknaapje weer met een prangende vraag zat. Sorry voor het storen en bedankt voor je geduld. Tim, motard en orakel van het INW, bedankt voor jouw cynische blik, stevige schouderklopjes en antwoorden op alles. In mijn hart blijf je voor altijd de *key to happiness*.

Dave, thank you for the insightful discussions and (perhaps unknowingly) helping us revamp our code; your initial wrapper of strangecalc paved the way. I wish to thank Prof. Wally Van Orden and Prof. Franz Gross for sharing their relativistic deuteron wave functions. I am indebted to Prof. Johann Haidenbauer who provided the Jülich-model hyperon-nucleon partial-wave amplitudes that are a crucial input to this work. Sergey, many thanks for the nice collaboration and giving me the opportunity to explore kaon capture. Model calculations are so much more meaningful when they can be confronted with experimental data. In this regard, I wish to express my gratitude to Prof. Hashimoto, Prof. Maeda, Prof. Kanda and Dr. Futatsukawa, who were so kind to share their preliminary results, and thus effectively quadruple the amount of data in the final chapter of this work.

Without the financial support of the Research Foundation – Flanders (FWO), this work could not have been carried out. A substantial portion of the calculations presented in Chapter 6 were carried out using the Stevin Supercomputer Infrastructure at Ghent University, which is funded by Ghent

University, the Hercules Foundation and the Flemish Government – department EWI. I wish to acknowledge the excellent technical support from the ICT Department of Ghent University.

Het INW, idyllisch gelegen tussen verbrandingscentrale, spoorwegberm en autosnelweg, is een unieke werkplek. Zonder zijn bewoners had de productiviteit bij momenten misschien iets hoger gelegen, maar zou doctoreren toch nooit hetzelfde geweest zijn. Allereerst een woord van dank voor zij die technische ondersteuning boden: Roland om mijn twee linkerhanden bij te staan wanneer mijn stalen ros het liet afweten, Daniella en Linda voor het opkuisen van mijn occasioneel geknoei in *SAP*, Rudy voor drukwerk allerhande, Bart om te hulp te snellen wanneer virtuele (en andere) servers het weer lieten afweten. Klaas, bedankt dat ik je geduld zo vaak op de proef mocht stellen. Arne, Klaas, Lesley en Sander, bedankt voor de vele discussies over *git* versus *svn*, *OO* versus *procedural*, *lua* versus de wereld, ... Arne, Karim, Ola en Tom, sorry voor de ontelbare keren dat ik jullie bureau binnenstormde om mijn caffeïneniveau opnieuw op peil te brengen en bedankt om altijd klaar te staan met een verkwikkende babbel. Iedereen die zich samen met mij gewaagd heeft aan de *haute cuisine* van het UZ, bedankt. Alle afvalligen die veilig boterhammetjes aten, en mij sporadisch lieten aanschuiven aan hun tafel, ook bedankt. Bart, Bright, Christophe, Freija, Lesley, Marc, Matthias, Piet, Simon, Tim, Tom, Ward en Wim, *thanks for keeping it mainstream.*

De vrienden uit de 'echte' wereld stonden altijd klaar om het fysicagebeuren in perspectief te plaatsen. Bedankt daarvoor en uiteraard ook voor de, via jullie belastingsformulier, indirect geleverde bijdragen. "*Ohne Musik wäre das Leben ein Irrtum*", aldus Nietzsche. Gelukkig waren *Broccoli* en *The Jealous Gays* daar om dat te onderschrijven. Mama, papa, vanuit de grond van mijn hart bedankt voor alle steun, logistiek en anders. Meestal laat ik het niet genoeg blijken, maar ik ben jullie oneindig dankbaar om me altijd de kans te geven om mijn ding te doen. Sylvie, al die jaren ben je er altijd geweest voor mij, soms dichtbij, te vaak veraf. Bedankt om alles kleur te geven.

Contents

Preface v

Contents vii

1 Introduction 1

2 The Regge-plus-resonance formalism 11
2.1 Kinematics and observables . . . 12
2.1.1 Reference frames . . . 12
2.1.2 Independent variables . . . 13
2.1.3 Transition amplitude . . . 13
2.1.4 Photoproduction observables . . . 14
2.1.5 Electroproduction observables . . . 16
2.2 Kaon production in the Regge limit . . . 18
2.3 Kaon production in the resonance region . . . 21
2.4 The RPR model: the good, the bad and the ugly . . . 23

3 Kaon production in data-poor reaction channels 31
3.1 Symmetry considerations at the strong-interaction vertex . . . 32
3.2 The unbound neutron as kaon-production target . . . 33
3.2.1 Gauge-invariance restoration . . . 33
3.2.2 Helicity amplitudes . . . 34
3.2.3 Results . . . 36
3.3 Regge formalism for neutral-kaon photoproduction . . . 43
3.3.1 The naive approach . . . 43
3.3.2 A third trajectory . . . 47
3.3.3 Adjusting the strength of the $K^*(892)$ trajectory . . . 49
3.3.4 Results . . . 51

4 Radiative kaon capture 55
4.1 Formalism . . . 55
4.2 Crystal-Ball data: an exploratory analysis . . . 57

5 Formalism for electromagnetic kaon production from the deuteron 61

5.1 Kinematics . . . 62
5.1.1 Reference frames . . . 62
5.1.2 Independent variables . . . 64
5.2 Transition amplitude . . . 66
5.2.1 Electroproduction . . . 66
5.2.2 Lorentz transformations . . . 67
5.2.3 Parity . . . 68
5.3 Photoproduction observables . . . 68
5.3.1 Differential cross section . . . 68
5.3.2 Polarisation observables . . . 70
5.4 Electroproduction observables . . . 72
5.5 Deuteron wave function . . . 76
5.5.1 Covariant *Dnp*-vertex . . . 77
5.5.2 Non-relativistic wave functions . . . 79
5.5.3 Relativistic wave functions . . . 80
5.6 Relativistic impulse approximation . . . 82
5.6.1 Different contributions to the relativistic impulse approximation . . . 83
5.6.2 Relativistic plane-wave impulse approximation . . . 84
5.6.3 Hyperon-nucleon final-state interaction . . . 86

6 Results for kaon production from the deuteron 91
6.1 Relativistic plane-wave impulse approximation . . . 92
6.1.1 Non-relativistic spectator-nucleon approximation . . . 92
6.1.2 Off-shell extrapolation . . . 95
6.1.3 Wave-function sensitivity . . . 96
6.1.4 Helicity-amplitude dependence . . . 97
6.2 Hyperon-nucleon final-state interactions . . . 97
6.3 Photoproduction data . . . 104
6.4 Electroproduction data . . . 111

7 Conclusions and outlook 113

A Notations and conventions 117
A.1 Four-vectors and tensors . . . 117
A.2 Rotations and Lorentz transformations . . . 118
A.3 Pauli and Dirac matrices . . . 120
A.4 Dirac spinors . . . 121

B Biquaternions 123
B.1 Definition . . . 124
B.2 Representation of the Lorentz group . . . 124

C Helicity spinors 127
C.1 Definition . . . 127
C.2 Lorentz transformations . . . 128

D Feynman rules 131
D.1 Cross sections and decay rates . . . 131
D.2 Transition amplitude . . . 132
D.3 Effective fields and interactions . . . 132
D.3.1 Propagators . . . 133

D.3.2 Effective Lagrangians . . . 133
D.3.3 $N(\gamma, K)Y$ transition amplitudes . . . 134

E Lorentz-invariant cross sections **137**
E.1 Dalitz cross section . . . 138
E.2 Chew-Low cross section . . . 139

F Density matrix **141**
F.1 Definition . . . 141
F.2 Spin-1/2 system . . . 142
F.3 Spin-1 system . . . 142
F.4 Photons . . . 145

G Parametrisations of the deuteron wave function **147**
G.1 Non-relativistic wave-function parametrisation . . . 147
G.2 Relativistic wave-function parametrisation I . . . 149
G.3 Relativistic wave-function parametrisation II . . . 149

H Connecting (non-)relativistic wave functions with the covariant Dnp-vertex **153**

I Parameters of the Regge-plus-resonance model **157**

J Experimental data **161**

K Hyperon-nucleon interaction **165**
K.1 Kinematics . . . 165
K.2 Transition amplitudes . . . 166
K.3 Off-shell scattering . . . 167
K.4 Jülich model . . . 168

Samenvatting **171**

List of publications **181**

Bibliography **183**

Nomenclature **199**

CHAPTER 1

Introduction

Conventional wisdom states that one should use the right tool for the right job. This statement is extremely relevant in physics. The first and most important step towards understanding any phenomenon boils down to identifying the relevant degrees of freedom.

The physics of hadrons confronts us with a prodigious diversity of processes and one cannot readily identify the appropriate ingredients to address them in a single, unified picture. At the low-energy end of the spectrum resides the deuteron, a proton-neutron pair, bound by only a fraction of its rest mass. At the other end, one encounters the rich phenomena occurring in the depths of space which we painstakingly try to reproduce in particle accelerators. Underlying all this is the theory of the strong force, quantum chromodynamics (QCD), and its elementary fields, quarks and gluons.

The strong interaction challenges our mathematical toolbox and defies our intuition. Contrary to the other fundamental forces in nature, it is asymptotically weak as interacting particles approach each other. When they move apart, inter-particle energy grows, thus forcing them to be *confined* into colourless objects. The quick variation, or running, of the strong coupling constant with the length and time scale, calls for ever-changing degrees of freedom.

The nucleon is the prevailing manifestation of quark confinement. Through deep-inelastic scattering, many details about its intricate structure have been uncovered. Structure functions, parton distribution functions, and form factors reveal that gluons carry up to half of the nucleon's momentum and that strange quarks in the sea make a significant contribution to the total spin. Yet, on average, this complex system can be interpreted as a bound state of three valence quarks. Constituent-quark models (CQM) encapsulate this perspective and their success in describing hadron spectra, magnetic moments and electromagnetic form factors is uncontested. Nevertheless, one needs to ask where the boundaries of this mean-field description lie and how they emerge from partonic degrees of freedom.

Nucleon spectroscopy

Mapping out the baryonic spectrum remains a paramount issue in hadron physics. The masses, widths, and transition form factors of the nucleon's excited states are invaluable tests of models aimed at understanding the internal structure of baryons. The experimental knowledge on excited nucleon states is gathered bi-yearly by the Particle Data Group in the Review of Particle Physics (RPP) [1]. Their major source of information stems from partial-wave analyses (PWA) of πN scattering data. In particular, the PWA performed by the Karlsruhe – Helsinki [2], Carnegie-Mellon – Berkeley [3] and George-Washington – Virginia-Polytechnic-Institute (SAID) [4] groups. Resonances are identified by examining the fitted amplitudes for poles in the complex energy plane. Alternatively, the amplitudes serve as input to coupled-channels (CC) PWA [5–10]. Besides the fitted elastic πN amplitudes, these analyses include data on inelastic channels and, in some cases, photon-induced processes to constrain their results. Despite partial-wave solutions of comparable goodness of fit, one often obtains conflicting information on the resonant content. Beyond the first few established nucleon excitations, many states are debated and the overall view on the resonance spectrum remains unclear [11].

A similar observation can be made when the experimental picture is confronted with nucleon spectra predicted by CQMs. The description of low-lying states is adequate. Yet, beyond the 1800-MeV mass range, an excessively dense spectrum is predicted. It is said that a number of resonances are "missing". This might be an indication of the fact that the effective degrees of freedom should be re-examined, since alternative nucleon-structure models, such as quark-diquark models [12], envision far fewer resonant states. On the other hand, the missing-resonance conundrum could be a direct consequence of the unbalanced contribution of πN data to PWA.

Strangeness production

Electromagnetic (EM) kaon production plays a key role in the ongoing theoretical and experimental efforts to explore the dynamics of QCD in the confinement regime. Since the production mechanism inevitably involves quark-antiquark components of the nucleon's sea, the reaction has the potential to probe unexplored aspects of the nucleon's structure. Hence, the presence of open strangeness in the final state holds out the prospect of finding some elusive resonant states. Several quark-model results indicate that a number of unobserved resonances couple weakly to the πN final state, but have considerable branching fractions to alternative reaction channels, including those with strangeness [13–15].

The earliest work on EM strangeness production can be dated back to the sixties of the previous century [16–18]. These studies were held back by the limited accuracy of the data available at that time. It was not until the advent of high-duty-cycle, high-intensity electron accelerators that the theoretical interest in kaon production was rekindled. Adelseck *et al.* constructed a kaon-photoproduction operator using a diagrammatic technique based on purely hadronic degrees of freedom [19]. This approach is known as the isobar model and has been applied to the analysis of kaon production in numerous studies [19–30]. In a different approach, quark models have been used directly to describe the reaction dynamics [31–37]. Focusing on a correct high-energy limit for the kaon-production operator, a number of studies inspired by Regge phenomenology have been published [38–42]. In recent years, several groups have undertaken the task of incorporating strangeness production in CC formalisms [5, 10, 43–48]. Motivated by the prospect of a complete

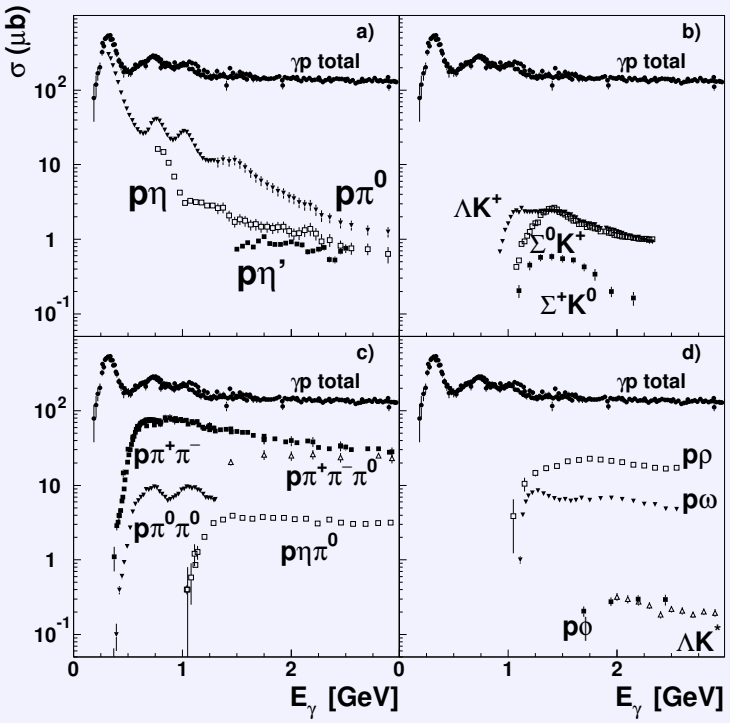

Figure 1.1 – Total photo-absorption cross section and exclusive cross sections for single- and multi-meson production. Figure taken from Ref. [11].

kaon-production experiment, some exploratory multipole analyses have been carried out [49–51]. At present, however, one is not yet able to extract a unique multipole solution from the data.

Leading experimental facilities[1] at ELSA (Bonn University, Germany), ESFR (Grenoble, France), Jefferson Lab (Newport News, Virginia), MAMI (Mainz, Germany) and SPring-8 (Osaka, Japan) have bestowed us with a large database of cross sections and polarisation observables, predominantly for the $p(\gamma, K^+)\Lambda$ and $p(\gamma, K^+)\Sigma^0$ reaction channels. The self-analysing weak decay of hyperons is an enormous asset, since it facilitates the determination of the recoiling particle's polarisation. Hence, a wide range of single- and double-polarisation observables can be accessed in combination with a polarised beam or target. This paves the way for the determination of a "complete" set of observables. Along with the unpolarised differential cross section, this requires the measurement of seven carefully chosen single- and double-polarisation observables [51, 53, 54]. Ideally, this leads to an unambiguous determination of the reaction amplitude and, as such, stringent constraints on dynamical models.

Building models for kaon production

Consider the total photo-absorption cross section on the proton given in Figure 1.1. At low energies, where single-pion production dominates, one can clearly discern peaks, which are unambiguous manifestations of the formation of nucleon resonances. Here, a description in terms of hadronic degrees of freedom is appropriate. Since mesons, baryons and their excited states cannot be described within a fundamental theory, one takes recourse to a field-theoretical framework adopting effective

[1] for a review see Refs. [11, 52].

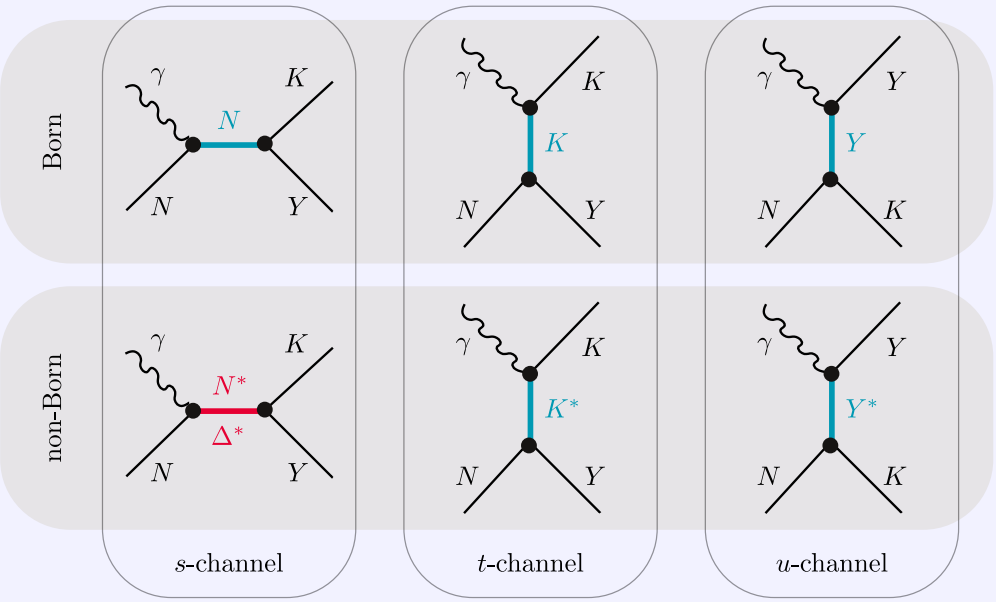

Figure 1.2 – Tree-level contributions to the $N(\gamma^{(*)}, K)Y$ amplitude. The Δ^*-exchange term is forbidden for Λ production. The diagram in the bottom-left corner is resonant. The others are considered background contributions.

interaction Lagrangians that reflect essential symmetry properties and conservation laws of the underlying fundamental interaction. The finite spatial extension of the hadrons is incorporated using phenomenological form factors. Care has to be taken, because this procedure breaks the vital property of gauge invariance [55].

In the so-called isobar approach, the reaction dynamics are restricted to tree-level amplitudes, consisting of two interaction vertices and one propagator. The considered diagrams are presented in Figure 1.2 and can be classified according to several aspects. Considering the diagrams in Figure 1.2 per column, we distinguish between the exchange of a non-strange baryon (N, N^*, Δ^*), a kaon (K) or a hyperon (Y, Y^*), labelled s-, t- and u-channel respectively. The contributions in the top row are known as Born terms and involve the exchange of a ground-state hadron (p, n, K, Λ, Σ). Finally, a diagram can be either resonant or non-resonant. In EM kaon production, the kinematical conditions are such that the intermediary particle in the N^*- and Δ^*-exchange amplitudes can be on mass shell. Consequently, the propagator goes through a pole and produces resonant structures in the observables. In the remaining diagrams of Figure 1.2, on the other hand, the exchanged particles cannot reach their resonant pole. As our interest in strangeness production is generated by the discovery potential for missing resonances, the contributions of the non-resonant diagrams are considered a *background*.

Contrary to fundamental field theories, effective Lagrangians represent parametrisations of the meson-baryon interaction in terms of unknown coupling constants. A phenomenological analysis in the isobar approach faces the challenge of determining the resonant content of a reaction while simultaneously fixing the unknown effective coupling strengths. This dual situation of model selection and model optimisation can be addressed via a Bayesian approach [56] at a substantial computational cost. In any case, because the parameters of the resonant and background contributions are simultaneously fitted to the data, they are inevitably strongly correlated.

The isobar framework has met with considerable success and has dominated the analysis of EM

meson-production processes in the resonance region. Its application to strangeness-production reactions should be regarded with caution. As seen in Figure 1.1, the total cross section lacks clear resonant structures, implying that resonant contributions do not dominate. For this reason, background diagrams make up a crucial element of the reaction dynamics. In the isobar approach, these non-resonant terms diverge as energy increases [57]. Over the years, several mechanisms to remedy this unrealistic behaviour have been proposed. The extracted resonance couplings, however, heavily depend on the background model [27, 58].

The tree-level diagrams of Figure 1.2, considered in the isobar model, infer a perturbation series which is truncated at lowest order. In practise, the effective coupling constants at the interaction vertices are by no means small, implying rescattering effects need to be taken into account. Numerous analyses of kaon production have been performed in different CC frameworks. Nevertheless, we wish to stress the continued relevance of single-channel descriptions.

An attractive quality of the CC approach is its natural fulfilment of unitarity. For this to hold true, however, all possible meson-baryon channels have to be considered. In view of the dominance of two-pion-production channels in the photo-absorption process as seen in Figure 1.1, troublesome channels such as $\pi\pi N$, with the inherent three-body cut, cannot be circumvented. Since CC models involve numerous reaction channels, the number of free parameters that need to be fitted is substantially larger than in single-channel approaches. Therefore, the task of optimising the model is far from being trivial. In addition, comparing the different $\gamma p \to X$ reactions in Figure 1.1, one immediately observes that the kaon-production channel is several orders of magnitude smaller than the dominant πN, $\pi\pi N$, and ρN final states. Due to the reduced size and quality of the strangeness-production database in comparison to these channels, constraining the model parameters to the kaon-production results is complicated.

Because CC models still require tree-level amplitudes as input, many conceptual ambiguities related to the isobar approach remain relevant. Issues, such as the restoration of gauge invariance [55, 59, 60], continue to be pertinent [10] and can be more easily addressed at the level of a single-channel reaction model.

The Regge model and beyond

Despite the publication of a large body of high-quality $p(\gamma^{(*)}, K)Y$ data in recent years, phenomenological analyses have not led to an unequivocal outcome. Disentangling the relevant resonant contributions is challenging, because of the large number of competing resonances above the kaon production threshold. Moreover, the smooth energy dependence of the measured observables hints at a dominant role for the background, i.e. non-resonant, processes. Hence, the treatment of the background is pivotal for any model.

At sufficiently high energies, the isobar description is no longer optimal. Whereas empirical information indicates a smooth fall off for the cross section as one moves away from threshold, hadrodynamical models reveal a pathological rise. It comes as no surprise that the use of hadronic degrees of freedom cannot be justified above centre-of-mass energies of a few GeV, which corresponds to length scales below 0.1 fm. In this energy region, the kaon-production amplitude can be elegantly described within the Regge framework, characterised by the exchange of whole families of particles, instead of individual hadrons [38]. The Regge formalism boasts a number of attractive properties. Its amplitude

naturally fulfils analyticity, crossing symmetry and unitarity. In addition, only a limited number of free parameters are required. The applicability of the Regge formalism is obviously not limited to kaon production. Successful Regge-based models have been considered for the EM production of pions [38, 61, 62], η mesons [63, 64], K^* mesons [65] and $\Lambda(1520)$ hyperons [66].

Interestingly, the Regge model, a high-energy theory by construction, allows to describe the gross features of the data in the resonance region [39, 40, 67]. Extrapolating the Regge model to intermediate energies results in a reliable account of the kaon-production background. Additional support for the validity of the Regge approach in the resonance region was furnished in a recent study, where scaling compatible with Regge-trajectory exchange was clearly observed [68]. Near threshold, however, the energy dependence of the measured observables exhibits structures which hint at the presence of resonances and cannot be reproduced by a pure background model.

In Refs. [41, 42], a phenomenological mixing of the isobar and Regge descriptions is proposed. In the resonance region a traditional hadrodynamical model is constructed and as energy rises the isobar amplitude makes a smooth transition to the Regge model. In a different approach [39, 40, 69], the Regge amplitude is constrained by the available data at high energies and subsequently enriched with a carefully chosen selection of resonance-exchange diagrams. This gives way to a hybrid model that incorporates resonant features akin with the isobar approach and simultaneously maintains the correct high-energy limit. The resulting formalism was coined Regge-plus-resonance (RPR) and is schematically illustrated in Figure 1.3.

The major virtue of the RPR formalism lies in the economical parametrisation of the non-resonant part of the reaction amplitude. The isobar model requires the exchange of vector mesons in the t-channel, hyperon resonances in the u-channel in addition to the three Born diagrams to deal with the eminent background of kaon production. The Regge model, by contrast, manages an effective description using two t-channel exchange diagrams and a mere three coupling constants. Moreover, these free parameters can be fixed at high energies, thus effectively decoupling the evaluation of the background and resonant contributions to the reaction dynamics.

The deuteron as effective neutron target

Thus far, the lion's share of research efforts has been directed towards reactions off proton targets. The current EM kaon-production database is heavily dominated by the $p(\gamma^{(*)}, K^+)\Lambda$ and $p(\gamma^{(*)}, K^+)\Sigma^0$ channels. A comprehensive survey of the four remaining reactions, namely $n(\gamma, K^0)\Lambda$, $p(\gamma, K^0)\Sigma^+$, $n(\gamma, K^0)\Sigma^0$ and $n(\gamma, K^+)\Sigma^-$, would provide useful complementary information to elucidate the strangeness-production reaction mechanism. In the absence of a free neutron target, a trustworthy description of kaon production from the deuteron is of chief importance, for the deuteron's weak binding energy makes it a prime candidate as effective neutron target.

Our understanding of the nucleon-nucleon interaction is on solid ground [70] and the description of the EM interaction with deuterons in elastic electron scattering and breakup reactions is reliable [71]. Deuterium is often used as an effective neutron target. Deuteron electrodisintegration with either polarised targets, beams or ejectiles has allowed for the extraction of the neutron's electric and magnetic form factors, while in deep-inelastic scattering the neutron's structure functions have been determined. In all these cases, corrections due to the deuteron structure and to the reaction mechanism were shown to be either negligible, or calculable [72].

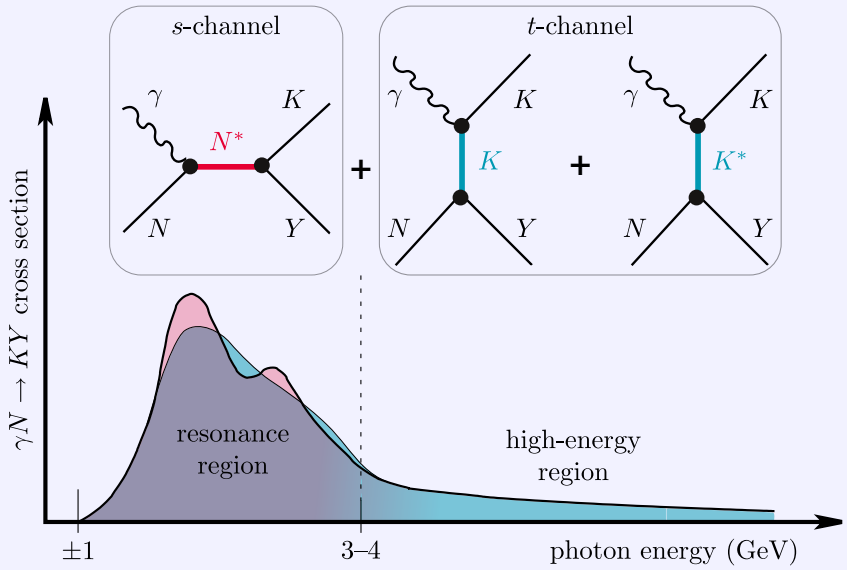

Figure 1.3 – Illustration of the RPR approach to EM strangeness production from the nucleon. At high energy, the structureless cross section is described via the exchange of $K(494)$ and $K^*(892)$ Regge-trajectories in the t-channel. This amplitude serves as an effective parametrisation of the non-resonant part of the reaction dynamics in the resonance region. An improved description of the data is realised by adding nucleon-resonance exchange in the s-channel. Figure adapted from Ref. [69].

The dominant contribution to kaon photoproduction off deuterium is expected to come from the quasi-elastic process. The incident photon interacts with a single nucleon inside the deuteron producing the strange meson and baryon. All final-state particles subsequently leave the region of interaction unperturbed as plane waves. As such, the kaon-production operator on a quasi-free neutron can readily be extracted. The influence of medium effects, however, significantly complicates this picture. The photoproduced hyperon and the spectator nucleon in the final state can undergo elastic and inelastic rescatterings before reaching the detector systems. This final-state interaction (FSI) can be considered a curse in case one wishes to examine elementary strangeness production. Yet, it also presents unique opportunities.

A wealth of information is available with regard to the interaction between nucleons. Yet, as Adelseck and Wright [73] elegantly put it, 'In order to obtain a comprehensive understanding of the strong interaction, it is essential that any theory reflect the underlying symmetry which is unveiled in the multiplet structure of the particles. Thus, it is indispensable to go beyond the nucleon-nucleon sector and incorporate and utilise aspects furnished by other members of the baryon multiplet, among them the Λ and Σ hyperon.'. The hyperon-nucleon (YN) interaction is currently only poorly constrained by experimental data. Direct measurements are held back by the challenges of building and operating a stable hyperon beam. A different possibility to study the YN interaction is offered by simultaneous production and scattering in the same target [74]. Hypernuclear spectroscopy is an active field and puts stringent constraints on our knowledge of the ΛN and ΣN potentials [74–76]. Exploiting hyperon-nucleon FSI in the kaon-production reaction gives access to an even larger dynamical range of the YN interaction. By focusing on kinematic regions where one expects important contributions from hyperons rescattering off the spectator nucleon, one can gain access to the elusive hyperon-nucleon interaction.

Renard and Renard were among the pioneers to study kaon production on the nucleon and also led the way in strangeness reactions from the deuteron [77, 78]. In their work, they employed a simple parametrisation of the YN interaction. Modern hyperon-nucleon potentials based on one-boson exchange were used in Refs. [73, 79, 80]. Yamamura *et al.* were the first to revisit the reaction adopting a modern elementary kaon-production operator optimised against high-quality data [81]. Including the effect of hyperon-nucleon FSI with the Nijmegen YN potential, the inclusive and exclusive charged-kaon-production cross sections were studied. At a later time, polarisation observables in exclusive kaon photoproduction were investigated [82]. The approach was extended in Refs. [83, 84] to include two-step production and kaon-nucleon rescattering. Adopting this model, neutral-kaon photoproduction has been studied. Refs. [85, 86] have focused on the extraction of the elementary amplitude. A different study on the influence of YN rescattering using the P-matrix approach was presented in Ref. [87]. Maxwell considered a host of rescattering diagrams where a π, η or K meson is exchanged between the active nucleon, which absorbs the incoming photon, and the spectator nucleon [28, 88]. In Refs. [89, 90], kaon photoproduction from deuteron is investigated using a variety of isobar models in the non-relativistic plane-wave impulse approximation, demonstrating the importance of a reliable elementary-production operator. Gasparyan *et al.* studied the possibility to extract the low-energy Λn scattering parameters [91]. They investigated specific polarisation observables and kinematics needed to isolate the singlet and triplet states of Λn scattering. Likewise, Laget identifies well-defined regions in phase space where KN and YN rescattering dominate while the elementary amplitude is on shell and the momentum of the spectator nucleon is low [92, 93]. To date, very few studies have considered electron-induced strangeness production from the deuteron. Hsiao and Cotanch [94, 95] used the elementary-production operator of Thom [17]. In Ref. [96] the Saclay-Lyon model [22] was adopted.

Outline

In this work, we present a covariant formalism for the photo- and electroproduction of kaons and hyperons from the deuteron, thereby accounting for hyperon-nucleon rescattering.

In Chapter 2, the elementary-production operator is introduced. We begin our discussion with an overview of the kinematics and observables relevant to EM kaon production from the nucleon. Then, we turn our attention to the RPR formalism. At high-energies, an adequate description of the data is realised using the Regge model. The Reggeization procedure is discussed and an elegant recipe to guarantee a gauge-invariant amplitude is outlined. In a next step, a model including resonance-exchange diagrams is optimised to the resonance-region data, while the three free parameters of the Regge model are held fixed. Successful descriptions of the $K^+\Lambda$- and $K^+\Sigma^0$-production data obtained before 2007 are realised. We conclude this chapter with a critical discussion of the RPR model as it was published in Refs. [39, 40, 69, 97]. Recent developments of the RPR formalism are highlighted and comparisons with the latest photo- and electroproduction results are shown. This illustrates the descriptive and predictive power of the RPR model in the data-rich reaction channels.

Chapter 3 is devoted to those kaon-production channels where little or no experimental results are at hand. A formalism is presented in order to transform the RPR transition amplitude that was fitted to $p(\gamma^{(*)}, K^+)\Lambda$ and $p(\gamma^{(*)}, K^+)\Sigma^0$ to the other $N(\gamma^{(*)}, K)Y$ reaction channels. At the strong-interaction vertices, one can rely on SU(2) isospin symmetry. The conversion of the EM coupling constants, on the other hand, requires experimental input. The resulting RPR-model predictions

are set against the world data for $K^+\Sigma^-$ production from the neutron and $K^0\Sigma^+$ production from the proton. The sensitivity to the errors bars of the applied photocoupling helicity amplitudes is investigated.

In Chapter 4, we make a small digression. The Regge model is employed in a exploratory study of new results on radiative kaon capture. This reaction is related to kaon photoproduction through crossing symmetry and is sensitive to the excited states of Λ and Σ hyperons.

After having established the RPR framework, we turn our attention to strangeness production from the deuteron in Chapter 5. The kinematics are reviewed and the observables of the reaction are defined in terms of the transition amplitude. The deuteron wave function is an essential ingredient of the reaction dynamics and is discussed at length. We examine relativistic and non-relativistic wave functions and introduce a covariant vertex operator for the deuteron-neutron-proton transition. The transition amplitude is given in the relativistic impulse approximation. We define the plane-wave approximation and provide a non-relativistic reduction. In addition, the contribution of hyperon-nucleon rescattering is derived. We find that it can be decomposed in two parts. The first term has all rescattering particles on mass shell, while the other involves off-mass-shell particles and allows for sub-threshold production.

Chapter 6 is dedicated to the numerical results of the calculations. In a first step, the relativistic plane-wave impulse approximation is thoroughly investigated. We study the sensitivity of the computed observables to relativistic effects, to the deuteron wave function, and to the off-shell extrapolation of the elementary-production operator. In addition, the propagation of the uncertainties related to kaon production from the neutron is investigated. Subsequently, the dynamics of the hyperon-nucleon rescattering contribution are examined. In the final section, we confront our predictions with the available experimental results. We state our conclusions in Chapter 7 and indicate directions for future work.

For reasons of readability, many technical details have been diverted to the appendices. Appendix A establishes the notations and conventions assumed in this dissertation. In Appendix B, we briefly introduce the number system of biquaternions and their applicability as representation of the Lorentz group.

Owing to their elegant transformation properties under Lorentz transformations, helicity spinors play an important role in our formalism. Appendix C is devoted to the subject. Appendix D summarises the rules and ingredients needed to compute cross sections. We list the interaction Lagrangians adopted in this work, as well as the transition amplitudes for the Feynman diagrams considered in the RPR model.

In Appendix E, the derivation of two Lorentz-invariant forms of the ${}^2\mathrm{H}(\gamma, KY)N$ cross section is given. The density-matrix formalism is the topic of Appendix F. Density matrices play an important role in the construction of polarisation observables.

This work makes use of a number of deuteron wave functions. Their parametrisations are provided in Appendix G. Subsequently, Appendix H retraces the connection between these wave functions and the covariant Dnp-vertex. In Appendix I, we tabulate the coupling constants of the adopted RPR model for all six strangeness-production reaction channels. An overview of the published experimental data for kaon photoproduction from the nucleon is given in Appendix J. Lastly, Appendix K presents some details about the hyperon-nucleon interaction and more specifically the Jülich potential.

CHAPTER 2

The Regge-plus-resonance formalism

It comes as no surprise that a trustworthy model for elementary kaon production is an essential ingredient in the description of strangeness production from the deuteron. With this in mind, we provide a detailed discussion of the RPR formalism in this chapter. Section 2.1 gives an overview of the kinematics of the $N(\gamma^{(*)}, K)Y$ reaction and defines the relevant observables for photo- and electroproduction. In the high-energy limit, pseudo-scalar meson production can be elegantly described via the exchange of Regge trajectories. In Section 2.2, we present a Regge model for both the $p(\gamma, K^+)\Lambda$ and $p(\gamma, K^+)\Sigma^0$ reaction channels. Extrapolating this Regge model into the resonance region provides an efficient parametrisation of the non-resonant contributions to the transition amplitude. By enriching the Regge-model amplitude with a number of s-channel nucleon-resonance exchange diagrams, a satisfactory account of the available kaon-production data in the resonance region can be achieved. This is the topic of Section 2.3.

The RPR model that we are about to introduce, dubbed RPR-2007, was the subject of T. Corthals' doctoral thesis [69]. The results for Λ and Σ photoproduction have been presented in Refs. [39, 40]. The formalism was extended to electroproduction reactions in Ref. [97]. Following the publication of these results, a considerable amount of additional experimental results have been made available (see Appendix J for an overview). These new data sets have confirmed the predictive power of the RPR formalism, in spite of its apparent simplicity. Nevertheless, a number of shortcomings exist. In Section 2.4, the merits and weaknesses of the current RPR model are identified. The reader should be aware that the RPR model is the subject of continuous efforts and is constantly being improved. For recent developments, we refer the reader to Refs. [56, 98, 99] for more information.

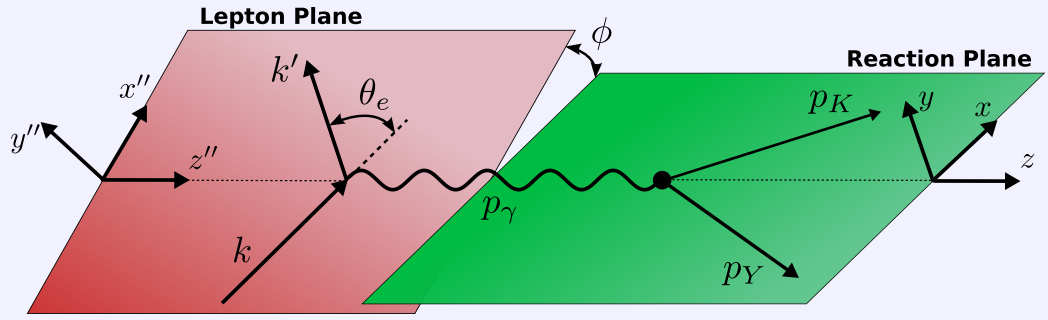

Figure 2.1 – Schematic representation of an electron scattering from a nucleon at rest, producing a kaon and hyperon in the final state.

2.1 Kinematics and observables

2.1.1 Reference frames

Electron-induced kaon production from a free nucleon assuming the OPE approximation is illustrated schematically in Figure 2.1. The incoming and outgoing electrons, with four-momenta $\boldsymbol{k}(E_e, \vec{k})$ and $\boldsymbol{k'}(E'_e, \vec{k}')$ respectively, radiate a virtual photon with four-momentum $\boldsymbol{p}_\gamma(E_\gamma, \vec{p}_\gamma) = \boldsymbol{k} - \boldsymbol{k'}$ and virtuality $Q^2 = -\boldsymbol{p}_\gamma \cdot \boldsymbol{p}_\gamma = |\vec{p}_\gamma|^2 - E_\gamma^2$. This photon interacts with a nucleon $\boldsymbol{p}_N(E_N, \vec{p}_N)$ and produces two outgoing particles, i.e. the kaon and hyperon, which are labelled $\boldsymbol{p}_K(E_K, \vec{p}_K)$ and $\boldsymbol{p}_Y(E_Y, \vec{p}_Y)$ respectively. The three-vectors $\vec{k}$ and $\vec{k}'$ span the lepton plane, whereas the three-momenta of the photon, nucleon, kaon and hyperon lie in the reaction plane. The relative inclination of both planes is given by the angle ϕ. For kaon photoproduction, this angle is arbitrary and the photon's virtuality Q^2 vanishes.

The $N(\gamma^{(*)}, K)Y$ reaction can be readily described in the KY-CM frame. Three different reference frames are commonly adopted in order to express the particles' four-momenta and polarisations. They are indicated in Figure 2.2. All three choices have their y axis perpendicular to the reaction plane. For the unprimed reference frame, we take the z axis along the photon three-momentum. The other reference frames have the z' (l) axis parallel to the kaon (hyperon). Explicitly we have,

$$\vec{z} = \frac{\vec{p}_\gamma}{|\vec{p}_\gamma|}\,, \qquad \vec{y} = \frac{\vec{p}_\gamma \times \vec{p}_K}{|\vec{p}_\gamma \times \vec{p}_K|}\,, \qquad \vec{x} = \vec{y} \times \vec{z}\,, \tag{2.1}$$

$$\vec{z}' = \frac{\vec{p}_K}{|\vec{p}_K|}\,, \qquad \vec{y}' = \vec{y}\,, \qquad \vec{x}' = \vec{y}' \times \vec{z}'\,, \tag{2.2}$$

$$\vec{l} = \frac{\vec{p}_Y}{|\vec{p}_Y|}\,, \qquad \vec{n} = \vec{y}\,, \qquad \vec{t} = \vec{n} \times \vec{l}\,. \tag{2.3}$$

In addition, a fourth double-primed reference frame is defined in Figure 2.1, which has its y'' axis perpendicular to the lepton plane.

$$\vec{z}'' = \frac{\vec{p}_\gamma}{|\vec{p}_\gamma|}\,, \qquad \vec{y}'' = \frac{\vec{k} \times \vec{k}'}{|\vec{k} \times \vec{k}'|}\,, \qquad \vec{x}'' = \vec{y}'' \times \vec{z}''\,. \tag{2.4}$$

Variables that are expressed in the KY-CM frame are labelled with an asterisk to make the distinction with those declared in the LAB frame where the target nucleon is at rest.

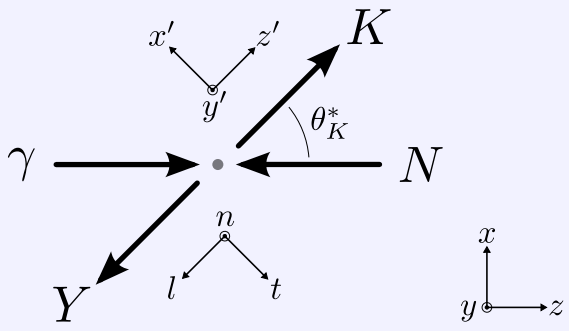

Figure 2.2 – Orientation of the different reference frames (x, y, z), (x', y', z') and (t, n, l) for the $N(\gamma, K)Y$ reaction in the KY-CM frame.

2.1.2 Independent variables

The CM scattering angle of the kaon θ_K^* and the system's invariant mass

$$W_{KY} = \sqrt{(\boldsymbol{p}_\gamma + \boldsymbol{p}_N)^2} = -Q^2 + m_N^2 + 2E_\gamma m_N \,, \tag{2.5}$$

determine the $N(\gamma^{(*)}, K)Y$ kinematics unambiguously. The photon energy in the CM and LAB frames are connected through a Lorentz transformation

$$E_\gamma^* = \frac{W_{KY}^2 - m_N^2 - Q^2}{2W_{KY}} \,. \tag{2.6}$$

By solving the energy-conservation relation in the KY-CM

$$E_\gamma^* + \sqrt{Q^2 + E_\gamma^{*2} + m_N^2} = \sqrt{|\vec{p}_K^*|^2 + m_K^2} + \sqrt{|\vec{p}_K^*|^2 + m_Y^2} \,, \tag{2.7}$$

the kaon momentum $|\vec{p}_K^*|$ can be determined.

Three Mandelstam variables are defined

$$\begin{aligned} s_{KY} &= (\boldsymbol{p}_\gamma + \boldsymbol{p}_N)^2 \,, \\ t &= (\boldsymbol{p}_\gamma - \boldsymbol{p}_K)^2 \,, \\ u &= (\boldsymbol{p}_\gamma - \boldsymbol{p}_Y)^2 \,. \end{aligned} \tag{2.8}$$

An elegant relation exists between these Lorentz-invariant variables

$$s_{KY} + t + u = -Q^2 + m_N^2 + m_K^2 + m_Y^2 \,. \tag{2.9}$$

2.1.3 Transition amplitude

The dynamics of the kaon-production reaction are contained in the hadronic transition amplitude

$$\mathcal{T}_{\lambda_N \lambda_Y}^{\lambda_\gamma} \equiv \langle \boldsymbol{p}_K; \boldsymbol{p}_Y, \lambda_Y | \, \epsilon_\mu^{\lambda_\gamma} \hat{J}^\mu \, | \boldsymbol{p}_N, \lambda_N \rangle \,. \tag{2.10}$$

This is the expectation value of the transition current operator $\hat{J}^\mu$ evaluated between the normalised states of the incoming and outgoing particles with definite polarisation. The polarisation vector $\epsilon^{\lambda_\gamma}$ for a linearly polarised photon along the x or y axis reads

$$\epsilon^{\lambda_\gamma = x} = (0, 1, 0, 0) \,, \quad \text{or} \quad \epsilon^{\lambda_\gamma = y} = (0, 0, 1, 0) \,. \tag{2.11}$$

For circularly polarised photons, one has

$$\epsilon^{\lambda_\gamma=\pm1} = \mp\frac{1}{\sqrt{2}}(0,1,\pm i,0)\,, \tag{2.12}$$

whereas virtual photons can also have a longitudinal polarisation

$$\epsilon^{\lambda_\gamma=0} = (0,0,0,1)\,. \tag{2.13}$$

The transition current operator can be constructed from a set of relevant Feynman diagrams. In Sections 2.2 and 2.3, the structure of this operator in the RPR formalism will be discussed in depth. The transition matrix elements fulfil the following useful property [100]

$$\mathcal{T}_{-\lambda_N-\lambda_Y}^{-\lambda_\gamma} = (-1)^{1+\lambda_\gamma-\lambda_N-\lambda_Y}\mathcal{T}_{\lambda_N\lambda_Y}^{\lambda_\gamma}\,, \quad \text{for} \quad \lambda_\gamma = 0,\pm1\,, \tag{2.14}$$

owing to the reaction's invariance under space inversions and rotations. This relation reduces the number of independent amplitudes by a factor of two. In the transversity basis for real photon reactions, one chooses the following set of independent amplitudes

$$\begin{aligned} b_1 &= \mathcal{T}^{y}_{+\frac{1}{2},+\frac{1}{2}}\,,\\ b_2 &= \mathcal{T}^{y}_{-\frac{1}{2},-\frac{1}{2}}\,,\\ b_3 &= \mathcal{T}^{x}_{-\frac{1}{2},+\frac{1}{2}}\,,\\ b_4 &= \mathcal{T}^{x}_{+\frac{1}{2},-\frac{1}{2}}\,, \end{aligned} \tag{2.15}$$

where photons have a linear polarisation and the baryon polarisations are quantised along the y axis, i.e. normal to the reaction plane.

2.1.4 Photoproduction observables

The differential cross section for the most general scattering reaction is given in Eq. (D.1). Applying this to the kaon photoproduction reaction, one finds

$$d\sigma = \frac{1}{2\sqrt{\lambda(s_{KY},0,m_N^2)}}\overline{\sum}|\mathcal{T}|^2\frac{d^3\vec{p}_K}{2E_K(2\pi)^3}\frac{d^3\vec{p}_Y}{2E_Y(2\pi)^3}(2\pi)^4\delta^{(4)}(\boldsymbol{p}_\gamma+\boldsymbol{p}_N-\boldsymbol{p}_K-\boldsymbol{p}_Y)\,. \tag{2.16}$$

Here, the symbol $\overline{\sum}$ implies that one sums (averages) over the polarisations of the outgoing (incoming) particles. After integrating out the energy-momentum conserving delta function, one commonly expresses the differential cross section as

$$\frac{d^2\sigma}{d\Omega_K^*} = \frac{1}{64\pi^2}\frac{|\vec{p}_K^{\,*}|}{E_\gamma^* W_{KY}^2}\overline{\sum}|\mathcal{T}|^2\,. \tag{2.17}$$

At higher energies, where the reaction becomes diffractive, the cross section is often reported in the following Lorentz-invariant form

$$\frac{d\sigma}{dt} = \frac{1}{64\pi}\frac{1}{E_\gamma^{*2}W_{KY}^2}\overline{\sum}|\mathcal{T}|^2\,. \tag{2.18}$$

In experiments where one or more external particles have a definite polarisation, one commonly presents the results in terms of asymmetries. Owing to the tremendous advances in accelerator and detector technology, in addition to the self-analysing weak-decay property of hyperons, kaon production offers a unique opportunity to measure a comprehensive set of polarisation observables. At leading experimental facilities, such research programs are currently being pursued [101, 102]. Given the differential cross section supplemented with seven well-chosen asymmetries, the transition amplitude can uniquely be deduced [51, 53, 54]. This is often referred to as a *complete* measurement. One should realise, however, that uncertainties inherent to experimental observables set restrictions on the theoretical completeness of a measurement [103].

The prospect of a complete experiment has fostered a large number of studies that aim at studying the most general expression for the differential pseudo-scalar meson-production cross section [20, 51, 104–107]. Among these works, some disagreements exist [51]. These arise from different sign conventions for the polarisation states. In this work, we adopt the definitions provided by Adelseck and Saghai [20], who express all observables in terms of the transversity amplitudes (2.15).

Single-polarisation asymmetries are defined as

$$\frac{d\sigma^{(+)} - d\sigma^{(-)}}{d\sigma^{(+)} + d\sigma^{(-)}} \,. \tag{2.19}$$

Double-polarisation asymmetries adopt the form

$$\frac{d\sigma^{(++)} + d\sigma^{(--)} - d\sigma^{(+-)} - d\sigma^{(-+)}}{d\sigma^{(++)} + d\sigma^{(--)} + d\sigma^{(+-)} + d\sigma^{(-+)}} \,. \tag{2.20}$$

Here, $d\sigma^{(\pm)}$ and $d\sigma^{(\pm\pm)}$ denote cross sections where one or two particles have a definite polarisation. The polarisation state of the incoming photon is determined by the polarisation vectors given in Eqs. (2.11)–(2.13). For the hadrons involved in the reaction, the polarisations are (anti-)parallel to their respective quantisation axes. The complete list of quantisation axes per polarisation asymmetry is given in Table II of Ref.[20]. For experiments that involve one polarised particle, one defines the photon-beam (Σ), recoil (P) and target asymmetries (T)

$$\begin{aligned} \Sigma &= \mathcal{N}^{-1} \times \left(|b_1|^2 + |b_2|^2 - |b_3|^2 - |b_4|^2 \right) \,, \\ P &= \mathcal{N}^{-1} \times \left(|b_1|^2 - |b_2|^2 + |b_3|^2 - |b_4|^2 \right) \,, \\ T &= \mathcal{N}^{-1} \times \left(|b_1|^2 - |b_2|^2 - |b_3|^2 + |b_4|^2 \right) \,, \end{aligned} \tag{2.21}$$

with

$$\mathcal{N} = |b_1|^2 + |b_2|^2 + |b_3|^2 + |b_4|^2 \,. \tag{2.22}$$

For double polarisation experiments, a total of twelve asymmetries exist. Here, we restrict ourselves to providing the definition of those involving beam and recoil polarisations

$$\begin{aligned} C_{x'} &= -2\mathcal{N}^{-1} \times \Im \left(b_1 b_4^* - b_2 b_3^* \right) \,, \\ C_{z'} &= 2\mathcal{N}^{-1} \times \Re \left(b_1 b_4^* + b_2 b_3^* \right) \,, \\ O_{x'} &= 2\mathcal{N}^{-1} \times \Re \left(b_1 b_4^* - b_2 b_3^* \right) \,, \\ O_{z'} &= 2\mathcal{N}^{-1} \times \Im \left(b_1 b_4^* + b_2 b_3^* \right) \,. \end{aligned} \tag{2.23}$$

The notation $C_{x',z'}$ ($O_{x',z'}$) refers to circularly (linearly) polarised photons. The former can also be expressed with the quantisation axis along the unprimed axes defined in Eq. (2.1). Applying a

straightforward rotation, they read

$$\begin{aligned} C_x &= C_{x'} \cos\theta_K^* + C_{z'} \sin\theta_K^* \,, \\ C_z &= -C_{x'} \sin\theta_K^* + C_{z'} \cos\theta_K^* \,. \end{aligned} \tag{2.24}$$

2.1.5 Electroproduction observables

Starting from the general expression (D.1), one finds the $N(e,e'K)Y$ differential cross section can be written in the following factorised form[1]

$$\frac{d^5\sigma}{dE'_e d\Omega'_e d\Omega_K^*} = \Gamma \frac{d^2\sigma^*}{d\Omega_K^*} \,, \tag{2.25}$$

where

$$\Gamma = \frac{\alpha}{2\pi^2} \frac{E'_e}{E_e} \frac{K_H}{Q^2} \frac{1}{1-\epsilon} \,, \tag{2.26}$$

is the virtual photon flux factor and

$$K_H = E_\gamma - \frac{Q^2}{2m_N} \,, \tag{2.27}$$

the equivalent-real-photon laboratory energy. The most general form for the virtual-photon cross section reads [105]

$$\begin{aligned} \frac{d^2\sigma^*}{d\Omega_K^*} = P_\alpha^N P_\beta^Y \frac{|\vec{p}_K^*|}{|\vec{p}_\gamma^*|} \Big[& \mathcal{R}_T^{\beta\alpha} + \epsilon \mathcal{R}_L^{\beta\alpha} + \epsilon \Big({}^c\mathcal{R}_{TT}^{\beta\alpha} \cos 2\phi + {}^s\mathcal{R}_{TT}^{\beta\alpha} \sin 2\phi \Big) \\ & + \sqrt{\epsilon(1+\epsilon)} \Big({}^c\mathcal{R}_{LT}^{\beta\alpha} \cos\phi + {}^s\mathcal{R}_{LT}^{\beta\alpha} \sin\phi \Big) \\ & + h\sqrt{1-\epsilon^2} \mathcal{R}_{T'}^{\beta\alpha} + h\sqrt{\epsilon(1-\epsilon)} \Big({}^c\mathcal{R}_{LT'}^{\beta\alpha} \cos\phi + {}^s\mathcal{R}_{LT'}^{\beta\alpha} \sin\phi \Big) \Big] \,, \end{aligned} \tag{2.28}$$

with h the electron-beam helicity and

$$\epsilon = \left(1 + \frac{2|\vec{p}_\gamma|^2}{Q^2} \tan^2 \frac{\theta_e}{2} \right)^{-1} \,, \tag{2.29}$$

the transverse linear polarisation of the virtual photon. In the expression for the virtual-photon cross section, a summation over the Greek indices ($\alpha, \beta = 0, 1, 2, 3$) is implied. The operators

$$P_\mu^i \equiv (1, \vec{P}^{\,i}) \,, \quad \text{with} \quad i = N, Y \,, \tag{2.30}$$

are given in terms of the polarisation vectors $\vec{P}^{\,N}$ and $\vec{P}^{\,Y}$ of the nucleon and hyperon respectively. The polarisations of these baryons can be evaluated in any of the frames presented in Figure 2.2. The dynamics of the EM kaon-production reaction is contained in the response functions, which are

[1] A detailed account of the factorisation of the electroproduction cross section for EM kaon production from the deuteron is given in Section 5.4. The derivation of the results given in Eqs. (2.25)–(2.31) proceeds along similar lines.

defined by

$$
\begin{aligned}
\mathcal{R}_T^{\beta\alpha} &= \chi\widetilde{\sum}_{\alpha,\beta}\Big(|\mathcal{T}^+|^2+|\mathcal{T}^-|^2\Big)\,, & \mathcal{R}_L^{\beta\alpha} &= 2\chi\widetilde{\sum}_{\alpha,\beta}|\mathcal{T}^0|^2\,,\\
{}^c\mathcal{R}_{TT}^{\beta\alpha} &= -2\chi\widetilde{\sum}_{\alpha,\beta}\Re\Big(\mathcal{T}^+\mathcal{T}^{-\dagger}\Big)\,, & {}^s\mathcal{R}_{TT}^{\beta\alpha} &= 2\chi\widetilde{\sum}_{\alpha,\beta}\Im\Big(\mathcal{T}^+\mathcal{T}^{-\dagger}\Big)\,,\\
{}^c\mathcal{R}_{LT}^{\beta\alpha} &= -2\chi\widetilde{\sum}_{\alpha,\beta}\Re\Big(\mathcal{T}^0\left(\mathcal{T}^+-\mathcal{T}^-\right)^\dagger\Big)\,, & {}^s\mathcal{R}_{LT}^{\beta\alpha} &= -2\chi\widetilde{\sum}_{\alpha,\beta}\Im\Big(\mathcal{T}^0\left(\mathcal{T}^++\mathcal{T}^-\right)^\dagger\Big)\,,\\
{}^c\mathcal{R}_{LT'}^{\beta\alpha} &= -2\chi\widetilde{\sum}_{\alpha,\beta}\Re\Big(\mathcal{T}^0\left(\mathcal{T}^++\mathcal{T}^-\right)^\dagger\Big)\,, & {}^s\mathcal{R}_{LT'}^{\beta\alpha} &= -2\chi\widetilde{\sum}_{\alpha,\beta}\Im\Big(\mathcal{T}^0\left(\mathcal{T}^+-\mathcal{T}^+\right)^\dagger\Big)\,,\\
\mathcal{R}_{T'}^{\beta\alpha} &= \chi\widetilde{\sum}_{\alpha,\beta}\Big(|\mathcal{T}^+|^2-|\mathcal{T}^-|^2\Big)\,,
\end{aligned}
\tag{2.31}
$$

with

$$
\chi = \frac{|\vec{p}^{\,*}_\gamma|}{(16\pi)^2 m_N W_{KY} K_H}\,. \tag{2.32}
$$

The response functions $\mathcal{R}_i^{\beta\alpha}$ are expressed in terms of the hadronic transition amplitudes (2.10) and are evaluated in the CM of the kaon-hyperon system at $\phi = 0$. For convenience, we have dropped the polarisation states λ_N and λ_Y from our notation for the transition amplitude. The symbol $\widetilde{\sum}_{\alpha,\beta}$ denotes the bilinear products are summed over the nucleon (hyperon) polarisation when $\alpha(\beta) = 0$, e.g.

$$
\mathcal{R}_L^{00} = 2\chi \sum_{\lambda_N\lambda_Y} |\mathcal{T}^0_{\lambda_N\lambda_Y}|^2\,. \tag{2.33}
$$

For $\alpha, \beta \neq 0$, the difference between the polarisation states is implied, e.g.

$$
\mathcal{R}_L^{y0} = 2\chi \sum_{\lambda_Y} \left(|\mathcal{T}^0_{\lambda_N=+y,\lambda_Y}|^2 - |\mathcal{T}^0_{\lambda_N=-y,\lambda_Y}|^2\right)\,. \tag{2.34}
$$

Owing to parity conservation (2.14), some response functions vanish identically (see Table I of Ref. [105] for an overview).

The expression (2.28) is of limited use since exclusive measurements with all incoming and outgoing particles polarised are extremely challenging. For undetermined target and recoil polarisations, the components of the polarisation vectors $\vec{P}^{\,N}$ and $\vec{P}^{\,Y}$ vanish and the cross section reduces to

$$
\frac{d^2\sigma^*}{d\Omega_K^*} = \frac{d^2\sigma_T}{d\Omega_K^*} + \epsilon\frac{d^2\sigma_L}{d\Omega_K^*} + \epsilon\frac{d^2\sigma_{TT}}{d\Omega_K^*}\cos 2\phi + \sqrt{\epsilon(1+\epsilon)}\frac{d^2\sigma_{LT}}{d\Omega_K^*}\cos\phi + h\sqrt{\epsilon(1-\epsilon)}\frac{d^2\sigma_{LT'}}{d\Omega_K^*}\sin\phi\,, \tag{2.35}
$$

with

$$
\begin{aligned}
\frac{d^2\sigma_i}{d\Omega_K^*} &= \frac{|\vec{p}^{\,*}_K|}{|\vec{p}^{\,*}_\gamma|}\mathcal{R}_i^{00}\,, && \text{for} \quad i = T, L\,,\\
\frac{d^2\sigma_i}{d\Omega_K^*} &= \frac{|\vec{p}^{\,*}_K|}{|\vec{p}^{\,*}_\gamma|}{}^c\mathcal{R}_i^{00}\,, && \text{for} \quad i = TT, LT\,,
\end{aligned}
\tag{2.36}
$$

and

$$
\frac{d^2\sigma_{LT'}}{d\Omega_K^*} = \frac{|\vec{p}^{\,*}_K|}{|\vec{p}^{\,*}_\gamma|}{}^s\mathcal{R}_{LT'}^{00}\,. \tag{2.37}
$$

Another expression of practical use involves the combination of a polarised beam impinging on an unpolarized target and a measurement which determines the polarisation of the outgoing hyperon. For this situation, the virtual-photon cross section can be parametrised as

$$\frac{d^2\sigma^*}{d\Omega_K^*} = \sigma_{\text{unpol}} \left(1 + hA_{LT'} + P_x\, \vec{x}\cdot\vec{P}^Y + P_y\, \vec{y}\cdot\vec{P}^Y + P_z\, \vec{z}\cdot\vec{P}^Y\right) , \tag{2.38}$$

where σ_{unpol} is the unpolarized differential cross section. The recoil-polarisation P_i, in turn, can be expressed as the sum of an induced polarisation P_i^0 and a transferred polarisation P_i'

$$P_i = P_i^0 + hP_i' , \quad \text{for} \quad i = x, y, z . \tag{2.39}$$

By equating the Eqs. (2.28) and (2.38), it is possible to express the induced and transferred polarisations in terms of the response functions. In practise, the statistics of an experiment can be improved by integrating over the angle ϕ between the lepton and reaction plane. This implies that the azimuthal-angle dependence of Eq. (2.28) can be integrated out. As such the number of terms is greatly reduced. After some easy algebra, one finds for the ϕ-integrated polarisations[2]

$$\begin{aligned}
P_x^0 &= P_z^0 = P_y' = 0 , \\
P_y^0 &= \frac{1}{2}\sqrt{\epsilon(1+\epsilon)}K_0^{-1}\left({}^s\mathcal{R}_{LT}^{x'0}\cos\theta_K^* + {}^c\mathcal{R}_{LT}^{y'0} + {}^s\mathcal{R}_{LT}^{z'0}\sin\theta_K^*\right) , \\
P_x' &= \frac{1}{2}\sqrt{\epsilon(1-\epsilon)}K_0^{-1}\left({}^c\mathcal{R}_{LT'}^{x'0}\cos\theta_K^* - {}^s\mathcal{R}_{LT'}^{y'0} + {}^c\mathcal{R}_{LT'}^{z'0}\sin\theta_K^*\right) , \\
P_z' &= \sqrt{1-\epsilon^2}K_0^{-1}\left(-\mathcal{R}_{T'}^{x'0}\sin\theta_K^* + \mathcal{R}_{T'}^{z'0}\cos\theta_K^*\right) ,
\end{aligned} \tag{2.40}$$

where $K_0 = \mathcal{R}_T^{00} + \epsilon\mathcal{R}_L^{00}$.

2.2 Kaon production in the Regge limit

The study of kaon production, and by extension all meson-production reactions, is primarily motivated by the exploration of the nucleon-resonance spectrum. Therefore, analyses of experimental data focus on the so-called resonance region, which roughly corresponds to $W_{KY} \lesssim 2.5\,\text{GeV}$. Nevertheless, one cannot ignore the contribution of non-resonant diagrams that are looked on as a *background* with an eye to extracting nucleon-resonance information. The kaon-production cross section lacks clear indications of dominant resonant states which hints that background contributions are by no means subordinate to resonance exchange. As such, the description of the background is crucial in order to extract reliable information on the nucleon-resonance spectrum. The RPR formalism takes an uncommon approach and first focuses on modelling kaon production at energies beyond the resonance region where only non-resonant diagrams subsist.

At high energies, hadronic scattering processes can be elegantly described in the framework of Regge theory. Based on the observation that it is useful to regard angular momentum as a complex variable when discussing solutions of the Schrödinger equation for non-relativistic potential scattering [108], a successful theory was developed. It describes a large variety of concepts and results in high-energy

[2] In literature, one commonly adopts the notation P_i^0 and P_i' for the ϕ-integrated induced and transferred polarisations. This notation can lead to confusion with the P_i^0/P_i' that feature in the cross-section decomposition of Eq. (2.38). For the remainder of this work, the symbols P_i^0 and P_i' will refer to ϕ-integrated observables.

scattering experiments. A comprehensive discussion of Regge phenomenology falls beyond the scope of this dissertation and we refer the interested reader to the works of Collins [109] and Donnachie [110].

Starting from the general principles of unitarity, analyticity and crossing symmetry, Regge theory puts forward a link between the existence of bound states in direct scattering reactions and the exchange of unstable particles in the crossed channels. This link is manifested by the existence of so-called Regge trajectories, which unify *families* of particles that share identical internal quantum numbers. Each trajectory represents an analytic relation $J = \alpha(m^2)$ between the mass m and the spin J of particles with even (odd) spin that belong to the same family. This relation can be conveniently visualised in a Chew-Frautschi plot (see Figure 3.9 for examples). Experimentally, the Regge trajectories for baryons and mesons turn out to be linear to a good approximation and appear to have a universal slope [111]. Conventionally, Regge trajectories are named after their first materialisation.

Building upon the work of Guidal, Laget and Vanderhaeghen [38, 112], we model the high-energy $p(\gamma, K^+)Y$ amplitude by means of $K^+(494)$ and $K^{*+}(892)$ Regge-trajectory exchange in the t-channel. A gauge-invariant amplitude is obtained by adding the Reggeized electric part of the nucleon s-channel Born diagram [69]. The strong forward-peaked character of the differential cross section, as shown in Figure 2.3, provides strong support for this approach. The exchange of a linear kaon Regge-trajectory

$$\alpha_{K^{(*)+}}(t) = \alpha_{K^{(*)+},0} + \alpha'_{K^{(*)+}} \left(t - m^2_{K^{(*)+}}\right) , \tag{2.41}$$

with $m_{K^{(*)+}}$ and $\alpha_{K^{(*)+},0}$ the kaon's mass and spin, is realised through a Reggeized amplitude that combines elements of the Regge formalism and a tree-level effective-Lagrangian model. Reggeization amounts to replacing the standard Feynman $(t - m^2_{K^{(*)+}})^{-1}$ propagator by the corresponding Regge propagator

$$\begin{aligned}
\mathcal{P}^{K^+(494)}_{\text{Regge}}(s,t) &= \left(\frac{s}{s_0}\right)^{\alpha_{K^+}(t)} \frac{\left\{\begin{array}{c} 1 \\ e^{-i\pi\alpha_{K^+}(t)} \end{array}\right\}}{\sin\big(\pi\alpha_{K^+}(t)\big)} \frac{\pi\alpha'_{K^+}}{\Gamma\big(1+\alpha_{K^+}(t)\big)} , \\
\mathcal{P}^{K^{*+}(892)}_{\text{Regge}}(s,t) &= \left(\frac{s}{s_0}\right)^{\alpha_{K^{*+}}(t)-1} \frac{\left\{\begin{array}{c} 1 \\ e^{-i\pi\alpha_{K^{*+}}(t)} \end{array}\right\}}{\sin\big(\pi\alpha_{K^{*+}}(t)\big)} \frac{\pi\alpha'_{K^{*+}}}{\Gamma\big(\alpha_{K^{*+}}(t)\big)} ,
\end{aligned} \tag{2.42}$$

with $s_0 = 1\,\text{GeV}^2$ a scale factor. The Regge trajectories are parametrised as

$$\begin{aligned}
\alpha_{K^+}(t) &= 0.70\ (t - m^2_{K^+}) , \\
\alpha_{K^{*+}}(t) &= 1 + 0.85\ (t - m^2_{K^{*+}}) ,
\end{aligned} \tag{2.43}$$

when t and $m^2_{K^{(*)+}}$ are expressed in units of GeV^2. The data [113, 114] indicate that the trajectories are strongly degenerate. Consequently, the Regge propagators (2.42) have either a constant (1) or rotating ($e^{-i\pi\alpha(t)}$) phase. These phases cannot be deduced from first principles and need to be determined from data.

In our implementation of the Regge model, the operatorial structure of the transition amplitudes is dictated by an effective Lagrangian approach[3], in which the t-channel propagators are replaced by the corresponding Regge ones, i.e.

$$\hat{\mathbf{J}}^{K^{(*)+}}_{\text{Regge}} = \hat{\mathbf{J}}^{K^{(*)+}}_{\text{Feynman}} \times \mathcal{P}^{K^{(*)+}}_{\text{Regge}} \times \left(t - m^2_{K^{(*)+}}\right) . \tag{2.44}$$

[3] Our choice of strong and electromagnetic interaction Lagrangians can be found in Section D.3.2.

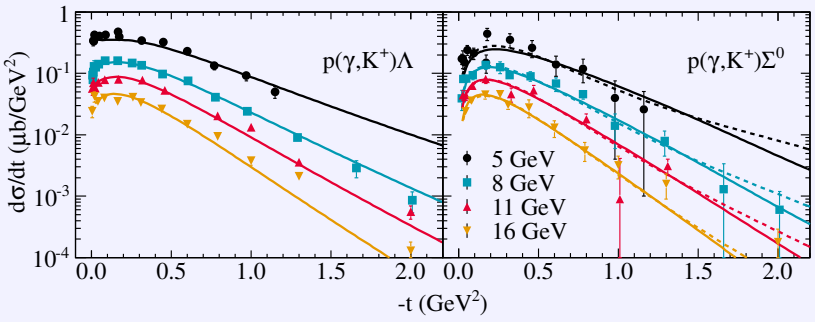

Figure 2.3 – Differential cross section as a function of the momentum transfer $|t|$ at four photon LAB energies $E_\gamma = 5$, 8, 11 and 16 GeV. For the $p(\gamma, K^+)\Lambda$ channel (left panel), the Regge-2 model is shown. The $p(\gamma, K^+)\Sigma^0$ results (right panel) are obtained with the Regge-3 (solid line) and Regge-4 (dashed line) models. Data from Ref. [113].

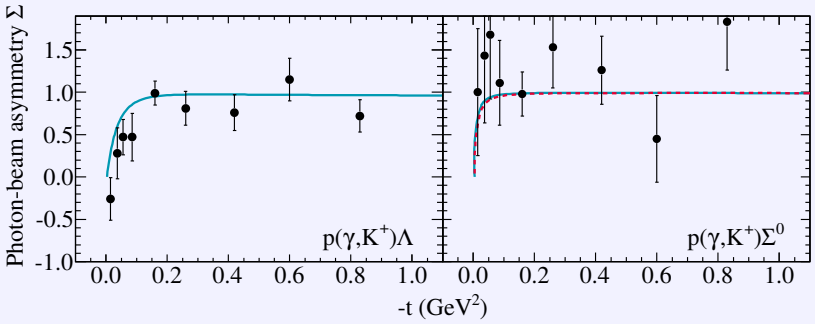

Figure 2.4 – Photon-beam asymmetry as a function of the momentum transfer $|t|$ at photon LAB energy $E_\gamma = 16$ GeV. For $p(\gamma, K^+)\Lambda$ results (left panel) are the Regge-2 model. The $p(\gamma, K^+)\Sigma^0$ results (right panel) are obtained with the Regge-3 (solid line) and Regge-4 (dashed line) models. Data from Ref. [114].

As a consequence, the amplitude corresponding to $K^{(*)+}$ exchange in the t-channel effectively incorporates the transfer of an entire trajectory. When considering the exchange of $K^+(494)$ and $K^{*+}(892)$ trajectories, the Regge model for $p(\gamma, K^+)Y$ has a mere three parameters

$$g_{K^+Yp}\,, \quad \text{and} \quad G^{v,t}_{K^{*+}} = \kappa_{K^{*+}K^+} \times g^{v,t}_{K^{*+}Yp}\,, \tag{2.45}$$

with g_{K^+Yp}, $g^v_{K^{*+}Yp}$ and $g^t_{K^{*+}Yp}$ the coupling constants at the strong-interaction vertex and $\kappa_{K^{*+}K^+}$ the $K^{*+}(892)$'s transition magnetic moment (see Paragraph D.3.3).

A crucial constraint for the kaon-production amplitude is gauge invariance. It is well-known that the t-channel Born diagram by itself does not conserve electric charge. In Ref. [38], an elegant recipe to correct for this was outlined. Adding the electric part of a Reggeized s-channel Born diagram ensures that the amplitude is gauge invariant. Thus, the transition current operator for high-energy kaon production in the Regge limit reads

$$\hat{\mathbf{J}}^{K^+(494)}_{\text{Regge}} + \hat{\mathbf{J}}^{K^{*+}(892)}_{\text{Regge}} + \hat{\mathbf{J}}^{\text{Born-}s\text{,elec}}_{\text{Feynman}} \times \mathcal{P}^{K^+(494)}_{\text{Regge}} \times \left(t - m^2_{K^+}\right)\,. \tag{2.46}$$

At sufficiently high energies ($E_\gamma \gtrsim 4$ GeV), a limited amount of $p(\gamma, K^+)Y$ data points are available. For the $K^+\Lambda$ channel a total of 72 data points exist, comprising 56 differential-cross-section data points [113], 9 photon-beam asymmetries [114], and 7 recoil asymmetries [115]. Even fewer data is available for $K^+\Sigma^0$ production: 48 differential cross sections [113] and 9 photon-beam

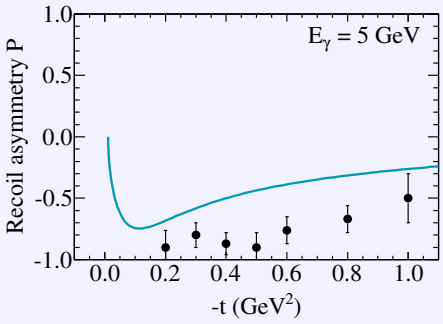

Figure 2.5 – Hyperon-recoil asymmetry for the $p(\gamma, K^+)\Lambda$ channel as function of the momentum transfer $|t|$ at photon LAB energy $E_\gamma = 5\,\text{GeV}$. Data from Ref. [115].

asymmetries [114]. In Refs. [39, 40], these data sets have been adopted to constrain the three free parameters (2.45) of the Regge model, as well as the phases of the exchanged trajectories. Because of the meagre database, a unique and optimal model could not be established and several model variants attain a comparable χ^2. After carrying through the full RPR strategy (see Section 2.3) and making use of photo- and electroproduction data in the resonance region, the number of possible Regge models can be significantly reduced. For the $K^+\Lambda$ amplitude, a single Regge model with two rotating trajectories, coined Regge-2, emerged. It is encouraging that a later Bayesian analysis of the Regge model in the high-energy domain was able to single out this particular model using high-energy data alone [56]. The $p(\gamma, K^+)\Sigma^0$ data was found to be compatible with a rotating phase for the $K^+(494)$ and a constant phase for the $K^{*+}(892)$ trajectory. The sign of the tensor coupling constant remained ambiguous, however. The $K^+\Sigma^0$-production models are labelled Regge-3 and Regge-4. The coupling constants for the Regge models that are employed in this work are summarised in Appendix I.

The Regge models are compared to the available high-energy data in Figures 2.3, 2.4 and 2.5. The differential cross section for both Λ and Σ^0 production are nicely reproduced. From Figure 2.3, one notices that both Regge models for the $K^+\Sigma^0$ channel give comparable results at low $|t|$. The photon-beam asymmetries of Figure 2.4 have a striking feature which is perfectly reproduced by the Regge model. The asymmetry rises quickly to $+1$ as a function of $-t$. This behaviour is reminiscent of the dominant exchange of a natural-parity state [116], which we identify as the $K^{*+}(892)$ trajectory. For the $p(\gamma, K^+)\Lambda$ reaction, a set of recoil-polarisation asymmetries at forward kaon angles are available. The sign and shape of the angular dependence can be reproduced in the model. The size of the asymmetry, on the other hand, is considerably underestimated.

2.3 Kaon production in the resonance region

The Regge model's amplitude can be interpreted as the asymptotic form of the full amplitude for large s and small $|t|$. Owing to the t-channel dominance and the absence of a prevailing resonance, the Reggeized background has been observed to account for the gross features of the kaon production data in the resonance region [39, 40, 67]. Near threshold, the energy dependence of the measured differential cross sections exhibits structures which hint at the presence of resonances. These are incorporated by supplementing the background with a number of resonant s-channel diagrams. This approach was coined Regge-plus-resonance (RPR) and has also been applied to double-pion

production [117], as well as the production of η and η' mesons [63, 64].

We describe the resonant contributions using standard tree-level Feynman diagrams. The exact form of the transition amplitudes for spin-1/2 and spin-3/2 nucleon-resonance exchange can be found in Section D.3. By substituting

$$s_{KY} - m_R^2 \to s_{KY} - m_R^2 + i m_R \Gamma_R \,, \tag{2.47}$$

in the propagator's denominator, we take into account the finite lifetime of resonances with mass m_R and width Γ_R. To limit the number of fit parameters, we keep the resonances' mass and width fixed at the values given in the Particle Data Group's Review of Particle Physics (RPP) [1]. Each spin-1/2 resonance introduces one free parameter

$$G_{N^*} = \kappa_{N^*p} \times g_{K^+YN^*} \,, \tag{2.48}$$

the product of the coupling constants at the electromagnetic and the strong-interaction vertex. Spin-3/2 resonances have an additional degree of freedom at the photon vertex and give rise to two free parameters

$$\begin{aligned} G_{N^*}^{(1)} &= \kappa_{N^*p}^{(1)} \times g_{K^+YN^*} \,, \\ G_{N^*}^{(2)} &= \kappa_{N^*p}^{(2)} \times g_{K^+YN^*} \,. \end{aligned} \tag{2.49}$$

The most general interaction Lagrangian for spin-3/2 fields allows for an additional three degrees-of-freedom, often called *off-shell* parameters, in the strong and EM vertices [118]. To ensure that the effects of the resonant diagrams fade at higher energies, we introduce Gaussian form factors at the strong interaction vertices [69]

$$g_{K^+YN^*} \to g_{K^+YN^*} \times \exp\left[-\frac{\left(s_{KY} - m_R^2\right)^2}{\Lambda_{\text{strong}}^4} \right] \,, \tag{2.50}$$

with Λ_{strong} a cutoff mass. A single cutoff mass is used for all resonance-exchange diagrams and it is considered a free parameter in the fitting procedure. For both Λ and Σ^0 production, the value of Λ_{strong} is about 1600 MeV.

The dynamics of EM kaon production can be fairly involved, with several contributing nucleon and delta resonances that interfere with an eminent background. Disentangling these contributions is challenging. In the RPR approach, we seek to determine the resonant and non-resonant terms separately. The Regge model that was the subject of the previous section has been fitted against the available high-energy data. Its parameters are frozen and the Regge amplitude serves as an effective parametrisation of the background. In the resonance region, a large body of data is available. Lists of published data sets for $p(\gamma, K^+)\Lambda$ and $p(\gamma, K^+)\Sigma^0$ are presented in Tables J.1 and J.2. In Refs. [39, 40], the database [119–122] published at that time was used to constrain the resonance parameters of the RPR model, while keeping the background unaltered. In the $K^+\Lambda$-production channel at forward angles, a substantial discrepancy exists between results from the CLAS [119, 121, 123] and SAPHIR [124, 125] collaborations [126]. This makes it impossible to find an optimal model that describes both data sets simultaneously. In the optimisation procedure, only the CLAS data are retained. Since the Regge model is derived in the limit of asymptotic CM energy s_{KY} and vanishing momentum transfer t, the RPR model analysis of Refs. [39, 40] was restricted to forward-kaon production. Only differential cross sections for $\cos\theta_K^* \geq 0.35$ and polarisation asymmetries satisfying $\cos\theta_K^* \geq 0$ were considered in the fitting procedure.

In the $K^+\Lambda$-production channel, a fair description of the considered data ($\chi^2/N_{dof} \approx 2.4$) is realised via the inclusion of the following set of resonances: $S_{11}(1650)$, $P_{11}(1710)$, $P_{13}(1720)$, $P_{13}(1900)$ and $D_{13}(1900)$. The first three are considered well-established resonances in the RPP [1]. The evidence for the $P_{11}(1710)$ state, however, has eroded in the past decade. Recent analyses of πN scattering by the SAID group no longer consider it [127]. Also in models for strangeness production, this resonance has been called into question [5, 128]. The $P_{13}(1900)$ resonance has a two-star status in the RPP. It plays an important role in the missing-resonance puzzle, since it is part of a quartet of nucleon resonances predicted by symmetric quark models but not by quark-diquark models [11]. In our RPR analysis, the $P_{13}(1900)$ state is cardinal to describe the data. Additionally, the optimal RPR model includes a missing $D_{13}(1900)$ resonance with a width of 200 MeV. Evidence for this state has also been obtained in other analyses [45, 49, 128].

In Ref. [40], we established the phases of the leading kaon trajectories for the $p(\gamma, K^+)\Sigma^0$ channel. With the available data, it turned out impossible to single out a unique parametrisation of the Regge model. The two model variants, that yield an equally good description of the high-energy data, were labelled Regge-3 and Regge-4. Subsequently, we added resonances to the Reggeized background amplitude, identifying the $S_{11}(1650)$, $D_{33}(1700)$, $P_{11}(1710)$, $P_{13}(1720)$, $P_{13}(1900)$, $S_{31}(1900)$, $P_{31}(1910)$ and $P_{33}(1920)$ as essential contributions. These are established resonances with a three- or a four-star status in the RPP [1], except for the $P_{13}(1900)$ and $S_{31}(1900)$, which are two-star resonances. Both the RPR-3 and RPR-4 models reach a goodness-of-fit of $\chi^2/N_{dof} = 2.0$. We found no direct need to include "missing" resonances in the $K\Sigma$ channel.

In order to assess the predictive power of the RPR model, we extended our formalism to kaon electroproduction in Ref. [97]. The Q^2-dependence of the EM coupling constants was incorporated using transition form factors as computed in the Bonn CQM [129]. Without refitting any parameters, we found that the RPR model gives a decent account of the available kaon electroproduction data.

2.4 The RPR model: the good, the bad and the ugly

In the previous sections, the RPR approach to EM strangeness production from the proton was presented and we introduced models for $K^+\Lambda$ and $K^+\Sigma^0$ production that were optimised against the pre-2007 world data. These models will be utilised in Chapter 6 for the calculation of kaon-production observables on the deuteron. Since their publication in Refs. [39, 40, 97], many new data sets have been published, encompassing high-statistics data at previously measured kinematics as well as totally new observables. Evidently, these experimental developments have prompted us to put the RPR model to a stringent test. In this section, we sketch some conceptual imperfections of the RPR formalism, many of which have been amended in recent years [56, 98, 99]. In addition, a selection of recently published data will be confronted with the RPR model in order to confirm its reliability and robustness.

New high-quality data with unprecedented statistics have been published by the CLAS collaboration. These data comprise differential cross sections and recoil-polarisation asymmetries for both the $p(\gamma, K^+)\Lambda$ [123] and $p(\gamma, K^+)\Sigma^0$ [130] reaction channels. The extended energy range, which reaches well beyond the resonance region, is of particular interest to the RPR model. The new data sets allow to cross-check the high-energy data that is used to tune the background parameters of the Regge model. Dey and Mayer point out in Ref. [131] that considerable discrepancies exist between

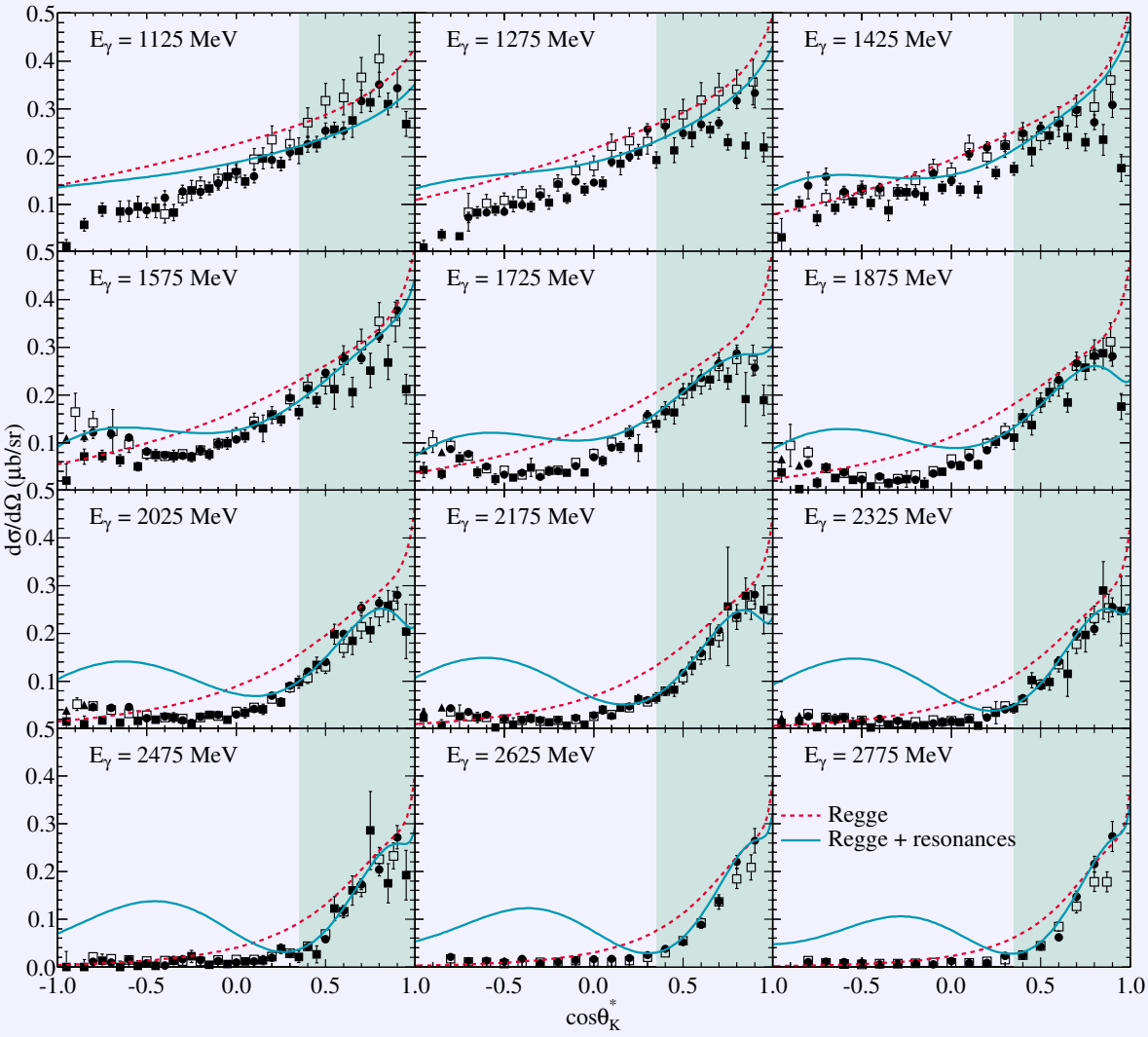

Figure 2.6 – Differential $p(\gamma, K^+)\Lambda$ cross sections as a function of θ^*_K for various photon energies E_γ. The solid and dashed curves are calculations with the RPR and Regge models respectively. The vertical band shows the angular range used for fitting. Data from Refs. [119] (•), [125] (■), [132] (▲) and [123] (□).

the newest CLAS results and the older data sets. This implies the Regge model can be further refined. The repercussions for the RPR model are thoroughly addressed in Ref. [98].

In order to keep the model uncertainties to a strict minimum and maintain a low number of fitting parameters, resonances of spin-5/2 and higher are not considered in Refs. [39, 40]. The RPP lists a number of well-established higher-spin resonances that are indispensable in the description of (double-)pion production amongst others. Previous strangeness-production models that have considered spin-5/2 resonance exchange [5, 22, 24, 29, 128], on the other hand, conclude that these states do not contribute significantly to the reaction dynamics. Nevertheless, the forthcoming analysis [98, 133] of the recent kaon-production data in the RPR approach takes spin-5/2 resonances into account.

Implementing resonances with spin $J \geq 3/2$ in a hadrodynamical framework is a non-trivial task. The conventional Rarita-Schwinger description of high-spin fermion fields [136], which is adopted in this work, involves some unphysical degrees of freedom, associated with their lower-spin content [137]. These degrees of freedom are manifested by the off-shell parameters (X, Y, Z) that feature in the

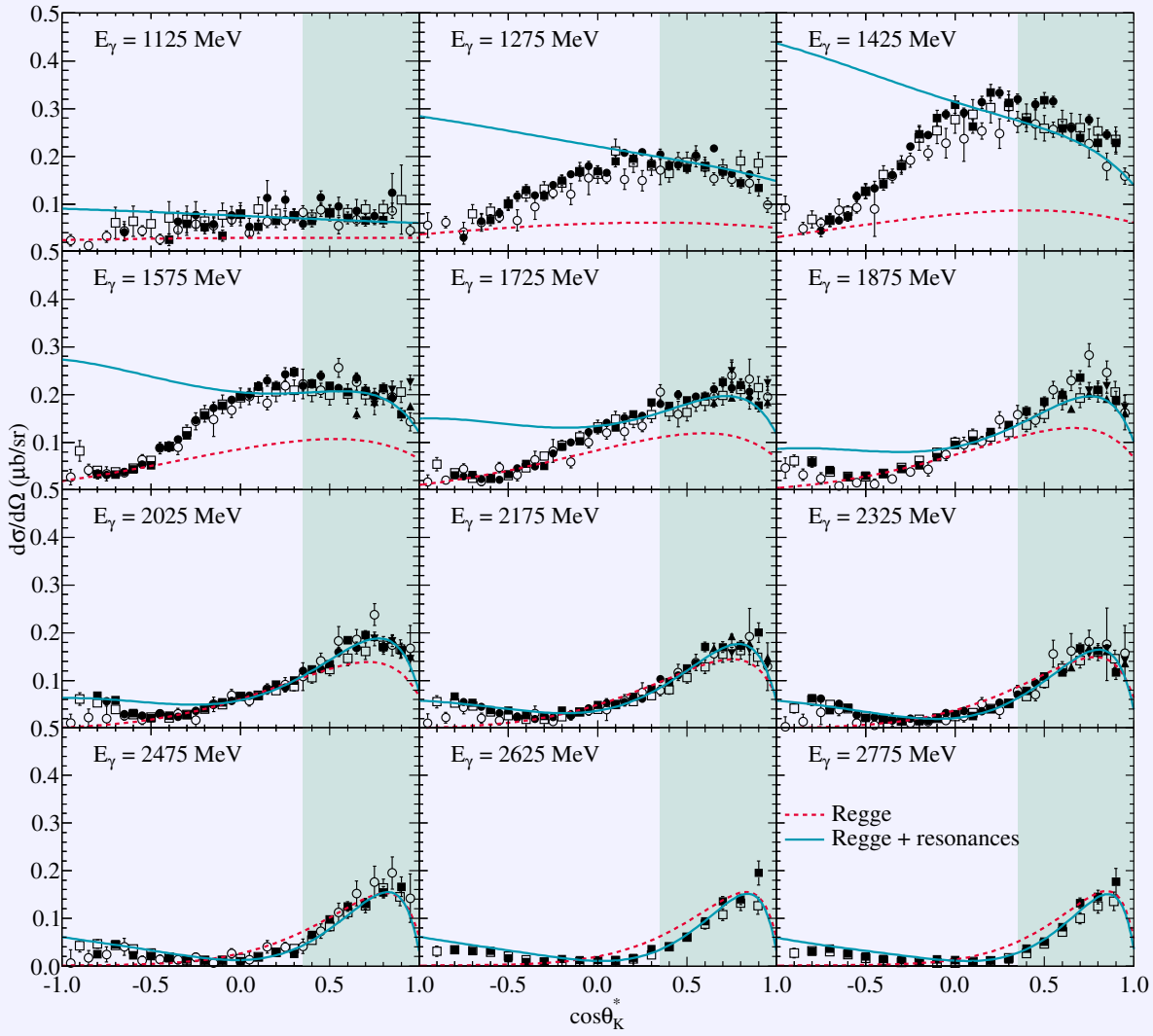

Figure 2.7 – Differential $p(\gamma, K^+)\Sigma^0$ cross sections as a function of θ^*_K for various photon energies E_γ. The solid and dashed curves are calculations with the RPR-3 and Regge-3 models respectively. The vertical band shows the angular range used for fitting. Data from Refs. [121] (•), [119] (■), [134] (▲), [135] (▼), [125] (○) and [130] (□).

interaction Lagrangians (see Section D.3) and give rise to unphysical structures in the transition amplitude [138]. Extending the work of Pascalutsa [139], a consistent interaction theory for high-spin fermions was formulated in Ref. [99]. In the forthcoming RPR model [98, 133], these consistent interaction Lagrangians will be adopted for spin-3/2 and spin-5/2 resonance exchange.

As mentioned in Section 2.3, the RPR-model analysis of Refs. [39, 40] was restricted to forward kaon-production angles. Later on in this work, the RPR elementary-production operator will constitute one of the basic ingredients of the strangeness-production calculations from the deuteron. To this end, we wish to assess the behaviour of the RPR model over the full angular range. In Figures 2.6 and 2.7, the $p(\gamma, K^+)\Lambda$ and $p(\gamma, K^+)\Sigma^0$ differential cross sections are shown for $1125 \leq E_\gamma \leq 2775$ MeV. Immediately, one notices that the Reggeized background model provides a fair description of the cross section even though it was optimised against high-energy data. In the threshold region, the Regge model overpredicts the Λ-production data, whereas it accounts for about half the strength of the $K^+\Sigma^0$ channel. At higher energies, the Regge model slightly overpredicts the data in both

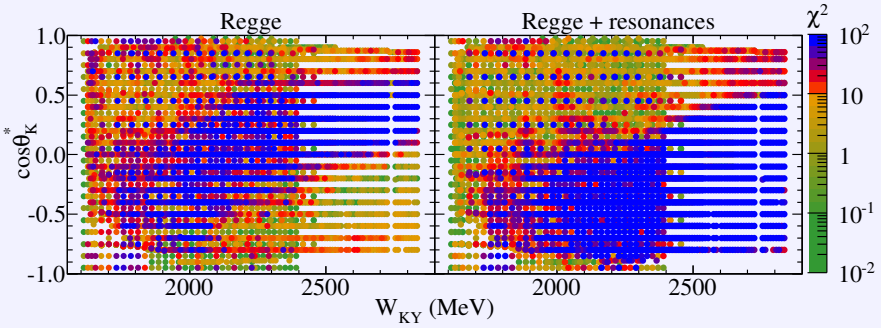

Figure 2.8 – The performance of the Regge (left panel) and RPR (right panel) model for the description of the $p(\gamma, K^+)\Lambda$ data. Every data point represents a (W_{KY}, θ^*_K) vector. The colour code indicates the χ^2 of the model for a particular data point. Data from Refs.[119–123, 125, 132, 140–142].

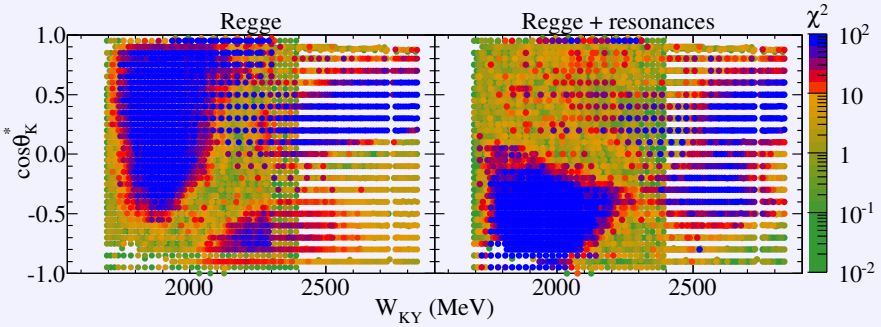

Figure 2.9 – The performance of the Regge-3 (left panel) and RPR-3 (right panel) model for the description of the $p(\gamma, K^+)\Sigma^0$ data. Every data point represents a (W_{KY}, θ^*_K) vector. The colour code indicates the χ^2 of the model for a particular data point. Data from Refs.[119–122, 125, 130, 134, 135, 140].

reaction channels. This is an indication of the data inconsistencies alluded to in Ref. [131].

Over the full energy range the RPR model nicely reproduces the data at forward angles. We remind the reader that only the $\cos\theta^*_K \geq 0.35$ data were included in the fits. In Figures 2.6 and 2.7, this region is indicated with a vertical band. At backward angles, on the other hand, the RPR predictions feature *bumps* that are absent in the data. These structures occur near threshold for $K^+\Sigma^0$ production and are prominent at higher energies in the $p(\gamma, K^+)\Lambda$ channel. The difficulty of the RPR model to account for the data in the backward hemisphere is readily visualised in Figures 2.8 and 2.9. They show the χ^2 for the Regge and RPR models per data point, that is cross sections as well as polarisation observables.

The RPR-model analysis of Refs. [39, 40, 97] was limited to forward angles, motivated by the Regge model's region of validity. At backward angles, one could expect that meson production can be parametrised with Reggeized hyperon exchange in the u-channel [112]. Such an approach has previously been applied in pion photoproduction [38]. For kaon production, however, the cross-section data shown in Figures 2.6 and 2.7 lack of any form of peaking at backward angles. This rules out the need for a Regge approach. We judge that the inclusion of nucleon resonances in the s-channel can account for strangeness production over the full solid angle. Therefore, the restriction on the angular range of the data used in the fitting database is relieved in the forthcoming RPR-model analysis [98, 133]. This allows for a successful description of kaon production at all angles.

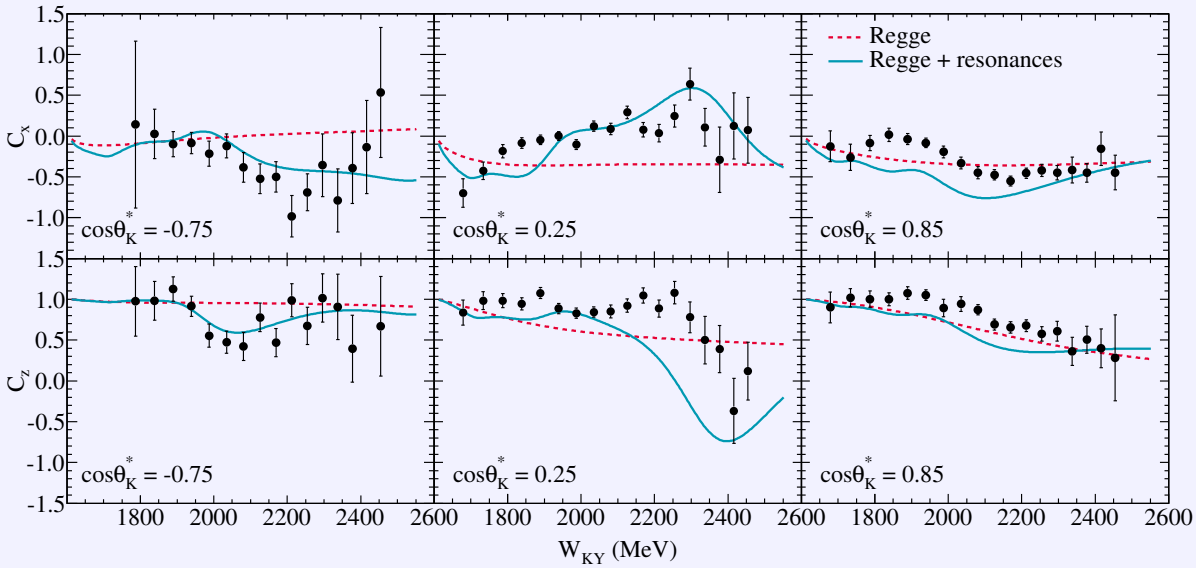

Figure 2.10 – Beam-recoil polarisation asymmetries C_x (upper panels) and C_z (lower panels) for the $p(\gamma, K^+)\Lambda$ reaction as function of the kaon-hyperon invariant mass W_{KY} at three kaon scattering angles. The solid and dashed curves are calculations with the RPR and Regge models respectively. Data from Ref. [140].

Despite its shortcomings, the RPR model provides an efficient description of EM kaon production. This is exemplified by the excellent predictions for the beam-recoil polarisation asymmetries (2.23). In Figure 2.10, the observables C_x and C_z are displayed at forward and backward angles. These asymmetries have the remarkable feature that at nearly all kinematics C_x remains close to zero and that C_z is near its upper limit $+1$. The Regge model reproduces these gross features. The addition of s-channel resonances further improves the model's correspondence with the data. Given that the results of Figure 2.10 are predictions, this illustrates the predictive power of the RPR formalism. Figure 2.11 features the beam-recoil asymmetries obtained with linearly polarised photons. The RPR models fails to reproduce the data near threshold, where the resonances provide marginal contributions. Since the lowest-mass resonance considered in the RPR-model analysis is the $S_{11}(1650)$, this might point at the need to consider sub-threshold resonances. At the higher energy bins, the predicted role of the resonances grows and their inclusion greatly improves the agreement with the data.

The extension of the RPR formalism to kaon electroproduction does not require any additional parameters. The electroproduction results are thus pure predictions. Nevertheless, an adequate description of the data is achieved [69, 97]. Here, we simply wish to illustrate this using two recently published data sets. In Ref. [143], new results for the separated longitudinal and transverse $p(e, e'K^+)\Lambda$ cross sections are presented. They are compared to predictions from the Saclay-Lyon isobar model [22] and a Regge model [144] that resembles the one presented in Section 2.2. We show the new data in Figure 2.12. It is clear the Regge model underpredicts σ_T, but exhibits the observed flat energy dependence. The longitudinal cross section is well described at $Q^2 = 1.90\,\mathrm{GeV}^2$. At the highest Q^2 bin, however, the predicted cross section lies below the data. The authors of Ref. [143] mention that the general EM kaon form factor is off shell when used in a t-channel diagram. Therefore, it becomes function of the momentum transfer t in addition to the photon's virtuality Q^2. In order to better describe the observed energy dependence with the Regge model, they introduce

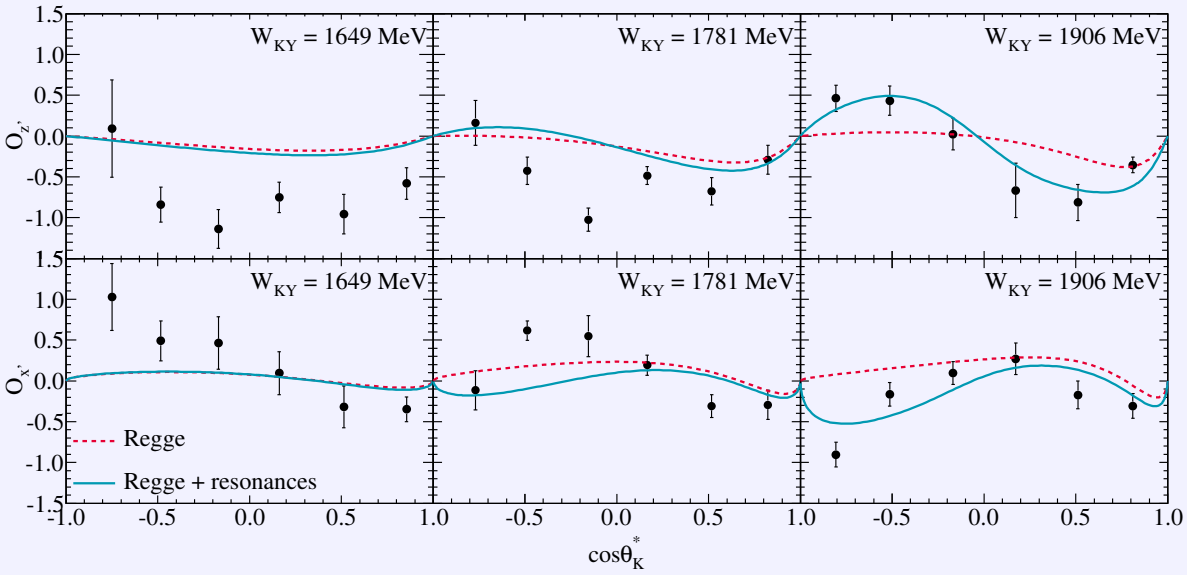

Figure 2.11 – The angular dependence of the beam-recoil polarisation asymmetries $O_{z'}$ (upper panels) and $O_{x'}$ (lower panels) for $p(\gamma, K^+)\Lambda$ at three values of W_{KY}. The solid and dashed curves are calculations with the RPR and Regge models respectively. Data from Ref. [141].

an off-shell extension to the traditional kaon form factor and fit the parameters corresponding to the degree of off-shellness to the data of Refs [143, 145]. This procedure significantly improves the description of the data. Our results indicate that the inclusion of resonance-exchange diagrams in the s-channel provides an alternative explanation. The coupling constants of these contributions are fixed in the real-photon point, and their Q^2 dependence is dictated by EM form factors computed in the Bonn CQM. The RPR-model results describe the W_{KY} dependence of the cross section in both Q^2 bins without having to fit additional parameters to the data.

Finally, we compare RPR-model predictions to measurements of the transferred polarisation over a large range of photon virtuality in Figure 2.13. This observable can be considered the electroproduction extension of the beam-recoil polarisation asymmetries C_x and C_z that have been presented in Figure 2.10. Again, a satisfactory correspondence is attained. The Regge model is able to account for the data, and the addition of resonances introduces only a slight modulation as function of Q^2.

In this chapter, EM strangeness production from the proton has been described within the RPR framework. The RPR-2007 models published in Refs. [39, 40] have been introduced. The values for their free parameters can be found in Appendix I. These parameters have been optimised to the available data in the $p(\gamma, K^+)\Lambda$ and $p(\gamma, K^+)\Sigma^0$ reaction channels, where experimental results are abundant. A successful description of strangeness production from the deuteron, however, requires a reaction model which accounts for all six kaon-production final states, including those where data is scarce or lacking. This issue constitutes the topic of the next chapter.

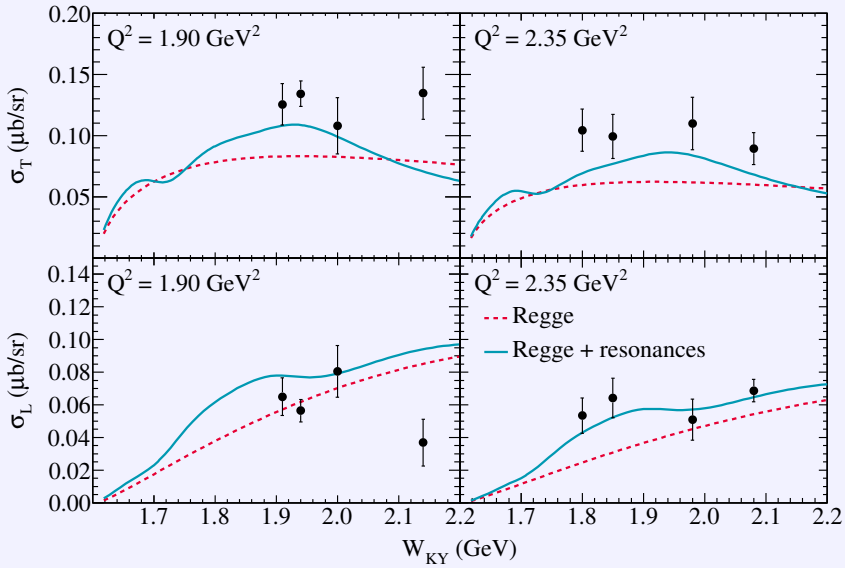

Figure 2.12 – Transverse (upper panel) and longitudinal (lower panel) differential $p(e, e'K^+)\Lambda$ cross sections as a function of the invariant mass W_{KY} for forward kaon production $\cos\theta^*_K \approx 1$ and at $Q^2 = 1.90\,\mathrm{GeV}^2$ (left panels) and $Q^2 = 2.35\,\mathrm{GeV}^2$ (right panels). The solid and dashed curves are calculations with the RPR and Regge models respectively. Data from Ref. [143].

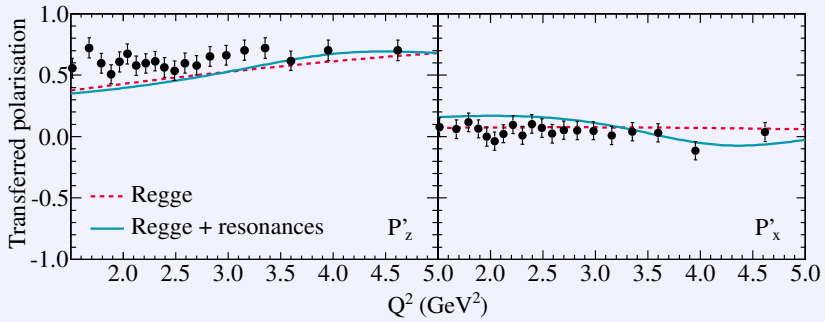

Figure 2.13 – Transferred polarisations (2.40) for the $p(e, e'K^+)\Lambda$ reaction as a function of the photon virtuality Q^2 at $\cos\theta^*_K = 0.43$. The electron-beam energy is fixed at 5754 MeV and the kaon-hyperon invariant mass is $W_{KY} = 1990\,\mathrm{MeV}$. The solid and dashed curves are calculations with the RPR and Regge models respectively. Data from Ref. [146].

CHAPTER 3

Kaon production in data-poor reaction channels

A total of six photon-induced reactions exist on the nucleon with a kaon-hyperon pair in the final state

$$\begin{aligned}
\gamma + p &\longrightarrow K^+ + \Lambda\,, \\
\gamma + p &\longrightarrow K^+ + \Sigma^0\,, \\
\gamma + p &\longrightarrow K^0 + \Sigma^+\,, \\
\gamma + n &\longrightarrow K^0 + \Lambda\,, \\
\gamma + n &\longrightarrow K^0 + \Sigma^0\,, \\
\gamma + n &\longrightarrow K^+ + \Sigma^-\,.
\end{aligned} \tag{3.1}$$

High-quality kaon-photoproduction information is only available for $p(\gamma, K^+)\Lambda$ and $p(\gamma, K^+)\Sigma^0$. As discussed in the previous chapter, this has allowed us to construct successful Regge and RPR models for these reactions. Here, we address the issue whether these models can be transformed in such a way that trustworthy predictions can be made for the remaining isospin channels.

In the RPR formalism, the reaction dynamics consist of pseudoscalar- and vector-meson exchange in the t-channel as well as nucleon-resonance exchange in the s-channel. The generic structure of the transition current operator is given by

$$\hat{\mathbf{J}}^{K^+(494)}_{\text{Regge}} + \hat{\mathbf{J}}^{K^{*+}(892)}_{\text{Regge}} + \hat{\mathbf{J}}^{\text{Born-}s\text{,elec}}_{\text{Feynman}} \times \mathcal{P}^{K^+(494)}_{\text{Regge}} \times \left(t - m^2_{K^+}\right) + \sum_{N^*} \hat{\mathbf{J}}^{N^*}_{\text{Feynman}} + \sum_{\Delta^*} \hat{\mathbf{J}}^{\Delta^*}_{\text{Feynman}}\,. \tag{3.2}$$

In order to relate different reaction channels with each other, it suffices to convert the coupling constants which feature in the interaction Lagrangians. As such, the two Λ-production channels and the four Σ-production reactions can both be described by a single set of parameters.

In the strong-interaction vertex, one can fall back on SU(2) isospin symmetry to find the relevant conversion factors. This concept is reviewed in Section 3.1. The transformation of the coupling constants in the EM-interaction vertex, on the other hand, cannot proceed without experimental input. The case of kaon-production from the neutron is considered in Section 3.2. The subsequent section deals with the production of neutral kaons.

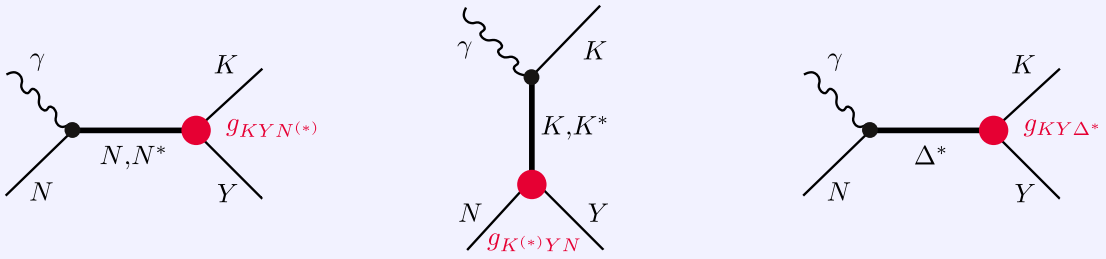

Figure 3.1 – The three tree-level diagrams considered in the RPR framework. Special emphasis is put on the strong-interaction vertices.

3.1 Symmetry considerations at the strong-interaction vertex

The relations among the coupling constants in the strong-interaction vertices of the various kaon-production reactions, depicted in Figure 3.1, can be derived effortlessly. This is made possible by means of the isospin symmetry of the strong force. In the strong-interaction vertex, the hadronic couplings are proportional to the Clebsch-Gordan coefficients

$$g_{K\Lambda N^{(*)}} \sim \left\langle I_K = \frac{1}{2}, M_K^I \,;\, I_\Lambda = 0, M_\Lambda^I = 0 \,\middle|\, I_{N^{(*)}} = \frac{1}{2}, M_{N^{(*)}}^I \right\rangle , \tag{3.3}$$

$$g_{K\Lambda\Delta^*} \sim \left\langle I_K = \frac{1}{2}, M_K^I \,;\, I_\Lambda = 0, M_\Lambda^I = 0 \,\middle|\, I_{\Delta^*} = \frac{3}{2}, M_{\Delta^*}^I \right\rangle , \tag{3.4}$$

and

$$g_{K\Sigma N^{(*)}} \sim \left\langle I_K = \frac{1}{2}, M_K^I \,;\, I_\Sigma = 1, M_\Sigma^I \,\middle|\, I_{N^{(*)}} = \frac{1}{2}, M_{N^{(*)}}^I \right\rangle , \tag{3.5}$$

$$g_{K\Sigma\Delta^*} \sim \left\langle I_K = \frac{1}{2}, M_K^I \,;\, I_\Sigma = 1, M_\Sigma^I \,\middle|\, I_{\Delta^*} = \frac{3}{2}, M_{\Delta^*}^I \right\rangle . \tag{3.6}$$

We adopt the following conventions for the isospin states of the $N^{(*)}$, Δ^*, $K^{(*)}$ and Σ particles,

$$\begin{aligned}
p, K^{(*)+}, N^{*+} &\rightarrow \left| I = \tfrac{1}{2},\ M^I = +\tfrac{1}{2} \right\rangle , \\
n, K^{(*)0}, N^{*0} &\rightarrow \left| I = \tfrac{1}{2},\ M^I = -\tfrac{1}{2} \right\rangle , \\
\Lambda &\rightarrow \left| I = 0,\ M^I = 0 \right\rangle , \\
\Sigma^+ &\rightarrow -\left| I = 1,\ M^I = 1 \right\rangle , \\
\Sigma^0 &\rightarrow \left| I = 1,\ M^I = 0 \right\rangle , \\
\Sigma^- &\rightarrow \left| I = 1,\ M^I = -1 \right\rangle , \\
\Delta^{*+} &\rightarrow \left| I = \tfrac{3}{2},\ M^I = +\tfrac{1}{2} \right\rangle , \\
\Delta^{*0} &\rightarrow \left| I = \tfrac{3}{2},\ M^I = -\tfrac{1}{2} \right\rangle .
\end{aligned} \tag{3.7}$$

The phase of the Σ^- state is taken to be positive. With this choice, the Condon-Shortley phase convention dictates a minus sign for the Σ^+ state. Using these isospin states to calculate the Clebsch-Gordan coefficients of Eqs. (3.3)–(3.6), we easily find the conversion factors of interest.

The strong coupling constants for the Λ-production channels are found to be isospin independent

$$\begin{aligned} g_{K^{(*)0}\Lambda n} &= g_{K^{(*)+}\Lambda p}\,, \\ g_{K^{(*)0}\Lambda N^{*0}} &= g_{K^{(*)+}\Lambda N^{*+}}\,. \end{aligned} \tag{3.8a}$$

Only two coupling-constant conversion factors are given, since the exchange of Δ isobars is forbidden. The strong-interaction vertices for $p(\gamma, K^0)\Sigma^+$ can be related to those for $p(\gamma, K^+)\Sigma^0$ through the following relations

$$\begin{aligned} g_{K^{(*)0}\Sigma^+ p} &= \sqrt{2}\, g_{K^{(*)+}\Sigma^0 p}\,, \\ g_{K^{(*)0}\Sigma^+ N^{*+}} &= \sqrt{2}\, g_{K^{(*)+}\Sigma^0 N^{*+}}\,, \\ g_{K^{(*)0}\Sigma^+ \Delta^{*+}} &= \frac{-1}{\sqrt{2}} g_{K^{(*)+}\Sigma^0 \Delta^{*+}}\,, \end{aligned} \tag{3.8b}$$

and for $K^+\Sigma^-$ production from the neutron one has

$$\begin{aligned} g_{K^{(*)+}\Sigma^- n} &= \sqrt{2}\, g_{K^{(*)+}\Sigma^0 p}\,, \\ g_{K^{(*)+}\Sigma^- N^{*0}} &= \sqrt{2}\, g_{K^{(*)+}\Sigma^0 N^{*+}}\,, \\ g_{K^{(*)+}\Sigma^- \Delta^{*0}} &= \frac{1}{\sqrt{2}} g_{K^{(*)+}\Sigma^0 \Delta^{*+}}\,. \end{aligned} \tag{3.8c}$$

Finally, the transformation of the $p(\gamma, K^+)\Sigma^0$ amplitude to the $n(\gamma, K^0)\Sigma^0$ one, only requires some minus signs

$$\begin{aligned} g_{K^{(*)0}\Sigma^0 n} &= -\, g_{K^{(*)+}\Sigma^0 p}\,, \\ g_{K^{(*)0}\Sigma^0 N^{*0}} &= -\, g_{K^{(*)+}\Sigma^0 N^{*+}}\,, \\ g_{K^{(*)0}\Sigma^0 \Delta^{*0}} &= g_{K^{(*)+}\Sigma^0 \Delta^{*+}}\,. \end{aligned} \tag{3.8d}$$

3.2 The unbound neutron as kaon-production target

In order to assess the predictive power of the RPR formalism, we will first focus our attention on reactions with a neutron target. Only data for the $n(\gamma, K^+)\Sigma^-$ channel have been published and we will use this reaction to judge the reliability of our formalism in Paragraph 3.2.3. Besides the conversion coefficients in the strong interaction vertex, one also needs transformation rules for the EM coupling constants. This is addressed in Paragraph 3.2.2. First, we touch on the subject of gauge invariance.

3.2.1 Gauge-invariance restoration

A crucial constraint for the kaon-production amplitude is gauge invariance. It is well-known that the t-channel Born diagram by itself does not conserve electric charge. In Ref. [38], an elegant recipe to correct for this was outlined. Adding the electric part of a Reggeized s-channel Born diagram ensures that the $p(\gamma, K^+)Y$ amplitude is gauge invariant.

For the $K^0\Lambda$- and $K^0\Sigma^0$-production reactions, this gauge-invariance-restoration procedure is irrelevant, because the kaon-exchange amplitude vanishes. The $n(\gamma, K^+)\Sigma^-$ reaction is the only channel with a neutron as target and a charged kaon in the final state. Since the neutron is electrically neutral, the electric part of the s-channel Born diagram is identically zero. A gauge-invariant amplitude is obtained by including the electric part of a Reggeized u-channel Born diagram.

3.2.2 Helicity amplitudes

In contrast to the hadronic parameters, the relations between electromagnetic couplings have to be distilled from experimental information. The partial decay width for the radiative decay of a resonance of spin S to the ground-state nucleon is given by [1]

$$\Gamma(N^* \to N\gamma) = \frac{\boldsymbol{p}_\gamma^{*2}}{\pi} \frac{2m_N}{(2S+1)m_{N^*}} \left(|\mathcal{A}_{1/2}^N|^2 + |\mathcal{A}_{3/2}^N|^2 \right) , \tag{3.9}$$

in terms of photocoupling helicity amplitudes $\mathcal{A}_J^N$. These helicity amplitudes can be directly linked with current matrix elements. Using the conventions of Ref. [129], we have

$$\begin{aligned} \mathcal{A}_{1/2}^N &= \sqrt{\frac{\pi\alpha}{2m_N(m_{N^*}^2 - m_N^2)}} \left\langle \boldsymbol{p}_{N^*}, \lambda_{N^*} = \frac{1}{2} \middle| \, j_x(0) + i\, j_y(0) \, \middle| \boldsymbol{p}_N, \lambda_N = \frac{1}{2} \right\rangle , \\ \mathcal{A}_{3/2}^N &= \sqrt{\frac{\pi\alpha}{2m_N(m_{N^*}^2 - m_N^2)}} \left\langle \boldsymbol{p}_{N^*}, \lambda_{N^*} = \frac{3}{2} \middle| \, j_x(0) + i\, j_y(0) \, \middle| \boldsymbol{p}_N, \lambda_N = \frac{1}{2} \right\rangle . \end{aligned} \tag{3.10}$$

Here, $j^\mu(\boldsymbol{x})$ is the current operator. It speaks for itself that $\mathcal{A}_{3/2}^N$ is zero when $S = 1/2$. The current matrix elements can be calculated within a quark model (see Ref. [129] for example), or using the phenomenological interaction Lagrangians defined in Section D.3.2. In this way, the N^* and Δ^* transition moments can be related to the photocoupling helicity amplitudes $\mathcal{A}_J^N$. One has [147]

$$\mathcal{A}_{1/2}^N = \mp \frac{e}{2m_N} \sqrt{\frac{m_{N^*}^2 - m_N^2}{2m_N}} \kappa_{N^*N} , \tag{3.11}$$

for spin-1/2 resonances and

$$\begin{aligned} \mathcal{A}_{1/2}^N &= \frac{e}{4m_{N^*}} \sqrt{\frac{m_{N^*}^2 - m_N^2}{3m_N}} \left(\pm\kappa_{N^*N}^{(1)} - \frac{m_{N^*}(m_{N^*} \mp m_N)}{4m_N^2} \kappa_{N^*N}^{(2)} \right) , \\ \mathcal{A}_{3/2}^N &= \frac{e}{4m_N} \sqrt{\frac{m_{N^*}^2 - m_N^2}{m_N}} \left(\pm\kappa_{N^*N}^{(1)} \mp \frac{m_{N^*} \mp m_N}{4m_N} \kappa_{N^*N}^{(2)} \right) , \end{aligned} \tag{3.12}$$

for spin-3/2 resonances. In Eqs. (3.11) and (3.12), the upper (lower) sign corresponds to positive- (negative-) parity resonances. Inverting these relations and neglecting the small proton-neutron mass difference, we find

$$\frac{\kappa_{N^*n}}{\kappa_{N^*p}} = \frac{\mathcal{A}_{1/2}^n}{\mathcal{A}_{1/2}^p} , \tag{3.13}$$

for spin-1/2 resonances and

$$\begin{aligned} \frac{\kappa_{N^*n}^{(1)}}{\kappa_{N^*p}^{(1)}} &= \frac{\sqrt{3}\mathcal{A}_{1/2}^n \pm \mathcal{A}_{3/2}^n}{\sqrt{3}\mathcal{A}_{1/2}^p \pm \mathcal{A}_{3/2}^p} , \\ \frac{\kappa_{N^*n}^{(2)}}{\kappa_{N^*p}^{(2)}} &= \frac{\sqrt{3}\mathcal{A}_{1/2}^n - \frac{m_p}{m_{N^*}}\mathcal{A}_{3/2}^n}{\sqrt{3}\mathcal{A}_{1/2}^p - \frac{m_p}{m_{N^*}}\mathcal{A}_{3/2}^p} . \end{aligned} \tag{3.14}$$

for spin-3/2 resonances. Note that these conversion rules are only meaningful for N^*'s, since the Δ-nucleon magnetic transition moments $\kappa_{\Delta^*N}^{(1,2)}$ are isospin independent.

Values for the published helicity amplitudes of the $S_{11}(1650)$, $P_{11}(1710)$, $P_{13}(1720)$, $P_{13}(1900)$ and $D_{13}(1900)$ resonance are presented in Table 3.1. The listed numbers are from the RPP [1] and two

Table 3.1 – Photocoupling helicity amplitudes of selected nucleon resonances in units $10^{-3}\,\mathrm{GeV}^{-1/2}$ from the Bonn relativistic constituent-quark model [148], the Review of Particle Physics [1] and two SAID analyses (SM95 [149] and SP09 [127]). No experimental information exists for the $P_{13}(1900)$ and $D_{13}(1900)$. SP09 provides photo-decay amplitudes to protons and does not find evidence for the $P_{11}(1710)$ resonance [150]. The ratio of EM couplings to proton and neutron (see Eqs. (3.13) and (3.14)) is listed as well. The SP09 ratios are obtained with the $\mathcal{A}^n_J$ of SM95.

Resonance		Bonn	RPP	SM95	SP09
$S_{11}(1650)$	$\mathcal{A}^n_{1/2}$	-16.00	-15.00 ± 21.00	-15.00 ± 5.00	–
	$\mathcal{A}^p_{1/2}$	4.30	53.00 ± 16.00	69.00 ± 5.00	9.00 ± 9.10
	$\frac{\kappa_{N^*n}}{\kappa_{N^*p}}$	-3.72	-0.28 ± 0.41	-0.22 ± 0.07	-1.67 ± 1.77
$P_{11}(1710)$	$\mathcal{A}^n_{1/2}$	-26.70	-2.00 ± 14.00	-2.00 ± 15.00	–
	$\mathcal{A}^p_{1/2}$	52.80	9.00 ± 22.00	7.00 ± 15.00	–
	$\frac{\kappa_{N^*n}}{\kappa_{N^*p}}$	-0.51	-0.22 ± 1.65	-0.29 ± 2.23	–
$P_{13}(1720)$	$\mathcal{A}^n_{1/2}$	-30.20	1.00 ± 15.00	7.00 ± 15.00	–
	$\mathcal{A}^p_{1/2}$	75.90	18.00 ± 30.00	-15.00 ± 15.00	90.50 ± 3.30
	$\mathcal{A}^n_{3/2}$	11.40	-29.00 ± 61.00	-5.00 ± 25.00	–
	$\mathcal{A}^p_{3/2}$	-25.40	-19.00 ± 20.00	7.00 ± 10.00	-36.00 ± 3.90
	$\frac{\kappa^{(1)}_{N^*n}}{\kappa^{(1)}_{N^*p}}$	-0.39	-2.24 ± 11.60	-0.38 ± 2.00	0.06 ± 0.30
	$\frac{\kappa^{(2)}_{N^*n}}{\kappa^{(2)}_{N^*p}}$	-0.40	0.42 ± 1.15	-0.50 ± 1.08	0.08 ± 0.17
$P_{13}(1900)$	$\mathcal{A}^n_{1/2}$	2.6	–	–	–
	$\mathcal{A}^p_{1/2}$	5.5	–	–	–
	$\mathcal{A}^n_{3/2}$	16.9	–	–	–
	$\mathcal{A}^p_{3/2}$	2.2	–	–	–
	$\frac{\kappa^{(1)}_{N^*n}}{\kappa^{(1)}_{N^*p}}$	1.83	–	–	–
	$\frac{\kappa^{(2)}_{N^*n}}{\kappa^{(2)}_{N^*p}}$	-0.46	–	–	–
$D_{13}(1900)$	$\mathcal{A}^n_{1/2}$	-17.7	–	–	–
	$\mathcal{A}^p_{1/2}$	47.9	–	–	–
	$\mathcal{A}^n_{3/2}$	12.3	–	–	–
	$\mathcal{A}^p_{3/2}$	-18.5	–	–	–
	$\frac{\kappa^{(1)}_{N^*n}}{\kappa^{(1)}_{N^*p}}$	-0.28	–	–	–
	$\frac{\kappa^{(2)}_{N^*n}}{\kappa^{(2)}_{N^*p}}$	-0.40	–	–	–

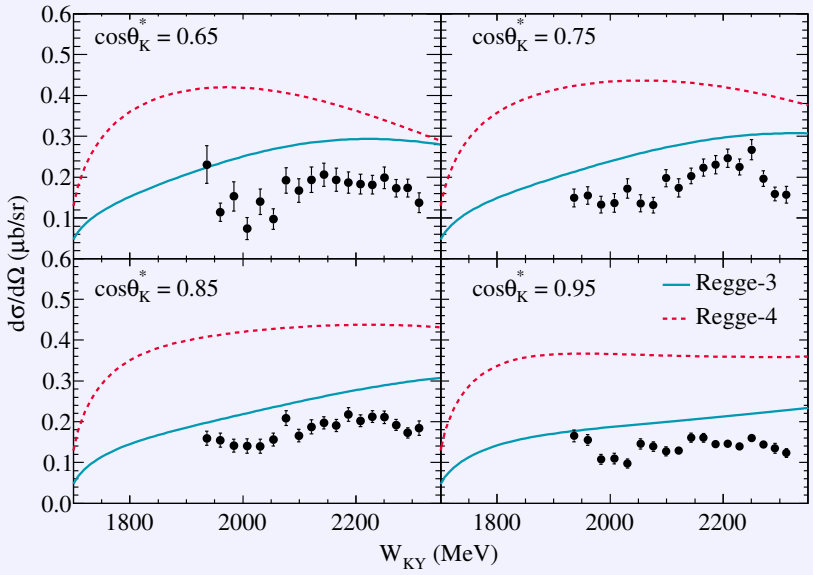

Figure 3.2 – Regge-model predictions for the $n(\gamma, K^+)\Sigma^-$ differential cross section as a function of the kaon-hyperon invariant mass for four different values of the kaon centre-of-mass scattering angle. Data from Ref. [134]. The error bars represent the statistical uncertainties only. The systematic uncertainty is of the order of 20%.

SAID analyses [127, 149]. It is clear that the photon couplings of those resonances pertinent to our calculations are poorly determined. The extracted values are often incompatible, even after taking into account the considerable error bars. No experimental information is available for the resonances of mass 1900 MeV, i.e. $P_{13}(1900)$ and $D_{13}(1900)$. Table 3.1 also features photon couplings as calculated in the Bonn CQM [148]. The theoretical predictions for the transition moments of the $S_{11}(1650)$ to neutron (proton) agree favourably with the SAID analysis SM95 [149] (SP09 [127]). When confronting the Bonn model calculations for the $P_{11}(1710)$ and $P_{13}(1720)$ resonances with the SM95 SAID analysis, one notices that the transition moments to proton and neutron are overestimated, while their ratio matches within the error. The Bonn CQM provides a fair account of all $\mathcal{A}_J^p$ from the SP09 analysis. This analysis, however, finds no evidence for the $P_{11}(1710)$ resonance [150].

3.2.3 Results

In Chapter 2, it became clear that the kaon-production reaction mechanism is dominated by the background contributions, which we parametrise in terms of Regge-trajectory exchange. Therefore, we will first examine the predictive power of the Reggeized-background model using the limited number of available experimental results. At a later stage, the predictions of the full RPR model will be investigated.

To our knowledge, only two data sets for the $n(\gamma, K^+)\Sigma^-$ reaction channel have been published in the past. The results by the LEPS collaboration [134] comprise differential cross sections and photon-beam asymmetries at forward angles ($\cos\theta_K^* \geq 0.65$) in the energy range $1.5\,\text{GeV} \leq E_\gamma \leq 2.4\,\text{GeV}$. This data set has been obtained through quasi-free kaon photoproduction from a deuterium target. Systematic errors originate from corrections for final-state interactions, the pion-mediated two-step process, and detector uncertainties. Quadratically summing the estimates given in Ref. [134] yields uncertainties of the order of 20 % for the differential cross section and $|\Delta\Sigma| \approx 0.2$ for the photon-beam

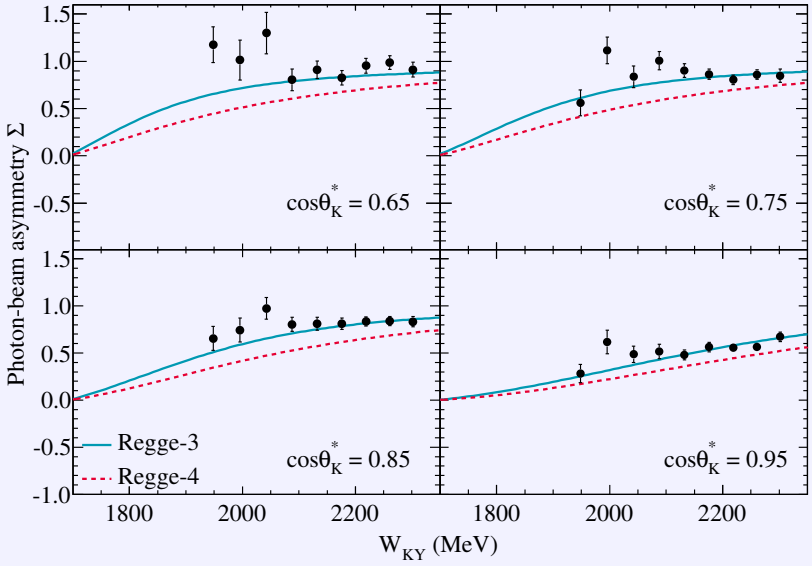

Figure 3.3 – Regge-model predictions for the $n(\gamma, K^+)\Sigma^-$ photon-beam asymmetry as a function of the kaon-hyperon invariant mass for four different values of the kaon centre-of-mass scattering angle. Data from Ref. [134]. The error bars represent the statistical uncertainties only. The systematics are estimated to be $|\Delta\Sigma| \approx 0.2$.

asymmetry.

Figures 3.2 and 3.3 show our Regge-model predictions for the measured observables. The differential cross section is fairly energy independent and settles between 0.1 and 0.2 μb. The predictions of the Regge models provide an acceptable description of the data. Overall, the quality of agreement is better for the Regge-3 variant. The Regge-4 model overpredicts the cross section by a factor of two, roughly. The LEPS data shows a clear predilection for the Regge-3 model.

As can be appreciated from Figure 3.3, both Regge models provide a satisfactory account of the photon-beam asymmetry, with a vanishing asymmetry at threshold and a steady rise as the energy increases. Again, it should be stressed that these results do not involve any free parameters and are anchored to the fitted $p(\gamma, K^+)\Sigma^0$ amplitude through $SU(2)$ isospin symmetry at the strong interaction vertex. Despite its simplicity, our approach can account quantitatively for the LEPS measurements.

Recently, the CLAS collaboration made available a large set of $n(\gamma, K^+)\Sigma^-$ differential-cross-section results covering a broad angular range [151]. The data have been obtained using photons, in an energy range from 0.8 GeV to 3.6 GeV, incident on a liquid-deuterium target. The photoproduced kaon and the pion and neutron coming from the decaying Σ^- hyperon are detected. Subsequently, the presence of the spectator proton is inferred by putting limits on the missing mass. In addition, a cut on the missing momentum $|\vec{p}_p| \leq 250$ MeV is applied. The systematic uncertainties are dominated by the background subtraction and the photon-flux calculations, and are estimated to be about 4.5–13.5%. Owing to the large energy coverage of the CLAS data, the dynamics of the $n(\gamma, K^+)\Sigma^-$ reaction can be investigated in the resonance region and at higher energies.

In Figure 3.4, Regge-model predictions are set against CLAS results at energies where the contribution of resonance exchange is judged to have died out. Clear peaks at forward scattering angles are visible. This indicates the dominance of $K^{(*)}$ exchange in the t-channel. The exponential decrease of the

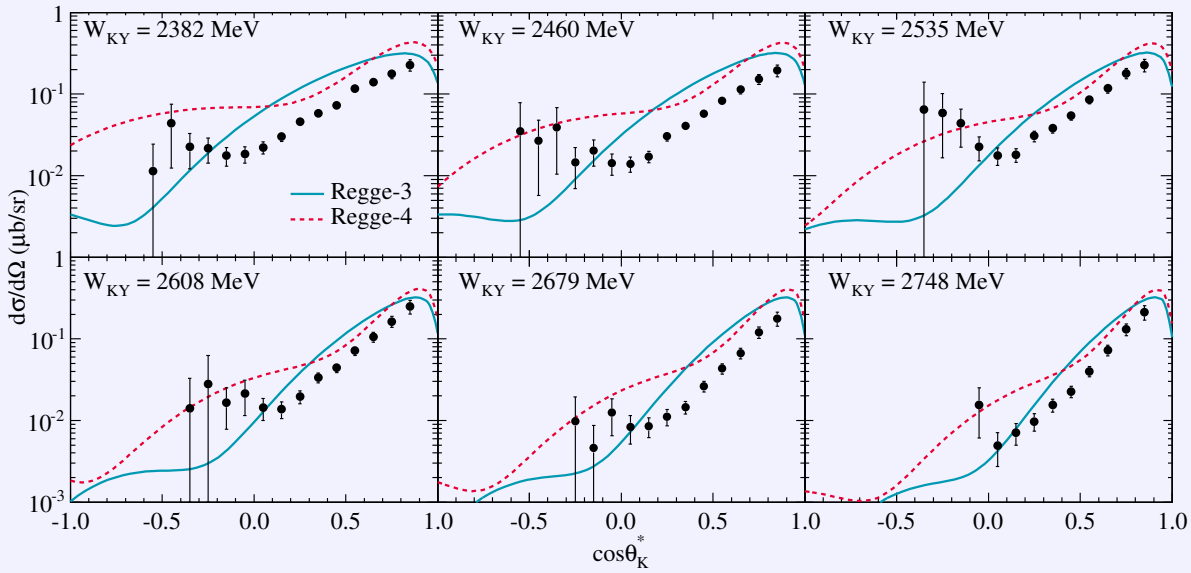

Figure 3.4 – Regge-model predictions for the $n(\gamma, K^+)\Sigma^-$ differential cross section as a function of θ_{K^*} for six different values of the kaon-hyperon invariant mass. Data from Ref. [151]. The error bars represent the total (statistical plus systematic) uncertainty.

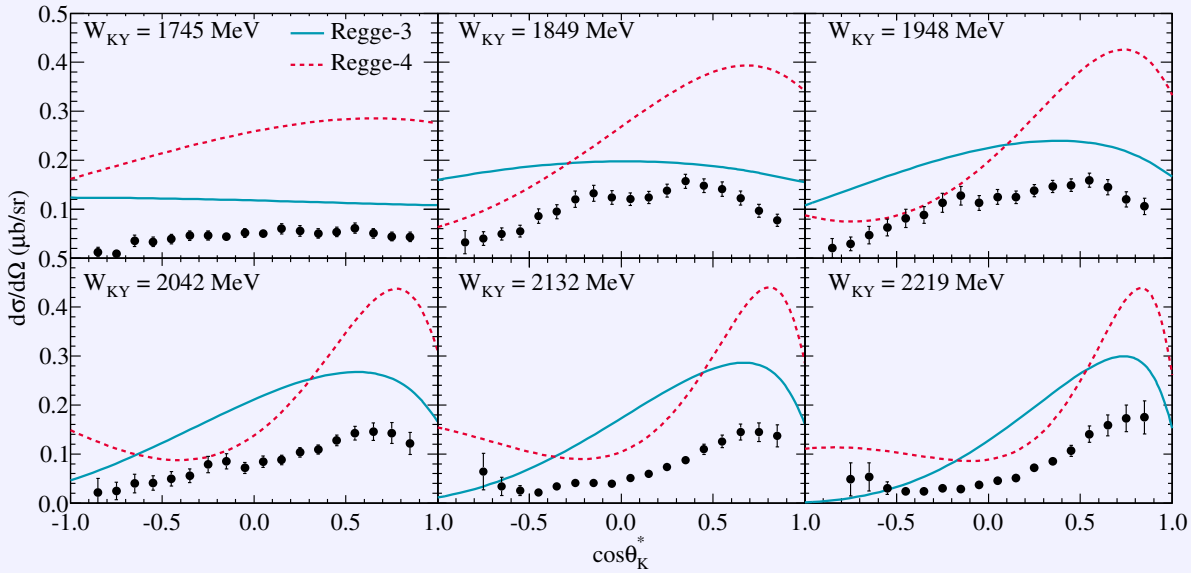

Figure 3.5 – Regge-model predictions for the $n(\gamma, K^+)\Sigma^-$ differential cross section as a function of θ_{K^*} for six different values of the invariant mass W. Data from Ref. [151]. The error bars represent the total (statistical plus systematic) uncertainty.

differential cross section as a function of the scattering angle is characteristic for Regge-trajectory exchange, and the Regge models naturally describe this trend. The magnitude at forward angles tends to be overpredicted however. In the backward hemisphere the experimental error bars are substantial. At these kinematics, the Regge-4 model predicts much larger cross sections compared to the Regge-3 model. Overall, the calculations with the Regge-3 model agree better with the data.

The angular dependence of the $n(\gamma, K^+)\Sigma^-$ differential cross section obtained by the CLAS collaboration in the resonance region is shown in Figure 3.5. The quality of agreement of the Regge models is analogous to the situation with the LEPS results of Figure 3.2. The shape of the cross section is reproduced by the Regge-3 model, yet its strength is overestimated. Again, the data favour the Regge-3 model.

In previous work [40, 97], we had not been able to discriminate between the two Regge models on the basis of the $p(\gamma^{(*)}, K^+)\Sigma^0$ data. In the $n(\gamma, K^+)\Sigma^-$ channel, on the other hand, the Regge-3 model clearly outperforms the Regge-4 variant. Accordingly, we will discard the latter from now on. This implies that, for the remainder of this dissertation, we have two unique kaon-production models at our disposal. For the Λ-production channels that is the Regge-2 and RPR-2 model. The Σ-production reactions will be described using the Regge-3 and RPR-3 models.

Both the differential cross section and the photon-beam asymmetry in Figures 3.2, 3.3 and 3.5 exhibit a rather smooth energy dependence. The Regge model predictions procure a fair description, yet discrepancies exist. These can possibly be attributed to nucleon and Δ resonances. Their role in the $n(\gamma, K^+)\Sigma^-$ reaction can be evaluated with the RPR amplitude. As was outlined in Paragraph 3.2.2, the transformation of the $p(\gamma, K^+)\Sigma^0$ amplitude requires a set of helicity amplitudes. The values extracted in the latest SAID analysis, SP09 [127], are ill-suited for our purposes, as this analysis does not provide resonance couplings to neutrons. We performed calculations with the two other sets (RPP and SM95), and found them to produce qualitatively similar results. In what follows, we will discuss the representative results obtained with the helicity amplitudes extracted in the SAID SM95 analysis [149]. No experimental information is available for the $P_{13}(1900)$ resonance. Therefore, we allow the ratios of its magnetic transition moments $\kappa^{(1,2)}_{N^*n}/\kappa^{(1,2)}_{N^*p}$ (see Eqs. (3.13) and (3.14)) to vary between -2 and $+2$. This range encompasses the Bonn model predictions. Since the EM transition strengths for delta resonances to protons and neutrons are identical, we include the $D_{33}(1700)$, $S_{31}(1900)$, $P_{31}(1910)$, and $P_{33}(1920)$ resonances with the EM coupling constants determined in the $p(\gamma, K^+)\Sigma^0$ reaction channel.

The amplitudes of the RPR-3 model are the sum of the Regge-3 background and resonance contributions. In Figures 3.6 and 3.7, we confront the RPR-3 and Regge-3 predictions for $n(\gamma, K^+)\Sigma^-$ with the LEPS data. One observes a destructive interference between the Reggeized background and the resonance diagrams. This reduces the reaction strength and marginally improves the agreement with the cross section data in all angular bins and for all energies. From Figure 3.7, it is plain that the Regge-3 and RPR-3 models provide similar predictions for the photon-beam asymmetry Σ. This observation leads us to conclude that the Σ observable is rather insensitive to resonance-exchange contributions.

From Table 3.1, we learn that the helicity amplitudes extracted in the SM95 analysis have considerable error bars. Their impact is assessed in Figures 3.6 and 3.7, and is quite dramatic. Using the error bars given in table 3.1, we considered 21 equidistant values for every $\frac{\kappa_{N^*n}}{\kappa_{N^*p}}$ and computed the $n(\gamma, K^+)\Sigma^-$ observables for each of these 21^6 combinations. The shaded area of Figures 3.6 and 3.7 indicates the

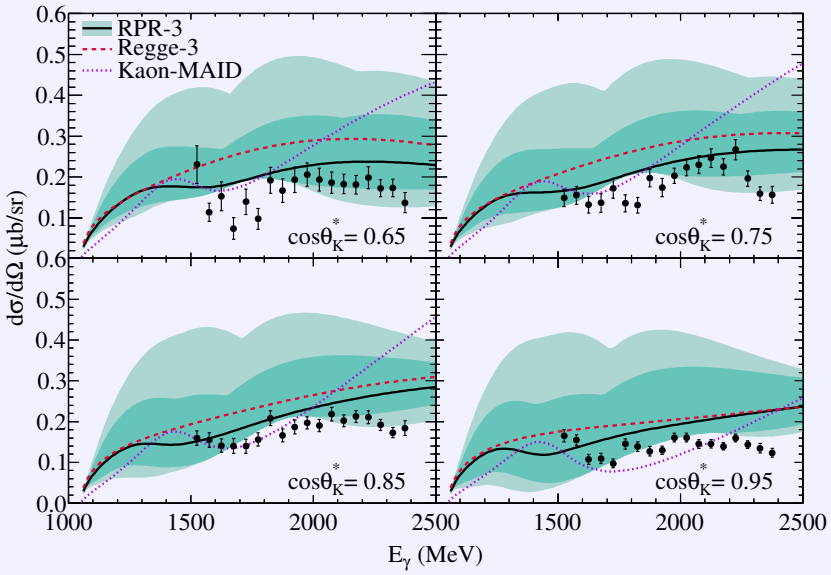

Figure 3.6 – The $n(\gamma, K^+)\Sigma^-$ differential cross section as a function of the incoming photon's LAB energy for four different values of the kaon centre-of-mass scattering angle. The dashed curve indicates the Regge-3 model, whereas the full curve corresponds to the RPR-3 amplitude, i.e. Regge-3 supplemented with $S_{11}(1650)$, $D_{33}(1700)$, $P_{11}(1710)$, $P_{13}(1720)$, $P_{13}(1900)$, $S_{31}(1900)$, $P_{31}(1910)$ and $P_{33}(1920)$ resonances. The shaded area takes the uncertainties of the adopted helicity amplitudes into account. These uncertainties are listed in table 3.1 under SM95. The ratios of EM coupling constants for the $P_{13}(1900)$ resonance are taken in the range $[-2, 2]$ (light band) and $[-1, 1]$ (dark band). The dotted curve represents the Kaon-MAID [23] predictions. Data from Ref. [134].

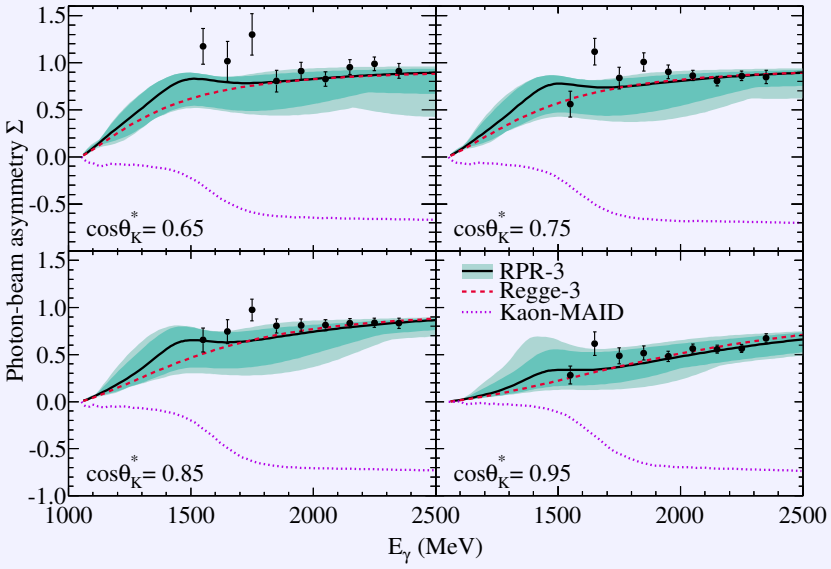

Figure 3.7 – The $n(\gamma, K^+)\Sigma^-$ photon-beam asymmetry as a function of the incoming photon's LAB energy for four different values of the kaon centre-of-mass scattering angle. The curves are as indicated in figure 3.6. Data from Ref. [134].

range of values for $d\sigma/d\Omega$ and Σ obtained with this procedure. The experimental ambiguities of the transformed photon couplings result in deviations up to 100 % for the differential cross section. The reduced sensitivity to resonant contributions leads to predictions for the photon-beam asymmetry that are affected to a smaller extent. Nevertheless, the uncertainty can be as large as $\Delta\Sigma \approx 0.8$.

One notices that the error band in Figure 3.6 is not positioned symmetrically around the RPR prediction. The addition of resonant diagrams to the Reggeized background amplitude produces destructive interference. By varying the EM coupling constants of the resonances within their allowed ranges, this destructive interference is easily destroyed. When one or more of the conversion factors is large, particular resonances will dominate the reaction dynamics and the cross section will be enlarged. We illustrate this by imposing a more restrictive range $[-1, 1]$ for the coupling-constant ratio of the $P_{13}(1900)$ state. The results using these limits are shown in Figures 3.6 and 3.7 with a darker shaded error band. The lower edge of the dark-coloured band coincides almost perfectly with that of the light-coloured one. Yet, the width of the dark-coloured area is substantially reduced. For the photon-beam asymmetry, the reduced error bars do not have a great effect on the size of the induced uncertainties.

From the previous discussion, it becomes clear that Regge models have considerable predictive power. As a consequence, one can rely solely on isospin arguments when transforming the K^+ production amplitude from proton to neutron targets. The RPR model, on the other hand, is less resilient. It is clear that the current errors on the extracted helicity amplitudes impose severe constraints on the predictive power of the RPR model. This result is not limited to the RPR model, but is inherent to any model that includes the exchange of nucleon resonances in the s-channel. To illustrate this, we have included model predictions for $n(\gamma, K^+)\Sigma^-$ from Kaon-MAID [23, 152] in Figures 3.6 and 3.7. This isobar model treats the background in terms of s-, t- and u-channel Born diagrams as well as $K^*(892)$ and $K_1(1270)$ exchange. In addition, Kaon-MAID considers a "minimal" set of resonances, consisting of $S_{11}(1650)$, $P_{11}(1710)$, $P_{13}(1720)$, $S_{31}(1900)$ and $P_{31}(1910)$. All of these resonances have a three- or four-star rating. In order to convert the $p(\gamma, K^+)\Sigma^0$ to the $n(\gamma, K^+)\Sigma^-$ amplitude, SM95 values for the helicity amplitudes were adopted. As can be appreciated from Figure 3.6, Kaon-MAID describes the measured differential cross section up to $E_\gamma \approx 2000\,\text{MeV}$ at forward angles. The predicted rise of the differential cross section with increasing E_γ is absent in the data. Furthermore, the predicted sign of the photon-beam asymmetry is opposite to the data.

The energy dependence of the $n(\gamma, K^+)\Sigma^-$ differential cross section is depicted in Figure 3.8 for different angular bins in the forward and backward hemisphere. One observes that the results from the CLAS and LEPS collaborations agree well with each other. At forward angles, the cross section becomes constant at high energies. As one moves to backward angles, a fall-off becomes evident. The Regge model reproduces this observation, but overpredicts the magnitude of the cross section in the forward hemisphere. The resonant diagrams interfere mostly destructively with the Reggeized background, thus bringing the model predictions closer to the data. At backward angles, however, the RPR model produces a clear resonant structure at an energy $W_{KY} \approx 1900\,\text{MeV}$. This *bump*, which is most likely a manifestation of either the $P_{13}(1900)$ or the $D_{13}(1900)$ resonance, is also present in the data for $-0.55 \leq \cos\theta_{K^*} \leq 0.35$, but is not as outspoken.

Figure 3.8 also illustrates the effect of the errors bars of the adopted helicity amplitudes. The results confirm that the induced uncertainties are big and the effect on the predicted cross sections can be as large as a factor five. Towards higher energies, the uncertainties dwindle. This comes as no surprise, since the highest mass of the resonances considered in the RPR model is 1900 MeV. One notices that

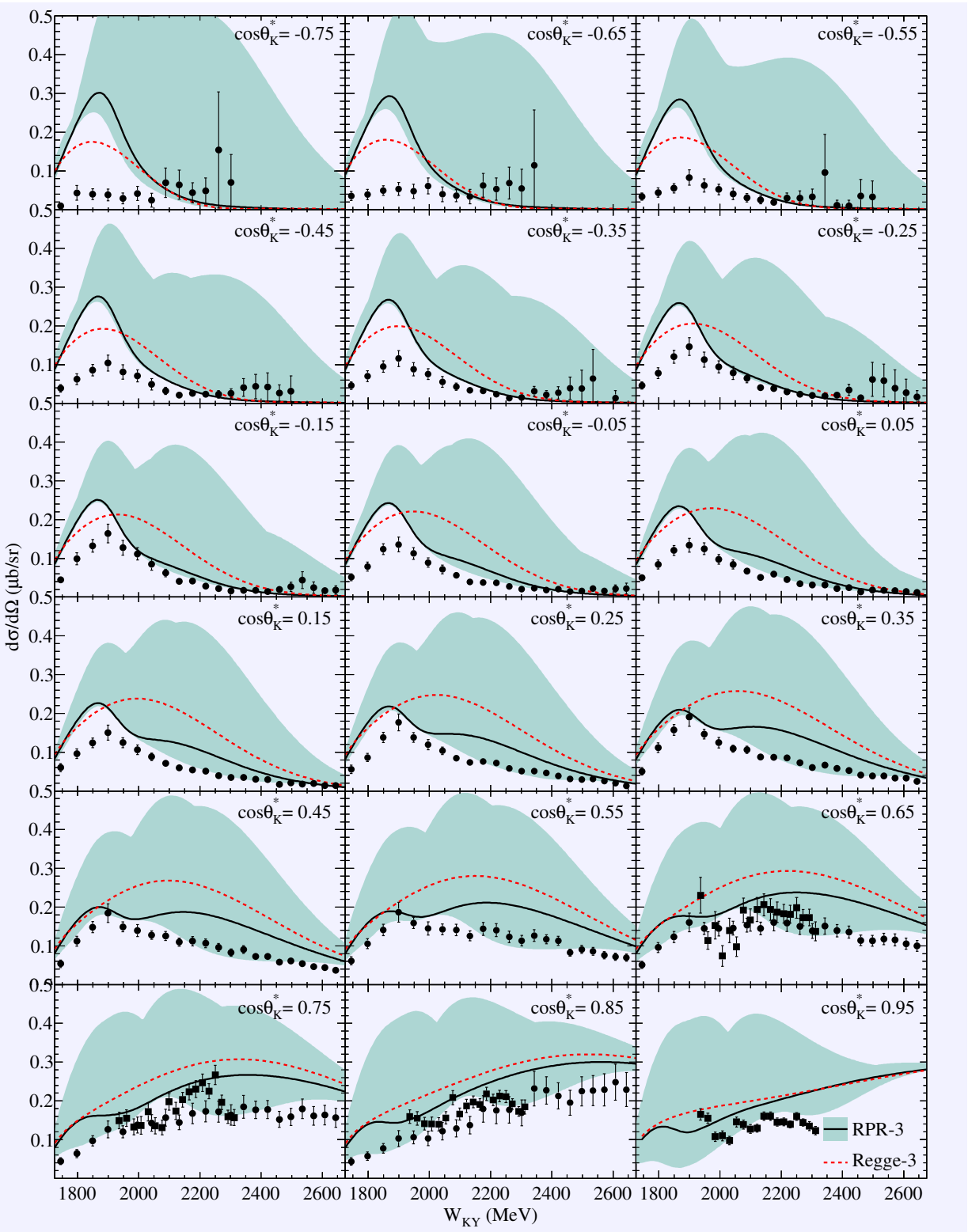

Figure 3.8 – The $n(\gamma, K^+)\Sigma^-$ differential cross section as a function of the kaon-hyperon invariant mass for 18 different values of the kaon centre-of-mass scattering angle. The dashed curve indicates the Regge-3 model, whereas the full curve corresponds to the RPR-3 amplitude. The shaded area takes the uncertainties of the adopted helicity amplitudes into account. Data from Refs. [151] (•) and [134] (■).

the RPR model that uses the central values for the coupling-constant ratios often corresponds to the situation of maximised destructive interference between the resonant and background contributions. This is especially true at backward scattering angles. Therefore, we can conclude that, in spite of the large theoretical uncertainties, the RPR model provides convincing predictions for the $n(\gamma, K^+)\Sigma^-$ reaction channel.

3.3 Regge formalism for neutral-kaon photoproduction

Another set of strangeness-production reactions where only limited amounts of data are available involves the production of neutral kaons. The $K^0\Lambda$ and $K^0\Sigma^0$ final states are produced when the incoming photon interacts with a neutron target. Recently, polarisation asymmetries for these channels have been presented in the dissertation of N. Hassall [153]. These data have been obtained during the g13 experiment using the CLAS spectrometer, and the final analysis is ongoing.

For the $p(\gamma, K^0)\Sigma^+$ reaction, several published data sets are available [154, 155], in addition to results presented in the context of dissertations [156, 157]. Therefore, we will focus on this reaction channel in order to evaluate our formalism for neutral-kaon production, which is the topic of the following section.

3.3.1 The naive approach

In Section 2.2, the Regge model for strangeness production was introduced. The production amplitude is modelled by the t-channel exchange of $K(494)$ and $K^*(892)$ Regge trajectories. In the left panel of Figure 3.9, we show their linear trajectories together with their RPP masses. To ensure the gauge invariance of the reaction amplitude, a Reggeized version of the electric part of the s-channel Born diagram was added. Transforming the $p(\gamma, K^+)\Lambda$ or $p(\gamma, K^+)\Sigma^0$ amplitudes to neutral-kaon production reactions requires modifications to the coupling constants of the relevant Feynman diagrams. The recipe at the strong-interaction vertex has been outlined in Section 3.1. The $n(\gamma, K^+)\Sigma^-$ results of the previous section have demonstrated this approach is reliable. The transformation rules for the three K^0-production channels are contained in Eq. (3.8).

The transformation of the EM vertex is more troublesome, since it inevitably requires experimental input from other reactions. When transforming $K^+(494)$ and $K^{*+}(892)$ exchange in the t-channel, the relevant coupling constants in the EM vertex are the charge of the kaon and the magnetic transition moment κ_{K^*K} respectively.

Neutral kaons have no charge, and therefore the contribution from the kaon-exchange diagram vanishes in the $N(\gamma, K^0)Y$ channels. For this reason, also the gauge-invariance-restoring s-channel diagram is no longer needed. This leaves us with the $K^{*0}(892)$ exchange diagram. The decay width of vector mesons to the ground-state kaon can be directly linked to the square of the magnetic transition moment[1]. Adopting the decay widths listed in the RPP [1]

$$\frac{\Gamma\left(K^{*0}(892) \to K^0(494)\gamma\right)/\Gamma_{\text{total}}}{\Gamma\left(K^{*+}(892) \to K^+(494)\gamma\right)/\Gamma_{\text{total}}} = \frac{2.31 \pm 0.20 \cdot 10^{-3}}{9.9 \pm 0.9 \cdot 10^{-4}} = 2.33 \pm 0.30\,, \tag{3.15}$$

[1] See the technical notes accompanying the Ph.D. thesis of S. Janssen [158].

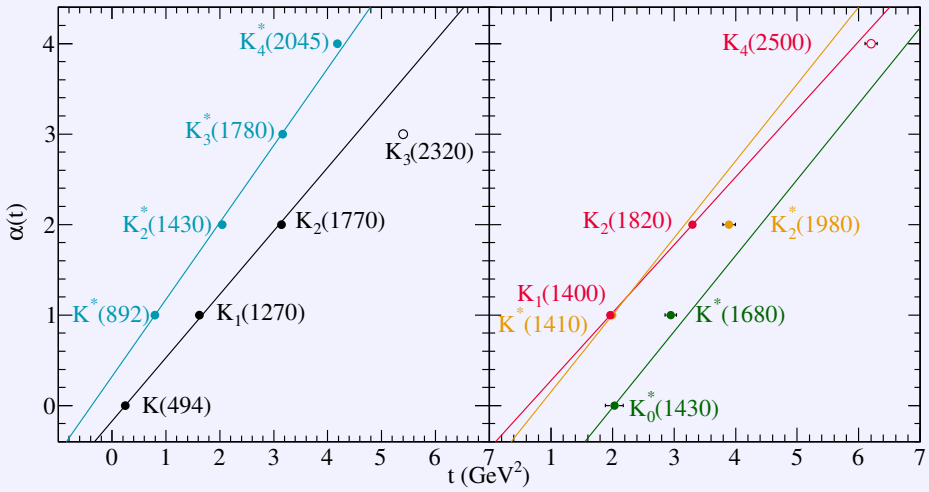

Figure 3.9 – Chew-Frautschi plot for a comprehensive set of strange mesons as listed in the RPP [1]. Unconfirmed states are marked with a hollow circle (○). All particles are colour-coded according to their respective trajectories.

we find the following relation

$$\frac{\kappa_{K^{*0}(892)K^0(494)}}{\kappa_{K^{*+}(892)K^+(494)}} = -1.53 \pm 0.10\,. \tag{3.16}$$

The relative sign for these coupling constants cannot be deduced from experiment. In Eq. (3.16), we adopt the sign predicted by the cloudy-bag quark model of Singer and Miller [159]. This sign is confirmed by the Bonn CQM [160].

At this point, we are ready to make predictions for $N(\gamma, K^0)Y$ observables using the Regge model which parametrises the background contributions. Adding resonances to these amplitudes does not introduce additional problems. The strong coupling constants can be transformed with the same rules as the t-channel coupling constants (see Eq. (3.8)). In case of a neutron target, we also require helicity amplitudes for the conversion of the EM coupling constants as was outlined in Section 3.2.

From Table J.3, we learn that very little data is available to test our formalism. For the $p(\gamma, K^0)\Sigma^+$ reaction, we have differential cross sections, total cross sections and recoil-polarisation asymmetries at our disposal. The SAPHIR collaboration has published differential cross sections in the energy range $1100\,\text{MeV} \leq E_\gamma \leq 2525\,\text{MeV}$ with full angular coverage, as well as total cross sections in the same energy range [154]. This data is supplemented with some low-statistics recoil-polarisation data for two wide E_γ bins. This complicates the comparison with model predictions, since the calculations need to be averaged. The CB/ELSA-TAPS collaboration [155][2] has published cross-section results covering angles and energies that almost coincide with those of the SAPHIR collaboration. The recoil-polarisation results, on the other hand, have a better energy and angular coverage. The CLAS collaboration has measured differential cross sections over a large energy range. These data have not yet been published, but are presented in the dissertation of B. Carnahan [157]. Given the scarcity of data in the $p(\gamma, K^0)\Sigma^+$ reaction channel, we will make use of them. In what follows, fits will be performed to $p(\gamma, K^0)\Sigma^+$ data. All above-mentioned data sets will be part of the fitting database,

[2]The same data set has been presented in smaller energy bins in R. Castelijn's dissertation [156]. This is the data we will use.

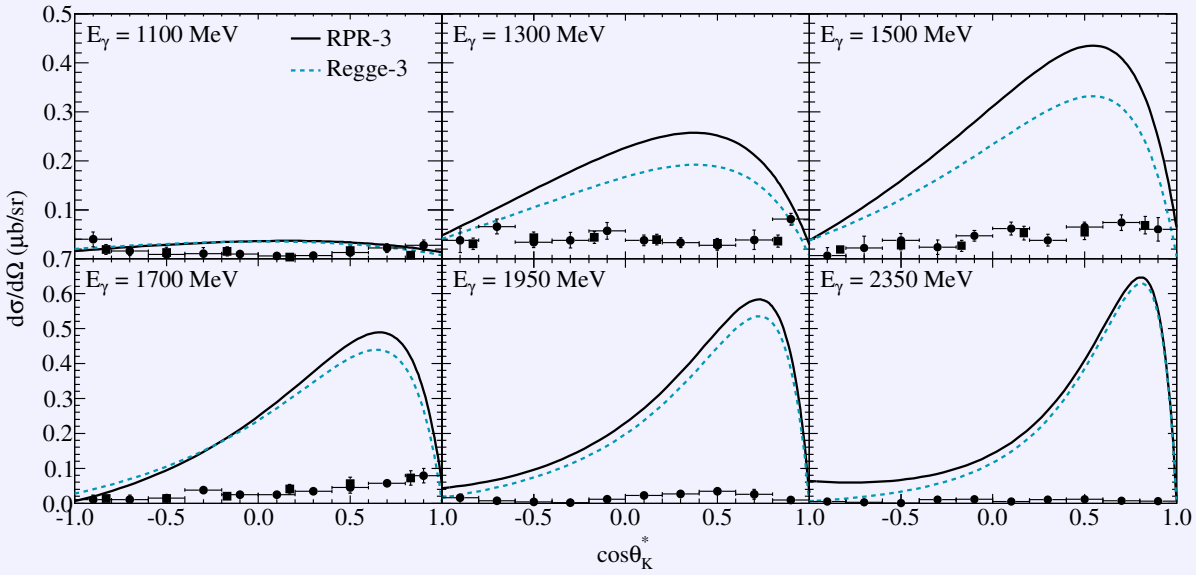

Figure 3.10 – The differential cross section for $p(\gamma, K^0)\Sigma^+$ as a function of the kaon's CM scattering angle. The solid and dashed curves represent the RPR-3 and Regge-3 models respectively. Data from Refs. [154] (•) and [155] (■).

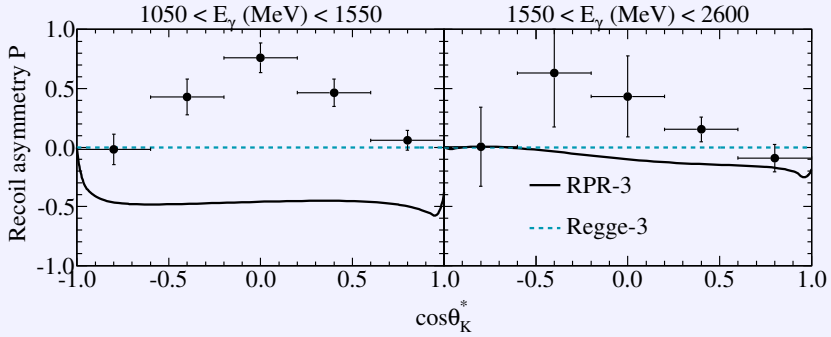

Figure 3.11 – The recoil polarisation for $p(\gamma, K^0)\Sigma^+$ as a function of the kaon's CM scattering angle. The solid and dashed curves represent the RPR-3 and Regge-3 models respectively. Data from Ref [154].

except for the recoil-polarisation asymmetries of the SAPHIR collaboration, which are presented in very wide energy bins.

The predictions using the Regge-3 and RPR-3 models are compared to the SAPHIR data in Figures 3.10 and 3.11. It is plain that the results are not convincing. For the differential cross sections, the strength is overpredicted by roughly one order of magnitude, except for the lowest energy bins where the predicted angular shape does not agree with the data.

As mentioned previously, the large energy bins for the recoil polarisation make it very difficult to compare the data to model calculations. The data do suggest that the asymmetry is positive and not small for $\cos\theta^*_K \neq \pm 1$. This qualitative behaviour is reproduced by neither the Regge nor RPR model. The former is zero, because it has a constant phase and is therefore real. This results in a vanishing asymmetry. Once resonances are added to the Regge amplitude, a non-zero asymmetry is obtained. The RPR-3 predicts a negative recoil-polarisation asymmetry, however.

Can we understand why the Regge model does a poor job in the $p(\gamma, K^0)\Sigma^+$ channel? In the left

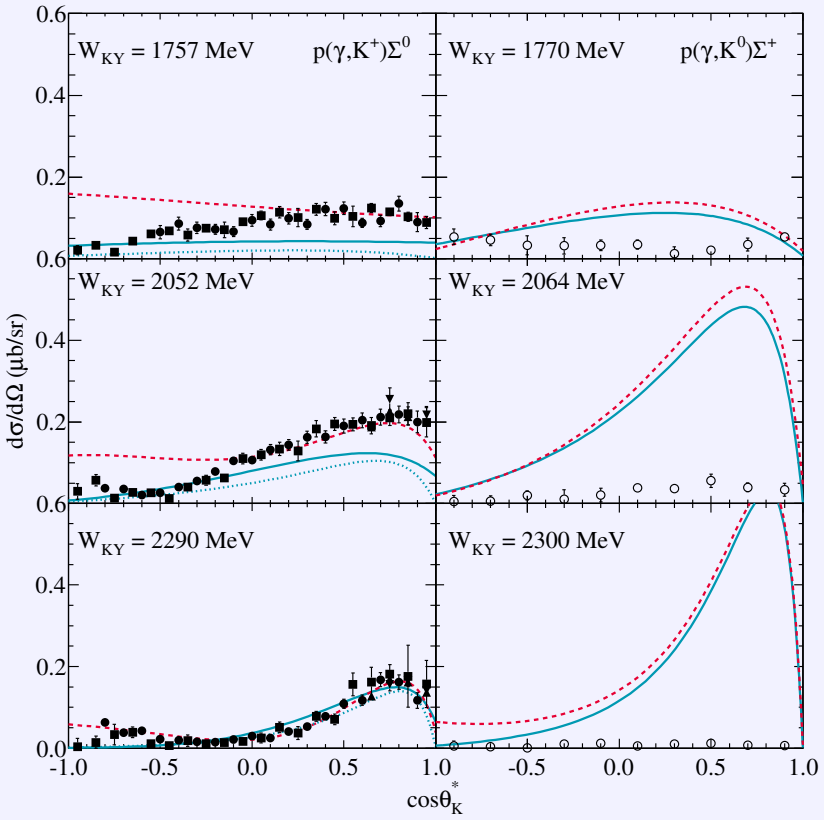

Figure 3.12 – The differential cross section for $p(\gamma, K^+)\Sigma^0$ (left panels) and $p(\gamma, K^0)\Sigma^+$ (right panels) as a function of the kaon's CM scattering angle. The solid and dashed curves are calculations with the Regge-3 and RPR-3 models respectively. The dotted line shows the contribution of the $K^*(892)$ trajectory. Data from Refs. [119] (•), [125] (■), [134] (▲), [135] (▼) and [154] (○).

panels of Figure 3.12, we compare the Regge-3 and RRP-3 models to a selection of differential-cross-section data in the $p(\gamma, K^+)\Sigma^0$ channel. The Reggeized-background parameters are fixed against high-energy data. The largest deviations between the predictions of the background model and the data are observed at forward angles and low energies. At these kinematics, one expects sizable contributions from nucleon-resonance exchange. The dotted curve depicts calculations where the $K(494)$-trajectory contribution has been left out. The latter plays an important role near threshold and at extreme forward angles, where the $K^*(892)$-exchange diagram vanishes. The full RPR model gives a nice description of the data in the forward hemisphere, where it has been fitted, but performs poorly at backward angles. This issue was mentioned in Section 2.4 and is addressed in Refs. [98, 133].

The $p(\gamma, K^0)\Sigma^+$ differential cross section in the right panels has roughly half the strength of its isospin partner in the lowest energy bin shown. This effect grows as the photon energy rises. The differential cross section is one order of magnitude smaller at the highest energy bin in Figure 3.12. This experimental observation is not at all confirmed by the Regge model. From Eqs. (3.8) and (3.16) we learn that the EM and strong coupling constants of the $K^*(892)$-exchange diagram are multiplied by $\sqrt{2}$ and -1.53 respectively. After squaring the amplitude, this implies the $p(\gamma, K^0)\Sigma^+$ differential cross section will be roughly 4.7 times as large as the $p(\gamma, K^+)\Sigma^0$ one. This is consistent with the results in Figure 3.12. Clearly, our naive approach to transform the fitted $K^+\Sigma^0$-production Regge amplitude to the $K^0\Sigma^+$-production channel fails and needs to be revised. In the forthcoming paragraphs, possible strategies to remedy this are presented.

3.3.2 A third trajectory

In Regge theory, one should, in principle, add all contributions from all possible trajectories in either the s-, t-, or u-channel. Fortunately, this is not necessary in practise. Assuming all coupling constants adopt the same value, those trajectories with the lightest first materialisation will have the largest contribution. For this reason, it suffices in the $p(\gamma, K^+)\Sigma^0$ channel to include only $K^+(494)$ and $K^{*+}(892)$ exchange. In the $p(\gamma, K^0)\Sigma^+$ reaction, however, we are left with just one diagram. This raises the question whether another trajectory should be added. A number of possible trajectories are suggested in the right panel of Figure 3.9.

The $K_1(1270)$ trajectory has negative signature and is considered the degenerate partner of the $K(494)$ trajectory. This degeneracy is easily spotted in Figure 3.9. The spin-parity J^P of the first materialisation is 1^+ and the trajectory can be parametrised as

$$\alpha(t) = 1 + 0.7(t - m^2_{K_1(1270)})\,. \tag{3.17}$$

Adopting EM decay widths as calculated with the Bonn CQM [160], one finds

$$\frac{\kappa_{K_1^0(1270)K^0(494)}}{\kappa_{K_1^+(1270)K^+(494)}} = -0.97\,. \tag{3.18}$$

Also the $K_1(1400)$ trajectory has negative signature. Its first materialisation has $J^P = 1^+$. As possible other members we consider $K_2(1820)$ and $K_4(2500)$. Fixing the trajectory's slope using the first two materialisations, one obtains

$$\alpha(t) = 1 + 0.75(t - m^2_{K_1(1400)})\,. \tag{3.19}$$

Adopting EM decay widths as calculated with the Bonn CQM [160], the ratio of EM coupling constants is given by

$$\frac{\kappa_{K_1^0(1400)K^0(494)}}{\kappa_{K_1^+(1400)K^+(494)}} = 2.5277\,. \tag{3.20}$$

Next, we consider the $K^*(1410)$ trajectory. The first materialisation of this positive-signature trajectory has the same spin-parity as the $K^*(892)$. A possible second member for this trajectory is $K_2^*(1980)$, which would result in a very small slope parameter. Relying on predictions for the kaon masses from the Bonn CQM, we parametrise the trajectory as [69]

$$\alpha(t) = 1 + 0.85(t - m^2_{K^*(1410)})\,. \tag{3.21}$$

The conversion factor for the EM coupling constants

$$\frac{\kappa_{K^{*0}(1410)K^0(494)}}{\kappa_{K^{*+}(1410)K^+(494)}} = -1.1592\,. \tag{3.22}$$

is obtained with EM decay widths from the Bonn CQM as input [160].

The RPR strategy, outlined in Chapter 2, fixes the background parameters of the Regge model at high energies. This background amplitude is subsequently extrapolated into the resonance region while keeping all parameters fixed. This allows one to optimise the coupling constants of the resonant diagrams unambiguously. Because of the absence of high-energy data in the $K^0\Sigma^+$ channel, it is impossible to determine the parameters of a possible additional Regge trajectory at high energies. A different strategy involves fitting a Regge amplitude consisting of three trajectories to the high-energy

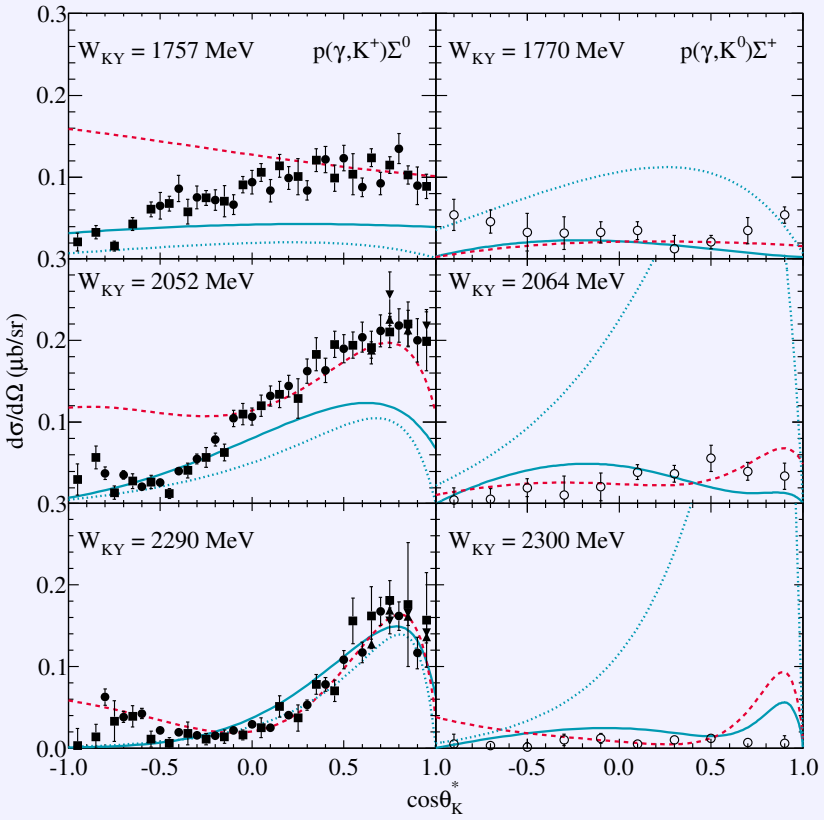

Figure 3.13 – The differential cross section for $p(\gamma, K^+)\Sigma^0$ (left panels) and $p(\gamma, K^0)\Sigma^+$ (right panels) as a function of the kaon's CM scattering angle. The calculations use the model labelled RPR-A in Table 3.2, i.e. the RPR-3 model supplemented with a $K^*(1410)$ trajectory in the $p(\gamma, K^0)\Sigma^+$ channel. The solid curves are calculations with the Regge model, whereas the dashed curves represent the full model including resonances. The dotted line shows the contribution of the $K^*(892)$ trajectory. Data from Refs. [119] (•), [125] (■), [134] (▲), [135] (▼) and [154] (○).

$K^+\Sigma^0$ channel data. This way, two trajectories with known coupling constants remain for the $p(\gamma, K^0)\Sigma^+$ reaction. Again, the quality of the data is a limiting factor. The high-energy fits with two trajectories in the $K^+\Sigma^0$ channel attain a $\chi^2/n.d.f \approx 1.1$. Clearly, the current data set does not require an extra trajectory. Introducing one nonetheless would not enable us to fix the free parameters of this third trajectory in a meaningful way. A third option is to use resonance-region data to determine a Regge amplitude consisting of three trajectories. This approach comes at a cost, since one of the attractive conceptual advantages of the RPR formalism is lost, namely the independent determination of resonant and non-resonant parameters.

In a first attempt, a pure Regge model consisting of 3 trajectories is fitted to the $p(\gamma, K^+)\Sigma^0$ and $p(\gamma, K^0)\Sigma^+$ photoproduction data in the resonance region. We take the $K(494)$ and $K^*(892)$ as core trajectories and add either a pseudovector $K_1(1400)$ or a vector $K^*(1410)$ trajectory. The coupling constants, five in total, are constrained to ± 100 and every possible combination of phases is considered. A number of acceptable models is obtained with different combinations of phases. The resulting goodness-of-fit is of the order $\chi^2/n.d.f. \approx 7 - 9$. None of these model variants, however, results in acceptable predictions for the $K^0\Sigma^+$ channel. The use of $p(\gamma, K^+)\Sigma^0$ and $p(\gamma, K^0)\Sigma^+$ data sets in a common fit does not lead to acceptable results, because of the disparity in the number of data points.

Table 3.2 – Revised RPR-3 models optimised against the available $p(\gamma, K^0)\Sigma^+$ data. Except for model RPR-A, the ratio of EM coupling constants for the $K^*(892)$ trajectory was considered a free parameter.

Label	Trajectories [Phases]	$\frac{\kappa_{K^{*0}(892)K^0(494)}}{\kappa_{K^{*+}(892)K^+(494)}}$	$\chi^2/n.d.f.$
RPR-A	$K(494)$ [rot] + $K^*(892)$ [cst] + $K^*(1410)$ [cst]	-1.530 ± 0.100	5.23
RPR-B	$K(494)$ [rot] + $K^*(892)$ [cst]	0.054 ± 0.010	3.39
RPR-C	$K(494)$ [rot] + $K^*(892)$ [cst] + $K_1(1270)$ [cst]	0.098 ± 0.015	2.78
RPR-D	$K(494)$ [rot] + $K^*(892)$ [cst] + $K_1(1270)$ [rot]	0.117 ± 0.013	2.47
RPR-E	$K(494)$ [rot] + $K^*(892)$ [cst] + $K_1(1400)$ [cst]	0.100 ± 0.015	2.79
RPR-F	$K(494)$ [rot] + $K^*(892)$ [cst] + $K_1(1400)$ [rot]	0.061 ± 0.012	3.31
RPR-G	$K(494)$ [rot] + $K^*(892)$ [cst] + $K^*(1410)$ [cst]	-0.430 ± 0.052	2.67
RPR-H	$K(494)$ [rot] + $K^*(892)$ [cst] + $K^*(1410)$ [rot]	0.070 ± 0.011	2.77

Next, a third trajectory is added exclusively to the $K^0\Sigma^+$ channel. We fit its coupling constants to the available data discussed on page 44, while the remaining parameters are kept fixed. Starting from the RPR-3 amplitude, which has been optimised against $K^+\Sigma^0$ data, either a $K_1(1270)$, $K_1(1400)$ or $K^*(1410)$ trajectory is added. Only the fit with an additional $K^*(1410)$ and a constant phase leads to an acceptable result ($\chi^2/n.d.f. = 5.23$). Why this particular trajectory leads to fair results is illustrated in Figure 3.13 where the RPR prediction is decomposed into its various contributions. In order to reduce the cross section to the level of the data, the additional trajectory needs to provide strong enough destructive interference with the problematic $K^*(892)$ trajectory. This can only be achieved by a trajectory with similar quantum numbers and the same phase, hence the $K^*(1410)$ trajectory.

3.3.3 Adjusting the strength of the $K^*(892)$ trajectory

In Paragraph 3.3.1, we conclude on the basis of Figure 3.12 that the RPR model overestimates the $p(\gamma, K^0)\Sigma^+$ cross section, because the dominant trajectory, the $K^*(892)$, is magnified by its isospin coefficient (3.8) and the ratio of EM decay widths (3.16). In the previous paragraph, we have attempted to suppress the $K^*(892)$ trajectory's contribution by adding an additional trajectory. Directly readjusting the $K^*(892)$'s coupling constants presents an alternative to control this taxing diagram's strength. The ratio of coupling constants in the strong interaction vertex is given by SU(2) isospin symmetry and is on solid ground. The ratio of EM coupling constants, on the other hand, is based on the EM decay widths of the $K^*(892)$ to charged and neutral $K(494)$. Although this ratio is well-known experimentally, we need to acknowledge that we are, in fact, dealing with phenomenological parameters. The t-channel diagrams in our Regge formalism correspond to the exchange of entire trajectories instead of merely their first materialisations. In this light, it is a viable option to consider the ratio of EM coupling constants as a free parameter left to be fitted.

Fitting the EM coupling constant of the $K^*(892)$ Regge trajectory to the available $K^0\Sigma^+$-production data, we find

$$\frac{\kappa_{K^{*0}(892)K^0(494)}}{\kappa_{K^{*+}(892)K^+(494)}} = 0.0540 \pm 0.0101\,. \tag{3.23}$$

All other parameters of the RPR-3 model have been kept fixed. Despite the fact that only one

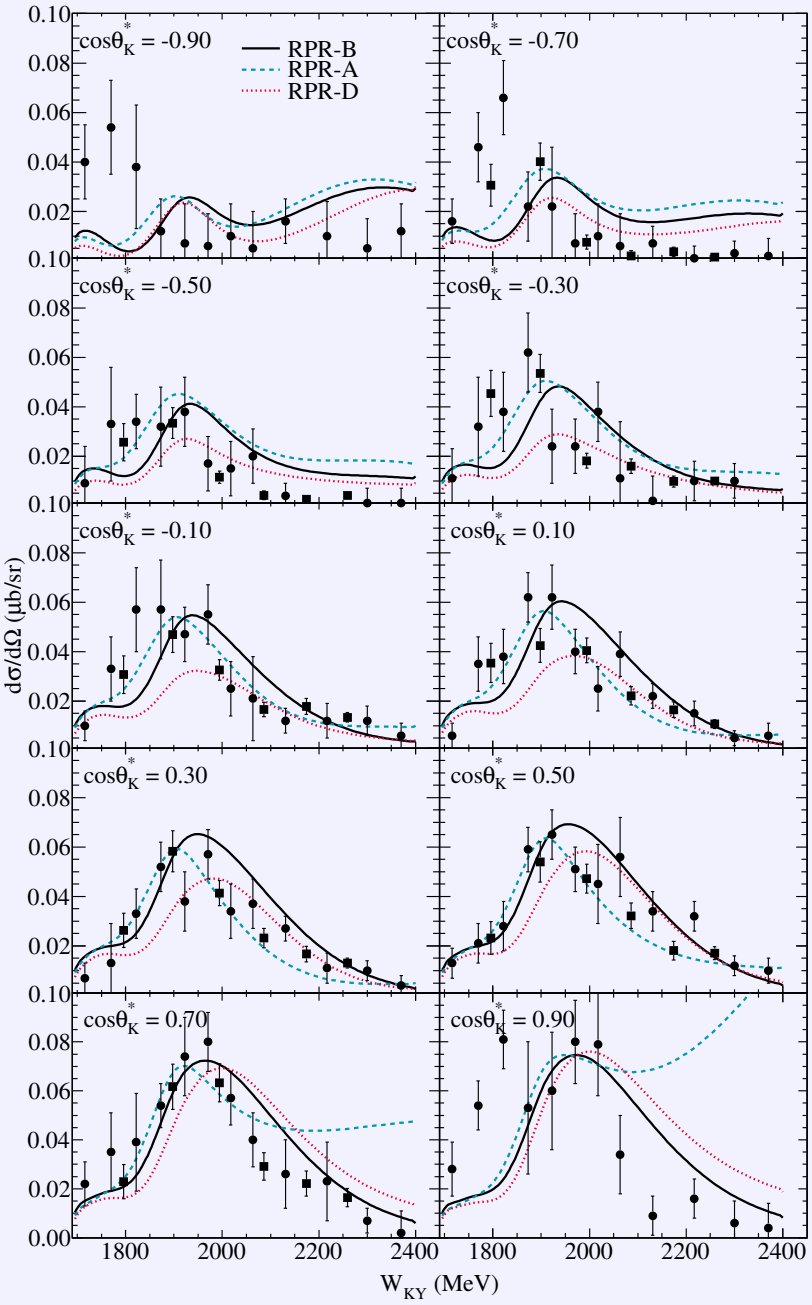

Figure 3.14 – The $p(\gamma, K^0)\Sigma^+$ differential cross section as a function of the kaon-hyperon invariant mass for various $\cos\theta_{K^*}$. The curves represent different models presented in Table 3.2. Data from Refs. [154] (•) and [157] (■).

free parameter is introduced, we attain $\chi^2/n.d.f. = 3.39$. The fitted ratio of the EM coupling constants given in Eq. (3.23) is approximately a factor of thirty smaller than the value (3.16) obtained with decay widths from the RPP. In addition, the sign has changed. With the fitted value for the EM coupling constant, the contribution of the $K^*(892)$ trajectory is strongly suppressed and the $p(\gamma, K^0)\Sigma^+$ reaction dynamics will be dominated by nucleon-resonance-exchange diagrams.

Since we have identified a mechanism to control the strength of the $K^*(892)$ trajectory, the possibility of a third trajectory in the $K^0\Sigma^+$ channel can be reconsidered. As in Paragraph 3.3.2, we add either

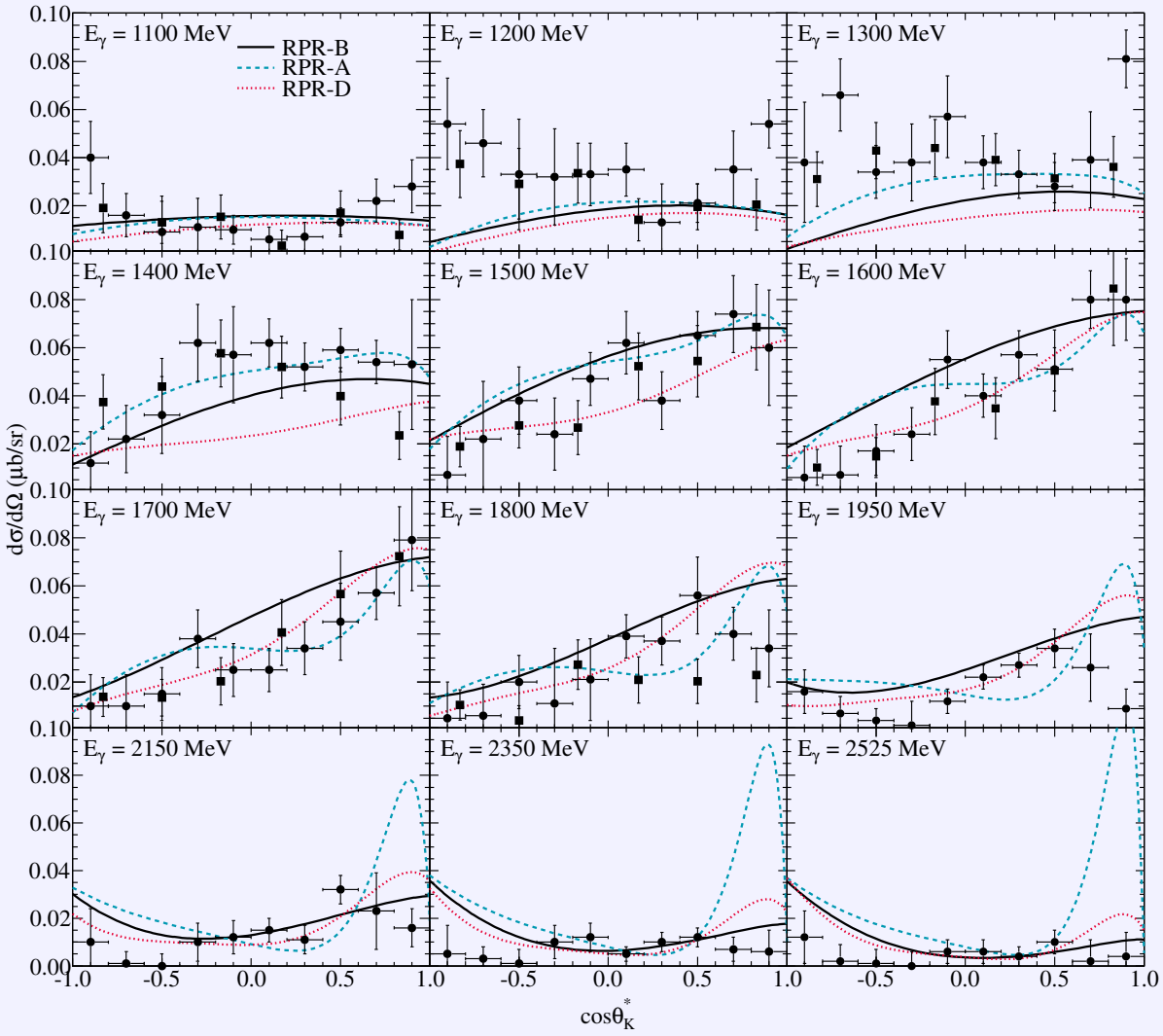

Figure 3.15 – The $p(\gamma, K^0)\Sigma^+$ differential cross section as a function of the kaon's CM scattering angle. The curves represent different models presented in Table 3.2. Data from Refs. [154] (•) and [155] (■).

a $K_1(1270)$, $K_1(1400)$ or $K^*(1410)$ trajectory to the RPR-3 model, while simultaneously allowing the ratio of EM coupling constants of the $K^*(892)$-exchange diagram to vary. The different model variants lead to acceptable χ^2 values as can be appreciated in Table 3.2. The reduction of the χ^2 in view of the two additional free parameters is small however. The optimal solution includes a $K_1(1270)$ trajectory with a constant phase. All fitted ratios of EM coupling constants are tiny compared to the experimental value (3.16), with the exception of the model with an additional $K^*(1410)$ trajectory with constant phase. As discussed in the previous paragraph, this trajectory manages strong destructive interference with the leading $K^*(892)$ trajectory.

3.3.4 Results

The different model variants introduced in the previous two paragraphs are listed in Table 3.2. In Figures 3.14 to 3.18, they are confronted with the $p(\gamma, K^0)\Sigma^+$ data. We do not show results for all three-trajectory models with a fitted EM coupling-constant ratio, and only retain the model variant

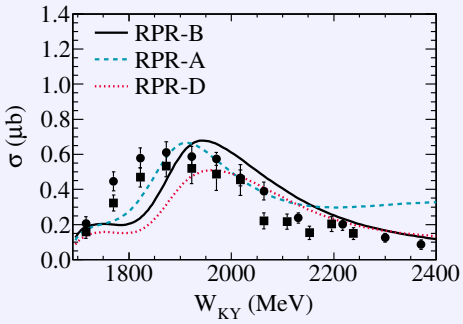

Figure 3.16 – The total $p(\gamma, K^0)\Sigma^+$ cross section as a function of the incoming photon's LAB energy. The curves represent different models presented in Table 3.2. Data from Refs. [154] (•) and [155] (■).

RPR-D with the lowest χ^2.

Figure 3.14 features the differential cross section as a function of the kaon-hyperon invariant mass. The different RPR models give a fair description of the data and have a similar qualitative behaviour. At forward angles, however, the RPR-A model exhibits a problematic trend towards higher energies. This is confirmed in Figure 3.15. All considered RPR models have a peak structure near forward scattering in the highest energy bins. This peak is most outspoken for the RPR-A model and is not observed. The angular dependence of the cross section is well accounted for by all model variants. The RPR-D model tends to predict smaller cross sections than the RPR-B variant. At forward angles, however, the RPR-D cross section peaks more strongly.

The total cross section is given in Figure 3.16. One immediately spots the troublesome high-energy behaviour of the RPR-A model. The cross section has a broad maximum about $W_{KY} \approx 1900\,\text{MeV}$. Apart from the RPR-D model, this feature is accounted for by our calculations.

Finally, we show the comparison of the RPR models with the recoil-polarisation data in Figures 3.17 and 3.18. The error bars on the experimental results are considerable and it is not obvious to differentiate between the different model variants. In general, the recoil asymmetry is positive and is matched by the models. Only the RPR-A model produces negative asymmetries towards higher energies.

The RPR-A, which consists of the RPR-3 model with an additional $K^*(1410)$ trajectory, gives the least optimal description of the available $K^0\Sigma^+$ data and can be discarded. The remaining model variants listed in Table 3.2 provide a comparable agreement with experiment. The RPR-B model takes precedence over the others, because it contains only a single free parameter, compared with three for models RPR-C to RPR-H. Therefore, we will adopt the fitted ratio in Eq. (3.23) without adding a third trajectory when transforming the $p(\gamma, K^+)\Sigma^0$ amplitude to channels with a neutral kaon in the final state.

In the Λ-production channels, no data is accessible to examine the predictions of the RPR model. Hence, we will stick with the naive approach and adopt the experimental ratio (3.16) for the EM coupling constants of the $K^*(892)$ trajectory.

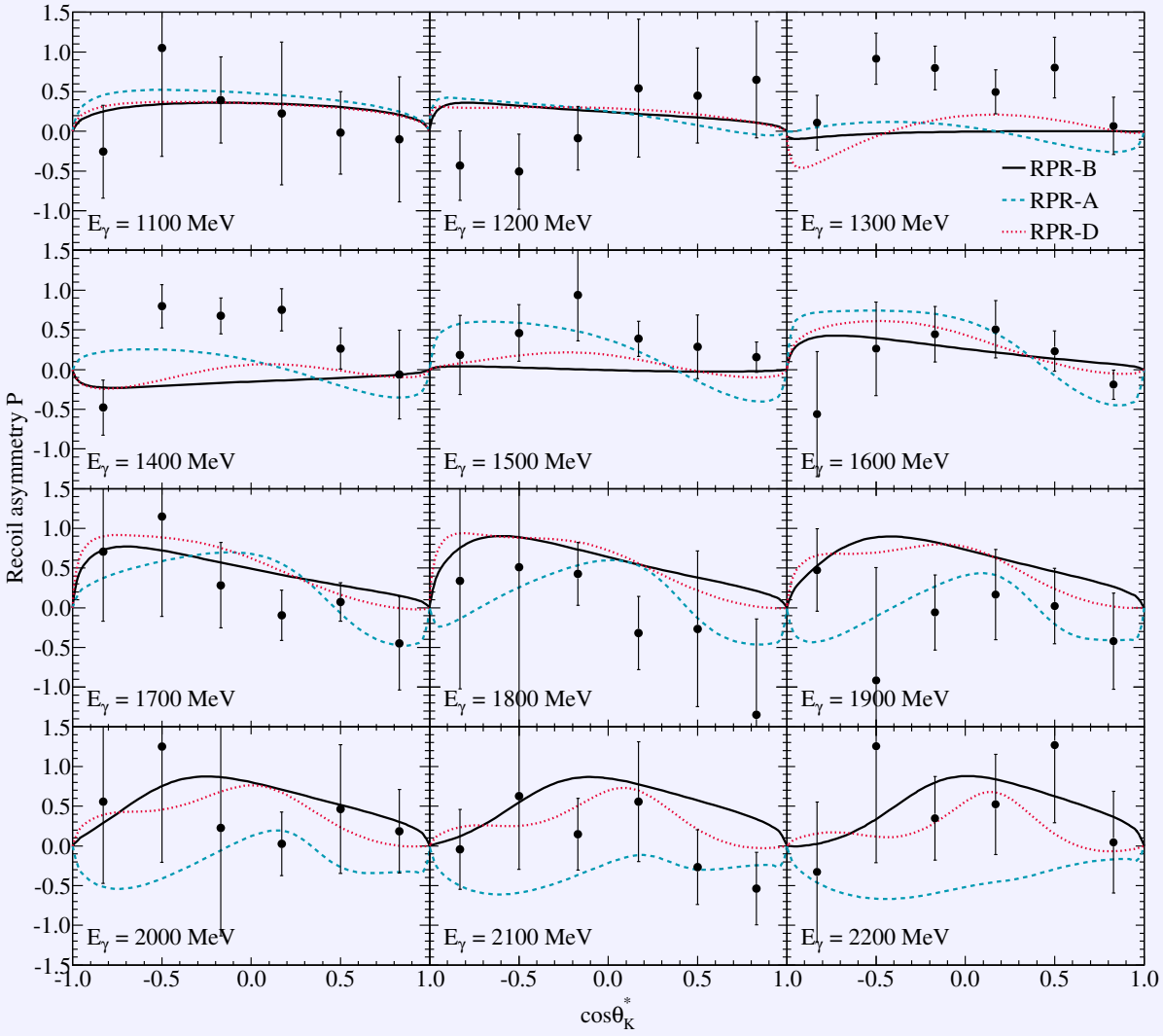

Figure 3.17 – The recoil-polarisation asymmetry for $p(\gamma, K^0)\Sigma^+$ as a function of the kaon's CM scattering angle. The curves represent different models presented in Table 3.2. Data from Ref [155].

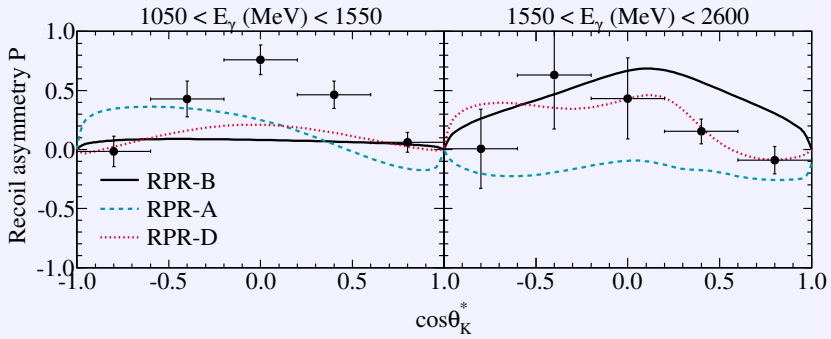

Figure 3.18 – The recoil-polarisation asymmetry for $p(\gamma, K^0)\Sigma^+$ as a function of the kaon's CM scattering angle. The curves represent different models presented in Table 3.2. The results are averaged over the range of photon energies. Data from Ref [154].

CHAPTER 4

Radiative kaon capture

After having introduced the RPR formalism for $N(\gamma^{(*)}, K)Y$ in Chapters 2 and 3, we are ready to build a framework in order to study strangeness production from the deuteron. Before proceeding, we illustrate the strength of the RPR approach by considering the radiative capture of kaons on protons. In Section 4.1, we establish the link between this reaction and photon-induced kaon production. Section 4.2 provides cross-section results obtained with the Crystal Barrel at Brookhaven National Laboratory that have been published recently. An exploratory analysis of these data is presented adopting the RPR formalism.

The experimental study of the radiative reactions $p(K^-, \gamma)\Lambda$ and $p(K^-, \gamma)\Sigma^0$ is of special physical interest because it is one of few cases in which one can get access to the excitation spectrum of hyperons. Measuring the masses and decay widths of these resonances constitutes important input to models that attempt to describe the internal structure of hadrons. The Particle Data Group's RPP [1] lists a number of established Λ and Σ resonances (see Table 4.1), albeit with large uncertainties for the masses, widths and branching ratios.

An abundant amount of data and several models for the radiative capture of kaons at rest exist (see Refs. [161, 162] and references therein). The reaction is dominated by the $\Lambda(1405)S_{01}$ resonance. A more comprehensive study of the hyperon spectrum is possible through the study of in-flight capture of kaons on a proton, for which only a meagre set of data is available. To date, no dedicated model calculations for this reaction channel are available. The radiative capture process can, however, be described with the help of models for kaon photoproduction, because both reactions are intimately related through crossing symmetry.

4.1 Formalism

We wish to study the reaction

$$K^- + p \to \gamma + Y\,, \tag{4.1}$$

Table 4.1 – Selection of established Λ and Σ resonances relevant to the data presented in the present work. We list the resonances' mass and total decay width ranges as given in the RPP [1], in addition to their star status. In the last two columns, we tabulate predictions by the Bonn constituent-quark model [163, 164] for the partial electromagnetic decay widths to the ground-state $\Lambda(1116)$ and $\Sigma^0(1193)$.

Resonance	$L_{I\,2J}$	status	Mass (MeV)	Width (MeV)	$\Gamma_{\Lambda\gamma}$ (MeV)	$\Gamma_{\Sigma^0\gamma}$ (MeV)
$\Lambda(1405)$	S_{01}	****	1406 ± 4	50 ± 2	0.912	0.233
$\Lambda(1520)$	D_{03}	****	1519.5 ± 1.0	15.6 ± 1.0	0.258	0.157
$\Lambda(1600)$	P_{01}	***	1560-1700	50-250	0.104	0.0679
$\Sigma(1660)$	P_{11}	***	1630-1690	50-70	0.451	0.578
$\Lambda(1670)$	S_{01}	****	1660-1680	25-50	$0.159 \cdot 10^{-3}$	3.827
$\Sigma(1670)$	D_{13}	****	1665-1685	40-80	1.457	0.214
$\Lambda(1690)$	D_{03}	****	1685-1695	50-70	0.0815	1.049

with Y either a Λ or Σ^0 hyperon. The four-momenta of the incoming and outgoing particles are given by $\boldsymbol{p}_K$, $\boldsymbol{p}_N$, $\boldsymbol{p}_\gamma$and $\boldsymbol{p}_Y$. One can define three Mandelstam variables

$$\begin{aligned} s'_{\gamma Y} &= \left(\boldsymbol{p}_\gamma + \boldsymbol{p}_Y\right)^2 , \\ t' &= \left(\boldsymbol{p}_K - \boldsymbol{p}_\gamma\right)^2 , \\ u' &= \left(\boldsymbol{p}_K - \boldsymbol{p}_Y\right)^2 . \end{aligned} \tag{4.2}$$

We have adopted a notation with primes to avoid confusion with the Mandelstam variables for kaon photoproduction defined in Eq. (2.8). The differential cross section for the radiative-capture reaction is derived as in Paragraph 2.1.4. It reads

$$\frac{d^2\sigma}{d\Omega^*_\gamma} = \frac{1}{64\pi^2} \frac{E^*_\gamma}{|\vec{p}^{\,*}_K| s'_{\gamma Y}} \overline{\sum} |\mathcal{T}_{Kp\to\gamma Y}|^2 , \tag{4.3}$$

and is expressed as a function of the transition amplitude.

In order to investigate the dynamics of this amplitude, one can exploit the fact that radiative kaon capture is linked with photon-induced strangeness production through crossing symmetry [21, 22, 165–167]. This relation is illustrated in Figure 4.1. The transition amplitude for radiative kaon capture $\mathcal{T}_{Kp\to\gamma Y}$ is the analytic continuation (AC) of the kaon-production amplitude with the signs of the kaon and photon momenta reversed

$$\mathcal{T}_{Kp\to\gamma Y}(\boldsymbol{p}_K, \boldsymbol{p}_N; \boldsymbol{p}_\gamma, \boldsymbol{p}_Y) \overset{\text{AC}}{=} \mathcal{T}_{\gamma p\to KY}(-\boldsymbol{p}_\gamma, \boldsymbol{p}_N; -\boldsymbol{p}_K, \boldsymbol{p}_Y) . \tag{4.4}$$

Since crossing symmetry flips the signs of the kaon and photon momenta, one has

$$\begin{aligned} s'_{\gamma Y} &= u , \\ t' &= t , \\ u' &= s_{KY} . \end{aligned} \tag{4.5}$$

Thus, the roles of the Mandelstam-s and -u variables are interchanged. The Mandelstam-t variable, on the other hand, remains the same. As a consequence, the contributions to the amplitude that arise from t-channel exchange do not change, but the role of s- and u-channel diagrams is turned

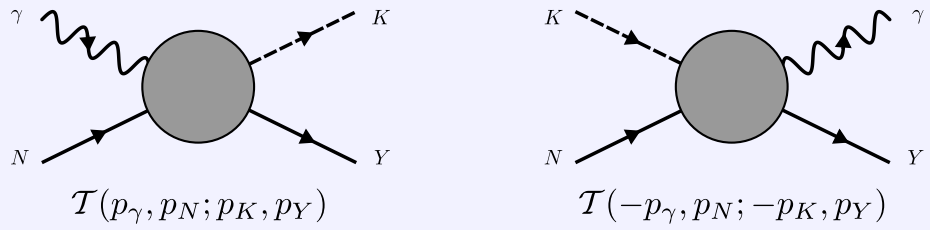

Figure 4.1 – Schematic representation of the transition amplitude for kaon photoproduction (left) and radiative kaon capture (right). The latter amplitude is the analytic continuation of the former with the signs of the kaon and photon momenta reversed.

around. In kaon photoproduction, the resonant contributions to the reaction amplitude are related to the exchange of nucleon resonances in the s-channel. For radiative kaon capture, this role is reserved for hyperon-resonance exchange. This explains the potential of the $p(K^-, \gamma)Y$ reaction to probe the hyperon spectrum.

4.2 Crystal-Ball data: an exploratory analysis

Recently, differential cross sections for K^- radiative capture in flight on the proton, leading to the $\gamma\Lambda$ and $\gamma\Sigma^0$ final states, have been measured for the first time [168]. The momenta of the K^- meson ranged between 514 and 750 MeV/c. The data were obtained with the Crystal Ball multiphoton spectrometer installed at the separated K/π beam line C6 of the Alternating Gradient Synchrotron at Brookhaven National Laboratory. The results improve substantially the existing experimental data available for studying radiative decays of excited hyperon states.

In Figures 4.2 and 4.3, the differential cross sections for the $p(K^-, \gamma)\Lambda$ and $p(K^-, \gamma)\Sigma^0$ reactions are shown. Since the radiative-kaon-capture reaction is related to photon-induced kaon production through crossing symmetry, the t-channel contributions to both reactions are the same. Therefore, one can apply the Regge model, developed for kaon photoproduction, to the description of radiative kaon capture, without introducing or adjusting any parameters. As can be appreciated in Figure 4.2, the Regge-model predictions for $p(K^-, \gamma)\Lambda$ are of the same order as the measured differential cross sections and are in reasonable agreement with the data except for the underpredicted strength at forward angles. The situation for the $p(K^-, \gamma)\Sigma^0$ channel is entirely different. Figure 4.3 shows that the Regge model underpredicts the data by almost an order of magnitude. This hints at an important role for resonance exchange in $p(K^-, \gamma)\Sigma^0$.

In order to assess the possible resonant contributions to the radiative capture reactions, the Regge-model amplitudes can be enriched with hyperon-resonance exchange terms, along similar lines as s-channel resonances have been added for the $p(\gamma, K)Y$ processes in Section 2.3. Table 4.1 lists six established hyperon resonances relevant to the energy range of the data presented here. Since there is no experimental data available on the electromagnetic decay widths of these resonances, we have included predictions by the Bonn CQM [163, 164]. Note the tiny EM branching fractions. Hyperon resonances decay almost exclusively to hadronic final states. Fixing the resonances' mass and width at the central value given in the RPP, inclusion of a spin-1/2 or spin-3/2 resonance introduces two or

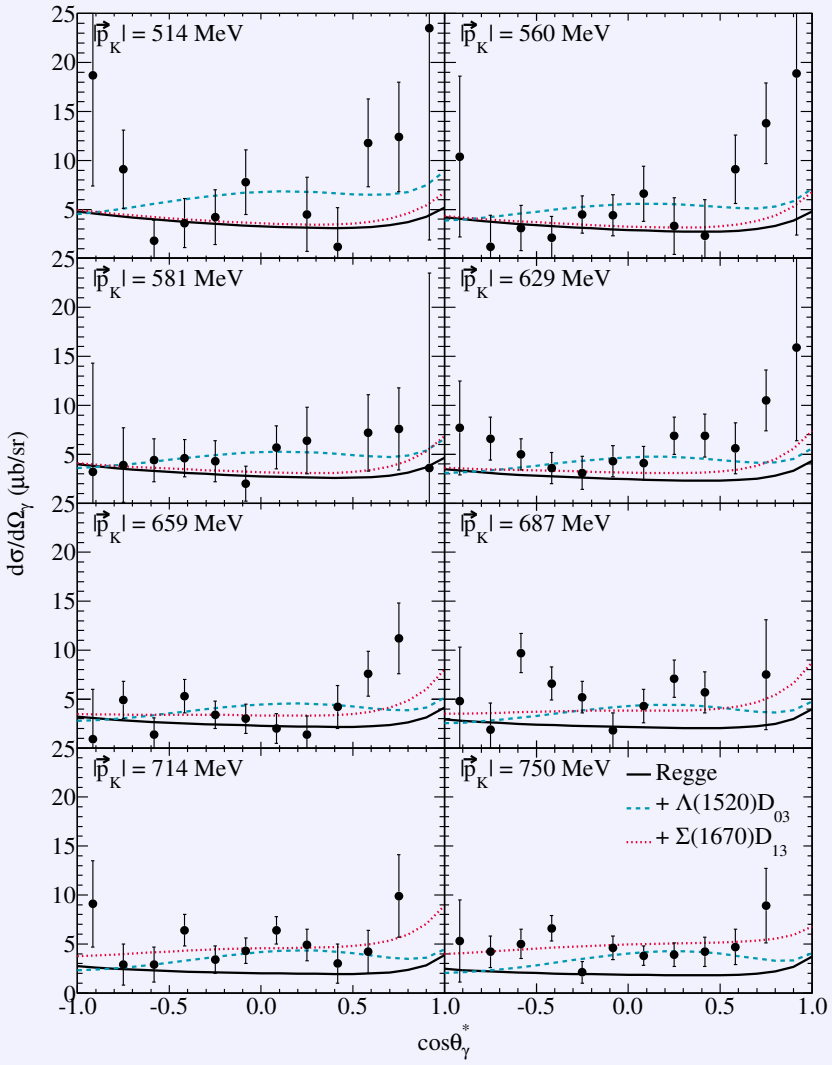

Figure 4.2 – Differential $p(K^-,\gamma)\Lambda$ cross section as a function of the photon CM scattering angle. Regge-model predictions are represented by the solid line. The dashed (dotted) curves show the RPR-model results including a $\Lambda(1520)D_{03}$ ($\Sigma(1670)D_{13}$) resonance. Data from Ref. [168].

three free parameters respectively[1]. The quality and amount of the considered data are not sufficient to perform fits with multiple resonances. Therefore we carried out fits with a single resonance at a time. For the $p(K^-,\gamma)\Lambda$ channel we obtain typically $\chi^2 \approx 115$ for 92 data points. The results for the $p(K^-,\gamma)\Sigma^0$ reaction are less satisfactory, since for all but one model χ^2 attained ≈ 230 for 96 data points. The fit including a $\Lambda(1670)S_{01}$ converged at $\chi^2 = 355$ for 96 data points.

In figure 4.2, we show the $p(K^-,\gamma)\Lambda$ model calculations including a $\Lambda(1520)D_{03}$ or a $\Sigma(1670)D_{13}$, since these resonance have the largest branching ratio to the $\Lambda\gamma$ channel according to the Bonn model. Both models predict a flat differential cross section with some enhancement at forward angles. The strength of the $\Sigma(1670)D_{13}$ resonance increases as the energy of the incoming kaon rises, whereas the contribution of the $\Lambda(1520)D_{03}$ is more uniformly spread. Figure 4.3 features model calculations for the $p(K^-,\gamma)\Sigma^0$ channel including either a $\Lambda(1600)P_{01}$ or a $\Lambda(1690)D_{03}$ resonance. Both models

[1]The most general Lagrangian for spin-3/2 resonances has three additional degrees-of-freedom, i.e. the off-shell parameters. To limit the total number of fitting parameters we discard the latter.

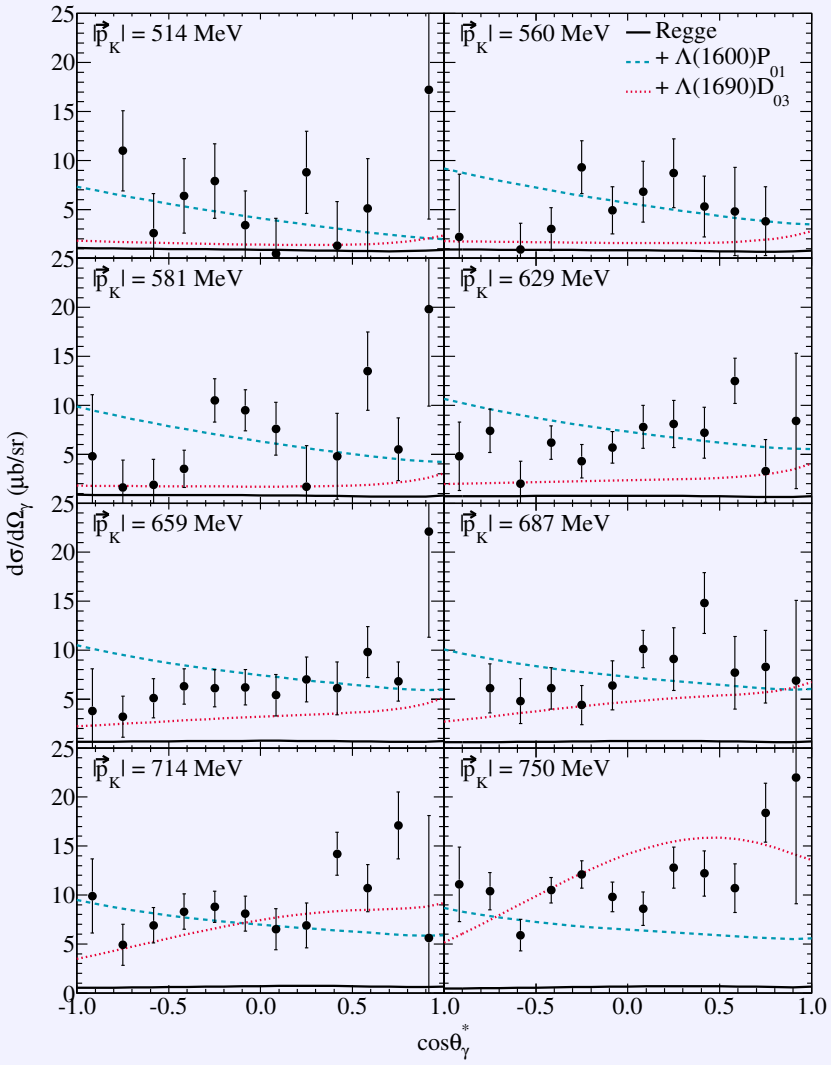

Figure 4.3 – Differential $p(K^-,\gamma)\Sigma^0$ cross section as a function of the photon CM scattering angle. Regge-model predictions are represented by the solid line. The dashed (dotted) curves show the RPR-model results including a $\Lambda(1600)P_{01}$ ($\Lambda(1690)D_{03}$) resonance. Data from Ref. [168].

are in good agreement with the data and show a slight enhancement of the differential cross section at backward angles.

The evaluation of the total cross sections for the radiative reactions $p(K^-,\gamma)\Lambda$ and $p(K^-,\gamma)\Sigma^0$ was based on fits to the differential-cross-section data with Legendre polynomials that were subsequently integrated. The systematic uncertainties in the total and the differential cross sections are considered similar. The results for the total cross sections of both the radiative reactions are shown in Figure 4.4 and 4.5, in conjunction with the RPR model calculations. For the $p(K^-,\gamma)\Sigma^0$ reaction, an analysis by the Valparaiso-Argonne group (V-A) [169] of the same data set is given as well.

For the $p(K^-,\gamma)\Lambda$ reaction, the total cross section falls off as the invariant energy $W_{\gamma Y}$ rises. This trend is predicted by the Regge model, which accounts for roughly half of the strength. The addition of a $\Lambda(1520)D_{03}$ resonance allows to largely make up for the missing strength. The Bonn CQM predicts a large electromagnetic decay width for the $\Sigma(1670)D_{13} \to \Lambda(1116)\gamma$ transition. The RPR fit including this resonance improves the description of the total cross section at the highest energy

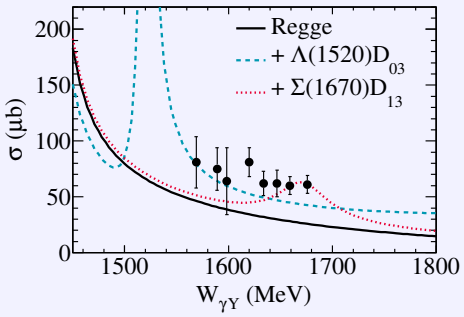

Figure 4.4 – Total $p(K^-,\gamma)\Lambda$ cross section. Regge-model predictions are represented by the solid line. The dashed (dotted) curves show the RPR-model results including a $\Lambda(1520)D_{03}$ ($\Sigma(1670)D_{13}$) resonance. Data from Ref. [168].

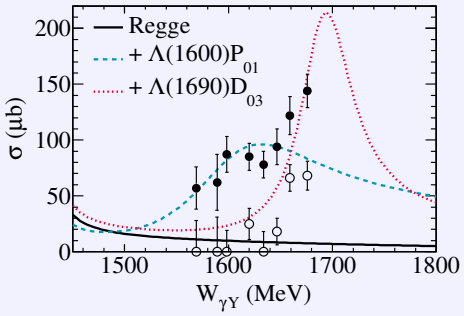

Figure 4.5 – Total $p(K^-,\gamma)\Sigma^0$ cross section. Regge-model predictions are represented by the solid line. The dashed (dotted) curves show the RPR-model results including a $\Lambda(1600)P_{01}$ ($\Lambda(1690)D_{03}$) resonance. Data from Refs. [168] (•) and [169] (○).

bins, but fails to account for the rise at lower energies.

The $p(K^-,\gamma)\Sigma^0$ total cross section is shown in Figure 4.5. The two available experimental results are incompatible, even though the same data set was analysed. The energy dependence of cross section is similar, but the V-A result is systematically smaller than the data from Ref. [168]. The authors of Ref. [168] attribute this disparity to an substantial oversubtraction of the background contributions in the V-A analysis. Since we have fitted our RPR-model amplitudes to the differential cross sections of Ref. [168], we will discard the V-A data points from now on. The energy dependence of the total cross section differs notably from the $\gamma\Lambda$ final state, peaking in the highest measured energy bin. This behaviour is opposite to the Regge-model result, which underestimates the total cross section by a factor of four and predicts a fall off as energy increases. A nice correspondence with the data at lower energies is realised through the inclusion of a $\Lambda(1600)P_{01}$ resonance, which has a particularly large value for the total decay width in the RPP. The Regge-model calculations supplemented with a $\Lambda(1670)S_{01}$ resonance, having a large value for $\Gamma_{\gamma\Sigma^0}$ in the Bonn model, allow to reproduce the apparent peak in the total-cross-section data, but fails at lower energies.

For both reaction channels presented in this work, the data cannot be understood in terms of a reaction amplitude consisting of non-resonant terms in conjunction with a single resonance. The energy dependence of the total cross sections, however, clearly suggest a prominent contribution for a resonance in the $\sim 1550\,\text{MeV}$ ($\sim 1700\,\text{MeV}$) range for the $\gamma\Lambda$ ($\gamma\Sigma^0$) final state.

CHAPTER 5

Formalism for electromagnetic kaon production from the deuteron

Up until now, we have focused on production reactions from unbound nucleons. It pays to consider the same reaction on more complex targets, such as the deuteron. We see three major reasons to extend the Regge-plus-resonance formalism to quasi-free production on the deuteron. First, owing to the deuteron's weak binding, it is ideally suited as an effective neutron target. Therefore, kaon production on the deuteron gives access to the elementary $n(\gamma, K)Y$ reaction process. Second, by comparing reactions off free and bound protons, our understanding of nuclear-medium effects is put to the test. An important source of medium effects are the rescatterings between the final-state hyperon, nucleon and kaon. These could be considered an undesirable background effect when the deuteron is being exploited as neutron target, since the interesting physics at the photon-neutron-kaon vertex would be partially obscured. On the other hand, the FSIs provide us with a tool to gain an improved understanding of the hyperon-nucleon and kaon-nucleon potentials, which cannot be assessed in a direct scattering experiment. Focusing on kinematic regions where one expects major contributions from hyperons rescattering off the spectator nucleon, allows one to gain access to the elusive hyperon-nucleon interaction.

In analogy to the kaon-production reaction on free nucleons, six different reactions with a kaon-hyperon pair in the final state can be identified

$$\begin{aligned}
\gamma^{(*)} + {}^2\mathrm{H} &\longrightarrow K^+ + \Lambda + n\,, \\
\gamma^{(*)} + {}^2\mathrm{H} &\longrightarrow K^+ + \Sigma^0 + n\,, \\
\gamma^{(*)} + {}^2\mathrm{H} &\longrightarrow K^0 + \Sigma^+ + n\,, \\
\gamma^{(*)} + {}^2\mathrm{H} &\longrightarrow K^0 + \Lambda + p\,, \\
\gamma^{(*)} + {}^2\mathrm{H} &\longrightarrow K^0 + \Sigma^0 + p\,, \\
\gamma^{(*)} + {}^2\mathrm{H} &\longrightarrow K^+ + \Sigma^- + p\,.
\end{aligned} \tag{5.1}$$

Each reaction can be induced by either a real photon (γ) or a virtual photon (γ^*) that is radiated by an electron scattering off the deuterium target. In this chapter, we present a formalism for

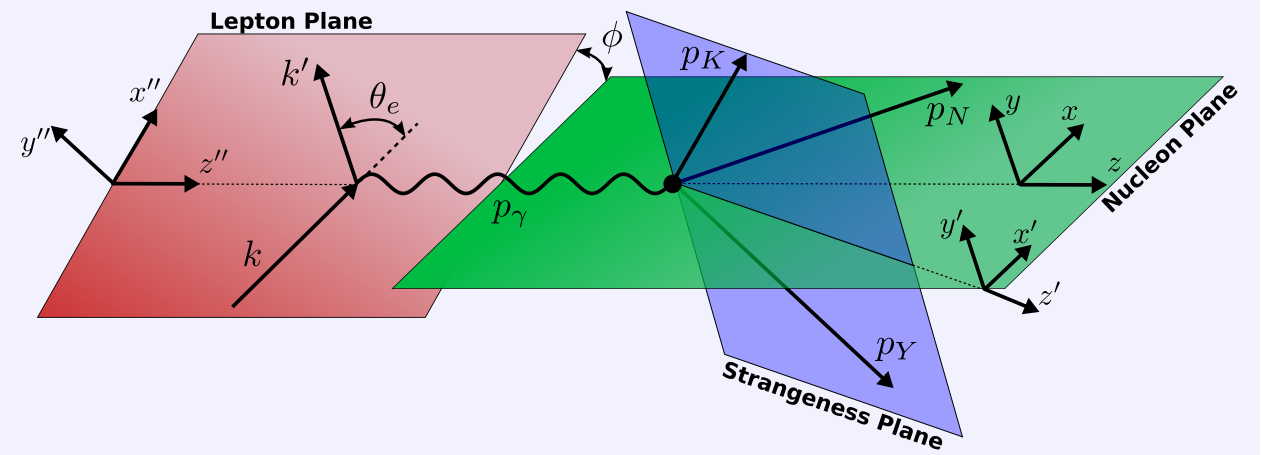

Figure 5.1 – Schematic representation of an electron scattering from a deuteron at rest, producing a kaon, hyperon and nucleon in the final state.

describing both the photoproduction and electroproduction of kaons from the deuteron. We start our discussions by presenting the kinematics of the reaction process. Next, we introduce the different photoproduction and electroproduction observables in Sections 5.3 and 5.4 respectively. One of the main ingredients to the nuclear transition amplitude is obviously the nuclear wave function. Consequently Section 5.5 elaborates on a covariant description of the deuteron-neutron-proton vertex and presents a comprehensive set of relativistic and non-relativistic deuteron wave functions. In the final section, we introduce the transition amplitude in the relativistic impulse approximation.

5.1 Kinematics

5.1.1 Reference frames

Producing a kaon on a deuterium target results in a three-body final state. This makes for a slightly more complicated situation than the $N(\gamma^*, K)Y$ kinematics we have described earlier in Section 2.1. In Figure 5.1 we show a schematic of the $^2\mathrm{H}(e, e'KY)N$ reaction in the LAB frame, where the struck deuterium target is at rest. We have assumed the OPE approximation. The four-vectors of the incoming and scattered electron, $\boldsymbol{k}(E_e, \vec{k})$ and $\boldsymbol{k'}(E'_e, \vec{k}')$, define the lepton plane. The electron emits a space-like photon with four-vector $\boldsymbol{p}_\gamma = \boldsymbol{k} - \boldsymbol{k'}$ and virtuality $Q^2 = -\boldsymbol{p}_\gamma \cdot \boldsymbol{p}_\gamma = |\vec{p}_\gamma|^2 - E_\gamma^2$, with $|\vec{p}_\gamma|$ and E_γ the virtual photons momentum and energy in the LAB frame. In what follows, all variables will be expressed in the LAB frame unless explicitly stated differently.

The four-vectors of the kaon, hyperon and nucleon in the final state are labelled $\boldsymbol{p}_K$, $\boldsymbol{p}_Y$ and $\boldsymbol{p}_N$ respectively. The photon and nucleon momenta span the nucleon plane, whereas the kaon and hyperon momenta lie in the strangeness plane. For kaon photoproduction, the picture simplifies as there is no electron plane and the virtuality Q^2 of the photon vanishes.

Because of the three-body final state, one can define a large number of coordinate systems. To keep our notation as general as possible, we will label the final state as $1 + (23)$, where the outgoing kaon, hyperon and nucleon are tagged 1, 2 and 3 at will. The coordinate system (x, y, z), in which we will describe the reaction, has its z axis along the photon momentum. The y axis is chosen perpendicular

to the plane spanned by the photon and particle 1. We define a second reference frame (x', y', z'), whose z' axis is oriented along $\vec{p}_2 + \vec{p}_3$. The y' axis is taken parallel to the y axis. This reference frame will be used to describe kinematics in the centre-of-mass (CM) frame of particles 2 and 3, for which we use the notation (23)-CM. Finally, we introduce a third reference frame (x'', y'', z'') in which we will define the photon's polarisation vector. The z'' axis will be taken along the photon momentum and the y'' axis normal to the lepton plane. We define ϕ as the angle between the electron plane and the plane spanned by the photon and particle 1. Obviously this angle becomes arbitrary in case of photoproduction. Explicitly we have,

$$\vec{z} = \frac{\vec{p}_\gamma}{|\vec{p}_\gamma|}\,, \qquad \vec{y} = \vec{z} \times \frac{\vec{p}_1}{|\vec{p}_1|}\,, \qquad \vec{x} = \vec{y} \times \vec{z}\,, \tag{5.2}$$

$$\vec{z}' = \frac{\vec{p}_2 + \vec{p}_3}{|\vec{p}_2 + \vec{p}_3|}\,, \qquad \vec{y}' = \vec{y}\,, \qquad \vec{x}' = \vec{y}' \times \vec{z}'\,, \tag{5.3}$$

$$\vec{z}'' = \frac{\vec{p}_\gamma}{|\vec{p}_\gamma|}\,, \qquad \vec{y}'' = \frac{\vec{k}}{|\vec{k}|} \times \frac{\vec{k}'}{|\vec{k}'|}\,, \qquad \vec{x}'' = \vec{y}'' \times \vec{z}''\,. \tag{5.4}$$

To illustrate the different coordinate systems, all three of them are shown in Figure 5.1 for the particular situation the outgoing nucleon is tagged as particle 1.

In the unprimed reference frame, every four-vector can be decomposed as follows

$$\begin{aligned} \boldsymbol{p}_i &= (E_i, \vec{p}_i) \\ &= (E_i, |\vec{p}_i| \cos\phi_i \sin\theta_i, |\vec{p}_i| \sin\phi_i \sin\theta_i, |\vec{p}_i| \cos\theta_i)\,, \quad i = \gamma, D, K, Y, N\,, \end{aligned} \tag{5.5}$$

where all variables are evaluated in the LAB frame. Alternatively, the four-vectors can be expressed in the (23)-CM frame using the primed reference frame,

$$\begin{aligned} \boldsymbol{p}_i^* &= (E_i^*, \vec{p}_i^*) \\ &= (E_i^*, |\vec{p}_i^*| \cos\phi_i^* \sin\theta_i^*, |\vec{p}_i^*| \sin\phi_i^* \sin\theta_i^*, |\vec{p}_i^*| \cos\theta_i^*)\,, \quad i = \gamma, D, K, Y, N\,. \end{aligned} \tag{5.6}$$

The representations in equations (5.5) and (5.6) are related to each other through a rotation about the y axis followed by a boost into the centre-of-mass of particles 2 and 3, i.e.

$$\boldsymbol{p}_i^* = \ell \boldsymbol{p}_i\,, \tag{5.7}$$

with

$$\Lambda(\ell) = \begin{pmatrix} \frac{E_{23}}{W_{23}} & 0 & 0 & -\frac{|\vec{p}_{23}|}{W_{23}} \\ 0 & 1 & 0 & 0 \\ 0 & 0 & 1 & 0 \\ -\frac{|\vec{p}_{23}|}{W_{23}} & 0 & 0 & \frac{E_{23}}{W_{23}} \end{pmatrix} \begin{pmatrix} 1 & 0 & 0 & 0 \\ 0 & \cos\theta_{23} & 0 & \sqrt{1-\cos^2\theta_{23}} \\ 0 & 0 & 1 & 0 \\ 0 & -\sqrt{1-\cos^2\theta_{23}} & 0 & \cos\theta_{23} \end{pmatrix}. \tag{5.8}$$

Here, we have defined the four-vector

$$\begin{aligned} \boldsymbol{p}_{23} &= \boldsymbol{p}_2 + \boldsymbol{p}_3 = \boldsymbol{p}_\gamma + \boldsymbol{p}_D - \boldsymbol{p}_1 \\ &= (E_{23}, -|\vec{p}_{23}|\sqrt{1-\cos^2\theta_{23}}, 0, |\vec{p}_{23}|\cos\theta_{23})\,, \end{aligned} \tag{5.9}$$

with

$$\begin{aligned} E_{23} &= E_\gamma + m_D - E_1\,, \\ |\vec{p}_{23}| &= |\vec{p}_\gamma - \vec{p}_1|\,, \\ s_{23} &= E_{23}^2 - |\vec{p}_{23}|^2\,, \\ \cos\theta_{23} &= \frac{|\vec{p}_\gamma| - |\vec{p}_1|\cos\theta_1}{\sqrt{(E_\gamma - E_1 + m_D)^2 - s_{23}}}\,. \end{aligned} \tag{5.10}$$

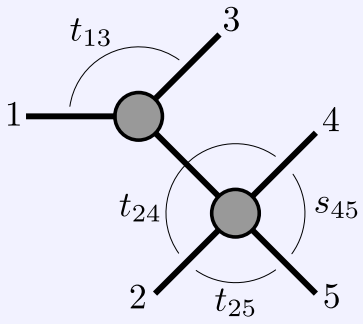

Figure 5.2 – Schematic representation of the reaction $1 + 2 \to 3 + 4 + 5$. Every particle has mass m_i and the Lorentz invariants are defined by $s_{ij} = (\boldsymbol{p}_i + \boldsymbol{p}_j)^2$ and $t_{ij} = (\boldsymbol{p}_i - \boldsymbol{p}_j)^2$.

Using the four-vectors of the particles participating in the ${}^2\mathrm{H}(\gamma^{(*)}, KY)N$ reaction, one can define ten Lorentz-invariant Mandelstam variables

$$s_{tot} = (\boldsymbol{p}_\gamma + \boldsymbol{p}_D)^2 , \tag{5.11a}$$
$$s_{KY} = (\boldsymbol{p}_K + \boldsymbol{p}_Y)^2 , \tag{5.11b}$$
$$s_{KN} = (\boldsymbol{p}_K + \boldsymbol{p}_N)^2 , \tag{5.11c}$$
$$s_{YN} = (\boldsymbol{p}_Y + \boldsymbol{p}_N)^2 , \tag{5.11d}$$
$$t_{\gamma i} = (\boldsymbol{p}_\gamma - \boldsymbol{p}_i)^2 , \quad i = K, Y, N , \tag{5.11e}$$
$$t_{Di} = (\boldsymbol{p}_D - \boldsymbol{p}_i)^2 , \quad i = K, Y, N . \tag{5.11f}$$

Several relations exist among these variables. They are straightforward to derive starting from the relation between the Mandelstam variables for $2 \to 2$ scattering, given by Eq. (2.9), and using the schematic representation of $2 \to 3$ scattering in Figure 5.2. Labelling the initial-state particles as 1 and 2, while denoting the outgoing particles as 3, 4 and 5, one has

$$t_{24} + t_{25} + s_{45} = t_{13} + m_2^2 + m_4^2 + m_5^2 . \tag{5.12}$$

Electromagnetic production of kaons from the deuteron can proceed when $W_{tot} \equiv \sqrt{s_{tot}} \geq (m_K + m_Y + m_N)$. This implies that E_γ obeys the inequality

$$E_\gamma \geq \frac{(m_K + m_Y + m_N)^2 - m_D^2 + Q^2}{2m_D} . \tag{5.13}$$

The thresholds for the different kaon-production channels are listed in Table 5.1.

5.1.2 Independent variables

Scattering reactions involving n particles are function of $(3n - 10)$ internal independent variables. This implies five variables for the ${}^2\mathrm{H}(\gamma^{(*)}, KY)N$ reaction, excluding the virtuality Q^2 of the photon. The general problem of expressing the physical region of reactions involving n particles in terms of $(3n - 10)$ Lorentz invariants has been addressed in Ref. [170]. The relevant formulae for the case $n = 5$ are concisely outlined in appendix E, where we derive expressions for Lorentz-invariant differential cross sections.

Alternatively, the kinematics are entirely determined when we specify

Table 5.1 – Threshold values of the invariant masses of the total system W_{tot}, the kaon-hyperon pair W_{KY} and the hyperon-nucleon pair W_{YN}, as well as the photon energy E_γ for the different photon-induced kaon production final states. All quantities are in MeV.

	E_γ	W_{tot}	W_{KY}	W_{YN}
^{2}H(γ,$K^+\ \Lambda\ $)$n$	792.12	2548.9	1609.36	2055.25
^{2}H(γ,$K^+\Sigma^0$)n	898.20	2625.9	1686.32	2132.21
^{2}H(γ,$K^0\Sigma^+$)n	899.22	2626.6	1687.04	2128.93
^{2}H(γ,$K^0\ \Lambda\ $)$p$	795.79	2551.6	1613.36	2053.95
^{2}H(γ,$K^0\ \Sigma^0$)p	901.99	2628.6	1690.31	2130.91
^{2}H(γ,$K^+\Sigma^-$)p	903.12	2629.4	1691.13	2135.72

- the photon's virtuality Q^2,
- the invariant mass W_{23} or the photon's LAB energy E_γ,
- the LAB energy E_1 of particle 1,
- particle 1's LAB scattering angle θ_1,
- the solid angle Ω_2^* of particle 2 in the (23)-CM frame.

Applying the definition of the invariant mass in conjunction with conservation of four-momentum, one finds

$$W_{23}^2 = \left(\boldsymbol{p}_\gamma + \boldsymbol{p}_D - \boldsymbol{p}_1\right)^2 = Q^2 + m_D^2 + m_1^2 + 2E_\gamma(m_D - E_1) + 2|\vec{p}_\gamma||\vec{p}_1|\cos\theta_1\,, \tag{5.14}$$

which gives W_{23} in terms of the photon's energy or vice-versa. The momentum $|\vec{p}_2^{\,*}|$ of particle 2 in the (23)-CM frame can be obtained by solving the energy-conservation relation

$$W_{23} = \sqrt{m_2^2 + |\vec{p}_2^{\,*}|^2} + \sqrt{m_3^2 + |\vec{p}_2^{\,*}|^2}\,. \tag{5.15}$$

Combining the solid angle Ω_2^* with $|\vec{p}_2^{\,*}|$ yields the four-vectors of particles 2 and 3 in their centre-of-mass. The latter can be boosted back into the LAB frame with Eq. (5.8), thus completely solving the kinematics.

At times, it is beneficial to express the kinematics solely in terms of LAB variables. With regard to the above-mentioned list, this implies replacing Ω_2^* by Ω_2. From Eq. (5.8), we deduce

$$E_2^* = \frac{E_{23}}{W_{23}}E_2 - \frac{|\vec{p}_{23}|}{W_{23}}|\vec{p}_2|\left(\cos\theta_{23}\cos\theta_2 - \sin\theta_{23}\sin\theta_2\cos\phi_2\right)\,. \tag{5.16}$$

Rearranging and squaring yields the following quadratic equation

$$\begin{aligned} 0 = |\vec{p}_2|^2 &\left[-E_{23}^2 + |\vec{p}_{23}|^2\left(\sin\theta_{23}\sin\theta_2\cos\phi_2 - \cos\theta_{23}\cos\theta_2\right)^2\right] \\ &- 2|\vec{p}_2||\vec{p}_{23}|E_2^* W_{23}\left(\sin\theta_{23}\sin\theta_2\cos\phi_2 - \cos\theta_{23}\cos\theta_2\right) + E_2^{*2}W_{23}^2 - E_{23}^2 m_2^2\,. \end{aligned} \tag{5.17}$$

Solving for $|\vec{p}_2|$ fixes the kinematics, albeit not in a unique way. Two physical solutions can correspond to the same set $\{Q^2, E_\gamma, E_1, \theta_1, \Omega_2\}$, making this group of independent variables less suited when (semi-)inclusive observables are considered (see page 69).

5.2 Transition amplitude

The dynamics of EM kaon production are contained in the nuclear transition amplitude for which we introduce the following notation

$$\mathcal{T}^{\lambda_\gamma}_{\lambda_D\lambda_Y\lambda_N}(\boldsymbol{p}_1,\theta_2^*,\phi_2^*)\,, \tag{5.18}$$

where λ_γ, λ_D, λ_Y and λ_N indicate the helicities of the incoming photon and deuteron and outgoing hyperon and nucleon respectively. Our notation explicitly shows that we take the three-momentum of the outgoing particle 1 in the LAB and the spherical angles of outgoing particle 2 in the (23)-CM as independent variables. The transition amplitude is obtained by evaluating the EM current operator $\mathcal{J}^\mu$ between the initial deuteron and final kaon-hyperon-nucleon states.

In Section 5.6, the explicit form of the transition current in the RIA is covered in detail. Here, we elaborate on some universal properties of the transition amplitude, which are valid irrespective of the concrete form of the transition current. First, we express the transition amplitude for kaon electroproduction in terms of the $N(\gamma^{(*)},K)Y$ amplitude. In the subsequent paragraphs, we touch on the transformation of amplitudes from one frame to the other and parity conservation.

5.2.1 Electroproduction

In the OPE approximation, the transition matrix element for kaon electroproduction on deuterium is given by

$$\mathcal{M}_{eD\to e'KYN} = \left\langle \boldsymbol{k}'\right| - ie\gamma_\mu \left|\boldsymbol{k}\right\rangle \left(\frac{-g^{\mu\nu}+\frac{p_\gamma^\mu p_\gamma^\nu}{\boldsymbol{p}_\gamma^2}}{\boldsymbol{p}_\gamma^2}\right) \left\langle \boldsymbol{p}_K;\boldsymbol{p}_Y;\boldsymbol{p}_N\right|\hat{\mathcal{J}}_\nu\left|\boldsymbol{p}_D\right\rangle\,, \tag{5.19}$$

where we have omitted the spin quantum numbers for the time being. The nuclear current operator $\hat{\mathcal{J}}^\nu$ acts on the states of the on-mass-shell initial- and final-state particles for whom we will assume a covariant normalisation

$$\langle \boldsymbol{p}\alpha|\boldsymbol{p}'\alpha'\rangle = 2p^0(2\pi)^3\delta^{(3)}(\vec{p}-\vec{p}')\delta_{\alpha\alpha'}\,. \tag{5.20}$$

The photon propagator can be decomposed as [171]

$$\frac{1}{\boldsymbol{p}_\gamma^2}\left(g^{\mu\nu}-\frac{p_\gamma^\mu p_\gamma^\nu}{\boldsymbol{p}_\gamma^2}\right) = \frac{1}{Q^2}\sum_{\lambda_\gamma=0,\pm1}(-1)^{\lambda_\gamma}(\epsilon^\mu_{\lambda_\gamma})^*\epsilon^\nu_{\lambda_\gamma}\,, \tag{5.21}$$

where λ_γ is the photon helicity. After introducing two covariant currents

$$j^{ss'}_{\lambda_\gamma} = \left\langle \boldsymbol{k}',s'\right|\gamma_\mu\left|\boldsymbol{k}\,,s\right\rangle(\epsilon^\mu_{\lambda_\gamma})^* \tag{5.22a}$$

$$\mathcal{M}^{\lambda_D\lambda_Y\lambda_N}_{\lambda_\gamma} = \left\langle \boldsymbol{p}_K;\boldsymbol{p}_Y,\lambda_Y;\boldsymbol{p}_N,\lambda_N\right|\hat{\mathcal{J}}_\mu\left|\boldsymbol{p}_D,\lambda_D\right\rangle\epsilon^\mu_{\lambda_\gamma}\,, \tag{5.22b}$$

we eventually rewrite the transition amplitude (5.19) as

$$\mathcal{M}_{eD\to e'KYN} = \frac{ie}{Q^2}\sum_{\lambda_\gamma}(-1)^{\lambda_\gamma}j_{\lambda_\gamma}\mathcal{M}_{\lambda_\gamma}\,. \tag{5.23}$$

In the (x'', y'', z'') frame, the photon polarisation vectors are given by

$$\begin{aligned} \epsilon_0''^{\mu} &= \left(\frac{|\vec{p}_\gamma|}{Q}, 0, 0, \frac{E_\gamma}{Q} \right) , \\ \epsilon_{\pm 1}''^{\mu} &= \mp \frac{1}{\sqrt{2}} (0, 1, \pm i, 0) . \end{aligned} \tag{5.24}$$

It is however more natural to evaluate the contraction in (5.22b) in the unprimed frame. To this end, the polarisation vectors of the photon need to be expressed in this frame. Both reference frames are related to each other by a rotation through the angle ϕ about the z axis,

$$\boldsymbol{\epsilon}_0 = \boldsymbol{\epsilon}_0'' \quad \text{and} \quad \boldsymbol{\epsilon}_\pm = e^{\pm i\phi} \boldsymbol{\epsilon}_\pm'' . \tag{5.25}$$

Accordingly, we get

$$\begin{aligned} \mathcal{M}_0^{\lambda_D \lambda_Y \lambda_N} &= \frac{Q}{|\vec{p}_\gamma|} \mathcal{T}^0_{\lambda_D \lambda_Y \lambda_N} , \\ \mathcal{M}_\pm^{\lambda_D \lambda_Y \lambda_N} &= e^{\pm i\phi} \mathcal{T}^\pm_{\lambda_D \lambda_Y \lambda_N} , \end{aligned} \tag{5.26}$$

in terms of the hadronic transition matrix elements

$$\begin{aligned} \mathcal{T}^0_{\lambda_D \lambda_Y \lambda_N} &= \langle \boldsymbol{p}_K; \boldsymbol{p}_Y, \lambda_Y; \boldsymbol{p}_N, \lambda_N | \, \hat{\mathcal{J}}^0 \, | \boldsymbol{p}_D, \lambda_D \rangle \\ \mathcal{T}^\pm_{\lambda_D \lambda_Y \lambda_N} &= \pm \frac{1}{\sqrt{2}} \langle \boldsymbol{p}_K; \boldsymbol{p}_Y, \lambda_Y; \boldsymbol{p}_N, \lambda_N | \left(\hat{\mathcal{J}}^x \pm i \hat{\mathcal{J}}^y \right) | \boldsymbol{p}_D, \lambda_D \rangle , \end{aligned} \tag{5.27}$$

where we have used current conservation

$$0 = p_\gamma^\mu \, \langle \boldsymbol{p}_K; \boldsymbol{p}_Y, \lambda_Y; \boldsymbol{p}_N, \lambda_N | \, \hat{\mathcal{J}}_\mu \, | \boldsymbol{p}_D, \lambda_D \rangle , \tag{5.28}$$

to express the longitudinal hadronic matrix element in terms of the time-component $\mathcal{T}^0_{\lambda_D \lambda_Y \lambda_N}$.

5.2.2 Lorentz transformations

For EM kaon production from the deuteron, a total of twenty-four transition matrix elements exist. Each one corresponds to a set of helicities for the incoming and outgoing particles. In this work, we will always define these helicities in the LAB frame using the unprimed reference frame (5.2). As we will see in Section 5.6, it is beneficial to calculate particular contributions to the current operator in the (23)-CM frame. Therefore a relation is needed to transform the transition matrix elements from one frame to the other.

Let μ_i denote helicities in the (23)-CM frame. Using the transformation properties for helicity states stated in Section C.2, we have

$$\mathcal{T}^{\lambda_\gamma}_{\lambda_D \lambda_Y \lambda_N} = \sum_{\mu_Y \mu_N} \left[\mathfrak{D}^{1/2}_{\mu_Y, \lambda_Y} \left(r(\ell, \boldsymbol{p}_Y) \right) \right]^* \left[\mathfrak{D}^{1/2}_{\mu_N, \lambda_N} \left(r(\ell, \boldsymbol{p}_N) \right) \right]^* \mathcal{T}^{\lambda_\gamma}_{\lambda_D \mu_Y \mu_N} , \tag{5.29}$$

where the transformation ℓ relates the LAB to the (23)-CM frame and has been defined in Eq. (5.8).

5.2.3 Parity

In Ref. [172], Arenhövel and Fix show how the general form of the transition amplitude for EM pion production from the deuteron can be rewritten using a partial-wave decomposition for the final state and an expansion of the transition current in electric and magnetic multipoles. From their expression and applying parity selection rules for the multipole transitions to the final-state partial waves, an expression for the invariance under parity transformations is derived. Their final result reads

$$\mathcal{T}^{\lambda_\gamma}_{-\lambda_D,-\lambda_Y,-\lambda_N}(\boldsymbol{p}_1,\theta_2^*,\phi_2^*) = (-1)^{1+\lambda_\gamma+\lambda_D+\lambda_Y+\lambda_N}\mathcal{T}^{\lambda_\gamma}_{\lambda_D\lambda_Y\lambda_N}(\boldsymbol{p}_1,\theta_2^*,-\phi_2^*)\,, \tag{5.30}$$

and is equally valid for EM kaon production from the deuteron.

The symmetry property is particularly useful when the dependence on the azimuthal angle is integrated out. The following equality illustrates this principle

$$\begin{aligned}\int_0^{2\pi} d\phi_2^* \sum_{\lambda_D\lambda_Y\lambda_N} |\mathcal{T}^{\lambda_\gamma=+1}_{\lambda_D,\lambda_Y,\lambda_N}(\boldsymbol{p}_1,\theta_2^*,\phi_2^*)|^2 &= \int_0^{2\pi} d\phi_2^* \sum_{\lambda_D\lambda_Y\lambda_N} |\mathcal{T}^{\lambda_\gamma=+1}_{\lambda_D,\lambda_Y,\lambda_N}(\boldsymbol{p}_1,\theta_2^*,-\phi_2^*)|^2\,,\\ &= \int_0^{2\pi} d\phi_2^* \sum_{\lambda_D\lambda_Y\lambda_N} |\mathcal{T}^{\lambda_\gamma=-1}_{\lambda_D,\lambda_Y,\lambda_N}(\boldsymbol{p}_1,\theta_2^*,\phi_2^*)|^2\,.\end{aligned} \tag{5.31}$$

5.3 Photoproduction observables

The differential cross section for the most general scattering reaction is given in Eq. (D.1). Applying this to the kaon photoproduction reaction, one finds

$$d\sigma = \frac{1}{2\sqrt{\lambda(s,0,m_D^2)}}\overline{\sum}|\mathcal{T}|^2 \frac{d^3\vec{p}_K}{2E_K(2\pi)^3}\frac{d^3\vec{p}_Y}{2E_Y(2\pi)^3}\frac{d^3\vec{p}_N}{2E_N(2\pi)^3}(2\pi)^4\delta^{(4)}(\boldsymbol{p}_\gamma+\boldsymbol{p}_D-\boldsymbol{p}_K-\boldsymbol{p}_Y-\boldsymbol{p}_N)\,. \tag{5.32}$$

The flux-factor λ, the transition matrix element $\mathcal{T}$, the phase space factors $\frac{d^3\vec{p}_i}{2E_i(2\pi)^3}$ of the outgoing particles i $(= K, Y, N)$ and the Dirac delta function, which expresses conservation of momentum and energy, are all Lorentz-invariant quantities. This enables one to evaluate the cross section in different reference frames. The symbol $\overline{\sum}$ denotes summing over the final-state and averaging over initial-state particle's polarisations. In Section 5.3.2, we will focus on scenarios where the incoming and/or outgoing particles have a definite polarisation. Beforehand, we will introduce several expressions for the differential cross section.

5.3.1 Differential cross section

In analogy to Section 5.1, we will keep our results as general as possible by labelling the three-particle final state as $1+(23)$. After integrating out the delta function in Eq. (5.32), the photoproduction reaction $^2\mathrm{H}(\gamma,KY)N$ is characterised by a five-fold differential cross section. In the LAB frame, it reads

$$\frac{d^5\sigma}{d|\vec{p}_1|d\Omega_1 d\Omega_2} = \frac{1}{32(2\pi)^5} f_{rec}^{-1}\frac{|\vec{p}_1|^2|\vec{p}_2|}{m_D E_\gamma E_1}\overline{\sum}|\mathcal{T}|^2\,, \tag{5.33}$$

with the recoil factor

$$f_{rec} = \left| E_2 + E_3 - \frac{E_2}{|\vec{p}_2|^2}(\vec{p}_\gamma - \vec{p}_1)\cdot\vec{p}_2 \right|\,. \tag{5.34}$$

Measuring exclusive cross sections with three particles in the final state is very challenging. In order to improve on the statistics, it is often more convenient to express the experimental results as semi-inclusive observables. Thereby, one integrates over the phase space of one or two undetected particles in the final state. As stressed on page 65, the kaon-production kinematics is not uniquely fixed when only LAB variables are given. Therefore, the exclusive cross section given in Eq. (5.33) cannot be readily integrated over the solid angle of particle 2. Partially expressing the cross section in the (23)-CM frame, solves this problem. We find

$$\frac{d^3\sigma}{d|\vec{p}_1|d\Omega_1} = \frac{1}{32(2\pi)^5}\frac{|\vec{p}_1|^2|\vec{p}_2^{\,*}|}{m_D E_\gamma E_1 W_{23}}\int d\Omega_2^* \overline{\sum}|\mathcal{T}|^2 \,. \tag{5.35}$$

Integrating the semi-inclusive differential cross section over the momentum and solid angle of particle 1 finally yields the total cross section

$$\sigma = 2\pi\int_{-1}^{1} d\cos\theta_1 \int_{|\vec{p}_1^{\,\min}|}^{|\vec{p}_1^{\,\max}|} d|\vec{p}_1|\frac{d^3\sigma}{d|\vec{p}_1|d\Omega_1} \,. \tag{5.36}$$

The integration limits for the three-momentum of particle 1 follow from the threshold condition

$$W_{23} \geq (m_2 + m_3)^2 \,. \tag{5.37}$$

Expanding this condition in the LAB, we find a quadratic equation in particle 1's momentum that yields as integration limits

$$|\vec{p}_1^{\,\max}| = \frac{|\vec{p}_\gamma|\cos\theta_1\left(s + m_1^2 - m_{23}^2\right) + (E_\gamma + m_D)\sqrt{\lambda(s, m_1^2, m_{23}^2) - 4m_1^2|\vec{p}_\gamma|^2\sin^2\theta_1}}{s_{tot} + |\vec{p}_\gamma|^2\sin^2\theta_1} \,, \tag{5.38}$$

and

$$|\vec{p}_1^{\,\min}| = \max\left\{0, \frac{|\vec{p}_\gamma|\cos\theta_1\left(s + m_1^2 - m_{23}^2\right) - (E_\gamma + m_D)\sqrt{\lambda(s, m_1^2, m_{23}^2) - 4m_1^2|\vec{p}_\gamma|^2\sin^2\theta_1}}{s_{tot} + |\vec{p}_\gamma|^2\sin^2\theta_1}\right\} \,. \tag{5.39}$$

In the previous expressions, we made use of the compact notation $m_{23} \equiv m_2 + m_3$.

Finally, we wish to introduce yet another representation of the $^2\mathrm{H}(\gamma, KY)N$ cross section. Upon expressing the differential cross section in terms of Mandelstam variables, the Lorentz invariance of the initial Eq. (5.32) can be preserved. The details of the derivation of Lorentz-invariant cross sections are diverted to Appendix E. Here, we merely report two useful distributions, i.e. the Dalitz cross section (E.17)

$$\frac{d\sigma}{dW_{KY}dW_{YN}} = \frac{4W_{KY}W_{YN}}{(4\pi)^4\lambda(s,0,m_D^2)}\int_{t_{\gamma K}^{\min}}^{t_{\gamma K}^{\max}} dt_{\gamma K}\int_{t_{DN}^{\min}}^{t_{DN}^{\max}} dt_{DN}\frac{1}{\sqrt{-\Delta_4}}\overline{\sum}|\mathcal{T}|^2 \,, \tag{5.40}$$

and the Chew-Low cross section (E.18)

$$\frac{d\sigma}{dW_{YN}dt_{\gamma K}} = \frac{2W_{YN}}{(4\pi)^4\lambda(s,0,m_D^2)}\int_{s_{KY}^{\min}}^{s_{KY}^{\max}} ds_{KY}\int_{t_{DN}^{\min}}^{t_{DN}^{\max}} dt_{DN}\frac{1}{\sqrt{-\Delta_4}}\overline{\sum}|\mathcal{T}|^2 \,. \tag{5.41}$$

The limits of integration as well as a definition of the Gram determinant Δ_4 can be found in Appendix E.

5.3.2 Polarisation observables

From our experience in meson production off free nucleons we know that polarisation observables are of great interest. Often they depend on interferences between different (non-) resonant contributions to the reaction amplitude. As such, they provide a handle on subtle contributions which cannot be discerned in the differential cross section. With this in mind, we present in this section a brief discussion on polarisation observables. To our knowledge, none of these observables will be measured in the near future, although experimental techniques are sufficient to carry out such a program.

In the expression (5.32) for the differential cross section, the polarisations of the particles involved in the reaction are omitted. Spin observables can be elegantly defined using the density-matrix formalism. The most general expression for the differential cross section is proportional to

$$d\sigma \sim \overline{\sum}|\mathcal{T}|^2 = \mathrm{Tr}\left[\mathcal{T}^\dagger \rho_{\mathrm{final}} \mathcal{T} \rho_{\mathrm{initial}}\right] . \tag{5.42}$$

The transition matrix elements (5.18) are evaluated in the helicity basis and the trace runs over the helicities of all incoming and outgoing particles. The density matrices of the initial and final systems are given by

$$\begin{aligned} \rho_{\mathrm{initial}} &= \rho^{(\gamma)} \otimes \rho^{(D)} , \\ \rho_{\mathrm{final}} &= \rho^{(Y)} \otimes \rho^{(N)} . \end{aligned} \tag{5.43}$$

In Appendix F, the most general decomposition of the density matrices of spin-1/2 particles, spin-1 systems and photons is discussed.

The unpolarised cross section is obtained by squaring the transition amplitude, averaging over initial spin states and summing over the final ones

$$\frac{d^5\sigma_{\mathrm{unpol}}}{d|\vec{p}_1|d\Omega_1 d\Omega_2^*} = \Phi(E_\gamma, \vec{p}_1)\, \frac{1}{6} \sum_{\lambda_\gamma \lambda_D \lambda_Y \lambda_N} |\mathcal{T}^{\lambda_\gamma}_{\lambda_D \lambda_Y \lambda_N}(\boldsymbol{p}_1, \theta_2^*, \phi_2^*)|^2 , \tag{5.44}$$

with

$$\Phi(E_\gamma, \vec{p}_1) = \frac{1}{32(2\pi)^5} \frac{|\vec{p}_1|^2 |\vec{p}_2^*|}{m_D E_\gamma E_1 W_{23}} , \tag{5.45}$$

the phase-space factor. Owing to the symmetry property of Eq. (5.31), the number of matrix elements that need to be evaluated can be halved for the semi-inclusive differential cross section

$$\frac{d^3\sigma_{\mathrm{unpol}}}{d|\vec{p}_1|d\Omega_1} = \Phi(E_\gamma, \vec{p}_1) \int d\Omega_2^*\, \frac{1}{3} \sum_{\lambda_D \lambda_Y \lambda_N} |\mathcal{T}^{\lambda_\gamma = +1}_{\lambda_D \lambda_Y \lambda_N}(\boldsymbol{p}_1, \theta_2^*, \phi_2^*)|^2 . \tag{5.46}$$

For kaon production with a polarised photon beam, we use the density-matrix composition given in Eq. (F.30)

$$\rho^{(\gamma)} = \frac{1}{2}\left(\mathbb{1}_2 + P_l^{(\gamma)}\sigma_x + P_t^{(\gamma)}\sigma_y + P_c^{(\gamma)}\sigma_z\right) . \tag{5.47}$$

It is parametrised using three polarisation coefficients. The helicity states of the incoming photon are conventionally defined in a reference frame that is tilted over an angle ϕ with respect to the scattering plane. The x axis of this frame can be taken in the direction of maximum linear polarisation, such that $P_t^{(\gamma)} = 0$. Inserting the density matrix into the expression for the differential cross section, one finds the following decomposition

$$\frac{d^5\sigma}{d|\vec{p}_1|d\Omega_1 d\Omega_2^*} = \frac{d^5\sigma_{\mathrm{unpol}}}{d|\vec{p}_1|d\Omega_1 d\Omega_2^*}\left(1 + P_l^{(\gamma)}\Sigma_l \cos 2\phi + P_c^{(\gamma)}\Sigma_c\right) , \tag{5.48}$$

with

$$\begin{aligned}\Sigma_l \frac{d^5\sigma_{\text{unpol}}}{d|\vec{p}_1|d\Omega_1 d\Omega_2^*} &= \Phi(E_\gamma, \vec{p}_1)\, \frac{1}{3} \sum_{\lambda_D \lambda_Y \lambda_N} \Re\left[\left(\mathcal{T}^{\lambda_\gamma=+1}_{\lambda_D \lambda_Y \lambda_N} \right)^* \mathcal{T}^{\lambda_\gamma=-1}_{\lambda_D \lambda_Y \lambda_N} \right] , \\ &= \Phi(E_\gamma, \vec{p}_1)\, \frac{1}{6} \sum_{\lambda_D \lambda_Y \lambda_N} \left(|\mathcal{T}^{\lambda_\gamma=y}_{\lambda_D \lambda_Y \lambda_N}|^2 - |\mathcal{T}^{\lambda_\gamma=x}_{\lambda_D \lambda_Y \lambda_N}|^2 \right) , \\ \Sigma_c \frac{d^5\sigma_{\text{unpol}}}{d|\vec{p}_1|d\Omega_1 d\Omega_2^*} &= \Phi(E_\gamma, \vec{p}_1)\, \frac{1}{6} \sum_{\lambda_D \lambda_Y \lambda_N} \left(|\mathcal{T}^{\lambda_\gamma=+1}_{\lambda_D \lambda_Y \lambda_N}|^2 - |\mathcal{T}^{\lambda_\gamma=-1}_{\lambda_D \lambda_Y \lambda_N}|^2 \right) ,\end{aligned} \tag{5.49}$$

the beam asymmetries for linearly and circularly polarised photons respectively. Using Eq. (5.31), one notices that Σ_c vanishes when only one particle is detected in the final state. In case particle 1 is emitted along the direction of the beam, the azimuthal angle ϕ becomes arbitrary and the (xy)-plane is no longer defined. Therefore, Σ_l vanishes when $\theta_1 = 0$.

In case the deuteron target is polarised along a quantisation axis $\vec{d}(\theta_d, \phi_d)$, the density matrix can be decomposed as (F.29)

$$\rho^{(1)}_{mm'}(\vec{z}) = \frac{(-1)^{1-m}}{\sqrt{3}} \sum_{IM} \sqrt{2I+1} \begin{pmatrix} 1 & 1 & I \\ m' & -m & M \end{pmatrix} e^{-iM\phi_d} d^I_{M0}(\theta_d) P_I \,, \tag{5.50}$$

with P_1 and P_2 the degree of vector and tensor polarisation defined in Eq. (F.28). For a tensor-polarised target, i.e. $P_1 = 0$, the differential cross section assumes the following form

$$\frac{d^5\sigma}{d|\vec{p}_1|d\Omega_1 d\Omega_2^*} = \frac{d^5\sigma_{\text{unpol}}}{d|\vec{p}_1|d\Omega_1 d\Omega_2^*} \left(1 + P_2 \sum_{M=0}^{2} T_{2M} \cos(M\phi_d) d^2_{M0}(\theta_d) \right) , \tag{5.51}$$

where we have introduced the tensor-polarisation asymmetries

$$\begin{aligned} T_{2M} \frac{d^5\sigma_{\text{unpol}}}{d|\vec{p}_1|d\Omega_1 d\Omega_2^*} &= (2 - \delta_{M0}) \frac{\sqrt{15}}{6} \Phi(E_\gamma, \vec{p}_1) \\ &\times \sum_{\lambda_D \lambda'_D} (-1)^{1-\lambda_D} \begin{pmatrix} 1 & 1 & 2 \\ \lambda'_D & -\lambda_D & M \end{pmatrix} \sum_{\lambda_\gamma \lambda_Y \lambda_N} \Re\left[\left(\mathcal{T}^{\lambda_\gamma}_{\lambda_D \lambda_Y \lambda_N} \right)^* \mathcal{T}^{\lambda_\gamma}_{\lambda'_D \lambda_Y \lambda_N} \right] , \end{aligned} \tag{5.52}$$

for $M = 0, 1, 2$.

The general case of simultaneous beam and target polarisation is treated thoroughly in Ref. [172]. Formulae are presented for exclusive as well as semi-inclusive differential cross sections.

Finally, we consider the situation where the polarisation of the recoiling hyperon is detected in the final state. Using the density-matrix decomposition (F.7) for spin-1/2 particles,

$$\rho^{(Y)} = \frac{1}{2} \left(\mathbb{1}_2 + \vec{P}^Y \cdot \vec{\sigma} \right) , \tag{5.53}$$

the five-fold cross section can be written as a function of four terms

$$\frac{d^5\sigma}{d|\vec{p}_1|d\Omega_1 d\Omega_2^*} = \frac{d^5\sigma_{\text{unpol}}}{d|\vec{p}_1|d\Omega_1 d\Omega_2^*} \left(1 + \vec{P}^Y \cdot \vec{\Pi} \right) , \tag{5.54}$$

with

$$\begin{aligned}
\Pi_x \frac{d^5\sigma_{\rm unpol}}{d|\vec{p}_1|d\Omega_1 d\Omega_2^*} &= \Phi(E_\gamma,\vec{p}_1)\,\frac{1}{3}\sum_{\lambda_\gamma\lambda_D\lambda_N} \Re\left[\left(\mathcal{T}^{\lambda_\gamma}_{\lambda_D,\lambda_Y=+\frac{1}{2},\lambda_N}\right)^* \mathcal{T}^{\lambda_\gamma}_{\lambda_D,\lambda_Y=-\frac{1}{2},\lambda_N}\right], \\
\Pi_y \frac{d^5\sigma_{\rm unpol}}{d|\vec{p}_1|d\Omega_1 d\Omega_2^*} &= \Phi(E_\gamma,\vec{p}_1)\,\frac{1}{3}\sum_{\lambda_\gamma\lambda_D\lambda_N} \Im\left[\left(\mathcal{T}^{\lambda_\gamma}_{\lambda_D,\lambda_Y=+\frac{1}{2},\lambda_N}\right)^* \mathcal{T}^{\lambda_\gamma}_{\lambda_D,\lambda_Y=-\frac{1}{2},\lambda_N}\right], \\
\Pi_z s \frac{d^5\sigma_{\rm unpol}}{d|\vec{p}_1|d\Omega_1 d\Omega_2^*} &= \Phi(E_\gamma,\vec{p}_1)\,\frac{1}{6}\sum_{\lambda_\gamma\lambda_D\lambda_N} \left(|\mathcal{T}^{\lambda_\gamma}_{\lambda_D,\lambda_Y=+\frac{1}{2},\lambda_N}|^2 - |\mathcal{T}^{\lambda_\gamma}_{\lambda_D,\lambda_Y=-\frac{1}{2},\lambda_N}|^2\right),
\end{aligned} \tag{5.55}$$

When only the outgoing hyperon is detected, one needs to integrate over the solid angle of particle 2. Owing to parity invariance (5.30), the following identities hold

$$\begin{aligned}
0 &= \int_0^{2\pi} d\phi_2^* \sum_{\lambda_\gamma\lambda_D\lambda_N} \Re\left[\left(\mathcal{T}^{\lambda_\gamma}_{\lambda_D,\lambda_Y=+\frac{1}{2},\lambda_N}\right)^* \mathcal{T}^{\lambda_\gamma}_{\lambda_D,\lambda_Y=-\frac{1}{2},\lambda_N}\right], \\
0 &= \int_0^{2\pi} d\phi_2^* \sum_{\lambda_\gamma\lambda_D\lambda_N} \left[|\mathcal{T}^{\lambda_\gamma}_{\lambda_D,\lambda_Y=+\frac{1}{2},\lambda_N}|^2 - |\mathcal{T}^{\lambda_\gamma}_{\lambda_D,\lambda_Y=-\frac{1}{2},\lambda_N}|^2\right].
\end{aligned} \tag{5.56}$$

Consequently, only one recoil-polarisation asymmetry remains. It reads

$$\Pi_y \frac{d^3\sigma_{\rm unpol}}{d|\vec{p}_Y|d\Omega_Y} = \Phi(E_\gamma,\vec{p}_Y)\,\frac{1}{3}\int_0^{2\pi} d\phi_2^* \sum_{\lambda_\gamma\lambda_D\lambda_N} \Im\left[\left(\mathcal{T}^{\lambda_\gamma}_{\lambda_D,\lambda_Y=+\frac{1}{2},\lambda_N}\right)^* \mathcal{T}^{\lambda_\gamma}_{\lambda_D,\lambda_Y=-\frac{1}{2},\lambda_N}\right]. \tag{5.57}$$

5.4 Electroproduction observables

In our formalism we will evaluate the electroproduction cross section in the LAB frame. After neglecting the electron's mass and integrating over $\vec{p}_3$ and $|\vec{p}_2|$, one finds

$$\frac{d^8\sigma}{dE_e' d\Omega_e' d\vec{p}_1 d\Omega_2} = \frac{1}{64(2\pi)^8} f_{rec}^{-1} \frac{E_e'|\vec{p}_2|}{E_e m_D E_1} \overline{\sum} |\mathcal{M}_{eD\to e'KYN}|^2, \tag{5.58}$$

where the recoil factor f_{rec} was defined in Eq. (5.34). Inserting (5.23) into this expression, we find

$$\frac{d^8\sigma}{dE_e' d\Omega_e' d\vec{p}_1 d\Omega_2} = \frac{1}{64(2\pi)^8} f_{rec}^{-1} \frac{|\vec{p}_2|}{m_D E_1} \left(\frac{\sqrt{4\pi\alpha}\cos\frac{\theta_e}{2}}{2E_e \sin^2\frac{\theta_e}{2}}\right)^2 \sum_{\lambda_\gamma\lambda_\gamma'} (-1)^{\lambda_\gamma+\lambda_\gamma'} L_{\lambda_\gamma\lambda_\gamma'} H^{fi}_{\lambda_\gamma\lambda_\gamma'}, \tag{5.59}$$

where we have introduced a leptonic and a hadronic tensor. The later is defined as

$$H^{fi}_{\lambda\lambda'} = \overline{\sum_{\lambda_D\lambda_Y\lambda_N}} \mathcal{M}^{\lambda_D\lambda_Y\lambda_N}_{\lambda} \left(\mathcal{M}^{\lambda_D\lambda_Y\lambda_N}_{\lambda'}\right)^\dagger. \tag{5.60}$$

The simple structure of the leptonic vertex allows one to compute the leptonic tensor analytically.

For an incoming electron with helicity $h/2$, one finds after summing over the final electron's spin,s

$$\begin{aligned} L_{\lambda\lambda'} &= \left(4E_eE'_e\cos^2\frac{\theta_e}{2}\right)^{-1}\sum_{s'} j_\lambda j^\dagger_{\lambda'} \\ &= \left(4E_eE'_e\cos^2\frac{\theta_e}{2}\right)^{-1}\frac{1}{2}\mathrm{Tr}\Big[\not\epsilon^*_\lambda(1+h\gamma_5\not s)(\not k+m_e)\not\epsilon_{\lambda'}(\not k'+m_e)\Big] \\ &= \left(4E_eE'_e\cos^2\frac{\theta_e}{2}\right)^{-1} 2\Big[(\boldsymbol{k}\cdot\boldsymbol{\epsilon}_{\lambda'})(\boldsymbol{k}'\cdot\boldsymbol{\epsilon}^*_\lambda)+(\boldsymbol{k}\cdot\boldsymbol{\epsilon}^*_\lambda)(\boldsymbol{k}'\cdot\boldsymbol{\epsilon}_{\lambda'})-(\boldsymbol{k}\cdot\boldsymbol{k}')(\boldsymbol{\epsilon}^*_\lambda\cdot\boldsymbol{\epsilon}_{\lambda'}) \\ &\qquad\qquad + ih\epsilon_{\mu\nu\alpha\beta}\epsilon^{\mu*}_\lambda\epsilon^{nu}_{\lambda'}k^\alpha k'^\beta\Big] \\ &= L^0_{\lambda\lambda'} + hL^h_{\lambda\lambda'}\,. \end{aligned} \tag{5.61}$$

In the final step, we have decomposed the tensor into a symmetric, helicity-independent and a asymmetric, helicity-dependent contribution. Those obey the following relations [173]

$$\begin{aligned} L^0_{-\lambda-\lambda'} &= (-1)^{\lambda-\lambda'}\left(L^0_{\lambda\lambda'}\right)^* \\ L^h_{-\lambda-\lambda'} &= (-1)^{1+\lambda-\lambda'}\left(L^h_{\lambda\lambda'}\right)^*, \end{aligned} \tag{5.62}$$

reducing the number of independent tensor elements to six. Evaluating them in the LAB frame, we find

$$L^0_{00} = \frac{Q^2}{|\vec{p}_\gamma|^2}\,, \tag{5.63a}$$

$$\begin{aligned} L^0_{11} &= L^0_{-1-1} \\ &= \frac{Q^2}{2|\vec{p}_\gamma|^2}+\tan^2\frac{\theta_e}{2}\,, \end{aligned} \tag{5.63b}$$

$$\begin{aligned} L^0_{01} &= L^0_{10} = -L^0_{0-1} = -L^0_{-10} \\ &= \frac{1}{\sqrt{2}}\frac{Q}{|\vec{p}_\gamma|}\sqrt{\frac{Q^2}{|\vec{p}_\gamma|^2}+\tan^2\frac{\theta_e}{2}}\,, \end{aligned} \tag{5.63c}$$

$$\begin{aligned} L^0_{1-1} &= L^0_{-11} \\ &= -\frac{Q^2}{2|\vec{p}_\gamma|^2}\,, \end{aligned} \tag{5.63d}$$

$$L^h_{00} = L^h_{1-1} = L^h_{-11} = 0\,, \tag{5.63e}$$

$$\begin{aligned} L^h_{01} &= L^h_{10} = L^h_{0-1} = L^h_{-10} \\ &= \frac{1}{\sqrt{2}}\frac{Q}{|\vec{p}_\gamma|}\tan\frac{\theta_e}{2}\,, \end{aligned} \tag{5.63f}$$

$$\begin{aligned} L^h_{11} &= -L^h_{-1-1} \\ &= \tan\frac{\theta_e}{2}\sqrt{\frac{Q^2}{|\vec{p}_\gamma|^2}+\tan^2\frac{\theta_e}{2}}\,. \end{aligned} \tag{5.63g}$$

The hadronic tensor, which we defined in Eq. (5.60), is a Lorentz-covariant quantity and is hermitian, i.e.

$$H^{fi}_{\lambda\lambda'} = \left(H^{fi}_{\lambda'\lambda}\right)^*. \tag{5.64}$$

We use this property in conjunction with the expressions (5.26) for the transition matrix elements to expand the contraction of the leptonic and hadronic tensor

$$\begin{aligned}
\sum_{\lambda_\gamma\lambda'_\gamma}(-1)^{\lambda_\gamma+\lambda'_\gamma}L_{\lambda_\gamma\lambda'_\gamma}H^{fi}_{\lambda_\gamma\lambda'_\gamma} &= L^0_{00}H^{fi}_{00}+L^0_{11}\Big(H^{fi}_{11}+H^{fi}_{-1-1}\Big)+2L^0_{1-1}\Re(H^{fi}_{1-1})\\
&\quad+2L^0_{01}\Big(\Re(H^{fi}_{01})-\Re(H^{fi}_{0-1})\Big)+hL^h_{11}\Big(H^{fi}_{11}-H^{fi}_{-1-1}\Big)\\
&\quad+2hL^h_{01}\Big(\Re(H^{fi}_{01})+\Re(H^{fi}_{0-1})\Big),\\
&= L^0_{00}\left(\frac{Q}{|\vec{p}_\gamma|}\right)^2\overline{\sum}|\mathcal{T}^0|^2+L^0_{11}\overline{\sum}\Big(|\mathcal{T}^+|^2+|\mathcal{T}^-|^2\Big)\\
&\quad+2L^0_{1-1}\overline{\sum}\Big(\cos 2\phi\,\Re(\mathcal{T}^+\mathcal{T}^{-\dagger})-\sin 2\phi\,\Im(\mathcal{T}^+\mathcal{T}^{-\dagger})\Big)\\
&\quad+2L^0_{01}\left(\frac{Q}{|\vec{p}_\gamma|}\right)\overline{\sum}\Big(\cos\phi\,\Re(\mathcal{T}^0\mathcal{T}^{+\dagger})+\sin\phi\,\Im(\mathcal{T}^0\mathcal{T}^{+\dagger})\\
&\qquad\qquad-\cos\phi\,\Re(\mathcal{T}^0\mathcal{T}^{-\dagger})+\sin\phi\,\Im(\mathcal{T}^0\mathcal{T}^{-\dagger})\Big)\\
&\quad+hL^h_{11}\overline{\sum}\Big(|\mathcal{T}^+|^2-|\mathcal{T}^-|^2\Big)\\
&\quad+2hL^h_{01}\left(\frac{Q}{|\vec{p}_\gamma|}\right)\overline{\sum}\Big(\cos\phi\,\Re(\mathcal{T}^0\mathcal{T}^{+\dagger})+\sin\phi\,\Im(\mathcal{T}^0\mathcal{T}^{+\dagger})\\
&\qquad\qquad+\cos\phi\,\Re(\mathcal{T}^0\mathcal{T}^{-\dagger})-\sin\phi\,\Im(\mathcal{T}^0\mathcal{T}^{-\dagger})\Big).
\end{aligned}\tag{5.65}$$

For the simplicity of the notations, we have omitted the polarisations of the deuteron, hyperon and nucleon.

With Eq. (5.65), the electroproduction cross section of Eq. (5.59) can be rewritten as a sum of longitudinal, transverse and interference contributions. This decomposition, however, is not unique. For the sake of completeness we will present the two most popular forms here. In nuclear physics, it is customary to express the cross section as [173]

$$\begin{aligned}
\frac{d^8\sigma}{dE'_e d\Omega'_e d\vec{p}_1 d\Omega_2} &= \frac{\alpha}{2\pi^2}K_H\left(\frac{\cos\frac{\theta_e}{2}}{2E_e\sin^2\frac{\theta_e}{2}}\right)^2\times\\
&\quad\Big[v_L R_L+v_T R_T+v_{TT}\Big({}^cR_{TT}\cos 2\phi+{}^sR_{TT}\sin 2\phi\Big)\\
&\quad+v_{LT}\Big({}^cR_{LT}\cos\phi+{}^sR_{LT}\sin\phi\Big)+hv_{T'}R_{T'}\\
&\quad+hv_{LT'}\Big({}^cR_{LT'}\cos\phi+{}^sR_{LT'}\sin\phi\Big)\Big],
\end{aligned}\tag{5.66}$$

with

$$K_H=\frac{W^2_{tot}-m^2_D}{2m_D},\tag{5.67}$$

the equivalent-real-photon laboratory energy. The expressions for the response functions and their corresponding prefactors can be found in table 5.2. Alternatively, introducing the transverse linear polarisation of the virtual photon

$$\epsilon=\left(1+\frac{2|\vec{p}_\gamma|^2}{Q^2}\tan^2\frac{\theta_e}{2}\right)^{-1},\tag{5.68}$$

Table 5.2 – Expressions for the response functions and kinematical factors used in Eqs. (5.66) and (5.71). The hadronic matrix elements, defined in Eq. (5.27), should be evaluated in the LAB frame. $\overline{\sum}$ implies appropriate summing and averaging over hadronic spin quantum numbers, which have been omitted as to not clog the notation. Furthermore, we have defined $\chi = \dfrac{1}{2(4\pi)^5}\dfrac{f_{rec}^{-1}}{K_H}\dfrac{|\vec{p}_2|}{m_D E_1}$.

	v_i	R_i	$\mathcal{R}_i$
T	$v_T = \dfrac{Q^2}{2\lvert\vec{p}_\gamma\rvert^2} + \tan^2\frac{\theta_e}{2}$	$R_T = \chi\overline{\sum}\left(\lvert\mathcal{T}^+\rvert^2 + \lvert\mathcal{T}^-\rvert^2\right)$	$\mathcal{R}_T = R_T$
L	$v_L = \dfrac{Q^4}{\lvert\vec{p}_\gamma\rvert^4}$	$R_L = \chi\overline{\sum}\lvert\mathcal{T}^0\rvert^2$	$\mathcal{R}_L = 2\dfrac{Q^2}{\lvert\vec{p}_\gamma\rvert^2}R_L$
TT	$v_{TT} = -\dfrac{Q^2}{2\lvert\vec{p}_\gamma\rvert^2}$	${}^cR_{TT} = 2\chi\overline{\sum}\Re\left(\mathcal{T}^+\mathcal{T}^{-\dagger}\right)$	${}^c\mathcal{R}_{TT} = -{}^cR_{TT}$
		${}^sR_{TT} = -2\chi\overline{\sum}\Im\left(\mathcal{T}^+\mathcal{T}^{-\dagger}\right)$	${}^s\mathcal{R}_{TT} = -{}^sR_{TT}$
LT	$v_{LT} = -\dfrac{Q^2}{\sqrt{2}\lvert\vec{p}_\gamma\rvert^2}\sqrt{\dfrac{Q^2}{\lvert\vec{p}_\gamma\rvert^2} + \tan^2\frac{\theta_e}{2}}$	${}^cR_{LT} = +2\chi\overline{\sum}\Re\left(\mathcal{T}^0\left(\mathcal{T}^+ - \mathcal{T}^-\right)^\dagger\right)$	${}^c\mathcal{R}_{LT} = -\dfrac{Q}{\lvert\vec{p}_\gamma\rvert}{}^cR_{LT}$
		${}^sR_{LT} = +2\chi\overline{\sum}\Im\left(\mathcal{T}^0\left(\mathcal{T}^+ + \mathcal{T}^-\right)^\dagger\right)$	${}^s\mathcal{R}_{LT} = -\dfrac{Q}{\lvert\vec{p}_\gamma\rvert}{}^sR_{LT}$
T'	$v_{T'} = \tan\frac{\theta_e}{2}\sqrt{\dfrac{Q^2}{\lvert\vec{p}_\gamma\rvert^2} + \tan^2\frac{\theta_e}{2}}$	$R_{T'} = \chi\overline{\sum}\left(\lvert\mathcal{T}^+\rvert^2 - \lvert\mathcal{T}^-\rvert^2\right)$	$\mathcal{R}_{T'} = R_{T'}$
LT'	$v_{LT'} = -\dfrac{Q^2}{\sqrt{2}\lvert\vec{p}_\gamma\rvert^2}\tan\frac{\theta_e}{2}$	${}^cR_{LT'} = +2\chi\overline{\sum}\Re\left(\mathcal{T}^0\left(\mathcal{T}^+ + \mathcal{T}^-\right)^\dagger\right)$	${}^c\mathcal{R}_{LT'} = -\dfrac{Q}{\lvert\vec{p}_\gamma\rvert}{}^cR_{LT'}$
		${}^sR_{LT'} = +2\chi\overline{\sum}\Im\left(\mathcal{T}^0\left(\mathcal{T}^+ - \mathcal{T}^-\right)^\dagger\right)$	${}^s\mathcal{R}_{LT'} = -\dfrac{Q}{\lvert\vec{p}_\gamma\rvert}{}^sR_{LT'}$

the cross section is given by

$$\frac{d^8\sigma}{dE'_e d\Omega'_e d\vec{p}_1 d\Omega_2} = \Gamma \frac{d\sigma^*}{d\vec{p}_1 d\Omega_2}\,, \tag{5.69}$$

with

$$\Gamma = \frac{\alpha}{2\pi^2}\frac{E'_e}{E_e}\frac{K_H}{Q^2}\frac{1}{1-\epsilon}\,, \tag{5.70}$$

the virtual photon flux factor. The virtual photon cross section can be cast in the following form [174],

$$\begin{aligned}\frac{d\sigma^*}{d\vec{p}_1 d\Omega_2} &= \mathcal{R}_T + \epsilon\mathcal{R}_L + \epsilon\Big({}^c\mathcal{R}_{TT}\cos 2\phi + {}^s\mathcal{R}_{TT}\sin 2\phi\Big) \\ &+ \sqrt{\epsilon(1+\epsilon)}\Big({}^c\mathcal{R}_{LT}\cos\phi + {}^s\mathcal{R}_{LT}\sin\phi\Big) \\ &+ h\sqrt{1-\epsilon^2}\mathcal{R}_{T'} + h\sqrt{\epsilon(1-\epsilon)}\Big({}^c\mathcal{R}_{LT'}\cos\phi + {}^s\mathcal{R}_{LT'}\sin\phi\Big)\,.\end{aligned} \tag{5.71}$$

In table 5.2 we list the different response function definitions.

5.5 Deuteron wave function

Owing to the deuteron's weak binding energy, it is the ideal laboratory for investigating kaon production off neutrons. Thereby, the deuteron's structure constitutes a crucial ingredient of the reaction dynamics. The deuteron is the sole observed two-nucleon bound state. The nucleon-nucleon interaction, which binds the deuteron, is composed of scalar, spin-spin, tensor and spin-orbit forces (see Ref. [175] for a review). It is primarily the tensor force that procures the necessary attraction to produce the stable isospin-singlet bound deuteron state. High precision experiments have determined the deuteron's mass [176]

$$m_D = 1.87614(19)\,\text{GeV}\,, \tag{5.72}$$

and

$$\epsilon_D \equiv m_p + m_n - m_D = 2.22463(4)\,\text{MeV}\,, \tag{5.73}$$

its binding energy to high accuracy.

Experimentally, spin and parity of the deuteron are found to be $J^P = 1^+$. The total spin of the deuteron is the vector sum of the spins of the two nucleons and of their relative orbital angular momentum

$$\vec{J} = \vec{S}_{N_1} + \vec{S}_{N_2} + \vec{L}\,. \tag{5.74}$$

The spin part of the deuteron's state with total spin projection λ_D can be decomposed in the basis of relative orbital momentum and total nuclear spin $\vec{S} = \vec{S}_{N_1} + \vec{S}_{N_2}$,

$$|J=1, J_z=\lambda_D\rangle = \sum_{S,m_S}\sum_{L,m_L} \langle L, m_L; S, m_S|\, 1, \lambda_D\rangle\ \chi_{Sm_S}\,|Lm_L\rangle \tag{5.75}$$

$$\begin{aligned}&= \chi_{1\lambda_D}\,|00\rangle + \sum_{m_S}\langle 2, \lambda_D\text{-}m_S; 1, m_S|\, 1, \lambda_D\rangle\,\chi_{1m_S}\,|2, \lambda_D\text{-}m_S\rangle \\ &+ \chi_{00}\,|1\lambda_D\rangle + \sum_{m_S}\langle 1, \lambda_D\text{-}m_S; 1, m_S|\, 1, \lambda_D\rangle\,\chi_{1m_S}\,|1, \lambda_D\text{-}m_S\rangle\ ,\end{aligned} \tag{5.76}$$

where

$$\chi_{00} = \frac{1}{\sqrt{2}}\Big(|+\rangle_1\,|-\rangle_2 - |-\rangle_1\,|+\rangle_2\Big)\,, \tag{5.77a}$$

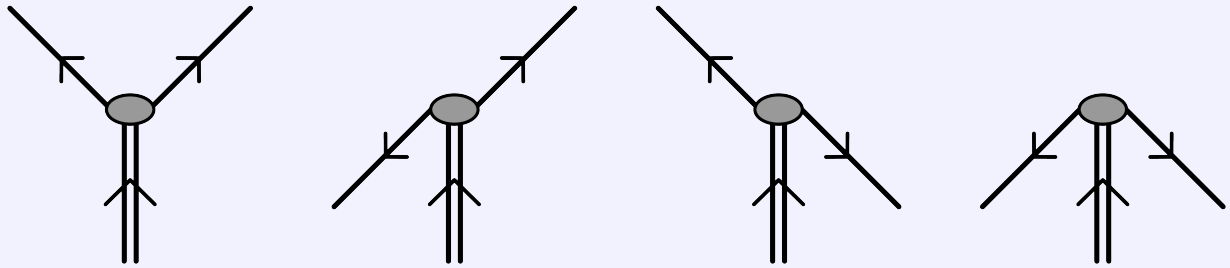

Figure 5.3 – The different contributions to the deuteron's wave function. Time flows from bottom to top. Lines moving backward in time are anti-particles.

and

$$\chi_{1+1} = |+\rangle_1 |+\rangle_2 \,, \tag{5.77b}$$

$$\chi_{10} = \frac{1}{\sqrt{2}}\Big(|+\rangle_1 |-\rangle_2 + |-\rangle_1 |+\rangle_2\Big) \,, \tag{5.77c}$$

$$\chi_{1-1} = |-\rangle_1 |-\rangle_2 \,, \tag{5.77d}$$

are the spin-singlet and spin-triplet wave functions respectively. Since each term in (5.75) can be labelled according to its J, L and S quantum number, we introduce the following spectroscopic notation: ${}^{2S+1}L_J$.

Before we proceed with our discussion of the deuteron's wave function, let us introduce some useful four-vectors. The nucleon's four-vectors in configuration and momentum space are $\boldsymbol{r}_{1,2}$ and $\boldsymbol{p}_{1,2}$ respectively. Furthermore, we define

$$\begin{array}{rclcrclcrcl} \boldsymbol{r} &=& \boldsymbol{r}_1 - \boldsymbol{r}_2 &,& \boldsymbol{R} &=& \frac{1}{2}(\boldsymbol{r}_1 + \boldsymbol{r}_2), & \boldsymbol{r}_1 &=& \boldsymbol{R} + \frac{1}{2}\boldsymbol{r} \;, & \boldsymbol{r}_2 &=& \boldsymbol{R} - \frac{1}{2}\boldsymbol{r} \;, \\ \boldsymbol{p} &=& \frac{1}{2}(\boldsymbol{p}_1 - \boldsymbol{p}_2), & \boldsymbol{p}_D &=& \boldsymbol{p}_1 + \boldsymbol{p}_2 &,& \boldsymbol{p}_1 &=& \frac{1}{2}\boldsymbol{p}_D + \boldsymbol{p}, & \boldsymbol{p}_2 &=& \frac{1}{2}\boldsymbol{p}_D - \boldsymbol{p}, \end{array} \tag{5.78}$$

as the relative four-vectors.

The polarisation vectors of a deuteron quantised along the z axis in its rest frame are given by

$$\begin{aligned} \boldsymbol{\xi}^0(\vec{z}) &= (0,0,0,1) \,, \\ \boldsymbol{\xi}^{\pm1}(\vec{z}) &= \mp\frac{1}{\sqrt{2}}(0,1,\pm i,0) \,. \end{aligned} \tag{5.79}$$

For different orientations of the spin quantisation axis, the polarisation four-vectors can be rotated with the help of Wigner rotation matrices (see Section A.2). For a deuteron polarised along an axis $\vec{n}(\theta,\phi)$, one has

$$\begin{aligned} \boldsymbol{\xi}^0(\vec{n}) &= (0,-\sin\theta,0,\cos\theta) \,, \\ \boldsymbol{\xi}^{\pm1}(\vec{n}) &= \mp\frac{e^{\mp i\phi}}{\sqrt{2}}(0,\cos\theta,\pm i,\sin\theta) \,. \end{aligned} \tag{5.80}$$

5.5.1 Covariant Dnp-vertex

The wave function of the deuteron describes its break-up in a proton and a neutron. Owing to the binding energy, both constituents are, in general, off their mass-shell, i.e. $\boldsymbol{p}_1^2 \neq \boldsymbol{p}_2^2 \neq m_N^2$. This

implies that one can break down the wave function in four different contributions as in figure 5.3, where each nucleon is either a particle moving forward in time or an anti-particle moving backward.

For our purposes, it suffices to consider the *Dnp*-vertex with one particle put on the mass shell. The covariant vertex function for a deuteron with momentum $\boldsymbol{p}_D$ and polarisation λ_D going to a state with nucleon 2 on mass shell ($\boldsymbol{p}_2^2 = m_N^2$) and nucleon 1 propagating off mass shell is given by

$$\langle \boldsymbol{p}_2 \lambda_2 | \, \Psi(0) \, | \boldsymbol{p}_D \lambda_D \rangle = \frac{m_N + \not{\boldsymbol{p}}_1}{m_N^2 - \boldsymbol{p}_1^2} \Gamma^\mu_{\text{Dnp}}(\boldsymbol{p}_2, \boldsymbol{p}_D) \xi_\mu^{\lambda_D} \mathcal{C} \overline{u}^T(\vec{p}_2; \lambda_2) \,, \tag{5.81}$$

where

$$\Gamma^\mu_{\text{Dnp}}(\boldsymbol{p}_2, \boldsymbol{p}_D) = F(|\vec{p}|)\gamma^\mu - \frac{G(|\vec{p}|)}{m_N} p^\mu - \frac{m_N - (\not{\boldsymbol{p}}_D - \not{\boldsymbol{p}}_2)}{m_N} \left(H(|\vec{p}|)\gamma^\mu - \frac{I(|\vec{p}|)}{m_N} p^\mu \right) , \tag{5.82}$$

with $\boldsymbol{p} = \frac{1}{2}\boldsymbol{p}_D - \boldsymbol{p}_2$. This 4x4-matrix in Dirac space was introduced by Blankenbecler and Cook [177] and features four scalar form factors F, G, H and I that depend only on the relative three-momentum. We will come back to these form factors and how they can be linked with (non-)relativistic wave functions in appendix H.

The decomposition of the single-nucleon propagator (A.45)

$$\frac{m_N + \not{\boldsymbol{p}}_1}{m_N^2 - \boldsymbol{p}_1^2} = \frac{1}{2E_p} \left(\sum_\lambda \frac{u(\vec{p}_1; \lambda)\overline{u}(\vec{p}_1; \lambda)}{E_p - p_1^0} - \sum_\lambda \frac{v(-\vec{p}_1; -\lambda)\overline{v}(-\vec{p}_1; -\lambda)}{E_p + p_1^0} \right) , \tag{5.83}$$

with $E_p = \sqrt{|\vec{p}_1|^2 + m_N^2}$, can be inserted into the expression for the *Dnp*-vertex. In the LAB frame, where $\boldsymbol{p}_D = (m_D, \vec{0})$, $\boldsymbol{p}_2 = (E_p, -\vec{p})$ and $\boldsymbol{p}_1 = (m_D - E_p, \vec{p})$, one gets

$$\langle \boldsymbol{p}_2 \lambda_2 | \, \Psi(0) \, | \boldsymbol{p}_D \lambda_D \rangle \overset{\text{LAB}}{=} \sqrt{(2\pi)^3 2 m_D} \left(\sum_{\lambda_1} u(\vec{p}; \lambda_1) \Psi^{++}_{\lambda_1 \lambda_2}(\vec{p}; \lambda_D) + \sum_{\lambda_1} v(-\vec{p}; -\lambda_1) \Psi^{-+}_{\lambda_1 \lambda_2}(\vec{p}; \lambda_D) \right) . \tag{5.84}$$

In the previous expression, we have introduced

$$\begin{aligned} \Psi^{++}_{\lambda_1 \lambda_2}(\vec{p}; \lambda_D) &= \frac{1}{\sqrt{(2\pi)^3 2 m_D}} \frac{\overline{u}(\vec{p}; \lambda_1) \Gamma^\mu \xi_\mu^{\lambda_D} \mathcal{C} \overline{u}^T(-\vec{p}; \lambda_2)}{2E_p \, (2E_p - m_D)} \,, \\ \Psi^{-+}_{\lambda_1 \lambda_2}(\vec{p}; \lambda_D) &= \frac{-1}{\sqrt{(2\pi)^3 2 m_D}} \frac{\overline{v}(-\vec{p}; -\lambda_1) \Gamma^\mu \xi_\mu^{\lambda_D} \mathcal{C} \overline{u}^T(-\vec{p}; \lambda_2)}{2E_p m_D} \,. \end{aligned} \tag{5.85}$$

This result brings us back to the components of the deuteron's wave function depicted in Figure 5.3. Since we put particle 2 on mass shell, the diagrams with particle 2 moving backward in time do not arise. The wave function Ψ^{++} is identified with the diagram of the deuteron going to two nucleons, whereas Ψ^{-+} can be interpreted as the wave function of an anti-nucleon and deuteron bound into a nucleon.

We would like to point out that a one-to-one correspondence can be made between the decomposition in ${}^{2S+1}L_J$-states in Eq. (5.75) and the wave functions Ψ^{++} and Ψ^{-+} we have come to define. The parity of the deuteron is given by

$$\eta_D = \eta_p \, \eta_n \, (-1)^L \,, \tag{5.86}$$

and is experimentally found to be $+1$. Since we have $\eta_p = \eta_n = +1$, the Ψ^{++} wave function must be an an admixture of ${}^3S_1$- and ${}^3D_1$-components. The $L = 1$ states in Eq. (5.75), on the other

Table 5.3 – The contribution of the $^3D_1$-, $^3P_1$- and $^1P_1$-waves to the deuteron's wave function for a collection of (non-)relativistic potential models. The D-state admixture is defined in Eq. (5.91). The definition for the probability of the singlet and triplet P-waves is analogous. All values are expressed as percentages (%).

	Paris [178]	CD-Bonn [179]	Nijm93 [180]	Gross-IIb [181]	WJC-1[a] [182]
$^3D_1$	5.77	4.85	5.754	4.538	7.3432
$^3P_1$	–	–	–	0.137	0.1119
$^1P_1$	–	–	–	0.006	0.2118

[a] As is explained in Section G.3, Ref. [182] presents two versions for the WJC-1 wave function. In this work, we always make use of the *scaled* wave function.

hand, contribute to Ψ^{-+}, because the intrinsic parity of an anti-particle is opposite that of the corresponding particle. A more detailed account on the connection between states of definite J, L and S and the wave-function decomposition introduced in (5.85) can be found in appendix H.

Finally, we wish to point out the wave functions in (5.85) can straightforwardly be expressed in configuration space through the Fourier transform:

$$\Psi^{\pm+}(\vec{r};\lambda_D) = \frac{1}{\sqrt{(2\pi)^3}} \int d^3\vec{p}\, e^{-i\vec{p}\cdot\vec{r}}\, \Psi^{\pm+}(\vec{p};\lambda_D)\,. \tag{5.87}$$

5.5.2 Non-relativistic wave functions

For numerous reactions involving the deuteron, it is not necessary to make use of the covariant *Dnp*-vertex introduced previously. Often, it suffices to apply a non-relativistic reduction. Obviously, the wave function Ψ^{-+} has no meaning in a non-relativistic context and can be set equal to zero.

The non-relativistic deuteron wave function is usually defined in terms of the well-known $^3S_1$- and $^3D_1$-wave components. In configuration space, it reads

$$\Psi^{++}(\vec{r};\lambda_D) = \frac{u(|\vec{r}|)}{|\vec{r}|}\chi_{1\lambda_D}Y_{00}(\theta,\phi) + \frac{w(|\vec{r}|)}{|\vec{r}|}\sum_{m_S}\langle 2,\lambda_D\text{-}m_S;1,m_S|\,1,\lambda_D\rangle\,\chi_{1m_S}Y_{2,\lambda_D\text{-}m_S}(\theta,\phi)\,, \tag{5.88}$$

with $u(|\vec{r}|)$, $w(|\vec{r}|)$ the radial $^3S_1$- and $^3D_1$-wave functions and $Y_{Lm_L}(\theta,\phi)$ the spherical harmonics.

The normalisation condition

$$\int d^3\vec{r}\,\left[\Psi^{++}(\vec{r};\lambda)\right]^\dagger \Psi^{++}(\vec{r};\lambda') = \delta_{\lambda\lambda'}\,, \tag{5.89}$$

implies

$$\int_0^\infty d|\vec{r}|\,\left(u^2(|\vec{r}|) + w^2(|\vec{r}|)\right) = 1\,. \tag{5.90}$$

Modern non-relativistic wave functions are calculated by solving the Schrödinger equation with *realistic* NN potentials. These phenomenological NN potentials are fitted to the world's NN scattering data and attain a typical χ^2/d.o.f. of ≈ 1. In figure 5.4, we depict the radial wave functions as calculated with three popular realistic potentials: the Paris potential [178], the charge-dependent Bonn potential [179] and the Nijmegen potential [180]. The figure also features two relativistic wave

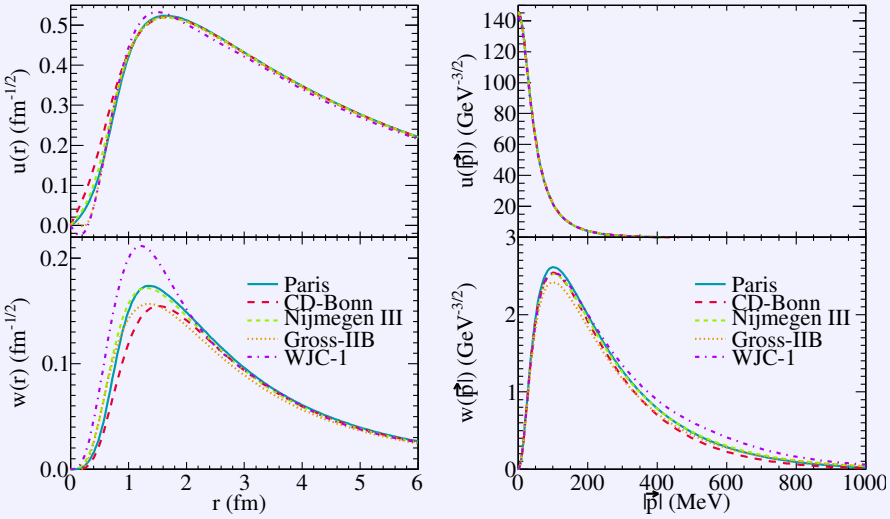

Figure 5.4 – $^3S_1$- and $^3D_1$-state radial wave functions in configuration (left panels) and momentum (right panels) space as calculated by various models: Paris [178], CD-Bonn [179], Nijmegen-III [180], Gross-IIB [181] and WJC-1 [183].

functions, which will be discussed in the forthcoming paragraph. For large spatial separations, or equivalently small relative momenta, the wave functions more or less coincide. For smaller values of r, a slight model dependence becomes apparent. We clearly see that the $L = 0$ wave dominates. The total probability of the $L = 2$ state is defined as

$$P_D = \int_0^\infty d|\vec{r}|w^2(|\vec{r}|)\,. \tag{5.91}$$

All models predict a D-state admixture of approximately 5% (see Table 5.3).

5.5.3 Relativistic wave functions

In a relativistic framework, the concept of a wave function is ill-defined and it is more natural to speak in terms of amplitudes and vertex functions. In order to make a direct link with the non-relativistic description, however, it can be instructive to define a relativistic wave function, even though the number of wave-function components is model dependent. Within the covariant Bethe-Salpeter approach a total of eight components are defined [184]. Covariant light-front dynamics considers six contributions [185], whereas in the covariant spectator theory (CST) or Gross formalism this number is reduced to four [173, 186]. In our formulation of the $^2\mathrm{H}(\gamma, KY)N$ transition amplitude, which is the subject of Section 5.6, the considered Feynman diagrams are always reduced to a deuteron-neutron-proton vertex with one nucleon on-mass-shell. For this reason, we will employ the CST approach and formulate two additional wave-function components of relativistic origin that supplement the $^3S_1$- and $^3D_1$-waves introduced in Paragraph 5.5.2.

We define

$$\Psi^{-+}(\vec{r};\lambda_D) = -i\frac{v_t(|\vec{r}|)}{|\vec{r}|}\sum_{m_S}\langle 1,\lambda_D\text{-}m_S;1,m_S|\,1,\lambda_D\rangle\,\chi_{1m_S}Y_{1,\lambda_D\text{-}m_S}(\hat{\vec{r}}) - i\frac{v_s(|\vec{r}|)}{|\vec{r}|}\chi_{00}Y_{1\lambda_D}(\hat{\vec{r}})\,. \tag{5.92}$$

The two new P-state wave functions $v_s(|\vec{r}|)$ and $v_t(|\vec{r}|)$ couple to the singlet and triplet spin-wave function respectively. Within our relativistic framework, u and w can be thought of as the upper

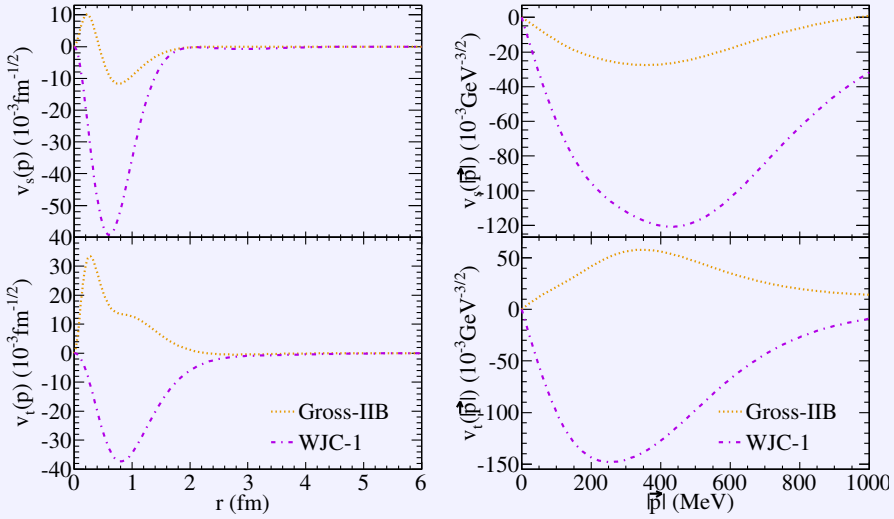

Figure 5.5 – $^3P_1$- and $^1P_1$-state radial wave functions in configuration (left panels) and momentum (right panels) space as calculated by the Gross-IIB model [181] and WJC-1 [183] models.

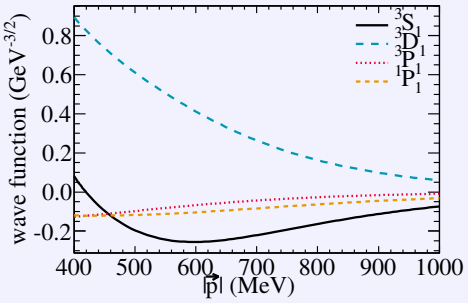

Figure 5.6 – Momentum-space wave functions calculated within the WJC-1 model [182] at high relative momenta.

components of the Dirac wave functions. The P-states act as the lower components and are comparatively much smaller, especially at small relative momenta. This intuitive picture is confirmed in figures 5.4 and 5.5. The $^3S_1$- and $^3D_1$-waves resemble their non-relativistic counterparts in size and shape.

As can be learned from table 5.3, the P-waves are minute. Nevertheless, by means of interference with the larger components of the wave function, they can produce significant contributions to actual observables. This is exemplified in the calculation of the deuteron form factors in the framework of CST [187].

In Figure 5.6, all four contributions to the deuteron wave function calculated within the WJC-1 model are drawn for high relative momenta ($|\vec{p}| > 400\,\text{MeV}$). The S-wave has a node and all components are of comparable sizes. This implies that at high relative momenta all wave-function components contribute to the transition matrix elements.

5.6 Relativistic impulse approximation

In Sections 5.3 and 5.4, we have given a comprehensive overview of observables for the EM production of kaons from deuterium targets. The essential ingredient for these observables is the nuclear transition amplitude $\mathcal{T}^{\lambda_\gamma}_{\lambda_D\lambda_Y\lambda_N}$, which contains all the physics of both the production process and the nuclear medium. In Eq. (5.27), it was defined in terms of the nuclear transition current operator $\hat{\mathcal{J}}^\mu_{\text{nucl}}$. For the reaction under study, we have a photon incident on a bound state of two nucleons producing a three-body final state, and in general $\hat{\mathcal{J}}^\mu_{\text{nucl}}$ represents an intricate many-body operator. In this work, we stay clear of the complexity of many-body currents and invoke the impulse approximation, which states the full nuclear many-body current operator can be approximated by a sum of one-body current operators $\hat{\mathcal{J}}^\mu_{\text{x}}$. We have

$$\hat{\mathcal{J}}^\mu_{\text{nucl}} \overset{\text{IA}}{\to} \sum_{i=1,2} \sum_{\text{x}} \hat{\mathcal{J}}^\mu_{\text{x}}(i)\,. \tag{5.93}$$

The sum over x represents the different contributions to the relativistic impulse approximation (RIA) that will be enumerated in Paragraph 5.6.1. Each operator acts on both particles 1 and 2 inside the deuteron. This is indicated by the sum over i. It is important to note that each contribution $\hat{\mathcal{J}}^\mu_{\text{x}}$ to the current operator contains an isospin filter and consequently acts either on a proton or a neutron.

To investigate the implications of the RIA, we adopt the occupation-number representation. The deuteron state is represented by

$$|\boldsymbol{p}_D,\lambda_D\rangle \equiv \sum_{\boldsymbol{p}_1,\boldsymbol{p}_2}\sum_{\lambda_1,\lambda_2}\sum_{t_1,t_2} \Psi^{++}_{\lambda_1\lambda_2}\!\left(\frac{\boldsymbol{p}_1-\boldsymbol{p}_2}{2};\boldsymbol{p}_D,\lambda_D\right)\!\langle\tfrac{1}{2},t_1;\tfrac{1}{2},t_2|0,0\rangle\; a^\dagger_{\boldsymbol{p}_1,\lambda_1,t_1}\, a^\dagger_{\boldsymbol{p}_2,\lambda_2,t_2}\,|0\rangle\;, \tag{5.94}$$

where we have restricted ourselves to the positive-energy states. When the negative-energy components of the wave function are taken into account, the discussion presented in this paragraph proceeds along the same lines. The nucleon creation and annihilation operators, that feature in Eq. (5.94), obey the usual anticommutation relations [188]

$$\begin{aligned}\{a_\alpha, a^\dagger_\beta\} &= \delta_{\alpha,\beta}\,,\\ \{a_\alpha, a_\beta\} &= \{a^\dagger_\alpha, a^\dagger_\beta\} = 0\,,\end{aligned} \tag{5.95}$$

and are labelled by the nucleon's four-momentum $\boldsymbol{p}_i$, polarisation λ_i and isospin component t_i, with $\alpha,\beta \equiv \{\boldsymbol{p}_i,\lambda_i,t_i\}$. In second quantisation, each one-body current-operator contribution $\hat{\mathcal{J}}^\mu_{\text{x}}$ for kaon-production from the deuteron can be written as

$$\sum \boldsymbol{p}\lambda,\boldsymbol{p}'\lambda'\,\langle \boldsymbol{p}_K;\boldsymbol{p}_Y,\lambda_Y;\boldsymbol{p}_N,\lambda_N|\,\hat{\mathcal{J}}^{\lambda_\gamma}_{\text{x};\boldsymbol{p},\lambda,t;\boldsymbol{p}',\lambda',-t}\,|\boldsymbol{p}_D,\lambda_D\rangle\; a^\dagger_{KYN}\; a_{\boldsymbol{p}',\lambda',-t}\; a_{\boldsymbol{p},\lambda,t}\,. \tag{5.96}$$

In this notation, we explicitly indicate that the photon interacts with a nucleon with quantum numbers $\{\boldsymbol{p},\lambda,t\}$. Like we have mentioned earlier, this nucleon is either a proton ($t=\frac{1}{2}$) or a neutron ($t=-\frac{1}{2}$). The primed quantum numbers reflect the state of the so-called spectator nucleon and the operator $a^\dagger_{KYN}$ is shorthand notation for the creation of the kaon-hyperon-nucleon final state.

Now, we wish to examine the result of $\hat{\mathcal{J}}^\mu_{\text{x}}$ acting on the deuteron state (5.94). Repeated application of the anticommutation relations (5.95), leads to the following identity

$$a_{\boldsymbol{p},\lambda,t}a^\dagger_{\boldsymbol{p}_1,\lambda_1,t_1}a^\dagger_{\boldsymbol{p}_2,\lambda_2,t_2}\,|0\rangle = \left(\delta_{\boldsymbol{p},\boldsymbol{p}_1}\delta_{\lambda,\lambda_1}\delta_{t,t_1}a^\dagger_{\boldsymbol{p}_2,\lambda_2,t_2} - \delta_{\boldsymbol{p},\boldsymbol{p}_2}\delta_{\lambda,\lambda_2}\delta_{t,t_2}a^\dagger_{\boldsymbol{p}_1,\lambda_1,t_1}\right)|0\rangle\;. \tag{5.97}$$

Taking into account the deuteron wave function Ψ^{++} is symmetric under the exchange of particle 1 with 2 and the antisymmetric property

$$\langle \frac{1}{2}, t; \frac{1}{2}, t' | 0, 0 \rangle = -\langle \frac{1}{2}, t'; \frac{1}{2}, t | 0, 0 \rangle \,, \tag{5.98}$$

we find that the action of the production operator (5.96) on the deuteron state (5.94) gives

$$(-1)^{\frac{1}{2}-t}\sqrt{2} \sum_{\boldsymbol{p}\lambda,\boldsymbol{p}'\lambda'} \langle \boldsymbol{p}_K; \boldsymbol{p}_Y, \lambda_Y; \boldsymbol{p}_N, \lambda_N | \, \hat{\mathcal{J}}^{\lambda_\gamma}_{\mathrm{x};\boldsymbol{p},\lambda,t;\boldsymbol{p}',\lambda',-t} \, | \boldsymbol{p}_D, \lambda_D \rangle$$
$$\times \, \Psi^{++}_{\lambda_1\lambda_2}(\frac{\boldsymbol{p}-\boldsymbol{p}'}{2}; \boldsymbol{p}_D, \lambda_D) a^\dagger_{KYN} \, |0\rangle \,. \tag{5.99}$$

This implies the nuclear transition amplitude in the RIA can be written as

$$\langle \boldsymbol{p}_K; \boldsymbol{p}_Y, \lambda_Y; \boldsymbol{p}_N, \lambda_N | \, \hat{\mathcal{J}}^{\lambda_\gamma}_{\mathrm{nucl}} \, | \boldsymbol{p}_D, \lambda_D \rangle \overset{\mathrm{IA}}{\to} \sum_{\mathrm{x}} \pm\sqrt{2} \, \langle \boldsymbol{p}_K; \boldsymbol{p}_Y, \lambda_Y; \boldsymbol{p}_N, \lambda_N | \, \hat{\mathcal{J}}^{\lambda_\gamma}_{\mathrm{x}}(1) \, | \boldsymbol{p}_D, \lambda_D \rangle \,. \tag{5.100}$$

Thus, the RIA entails that the full nuclear transition amplitude is approximated by a coherent sum of current matrix elements, where each current operator acts on particle 1. Every contribution comes with a plus- (minus-)sign that depends on whether the incoming photon interacts with the proton or neutron inside the deuteron.

In the remainder of this chapter, the different contributions to the RIA transition amplitude are considered. In order not to overload the notation, we no longer indicate that the one-body current operator acts on particle 1 inside the deuteron. In paragraphs 5.6.2 and 5.6.3, expressions for the different matrix elements

$$\langle \boldsymbol{p}_K; \boldsymbol{p}_Y, \lambda_Y; \boldsymbol{p}_N, \lambda_N | \, \hat{\mathcal{J}}^{\lambda_\gamma}_{\mathrm{x}} \, | \boldsymbol{p}_D, \lambda_D \rangle \,, \quad \mathrm{x} = \mathrm{RPWIA, \ NRPWIA, \ YN\text{-}FSI, \ etc.} \,, \tag{5.101}$$

are presented. When observables are calculated in Chapter 6, we sum the relevant contributions multiplied with the correct RIA-factor $\pm\sqrt{2}$ to form the nuclear transition amplitude.

5.6.1 Different contributions to the relativistic impulse approximation

A multitude of reaction mechanisms can contribute to the nuclear transition amplitude. The contributions which we identified as dominant for the $^2\mathrm{H}(\gamma, KY)N$ reaction are illustrated in Figure 5.7.

In the lowest-order diagram, the kaon and hyperon are produced on a single nucleon and all three final-state particles subsequently leave the reaction unperturbed as plane waves. This reaction picture is known as the relativistic plane-wave impulse approximation (RPWIA) and constitutes the subject of Paragraph 5.6.2.

A higher-order diagram, a so-called two-step process, is depicted in figure 5.7(b). Here the incident photon creates a pion-nucleon pair. The former consequently rescatters inelastically off the spectator nucleon producing the final kaon and hyperon.

After the initial photon-induced production of strangeness, either directly or via an intermediary pion, the outgoing particles in the three-body final state can interact. These final-state interactions (FSIs) involve, in principle, a three-body operator, but are typically approximated by a sum of two-body interactions. Since the elementary strangeness-production vertex is adjusted to data, one

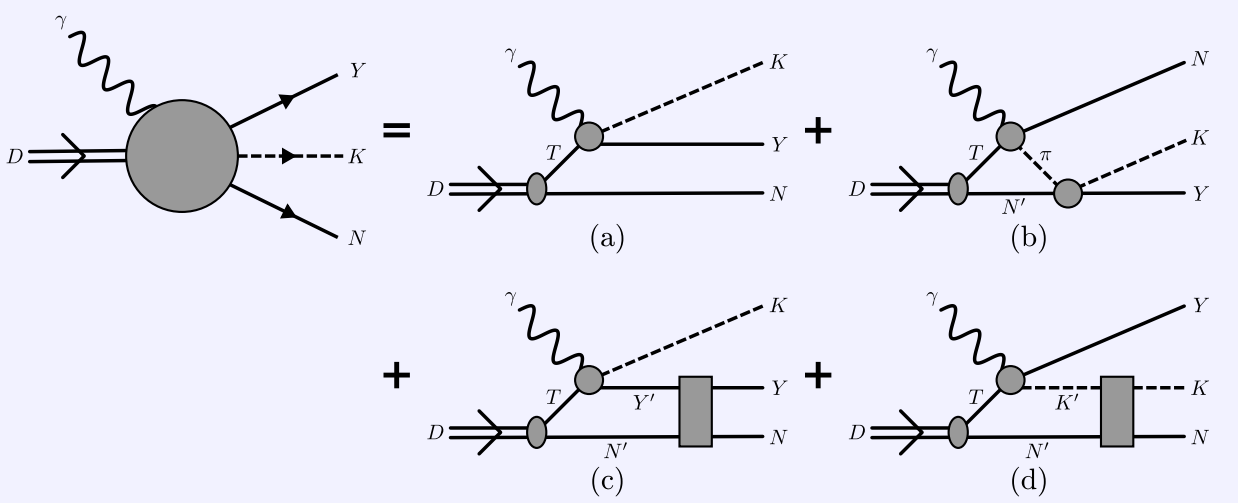

Figure 5.7 – The relevant contributions to the ${}^2\mathrm{H}(\gamma^{(*)}, KY)N$ reaction in the RIA: (a) plane-wave impulse approximation, (b) two-step process with initial photoproduction of a pion π and (c,d) single rescattering in the final state. The target nucleon inside the deuteron D is labelled T.

assumes it effectively incorporates the kaon-hyperon FSI. The remaining FSI diagrams are shown in figures 5.7(c) and 5.7(d). Their contribution can naively be expected to be most significant at the thresholds of the different reaction channels. As the kaon's scattering length is considerably smaller than in the case of hyperon-nucleon scattering, we will limit our formalism to the hyperon-nucleon final-state interaction (YN-FSI). It will be discussed in Paragraph 5.6.3.

5.6.2 Relativistic plane-wave impulse approximation

We will start our discussion of the RIA by writing down the transition matrix element in the relativistic plane-wave impulse approximation (RPWIA). The corresponding Feynman diagram is given in figure 5.7(a). Applying the Feynman rules summarised in Appendix D, one has

$$\begin{aligned}\langle \boldsymbol{p}_K; \boldsymbol{p}_Y, \lambda_Y; \boldsymbol{p}_N, \lambda_N | \, \hat{\mathcal{J}}^{\lambda_\gamma}_{\mathrm{RPWIA}} \, | \boldsymbol{p}_D, \lambda_D \rangle = \\ - \, \overline{u}(\vec{p}_Y, \lambda_Y) \epsilon^{\lambda_\gamma}_\nu \hat{J}^\nu(W_{KY}, \theta^*_K) \frac{m_T + \not{p}_D - \not{p}_N}{m_T^2 - (\boldsymbol{p}_D - \boldsymbol{p}_N)^2} \xi^{\lambda_D}_\mu \Gamma^\mu_{\mathrm{Dnp}}(\boldsymbol{p}_N, \boldsymbol{p}_D) \mathcal{C} \overline{u}^T(\vec{p}_N, \lambda_N) \, , \end{aligned} \quad (5.102)$$

with $\hat{J}^\nu$ the elementary kaon-production operator which we have covered thoroughly in Chapter 2. For clarity, we have explicitly indicated this operator is to be evaluated at the invariant mass $W^2_{KY} = (\boldsymbol{p}_K + \boldsymbol{p}_Y)^2$ and for the scattering angle θ^*_K, i.e. the angle $\widehat{\vec{p}^{\,*}_\gamma \vec{p}^{\,*}_K}$ in the KY-CM frame.

In order to make the connection with the NRPWIA, we consider the decomposition of the deuteron-neutron-proton vertex of Eq. (5.84), retaining only the positive-energy contribution. This yields an expression for the transition amplitude that is no longer covariant and should be evaluated in the rest frame of the deuteron

$$\begin{aligned}\langle \boldsymbol{p}_K; \boldsymbol{p}_Y, \lambda_Y; \boldsymbol{p}_N, \lambda_N | \, \hat{\mathcal{J}}^{\lambda_\gamma}_{\mathrm{NRPWIA}} \, | \boldsymbol{p}_D, \lambda_D \rangle \overset{\mathrm{LAB}}{=} \\ - \sqrt{(2\pi)^3 2 m_D} \sum_{\lambda_T} \langle \boldsymbol{p}_K; \boldsymbol{p}_Y, \lambda_Y | \, \hat{J}^{\lambda_\gamma} \, | \boldsymbol{p}_T \lambda_T \rangle \, \Psi^{++}_{\lambda_T \lambda_N}(-\vec{p}_N, \lambda_D) \, . \end{aligned} \quad (5.103)$$

The target nucleon absorbs the incoming photon and has four-momentum $\boldsymbol{p}_T = \boldsymbol{p}_D - \boldsymbol{p}_N$. It is obviously off its mass shell and has a non-vanishing virtuality

$$m_T^2 - \boldsymbol{p}_T^2 > 0\,. \tag{5.104}$$

Accordingly, the elementary-production vertex in both the RPWIA and NRPWIA are evaluated with one off-mass-shell leg. Owing to the tiny binding energy of the deuteron, the virtuality is minor as long as the momentum of the spectator nucleon is small. As $|\vec{p}_N|$ rises, the effective mass of the target nucleon tends to zero. The physics of tachyons falls beyond the scope of this dissertation. For this reason we impose an upper limit on the LAB energy of the spectator,

$$E_N \leq \frac{m_D^2 + m_N^2}{2m_D}\,, \tag{5.105}$$

which ensures that $\boldsymbol{p}_T^2 \geq 0$. This hard cutoff does not pose a serious problem, since we expect an intrinsic falloff for the elementary kaon-production reaction as the target nucleon's virtuality mounts. Moreover, examining figures 5.4 and 5.5, we notice the deuteron's wave function drops dramatically at large relative momenta, and hence the transition amplitude will be incredibly small when the spectator reaches its imposed upper bound.

Nevertheless, we wish to assess the level of uncertainty related to the off-shell extrapolation of the elementary-production operator. To this end, we introduce the on-shell four-vector of the target nucleon in the LAB frame as

$$\widetilde{\boldsymbol{p}}_T \overset{\text{LAB}}{\equiv} \left(\sqrt{|\vec{p}_N|^2 + m_T^2}, -\vec{p}_N\right)\,. \tag{5.106}$$

Accordingly, the propagator of the target nucleon can be divided into an on-shell and off-shell part,

$$\not{\boldsymbol{p}}_T + m_N = \widetilde{\not{\boldsymbol{p}}}_T + m_N - \gamma^0\left(E_T - \widetilde{p}_T^0\right)\,. \tag{5.107}$$

For the remainder of this section, we will neglect the proton-neutron mass difference. This implies $\widetilde{p}_T^0 = E_N$. After we insert the propagator's decomposition in the expression for the transition amplitude in the RPWIA, the current operator falls apart in two contributions

$$\hat{\mathcal{J}}_{\text{RPWIA}} \overset{\text{LAB}}{=} \hat{\mathcal{J}}_{\text{RPWIA,onshell}} + \hat{\mathcal{J}}_{\text{RPWIA,offshell}}\,. \tag{5.108}$$

We define an on-shell piece

$$\begin{aligned}\langle \boldsymbol{p}_K; \boldsymbol{p}_Y, \lambda_Y; \boldsymbol{p}_N, \lambda_N|\, \hat{\mathcal{J}}^{\lambda_\gamma}_{\text{RPWIA,onshell}}\, |\boldsymbol{p}_D, \lambda_D\rangle \overset{\text{LAB}}{=}& \\ -\,\overline{u}(\vec{p}_Y, \lambda_Y)\epsilon_\nu^{\lambda_\gamma}\hat{J}^\nu \frac{m_N + \widetilde{\not{\boldsymbol{p}}}_T}{m_N^2 - \boldsymbol{p}_T^2}\xi_\mu^{\lambda_D}\Gamma^\mu_{\text{Dnp}}(\boldsymbol{p}_N, \boldsymbol{p}_D)\mathcal{C}\overline{u}^T(\vec{p}_N, \lambda_N)\,,&\end{aligned} \tag{5.109}$$

and an off-shell component

$$\begin{aligned}\langle \boldsymbol{p}_K; \boldsymbol{p}_Y, \lambda_Y; \boldsymbol{p}_N, \lambda_N|\, \hat{\mathcal{J}}^{\lambda_\gamma}_{\text{RPWIA,offshell}}\, |\boldsymbol{p}_D, \lambda_D\rangle \overset{\text{LAB}}{=}& \\ \frac{E_N - E_T}{m_N^2 - \boldsymbol{p}_T^2}\overline{u}(\vec{p}_Y, \lambda_Y)\epsilon_\nu^{\lambda_\gamma}\hat{J}^\nu\gamma^0\xi_\mu^{\lambda_D}\Gamma^\mu_{\text{Dnp}}(\boldsymbol{p}_N, \boldsymbol{p}_D)\mathcal{C}\overline{u}^T(\vec{p}_N, \lambda_N)\,.&\end{aligned} \tag{5.110}$$

In the LAB frame, the denominator of the target-nucleon's propagator can be rewritten as

$$m_N^2 - \boldsymbol{p}_T^2 = m_D(2E_N - m_D)\,. \tag{5.111}$$

Applying this in the expression for the on-shell part of the RPWIA transition amplitude (5.109), and using Eq. (A.42), we obtain

$$\langle \boldsymbol{p}_K; \boldsymbol{p}_Y, \lambda_Y; \boldsymbol{p}_N, \lambda_N | \, \hat{\mathcal{J}}^{\lambda_\gamma}_{\text{RPWIA,onshell}} \, | \boldsymbol{p}_D, \lambda_D \rangle \overset{\text{LAB}}{=} \\ - \sqrt{(2\pi)^3 2m_D} \frac{2E_N}{m_D} \sum_{\lambda_T} \langle \boldsymbol{p}_K; \boldsymbol{p}_Y, \lambda_Y | \, \hat{J}^{\lambda_\gamma} \, | \widetilde{\boldsymbol{p}}_T, \lambda_T \rangle \, \Psi^{++}_{\lambda_T \lambda_N}(-\vec{p}_N, \lambda_D) \,, \quad (5.112)$$

where we have used the definition of the positive-energy deuteron wave function Ψ^{++} in terms of the covariant *Dnp*-vertex (5.85). We remark that the on-shell contribution to the RPWIA amplitude is equal to the NRPWIA form, except for a kinematical factor that is close to one for moderate spectator-nucleon momenta. In addition, the transition amplitude on the right-hand side of Eq. (5.112) is evaluated with all incoming and outgoing particles on their respective mass shells.

Before we conclude our discussion of the RPWIA, we try to estimate the contribution of the off-shell correction to the transition amplitude in the RPWIA. Starting from Eq. (A.41), we can introduce the following, alternative completeness relation for spinors,

$$2E_N \gamma^0 = \Lambda_+(\vec{p}_T) - \Lambda_-(-\vec{p}_T) \,, \quad (5.113)$$

in Eq. (5.110) and applying the definition of the positive- and negative-energy deuteron wave functions (5.85), we find

$$\langle \boldsymbol{p}_K; \boldsymbol{p}_Y, \lambda_Y; \boldsymbol{p}_N, \lambda_N | \, \hat{\mathcal{J}}^{\lambda_\gamma}_{\text{RPWIA,offshell}} \, | \boldsymbol{p}_D, \lambda_D \rangle \overset{\text{LAB}}{=} \\ \sqrt{(2\pi)^3 2m_D} \frac{E_N - E_T}{m_D} \left[\sum_{\lambda_T} \overline{u}(\vec{p}_Y, \lambda_Y) \epsilon^{\lambda_\gamma}_\nu \hat{J}^\nu u(-\vec{p}_N, \lambda_T) \Psi^{++}_{\lambda_T \lambda_N}(-\vec{p}_N, \lambda_D) \right. \\ \left. + \frac{m_D}{2E_N - m_D} \sum_{\lambda_T} \overline{u}(\vec{p}_Y, \lambda_Y) \epsilon^{\lambda_\gamma}_\nu \hat{J}^\nu v(\vec{p}_N, -\lambda_T) \Psi^{-+}_{\lambda_T \lambda_N}(-\vec{p}_N, \lambda_D) \right] . \quad (5.114)$$

The kinematic factor in front of the off-shell contribution can be approximated by

$$\frac{E_N - E_T}{m_D} \approx \frac{\epsilon_D}{m_D} + \frac{|\vec{p}_N|^2}{m_N m_D} \,, \quad (5.115)$$

at lowest-order of the spectator-nucleon's momentum, with ϵ_D the deuteron's binding energy (5.73). Obviously, the off-shell part of the RPWIA transition matrix element is modest as long as the three-momentum of the outgoing nucleon is small compared to its mass. It generates a 5 % correction at $|\vec{p}_N| \approx 300\,\text{MeV}$.

5.6.3 Hyperon-nucleon final-state interaction

We wish to evaluate the Feynman diagram for the YN-FSI process that is depicted in Figure 5.7 (c). It involves a loop where we choose to integrate over the four-momentum $\boldsymbol{p}_{N'}$ of the spectator nucleon. The four-vectors of the remaining particles in the loop, i.e. the target nucleon T and the rescattering hyperon Y', are fixed by energy-momentum conservation. We have

$$\begin{aligned} \boldsymbol{p}_T &= \boldsymbol{p}_D - \boldsymbol{p}_{N'} \,, \\ \boldsymbol{p}_{Y'} &= \boldsymbol{p}_Y + \boldsymbol{p}_N - \boldsymbol{p}_{N'} \,. \end{aligned} \quad (5.116)$$

Based on the Feynman rules given in Section D.2, the YN-FSI contribution to the transition amplitude reads

$$\begin{aligned}\langle \boldsymbol{p}_K;\boldsymbol{p}_Y,\lambda_Y;\boldsymbol{p}_N,\lambda_N|\,\hat{\mathcal{J}}^{\lambda_\gamma}_{\text{YN-FSI}}\,|\boldsymbol{p}_D,\lambda_D\rangle =& \\ i\int\frac{d^4\boldsymbol{p}_{N'}}{(2\pi)^4}\overline{u}_b(\vec{p}_N,\lambda_N)\overline{u}_a(\vec{p}_Y,\lambda_Y)\Gamma^{\text{YN}}_{ab;cd}G_{\frac{1}{2},df}(\boldsymbol{p}_{N'},m_{N'})G_{\frac{1}{2},ce}(\boldsymbol{p}_{Y'},m_{Y'})& \\ \times\left[\epsilon^{\lambda_\gamma}_\nu\hat{J}^\nu G_{\frac{1}{2}}(\boldsymbol{p}_T,m_N)\xi^{\lambda_D}_\mu\Gamma^\mu_{\text{Dnp}}(\boldsymbol{p}_N,\boldsymbol{p}_D)\mathcal{C}\right]_{ef}\,,&\end{aligned}\tag{5.117}$$

where we have written the Dirac indices explicitly for clarity. The vertex operator Γ^{YN} represents the (in)elastic hyperon-nucleon rescattering process and is covered in appendix K.

The transition amplitude features three fermion propagators $G_{\frac{1}{2}}$. All three exhibit singularities as they move on mass shell. Clearly, the largest contributions to the amplitude are realised when at least one pole is reached. Working within the constraints of CST [186, 189], we choose to restrict one particle on its mass-shell. One can prove that this approach can be used without loosing the manifest covariance of the transition amplitude. Making use of the residue theorem, forcing the spectator nucleon on mass shell is equivalent to the following substitution

$$i\int\frac{d^4\boldsymbol{p}_{N'}}{(2\pi)^4}\frac{\not{\boldsymbol{p}}_{N'}+m_{N'}}{\boldsymbol{p}^2_{N'}-m^2_{N'}+i\epsilon}\to-\sum_{\lambda_{N'}}\int\frac{d^3\vec{p}_{N'}}{(2\pi)^3 2E_{N'}}u(\vec{p}_{N'},\lambda_{N'})\overline{u}(\vec{p}_{N'},\lambda_{N'})\,.\tag{5.118}$$

Consequently, the YN-FSI contribution to the transition-current matrix element becomes

$$\begin{aligned}\langle \boldsymbol{p}_K;\boldsymbol{p}_Y,\lambda_Y;\boldsymbol{p}_N,\lambda_N|\,\hat{\mathcal{J}}^{\lambda_\gamma}_{\text{YN-FSI}}\,|\boldsymbol{p}_D,\lambda_D\rangle =& \\ -\sum_{\lambda_{N'}}\int\frac{d^3\vec{p}_{N'}}{(2\pi)^3 2E_{N'}}\overline{u}_b(\vec{p}_N,\lambda_N)\overline{u}_a(\vec{p}_Y,\lambda_Y)\Gamma^{\text{YN}}_{ab;cd}u_d(\vec{p}_{N'},\lambda_{N'})G_{\frac{1}{2},ce}(\boldsymbol{p}_{Y'},m_{Y'})& \\ \times\left[\epsilon^{\lambda_\gamma}_\nu\hat{J}^\nu G_{\frac{1}{2}}(\boldsymbol{p}_T,m_N)\xi^{\lambda_D}_\mu\Gamma^\mu_{\text{Dnp}}(\boldsymbol{p}_N,\boldsymbol{p}_D)\mathcal{C}\right]_{ef}\overline{u}_f(\vec{p}_{N'},\lambda_{N'})\,.&\end{aligned}\tag{5.119}$$

With the spectator nucleon on mass shell, the target nucleon absorbs all the binding energy and therefore never fulfils Einstein's relation. The propagator of the rescattering hyperon, on the other hand, passes through its singularity. It can be decomposed as (A.45)

$$G_{\frac{1}{2}}(\boldsymbol{p}_{Y'},m_{Y'})=\frac{1}{2\widetilde{E}_{Y'}}\left(\frac{\Lambda_+(\vec{p}_{Y'})}{p^0_{Y'}-\widetilde{E}_{Y'}+i\epsilon}-\frac{\Lambda_-(-\vec{p}_{Y'})}{p^0_{Y'}+\widetilde{E}_{Y'}-i\epsilon}\right)\,,\tag{5.120}$$

where we have defined an on-shell four-vector for the rescattering hyperon

$$\widetilde{\boldsymbol{p}}_{Y'}\equiv(\widetilde{E}_{Y'},\vec{p}_{Y'})\,,\quad\text{with}\quad\widetilde{E}_{Y'}=\sqrt{|\vec{p}_{Y'}|^2+m_{Y'}}\,.\tag{5.121}$$

The denominator of the second term will be large compared to the one of the positive-energy part. Its contribution will be neglected in our calculations. Thereby, the covariance of our formalism is lost. Our approximate expression for the YN-FSI contribution to the transition amplitude then reads

$$\begin{aligned}\langle \boldsymbol{p}_K;\boldsymbol{p}_Y,\lambda_Y;\boldsymbol{p}_N,\lambda_N|\,\hat{\mathcal{J}}^{\lambda_\gamma}_{\text{YN-FSI}}\,|\boldsymbol{p}_D,\lambda_D\rangle \approx& \\ -\sum_{\lambda_{N'}}\int\frac{d^3\vec{p}_{N'}}{(2\pi)^3 2E_{N'}2\widetilde{E}_{Y'}}\overline{u}_b(\vec{p}_N,\lambda_N)\overline{u}_a(\vec{p}_Y,\lambda_Y)\Gamma^{\text{YN}}_{ab;cd}u_d(\vec{p}_{N'},\lambda_{N'})\frac{\left[\Lambda_+(\vec{p}_{Y'})\right]_{ce}}{p^0_{Y'}-\widetilde{E}_{Y'}+i\epsilon}& \\ \times\left[\epsilon^{\lambda_\gamma}_\nu\hat{J}^\nu G_{\frac{1}{2}}(\boldsymbol{p}_T,m_N)\xi^{\lambda_D}_\mu\Gamma^\mu_{\text{Dnp}}(\boldsymbol{p}_N,\boldsymbol{p}_D)\mathcal{C}\right]_{ef}\overline{u}_f(\vec{p}_{N'},\lambda_{N'})\,.&\end{aligned}\tag{5.122}$$

This amplitude will have its largest contribution when the singularity corresponding to an on-mass-shell rescattering hyperon is reached. With the use of the general relation

$$\frac{1}{p^0_{Y'} - \widetilde{E}_{Y'} + i\epsilon} = \mathcal{P}\left[\frac{1}{p^0_{Y'} - \widetilde{E}_{Y'}}\right] - i\pi\delta(p^0_{Y'} - \widetilde{E}_{Y'})\,, \tag{5.123}$$

where $\mathcal{P}[\ldots]$ stands for a Cauchy principal-value integration, the current operator breaks up into an on-shell and an off-shell part, i.e.

$$\hat{\mathcal{J}}_{\text{YN-FSI}} = \hat{\mathcal{J}}_{\text{YN-FSI,onshell}} + \hat{\mathcal{J}}_{\text{YN-FSI,offshell}}\,. \tag{5.124}$$

The on-shell contribution is defined as

$$\begin{aligned}\langle \boldsymbol{p}_K; \boldsymbol{p}_Y, \lambda_Y; \boldsymbol{p}_N, \lambda_N |\, \hat{\mathcal{J}}^{\lambda_\gamma}_{\text{YN-FSI,onshell}} \,|\boldsymbol{p}_D, \lambda_D\rangle = \\ - i\pi \sum_{\lambda_{N'}\lambda_{Y'}} \int \frac{d^3\vec{p}_{N'}}{(2\pi)^3 2E_{N'} 2\widetilde{E}_{Y'}} \delta(p^0_{Y'} - \widetilde{E}_{Y'})\, \langle \boldsymbol{p}_Y, \lambda_Y; \boldsymbol{p}_N, \lambda_N |\, \hat{\mathrm{J}}_{\text{YN}} \,|\widetilde{\boldsymbol{p}}_{Y'}, \lambda_{Y'}; \boldsymbol{p}_{N'}, \lambda_{N'}\rangle \\ \times \langle \boldsymbol{p}_K; \widetilde{\boldsymbol{p}}_{Y'}, \lambda_{Y'}; \boldsymbol{p}_{N'}, \lambda_{N'} |\, \hat{\mathcal{J}}^{\lambda_\gamma}_{\text{RPWIA}} \,|\boldsymbol{p}_D, \lambda_D\rangle\,.\end{aligned} \tag{5.125}$$

We can dispose of the delta function by integrating over the three-momentum of the spectator nucleon in the YN-CM frame. The spectator-nucleon three-momentum $|\check{\vec{p}}^{\,*}_{N'}|$, for which the rescattering hyperon is put on mass shell, fulfils the following constraint

$$W_{YN} = \sqrt{|\check{\vec{p}}^{\,*}_{N'}|^2 + m^2_{Y'}} + \sqrt{|\check{\vec{p}}^{\,*}_{N'}|^2 + m^2_{N'}}\,. \tag{5.126}$$

After solving this equation, we obtain

$$\check{E}^*_{N'} = \sqrt{|\check{\vec{p}}^{\,*}_{N'}|^2 + m^2_{N'}} = \frac{W^2_{YN} + m^2_{N'} - m^2_{Y'}}{2W_{YN}}\,. \tag{5.127}$$

Carrying out the integration over $|\vec{p}_{N'}|$ in Eq. (5.125) yields

$$\begin{aligned}\langle \boldsymbol{p}_K; \boldsymbol{p}_Y, \lambda_Y; \boldsymbol{p}_N, \lambda_N |\, \hat{\mathcal{J}}^{\lambda_\gamma}_{\text{YN-FSI,onshell}} \,|\boldsymbol{p}_D, \lambda_D\rangle \overset{\text{YN-CM}}{=} \\ \frac{-i}{32\pi^2} \frac{|\check{\vec{p}}^{\,*}_{N'}|}{W_{YN}} \sum_{\lambda_{N'}\lambda_{Y'}} \int d^2\Omega^*_{N'}\, \langle \boldsymbol{p}_Y, \lambda_Y; \boldsymbol{p}_N, \lambda_N |\, \hat{\mathrm{J}}_{\text{YN}} \,|\widetilde{\boldsymbol{p}}_{Y'}, \lambda_{Y'}; \check{\boldsymbol{p}}_{N'}, \lambda_{N'}\rangle \\ \times \langle \boldsymbol{p}_K; \widetilde{\boldsymbol{p}}_{Y'}, \lambda_{Y'}; \check{\boldsymbol{p}}_{N'}, \lambda_{N'} |\, \hat{\mathcal{J}}^{\lambda_\gamma}_{\text{RPWIA}} \,|\boldsymbol{p}_D, \lambda_D\rangle\,.\end{aligned} \tag{5.128}$$

This amplitude features the transition matrix element for the hyperon-nucleon interaction with all incoming and outgoing particles on mass-shell. In Appendix K, we elaborate on the properties of the hyperon-nucleon interaction $\hat{\mathrm{J}}_{\text{YN}}$.

In the second contribution to the YN-FSI diagram the hyperon-nucleon interaction vertex has one off-mass-shell leg. It reads

$$\begin{aligned}\langle \boldsymbol{p}_K; \boldsymbol{p}_Y, \lambda_Y; \boldsymbol{p}_N, \lambda_N |\, \hat{\mathcal{J}}^{\lambda_\gamma}_{\text{YN-FSI,offshell}} \,|\boldsymbol{p}_D, \lambda_D\rangle = \\ \sum_{\lambda_{N'}\lambda_{Y'}} \int \frac{d^2\Omega_{N'}}{4(2\pi)^3} \mathcal{P} \int d|\vec{p}_{N'}| \frac{|\vec{p}_{N'}|^2}{E_{N'}\widetilde{E}_{Y'}} \frac{1}{p^0_{Y'} - \widetilde{E}_{Y'}}\, \langle \boldsymbol{p}_Y, \lambda_Y; \boldsymbol{p}_N, \lambda_N |\, \hat{\mathrm{J}}_{\text{YN}} \,|\boldsymbol{p}_{Y'}, \lambda_{Y'}; \boldsymbol{p}_{N'}, \lambda_{N'}\rangle \\ \times \langle \boldsymbol{p}_K; \boldsymbol{p}_{Y'}, \lambda_{Y'}; \boldsymbol{p}_{N'}, \lambda_{N'} |\, \hat{\mathcal{J}}^{\lambda_\gamma}_{\text{RPWIA}} \,|\boldsymbol{p}_D, \lambda_D\rangle\,.\end{aligned} \tag{5.129}$$

As is pointed out in Appendix K, the non-vanishing virtuality of the rescattered hyperon allows the rescattering process to occur below threshold. Similar to the evaluation of the delta function in the on-shell contribution to the YN-FSI amplitude, we will abandon our covariant notation to further simplify the principal-value integral in Eq. (5.129). With the help of the following identity

$$\left(p^{*0}_{Y'}\right)^2 - \left(\widetilde{E}^*_{Y'}\right)^2 = -2W_{YN}\left(E^*_{N'} - \check{E}^*_{N'}\right) , \tag{5.130}$$

we are able to rewrite the off-shell contribution to the YN-FSI diagram in a form suitable for numerical integration, i.e.

$$\begin{aligned}\langle \boldsymbol{p}_K; \boldsymbol{p}_Y, \lambda_Y; \boldsymbol{p}_N, \lambda_N | \, \hat{\mathcal{J}}^{\lambda_\gamma}_{\text{YN-FSI,offshell}} \, | \boldsymbol{p}_D, \lambda_D \rangle \overset{\text{YN-CM}}{=} \\ - \sum_{\lambda_{N'}\lambda_{Y'}} \int \frac{d^2\Omega^*_{N'}}{64\pi^3} \mathcal{P} \int_{m_{N'}}^{E^{*,\max}_{N'}} dE^*_{N'} \frac{|\vec{p}^{\,*}_{N'}|}{W_{YN}\widetilde{E}^*_{Y'}} \frac{W_{YN} - E^*_{N'} + \widetilde{E}^*_{Y'}}{E^*_{N'} - \check{E}^*_{N'}} \\ \times \langle \boldsymbol{p}_Y, \lambda_Y; \boldsymbol{p}_N, \lambda_N | \, \hat{\mathrm{J}}_{\mathrm{YN}} \, | \boldsymbol{p}_{Y'}, \lambda_{Y'}; \boldsymbol{p}_{N'}, \lambda_{N'} \rangle \langle \boldsymbol{p}_K; \boldsymbol{p}_{Y'}, \lambda_{Y'}; \boldsymbol{p}_{N'}, \lambda_{N'} | \, \hat{\mathcal{J}}^{\lambda_\gamma}_{\text{RPWIA}} \, | \boldsymbol{p}_D, \lambda_D \rangle \, . \end{aligned} \tag{5.131}$$

The integration over the solid angle $\Omega^*_{N'}$ and CM energy $E^*_{N'}$ are performed with the aid of the quadrature routines from GSL [190]. At threshold, where the singularity is located at the integral's lower bound, we adopt the QAWS routine. For all other energies, the QAWC routine is employed.

Finally, we need to specify the upper bound $E^{*,\max}_{N'}$. In principle, the integral is unbounded. In practise, however, the effective masses of the target nucleon and the rescattering hyperon depend on the three-momentum of the spectator nucleon. As was pointed out in Paragraph 5.6.2 in the context of the RPWIA contribution to the transition amplitude, an effective upper bound for $|\vec{p}^{\,*}_{N'}|$ is needed to prevent the target nucleon's effective mass from becoming negative. A similar constraint is imposed for the effective mass of the rescattering hyperon. It yields

$$E^*_{N'} \leq \frac{W^2_{YN} + m^2_{N'}}{2W_{YN}} \, . \tag{5.132}$$

Because of the specific structure of the elementary kaon-production operator in the RPR model a third restriction is needed. In case the kaon-production vertex has both an incoming and outgoing particle off mass-shell, the elementary operator can be evaluated below the physical production threshold. Besides the uncertainties related to this off-shell extrapolation, an artificial singularity can arise once the invariant mass in the vertex reaches down to the physical nucleon mass. This singularity is caused by the presence of the s-channel Born diagram needed to guarantee gauge-invariance in the context of the Regge model. When

$$\left(\boldsymbol{p}_K + \boldsymbol{p}_{Y'}\right)^2 = m^2_T \, , \tag{5.133}$$

the pole of this diagram is reached. We stay clear of this singularity by solving Eq. (5.133) for $E^*_{N'}$ and imposing it as an upper bound.

CHAPTER 6

Results for kaon production from the deuteron

In Chapter 2, we introduced the RPR formalism as a trustworthy and economical description of EM kaon production from the unbound proton. Chapter 3 dealt with extensions to the RPR model which aimed at describing reaction channels for which only limited data sets are available. A relativistic formalism for the EM production of kaons off deuterium targets was the subject of the previous chapter. We presented the RPWIA and discussed the different contributions to the hyperon-nucleon FSI. In this chapter, we collect all these different ingredients and present calculations for strangeness production from the deuteron.

The results are obtained utilising the RPR-2007 elementary-production operator presented in Chapter 2 and Refs. [39, 40, 69]. For the sake of clarity, the coupling constants of the adopted models are listed in Appendix I. Although a variety of deuteron wave functions have been presented in Section 5.5, all calculations employ the relativistic wave function obtained with the WJC-1 nucleon-nucleon potential of Gross and Stadler [183], unless mentioned otherwise. For the investigation of the YN-FSI, we use helicity amplitudes calculated with the Jülich hyperon-nucleon potential as input. The Jülich model is briefly reviewed in Section K.4.

We start this chapter with an in-depth discussion of the $^2\mathrm{H}(\gamma, KY)N$ cross sections obtained in the RPWIA. We investigate which kinematic regions dominate the reaction and explore the sensitivity of the formalism to its different ingredients. Section 6.2 is devoted to the YN-FSI contribution. We conclude this chapter by confronting our model calculations with the available photo- and electroproduction data in Sections 6.3 and 6.4 respectively.

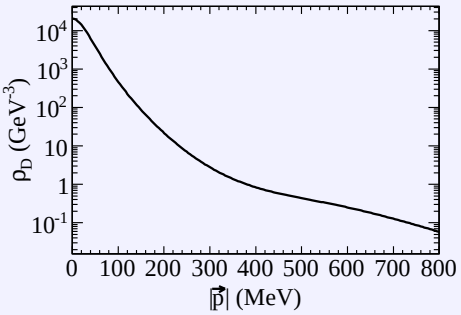

Figure 6.1 – Deuteron density (6.2) calculated within the WJC-1 model [183] as function of the relative proton-neutron three-momentum $|\vec{p}|$.

6.1 Relativistic plane-wave impulse approximation

6.1.1 Non-relativistic spectator-nucleon approximation

Starting from the on-shell contribution to the RPWIA transition amplitude (5.112), one can show that

$$\overline{\sum}|\left\langle \boldsymbol{p}_K;\boldsymbol{p}_Y,\lambda_Y;\boldsymbol{p}_N,\lambda_N\right|\hat{\mathcal{J}}^{\lambda_\gamma}_{\text{RPWIA,onshell}}\left|\boldsymbol{p}_D,\lambda_D\right\rangle|^2 \sim \rho_D(|\vec{p}_N|)\overline{\sum}|\left\langle \boldsymbol{p}_K;\boldsymbol{p}_Y,\lambda_Y\right|\hat{J}^{\lambda_\gamma}\left|\widetilde{\boldsymbol{p}}_T\lambda_T\right\rangle|^2\,, \tag{6.1}$$

where we have defined the deuteron density as

$$\rho_D(p) = u^2(p) + w^2(p) + v_t^2(p) + v_s^2(p)\,. \tag{6.2}$$

Inserting this relation in the expression for the exclusive differential cross section (5.35), we find for small values of the spectator momentum $|\vec{p}_N|$

$$\frac{d^5\sigma}{d\vec{p}_N d\Omega_K^*} \approx \frac{1}{2\pi}\left(1+\frac{|\vec{p}_N|}{E_N}\cos\theta_N\right)\rho_D(|\vec{p}_N|)\frac{d^2\sigma_{KY}}{d\Omega_K^*}\,. \tag{6.3}$$

This relation is known as the non-relativistic spectator-nucleon approximation to the cross section and is valid as long as $|\vec{p}_N| \ll m_N$. Assuming that FSI effects are negligible, Eq. (6.3) provides a straightforward recipe to extract information on the elementary kaon-production reaction from exclusive cross section measurements at small $|\vec{p}_N|$s.

Because of the non-trivial phase space of a three-particle final state, the $^2\text{H}(\gamma,KY)N$ results can be presented in terms of a plethora of combinations of the kinematic variables. Owing to the convenient factorised form (6.3) of the cross section, we can easily assess which regions in phase space are to contribute most to the reaction's strength. The transition amplitude of the elementary kaon-production process is obviously an essential component, but exhibits only mild variations with energy. The deuteron density $\rho_D(|\vec{p}_N|)$, by contrast, falls off exponentially as the relative three-momentum of the proton and neutron inside the deuteron increases. This is illustrated in Figure 6.1 with the WJC-1 deuteron wave function [183]. Assuming that the reaction is dominated by the RPWIA contribution to the transition amplitude, the cross section will thus exhibit most strength for low momenta of the outgoing nucleon. Our intuition is confirmed in Figure 6.2, where the semi-inclusive differential cross section for charged-kaon production is shown as function of $|\vec{p}_N|$ and $\cos\theta_N$ for three representative values of the kaon-hyperon invariant mass. We notice an exponential falloff

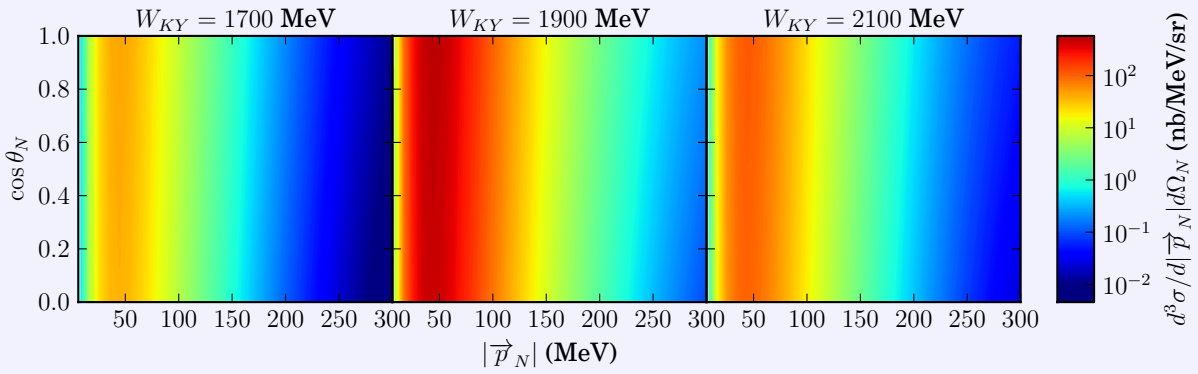

Figure 6.2 – The semi-inclusive $^2\mathrm{H}(\gamma, K^+)YN$ differential cross section using the full RPR operator in the RPWIA as a function of the nucleon momentum $|\vec{p}_N|$ and scattering angle $\cos\theta_N$ in the LAB frame at three different values of the invariant mass of the kaon-hyperon system (from left to right: $W_{KY} = 1700$, 1900 and 2100 MeV).

as $|\vec{p}_N|$ increases, reminiscent of the deuteron density ρ_D. The differential cross section is nearly isotropic, yet the coloured bands in Figure 6.2 are slightly tilted in the clockwise direction. This indicates a mild dependence on $\cos\theta_N$ that becomes stronger as the spectator momentum rises.

In case the $^2\mathrm{H}(\gamma, K)YN$ observables are presented as a function of the momentum and scattering angle of the outgoing kaon, e.g.

$$\frac{d^3\sigma}{d|\vec{p}_K|d\Omega_K} = \int d\Omega_Y^* \, \frac{d^5\sigma}{d|\vec{p}_K|d\Omega_K d\Omega_Y^*} \,, \tag{6.4}$$

the spectator-nucleon momentum and hence the deuteron density are function of $|\vec{p}_K|$, θ_K, the photon energy E_γ and the hyperon's scattering angle θ_Y^* in the YN-CM frame. We exemplify this dependence in Figure 6.3 for three photon energies and at forward scattering angles in the YN-CM frame. It stands out that the deuteron density is strongly peaked at small values of θ_Y^*. At $E_\gamma = 1000\,\mathrm{MeV}$, that is close to threshold, ρ_D is concentrated at forward scattering angles for the photoproduced kaon. As energy rises, this distribution spreads over a larger region of kaon momenta and shifts towards more backward angles.

Figure 6.4 shows RPWIA results for semi-inclusive charged-kaon photoproduction. This reaction receives contributions from elementary $K^+\Lambda$ and $K^+\Sigma^0$ production from the proton, in addition to $K^+\Sigma^-$ production off the neutron. The threefold differential cross section is given as a function of the kaon's momentum and scattering angle in the LAB frame. These results are obtained with the full RPR current operator. A comparison with Figure 6.3 reveals that the shape of the semi-inclusive cross section is mainly determined by the deuteron density distribution. Whereas the available phase-space volume makes sure the cross section vanishes as the kaon's momentum approaches zero. The cross section is largest for kaons created along or near the direction of the incoming photon. At all but the lowest photon energy, the cross section consists of two modi. The one at the highest kaon momenta corresponds to quasi-free Λ production, the second to the production of a Σ^0 and Σ^- hyperon. As the photon energy increases, the gap between both ridges becomes smaller.

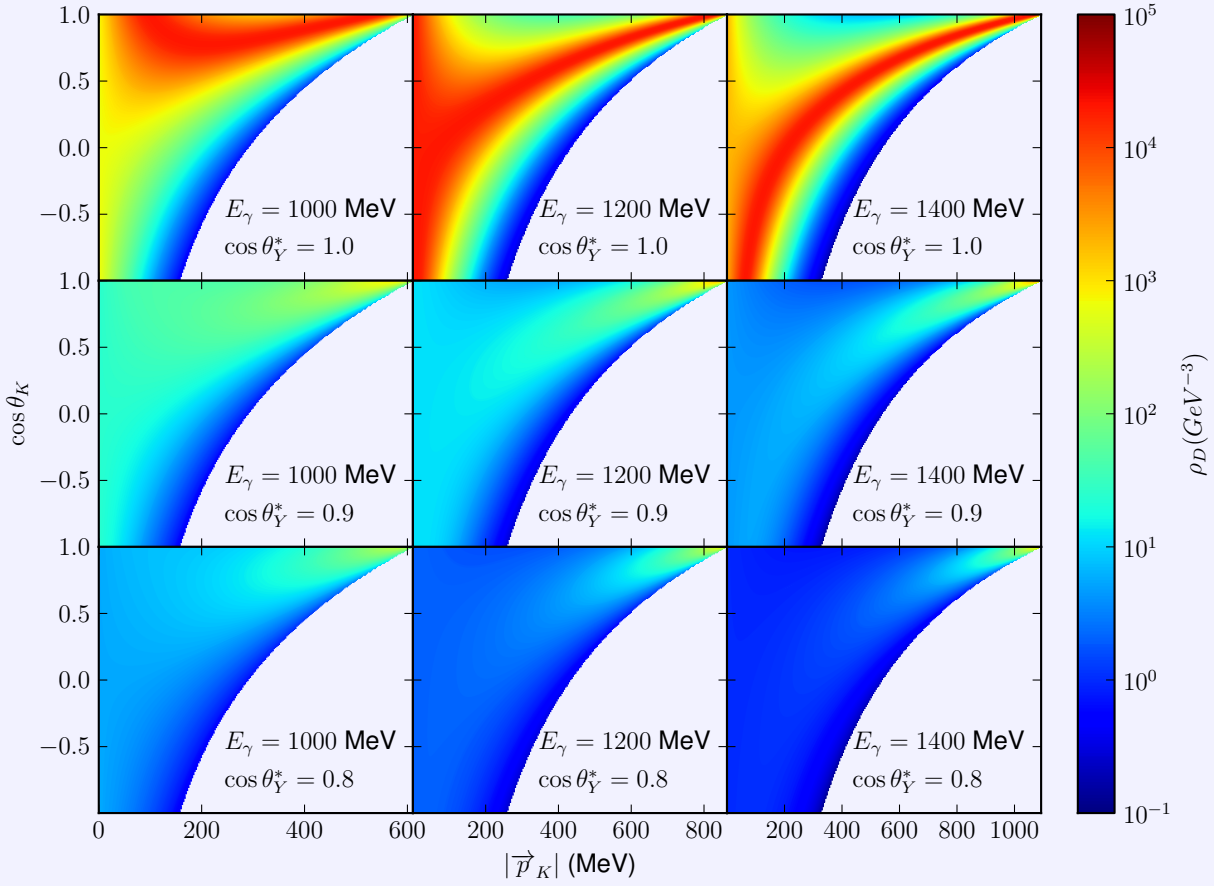

Figure 6.3 – Deuteron density (6.2) as calculated within the WJC-1 model [183] as a function of $\cos\theta_K$ and $|\vec{p}_K|$ at various values of E_γ and $\cos\theta^*_Y$. Each point in the phase space of the $^2\mathrm{H}(\gamma, K^+\Lambda)n$ reaction determines a single value for $|\vec{p}_N|$ assuming the RPWIA and the corresponding deuteron density is plotted.

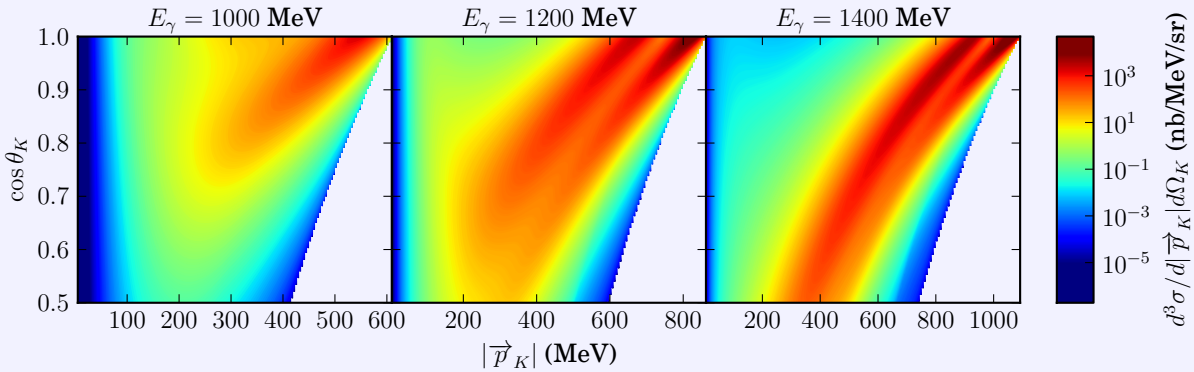

Figure 6.4 – The semi-inclusive $^2\mathrm{H}(\gamma, K^+)YN$ differential cross section using the full RPR operator in the RPWIA as a function of the kaon momentum $|\vec{p}_K|$ and scattering angle $\cos\theta_K$ in the LAB frame at three different photon energies (from left to right $E_\gamma = 1000$, 1200 and 1400 MeV).

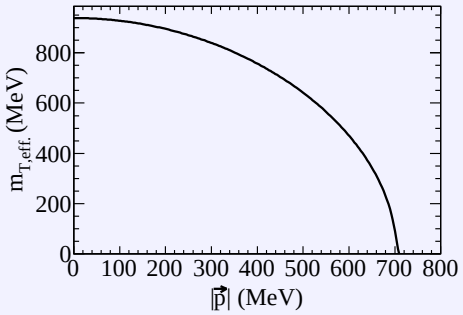

Figure 6.5 – Effective mass (6.5) of the target nucleon that absorbs the incoming photon as a function of the relative proton-neutron three-momentum $|\vec{p}|$.

6.1.2 Off-shell extrapolation

As mentioned in Section 5.6, in our implementation of the RIA we put the spectator nucleon in the Dnp-vertex on its mass shell. As a consequence, the nucleon that absorbs the photon carries the complete binding energy of the deuteron. As such, the elementary-production operator needs to be evaluated with an effective mass

$$m_{T,\text{eff.}} = \sqrt{(\boldsymbol{p}_D - \boldsymbol{p}_N)^2} = \sqrt{m_D^2 + m_N^2 - 2m_D\sqrt{|\vec{p}_N|^2 + m_N^2}}\,, \tag{6.5}$$

for the target nucleon Since the RPR operator is not constrained by data for $m_{T,\text{eff.}} \neq m_N$, this involves an off-shell extrapolation. In Figure 6.5, the effective mass of the target nucleon is shown as a function of the relative proton-neutron three-momentum $|\vec{p}|$. At low values of $|\vec{p}|$, $m_{T,\text{eff.}}$ remains close to the physical nucleon mass. As the relative momentum approaches 700 MeV, it becomes zero. For higher values of $|\vec{p}|$, the effective mass is imaginary.

We illustrate the off-shell extrapolation of the elementary production operator in Figure 6.6. The squared transition amplitude for the $p(\gamma, K^+)\Lambda$ reaction as calculated within the RPR formalism is given as function of the kaon's CM scattering angle at three representative values of the invariant mass of the kaon-hyperon system. We remind the reader that with our choice of normalisations this quantity is dimensionless. For $m_{T,\text{eff.}} \approx m_N$, i.e. at the top of the panels, the transition amplitude is computed with the physical nucleon mass. The matrix element is evaluated at smaller masses as we go down the ordinate axis. It is clear the elementary-production operator exhibits off-shell structures and does not disappear as the target-nucleon mass approaches zero. We have carefully scanned the phase space of the different elementary reaction channels and conclude the transition amplitude is free of singularities. The off-shell structure of the elementary reaction is likely to play a role in observables, but we do not expect any dramatic effects.

The effect of the off-shell extrapolation is most readily investigated by comparing the RPWIA contribution (5.102) to the transition amplitude with its on-shell reduction given in Eq. (5.112). In Figure 6.7, we compare the one-fold differential $^2\text{H}(\gamma, K^+\Lambda)n$ cross section as calculated with both forms of the transition amplitude. Clearly, the RPWIA result and the on-shell approximation coincide for small values of the spectator-nucleon momentum. At the lowest energy, the agreement holds up to $|\vec{p}_N| \lesssim 200\,\text{MeV}s$, and the region of similarity becomes larger for higher values of W_{KY}. At large missing momenta, the results bifurcate, with the on-shell form of the transition amplitude giving significantly larger cross-section predictions compared to the RPWIA result. This discrepancy is not

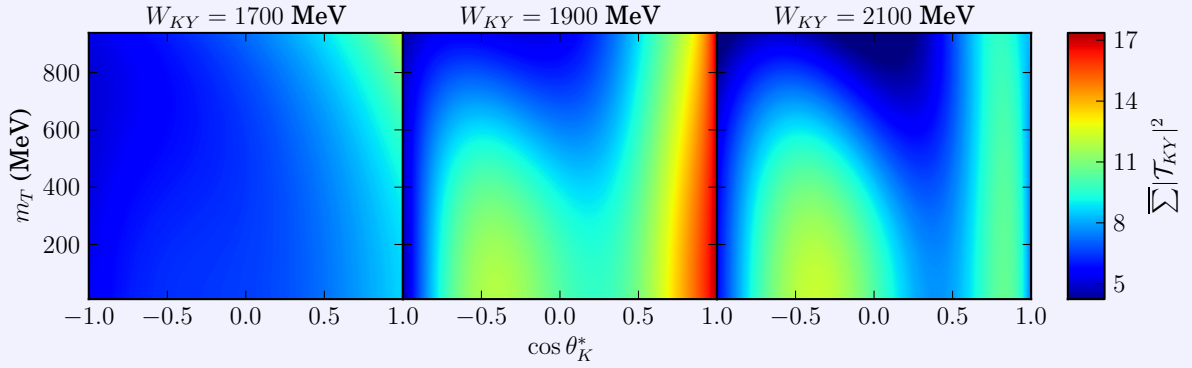

Figure 6.6 – Squared $p(\gamma, K^+)\Lambda$ transition amplitude at three values of W_{KY} as a function of $\cos\theta^*_K$ and $m_{T,\text{eff.}}$. The result involves a sum over the polarisations of the initial photon and proton and outgoing hyperon.

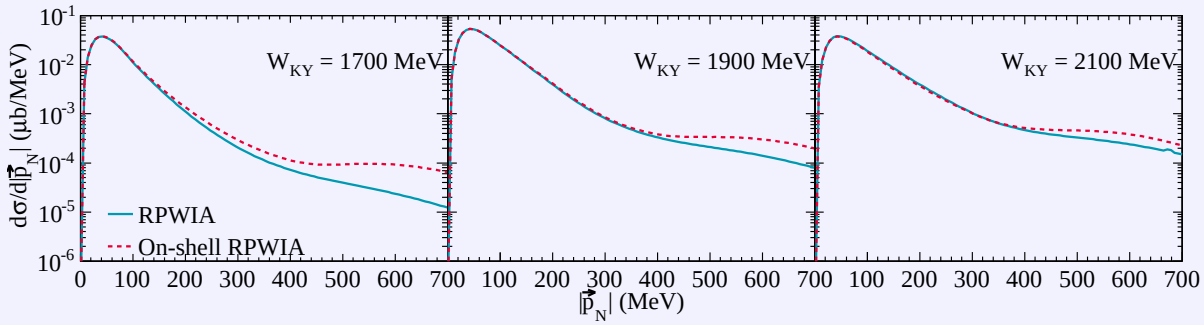

Figure 6.7 – The $^2\text{H}(\gamma, K^+\Lambda)n$ differential cross section as a function of the nucleon momentum $|\vec{p}_N|$ at three different values of W_{KY}. The solid curve is the RPWIA result (5.102). The dashed line is obtained with the on-shell reduction of Eq. (5.112).

only due to the off-shell extrapolation of the elementary-production operator, but stems in part from the additional contribution (5.110) to the RPWIA amplitude that is omitted. In Paragraph 5.6.2, we argued that this contribution is kinematically suppressed for small missing momenta. At higher values of $|\vec{p}_N|$, however, it can no longer be neglected.

6.1.3 Wave-function sensitivity

The deuteron wave function is an essential ingredient in the description of EM kaon production from the deuteron. This can be most clearly illustrated within the non-relativistic spectator-nucleon approximation which gives rise to the expression (6.3) for the cross section. Figure 6.8 shows the missing-momentum dependence of the $^2\text{H}(\gamma, K^+\Lambda)n$ cross section for various choices of the deuteron wave functions[1]. For missing momenta up to approximately 250 MeV, the different wave functions give nearly indistinguishable results. This comes as no surprise, because all NN potentials produce comparable $^3S_1$ waves which dominate in this kinematic region. As the spectator nucleon's momentum rises, the cross-section predictions start to diverge. It is worth noting that the non-relativistic wave functions of the Paris and Nijmegen potentials and the relativistic Gross-IIB wave function generate

[1] See Sections 5.5.2 and 5.5.3

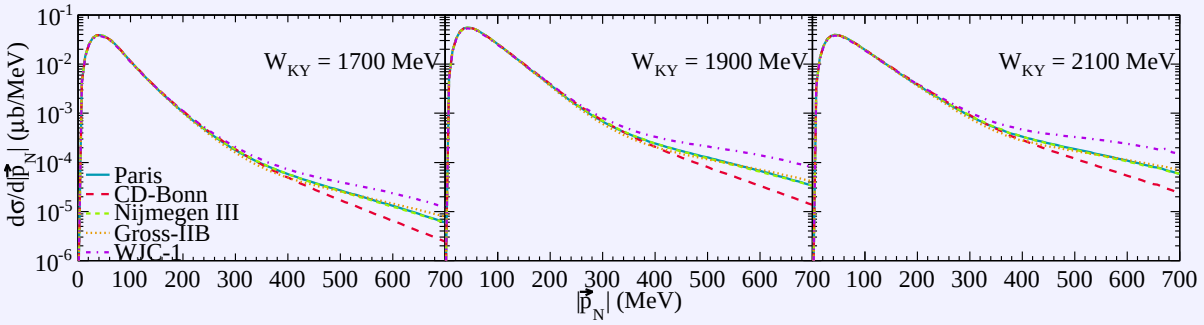

Figure 6.8 – The $^2\mathrm{H}(\gamma, K^+\Lambda)n$ differential cross section as a function of the nucleon momentum $|\vec{p}_N|$ at three different values of the invariant mass of the kaon-hyperon system . The results are obtained within the RPWIA adopting different versions of the deuteron wave function: Paris [178], CD-Bonn [179], Nijmegen-III [180], Gross-IIB [181] and WJC-1 [183].

very similar predictions. The cross sections based on the CD-Bonn and WJC-1 potentials, on the other hand, differ up to an order of magnitude for high missing momenta.

6.1.4 Helicity-amplitude dependence

Evidently, the elementary kaon-production vertex is a crucial ingredient of strangeness production from the deuteron. The RPR model, that was introduced in Chapter 2, is optimised against data in the $p(\gamma, K^+)\Lambda$ and $p(\gamma, K^+)\Sigma^0$ channels. In the description of the $N(\gamma^{(*)}, K)Y$ process, the four remaining final states, where little or no data is available, cannot be ignored. In Section 3.2, we demonstrated that the major source of uncertainties for modelling the $n(\gamma, K)Y$ reaction channels stems from the helicity amplitudes of the considered nucleon resonances. Here, we wish to assess to what extend these uncertainties propagate in (semi-)inclusive reactions on the deuteron.

The semi-inclusive charged-kaon-production cross section is depicted as function of the outgoing kaon's LAB momentum in Figure 6.9. The cross section clearly exhibits two maxima where the quasi-free condition for Λ and Σ production are realised. Below the Σ-production threshold, i.e. $|\vec{p}_K| \gtrsim 619\,\mathrm{MeV}$, only the $K^+\Lambda$ channel contributes to the reaction. At lower kaon momenta, both the $p(\gamma, K^+)\Sigma^0$ and $n(\gamma, K^+)\Sigma^-$ reactions play a role. The later takes place on the neutron and, consequently, is prone to the uncertainties related to the unconstrained helicity amplitudes. The effect is sizable as can be deduced from the magnitude of the shaded area. In the quasi-elastic peak, variations of the order of two are possible. From the above discussions, we conclude that the resonance contributions to the elementary-production operator are the major source of uncertainties for the $^2\mathrm{H}(\gamma, KY)N$ predictions. Those stemming from the off-shell extrapolation (Paragraph 6.1.2) or the deuteron wave function (Paragraph 6.1.3) are substantially smaller.

6.2 Hyperon-nucleon final-state interactions

In the previous section, we explored kaon photoproduction from the deuteron in the RPWIA formalism. The momentum distribution of the spectator nucleon emerged as dominant in shaping the differential cross sections. Besides the RPWIA contribution, Paragraph 5.6.1 introduced a set of interesting higher-order diagrams. Our motivation to study these additional contributions is two-fold.

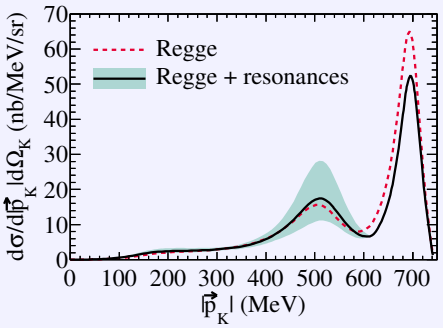

Figure 6.9 – The three-fold differential $^2\mathrm{H}(\gamma, K^+)YN$ cross section in the RPWIA as a function of the kaon LAB three-momentum $|\vec{p}_K|$ at $\theta_K = 0°$ and $E_\gamma = 1100\,\mathrm{MeV}$. The dashed curve shows the contribution of the Reggeized background, whereas the solid curve also includes the s-channel resonant contributions of the full RPR amplitude. The shaded area indicates the effect of the uncertainties in the adopted helicity amplitudes.

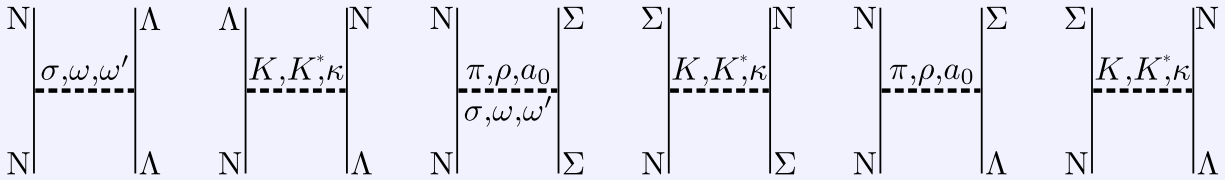

Figure 6.10 – Meson-exchange diagrams considered in the context of non-relativistic potential models for elastic ΛN and ΣN as well as inelastic ΛN – ΣN scattering. The interpretation and dynamical origin of the exchange diagrams involving scalar mesons (σ, ρ, a_0, κ, ω') differs greatly among different models [191].

In case the deuteron is exploited as a neutron target, one wishes to identify regions in phase space where higher-order effects are minimal. Kinematical conditions with significant roles for kaon-nucleon or hyperon-nucleon final-state interactions, on the other hand, provide access to the elusive KN and YN interactions.

In this work, we concentrate on the influence of the hyperon-nucleon final-state interaction. The expressions for this contribution to the transition amplitude are discussed in Paragraph 5.6.3. When both the photoproduced hyperon as well as the spectator nucleon are on mass shell, the amplitude is given by Eq. (5.128). In case the rescattering hyperon is off mass shell, the off-shell dynamics of the hyperon-nucleon interaction vertex play a role and sub-threshold production is possible. Details on the off-shell extrapolation of the hyperon-nucleon interaction are diverted to Section K.3. The off-shell YN-FSI diagram (5.131) involves a principal-value integral. Integrating over the spectator momentum comes at a significant computational cost. For this reason, we restrict calculations with the RPWIA plus full YN-FSI amplitude to exclusive conditions. For semi-inclusive results, we adopt a truncation scheme and retain the on-shell part of the YN-FSI diagram.

Evidently, a trustworthy description of the hyperon-nucleon interaction is an essential component in order to assess the role of rescattering to kaon production in the nuclear medium. In the low- and medium-energy domain, hadron-hadron interactions can be adequately described in the context of a meson-exchange picture. A hallmark result is the success of realistic nucleon-nucleon potential models that fit the available data with an astonishing $\chi^2/N_{\mathrm{data}} \approx 1$. The results from NN phase-shift analyses are considered equivalent representations of the data. For hadronic interactions involving strangeness, similar descriptions can be adopted. Model builders are hindered, however, by the small

amount of experimental data with mediocre statistics over a limited kinematical range, as well as the lack of information on polarisation observables.

For the purpose of describing the hyperon-nucleon interaction, an effective potential can be constructed by considering a set of scalar, pseudo-scalar, vector and axial-vector meson-exchange diagrams [192, 193]. Figure 6.10 provides a graphical representation of these contributions. Relying on SU(3) flavor symmetry or the SU(6) symmetry of the quark model, most coupling constants at the strange vertices can be related to nucleon-nucleon-meson coupling constants which are constrained by nucleon-nucleon scattering data. The remaining free parameters are optimised against the available hyperon-nucleon total cross section data [194–198]. All modern hyperon-nucleon potential models [199–201] successfully reproduce these data, notwithstanding the substantial differences in implementation between the different models. Especially the treatment of the (iso)scalar-meson sector, which effectively incorporates two-meson-exchange diagrams and accounts for the intermediate range of the interaction, is vastly different. In recent years, an alternative formalism for the description of the hyperon-nucleon interaction has come forth. Effective-field theory (EFT) is based on chiral-perturbation theory and provides a powerful diagrammatic expansion. The accuracy of calculations can be systematically improved by going to higher orders and the theoretical uncertainties can be evaluated. An EFT model for the hyperon-nucleon potential is available at leading order [202] and is currently being extended to next-to-leading order [203].

In Figure 6.11, total-cross-section data for elastic and inelastic hyperon-nucleon scattering are presented. They are compared to two conventional meson-exchange potentials, the Nijmegen97f potential [205] and the Jülich '04 model [199], in addition to the leading-order chiral EFT model of the Jülich group [202]. All models provide a good description of the data, even though the EFT model shows some minor discrepancies. Our YN-FSI calculations are performed with scattering amplitudes obtained with the Jülich '04 model [199]. More details on these amplitudes can be found in Section K.4. The cross-section data in Figure 6.11 show that the hyperon-nucleon interaction is strongest close to threshold. Therefore, phase-space regions where W_{YN} is small are expected to exhibit the largest sensitivity to YN-FSI effects. In addition, one notes that the YN-FSI contributions (5.128) and (5.131) to the transition amplitude are proportional to the RPWIA amplitude. This implies that rescattering will be important in phase-space regions close to hyperon-nucleon thresholds where the spectator momentum is small.

Figure 6.2 demonstrated that the missing-momentum distribution for kaon photoproduction in the RPWIA has two prominent features: near isotropy and an exponential fall off as the spectator nucleon's momentum rises. There is no published data available to verify these characteristics, but preliminary momentum distributions have been obtained with the CLAS spectrometer in Jefferson Lab's Hall-B and are shown in Figure 6.12. This data exhibits the predicted qualitative behaviour for low missing momenta. The data reveal a peak near $|\vec{p}_N| \approx 50\,\mathrm{MeV}$ and barely any $\cos\theta_N$ dependence in accordance with RPWIA calculations. At high missing momenta and forward angles, an excess of events is observed.

Figure 6.13 presents exclusive cross section results for $^2\mathrm{H}(\gamma, K^+\Lambda)n$ production at three representative values for W_{KY}. The kinematics are coplanar and the photoproduced kaon moves forward in the KY-CM to maximise the cross section. The top panels are calculated at the quasi-elastic peak. At these kinematics, the YN-FSI have a small impact and do not alter the isotropic aspect of the cross section. The results in the lower panels, by contrast, are obtained at a moderate value for the missing momentum and are clearly forward peaked as a result of the YN-FSI. This behaviour

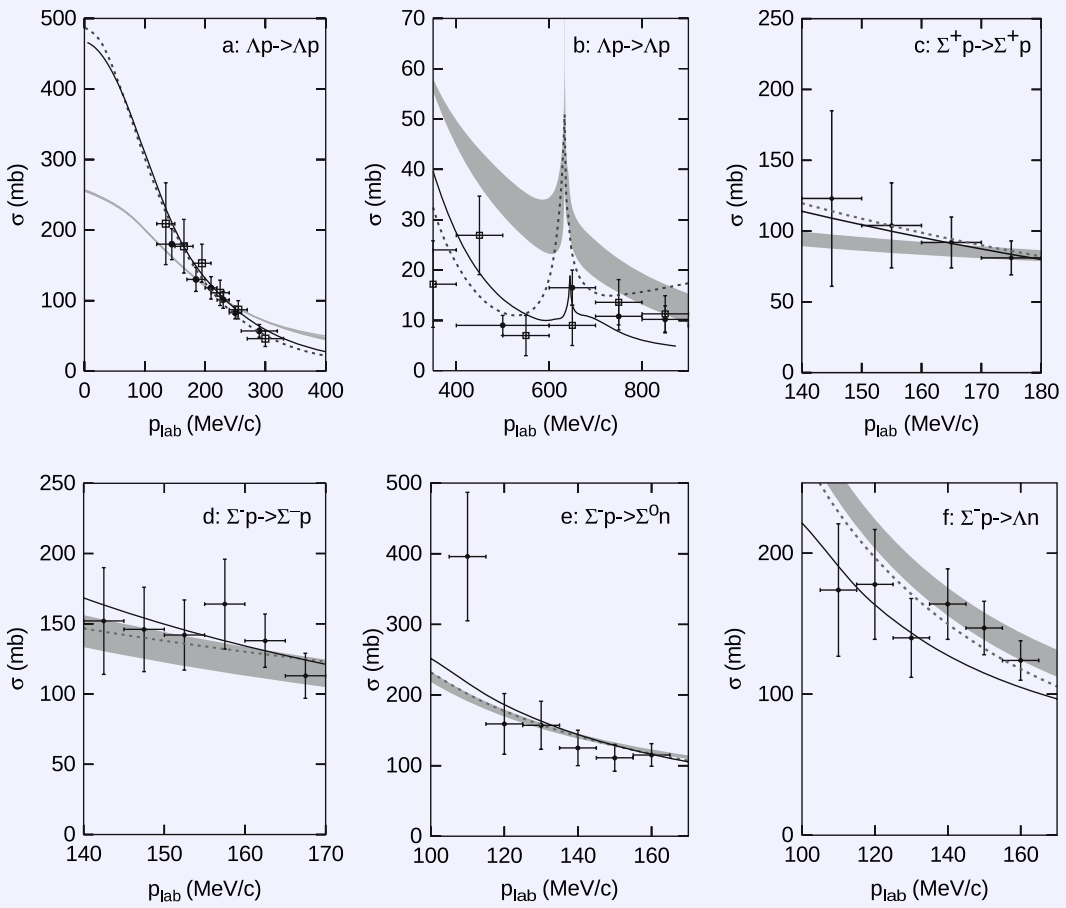

Figure 6.11 – *Total* cross section $\sigma = \frac{2}{\cos\theta_{\rm max} - \cos\theta_{\rm min}} \int_{\cos\theta_{\rm min}}^{\cos\theta_{\rm max}} \frac{d\sigma(\theta)}{d\cos\theta} d\cos\theta$ as a function of $p_{\rm lab}$. The integration limits are ± 1 except for the $\Sigma^+ p \to \Sigma^+ p$ and $\Sigma^- p \to \Sigma^- p$ cross sections where $\cos\theta_{\rm max,min} = \pm 0.5$ was taken. The experimental cross sections in (a) are taken from Refs. [194] (□) and [195] (•), in (b) from Refs. [196] (•) and [204] (□), in (c),(d) from [197] and in (e),(f) from [198]. The shaded band is the Jülich chiral EFT result [202], the solid curve is the Jülich '04 model [199], and the dashed curve is the Nijmegen NSC97f potential [205]. The figure was taken from Ref. [191].

is characteristic for the high-momentum tails of the cross section and provides an opportunity to extract information on the hyperon-nucleon potential. In an experimental analysis that focuses on phase-space regions with high missing-momenta, any strong anisotropy will reveal the presence of hyperon-nucleon rescattering. Note that at these kinematic conditions the cross sections are small and count rates will be reduced.

The exclusive $^2\mathrm{H}(\gamma, K^+\Lambda)n$ cross section is shown in Figure 6.14 as function of the LAB scattering angle of the outgoing hyperon for kaons produced along the photon momentum. The calculations are performed at energies ($E_\gamma = 1100$ and 1300 MeV) relevant for contemporary experimental facilities. The tendency of the hyperon to be produced co-linear with the photon is evident at all values for the kaon momentum. The panels on the left correspond to kaon momenta slightly above the reaction's threshold. Here, the hyperons are restricted to a small solid angle in the forward hemisphere and both the on-shell and off-shell parts of the YN-FSI diagram contribute constructively to the reaction's strength. In the vicinity of the quasi-free Λ-production peak, corresponding to the $|\vec{p}_K|$ values of the middle panels, YN-FSI effects are absent in the forward direction, but play an increasingly important

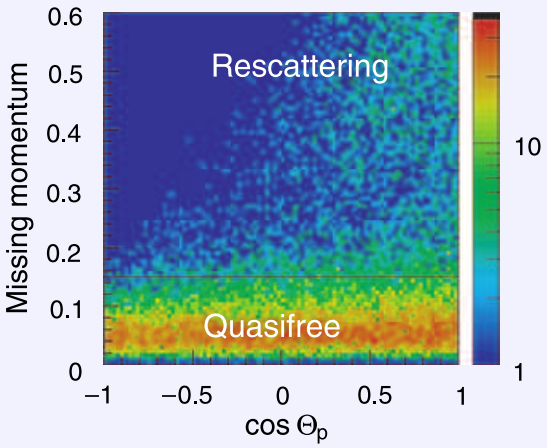

Figure 6.12 – Exclusive $^2\mathrm{H}(\gamma, K_s^0\Lambda)p$ events from JLab run g10 obtained with the CLAS spectrometer. The data are shown as function of the LAB momentum (in GeV) and scattering angle of the outgoing proton. The figure was taken from Ref. [206].

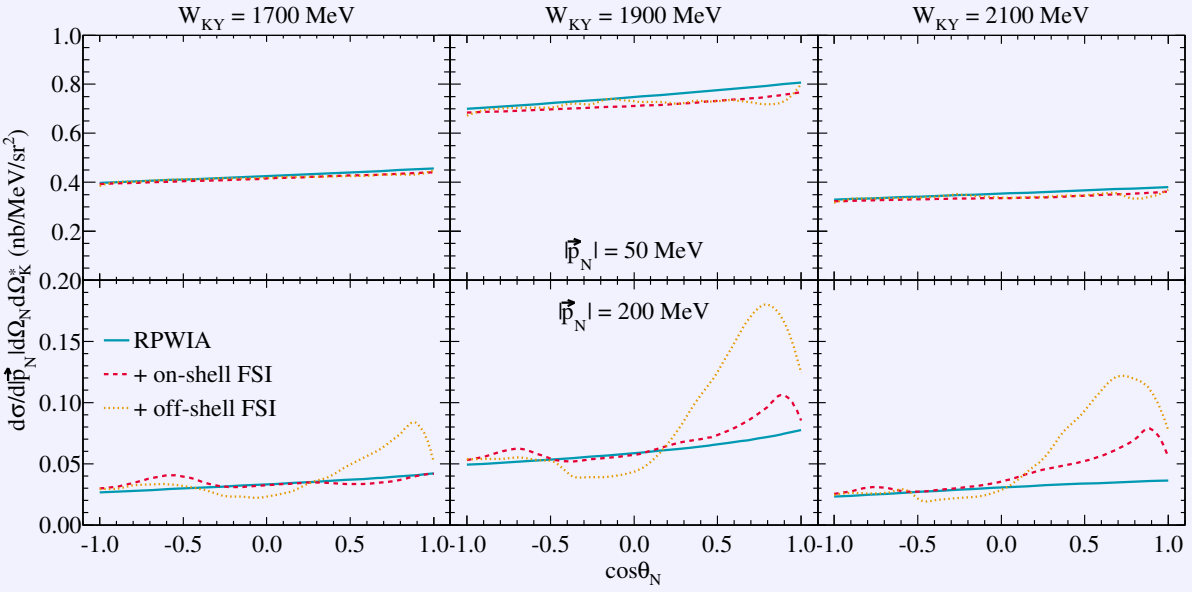

Figure 6.13 – The exclusive $^2\mathrm{H}(\gamma, K^+\Lambda)n$ differential cross section at three values of W_{KY} as a function of θ_N for forward, in plane, kaon scattering, i.e. $\theta_K^* = \phi_K^* = 0°$. The upper (lower) panels are obtained for a missing momentum $|\vec{p}_N| = 50$ (200) MeV. The solid curve corresponds to RPWIA calculations. The dashed and dotted results include the on-shell and off-shell YN-FSI contribution.

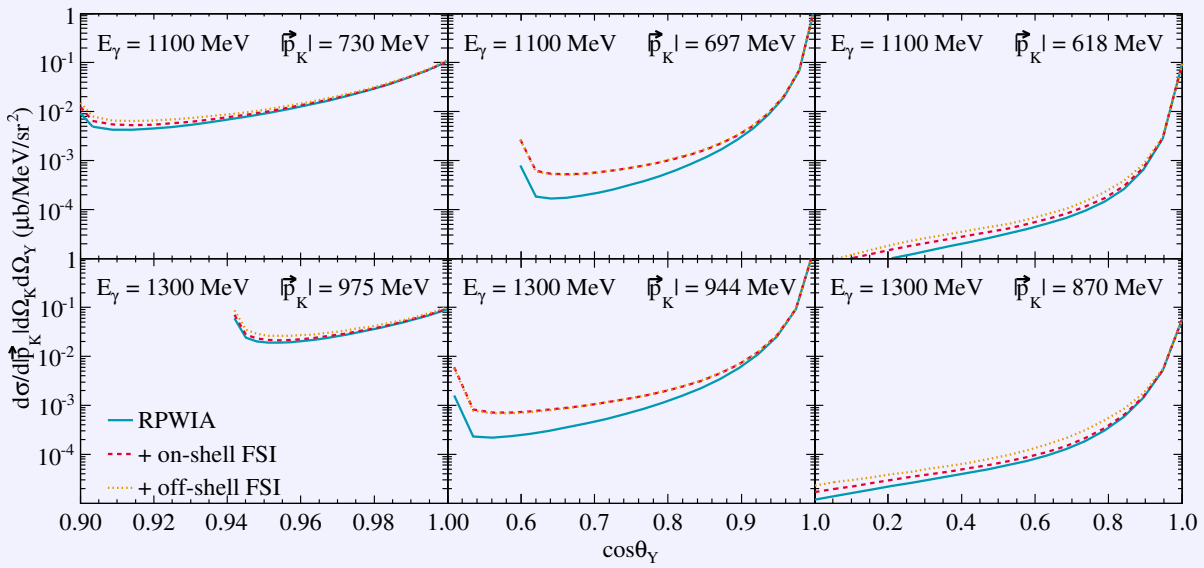

Figure 6.14 – The exclusive $^2\mathrm{H}(\gamma, K^+\Lambda)n$ differential cross section as a function of θ_Y for coplanar kinematics (ϕ_Y=0) at $\theta_K = 0°$. The top (bottom) row corresponds to a photon energy $E_\gamma = 1100$ (1300) MeV. The left panels are close to threshold, the middle panels correspond to quasi-free Λ production and the right panels are near the Σ-production threshold. The solid curve corresponds to RPWIA calculations. The dashed and dotted results include the on-shell and off-shell YN-FSI contribution.

role as the hyperon moves away from the z axis. Remarkably, the off-shell contribution to the YN-FSI amplitude is negligible. Finally, the panels on the right hand side present calculations a little beyond the Σ-production threshold. Both components of the YN-FSI amplitude contribute equally to the reaction strength. At extreme forward angles, however, the effects of YN-FSI are negligible.

The role of the YN-FSI contribution appears largest close to the threshold of a reaction channel. This observation is illustrated in Figure 6.15. It features the exclusive differential cross section at fixed values of W_{YN}. The cross section is given as a function of the kaon's LAB momentum. As $|\vec{p}_K|$ rises, the energy of the incoming photon grows and the maximum momentum in the figure is equivalent with a photon energy $E_\gamma \approx 1500\,\mathrm{MeV}$. The thresholds for the different kaon production channels are listed in Table 5.1. The results in the panel at the top are obtained at the $^2\mathrm{H}(\gamma, K^+\Lambda)n$ threshold. This leads to very small cross sections. The effect of the YN-FSI diagram is considerable and stems predominantly from the off-shell contribution. The calculations in the middle panel are a mere 5 MeV above threshold, yet the influence of YN-FSI has dwindled. The on-shell rescattering contribution overpowers the off-shell part. Away from threshold, the reaction's strength can be entirely attributed to the RPWIA diagram and the role of the hyperon-nucleon interaction is negligible.

From an experimental point of view, EM kaon production from the deuteron sets a challenge due to its small cross sections. Exclusive measurements are mandatory in order to extract information on the elementary kaon-production amplitude. Through (semi-)inclusive measurements, the statistics of an experiment can be significantly improved. This comes at the cost of losing sensitivity to higher-order effects, such as the hyperon-nucleon rescattering contribution. Note that our results including hyperon-nucleon rescattering have made it clear that the regions with the largest sensitivity to YN-FSI are marked by small cross sections. Therefore, the effects of the rescattering diagrams risk to be washed out when (partially) integrated observables are considered.

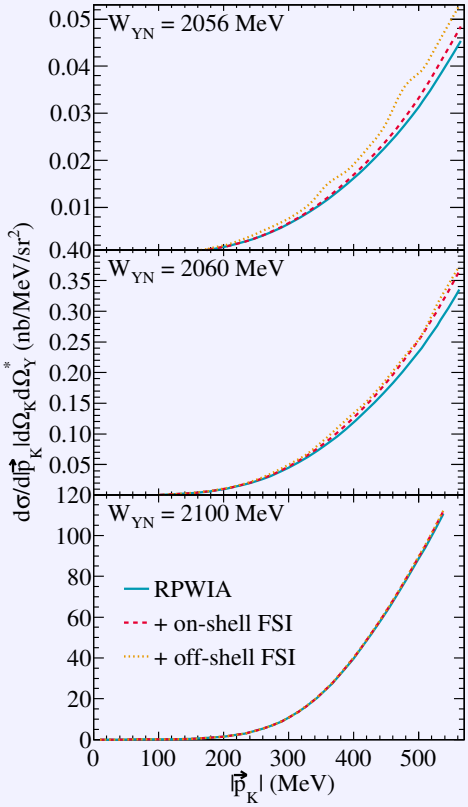

Figure 6.15 – The exclusive $^2\mathrm{H}(\gamma, K^+\Lambda)n$ differential cross section at $\theta_K = 0°$ and $\theta^*_Y = \phi^*_Y = 0°$ as a function of $|\vec{p}_K|$ at three different values of W_{YN}. The solid curve corresponds to RPWIA calculations. The dashed and dotted results include the on-shell and off-shell YN-FSI contribution.

One expects important contributions from YN-FSI when W_{YN} is close to the reaction threshold. For $^2\mathrm{H}(\gamma, K)YN$) observables, the invariant mass is given by

$$W^2_{YN} = \left(\boldsymbol{p}_\gamma + \boldsymbol{p}_D - \boldsymbol{p}_K\right)^2 = s_{tot} + m^2_K + 2m_D E_K + 2E_\gamma \left(E_K - |\vec{p}_K| \cos\theta_K\right) , \tag{6.6}$$

which implies W_{YN} reaches a minimum when $\theta_K \approx 0°$. Therefore, one anticipates the influence of YN-FSI to be largest when the kaon is produced along the beam direction. This is exemplified in Figure 6.16 where charged- and neutral-kaon production are shown at three representative photon-beam energies. The forward-peaked aspect of the cross section is prominent and for $\cos\theta_K \approx 1$, hyperon-nucleon rescattering leads to an enhancement. This effect is more pronounced at somewhat higher photon energies. For neutral-kaon production the heightening due to the YN-FSI diagram is less dramatic, because the cross section peaks near $\cos\theta_K \approx 0.9$.

In Figure 6.17, we zoom in on the charged-kaon production reaction. Kaon-momentum distributions are given at the same photon energies as in Figure 6.16 for $\cos\theta_K = 0.9$, 0.95 and 1. As discussed in Section 6.1, the shape of the differential cross section is mainly determined by the momentum distribution of the spectator nucleon in the RPWIA. At the lowest photon energy, one is close to the Σ-production threshold and the cross section only peaks when the condition for quasi-free Λ-production is fulfilled. At both other photon energies, the distribution is bimodal. The height of each quasi-elastic peak is determined by the strength of the underlying elementary kaon-production reaction and varies markedly as function of the photon energy and kaon scattering angle. Deviations from the RPWIA result are only noticeable when the kaon is produced along the photon three-

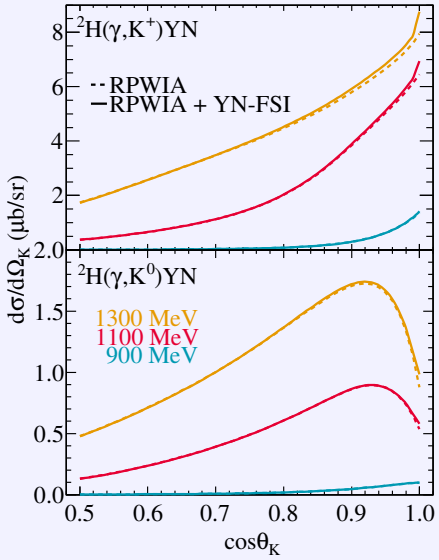

Figure 6.16 – The semi-inclusive differential cross section for charged-kaon (upper panel) and neutral-kaon (lower panel) photoproduction from the deuteron as a function of θ_K at three different photon energies. The dashed lines represent the RPWIA result. The solid lines also include the on-shell YN-FSI contribution.

momentum. The YN-FSI strengthen the cross section especially for higher photon-beam energies. The effect leads to enhancements up to 10 % in the quasi-elastic peaks. The global appearance of the cross section remains unaffected however.

6.3 Photoproduction data

To date, a limited amount of fully analysed experimental results are available to confront model calculations with. At Jefferson Lab, the CLAS collaboration has collected data during three run periods with a photon beam incident on a deuterium target. No data from the g2 experiment [207] have been made public so far. The g10 run period [206, 208] provided data for the elementary $n(\gamma, K^+)\Sigma^-$ reaction [151]. The RPR-model calculations are compared to these data in Figure 3.8. The g13 experiment [209] ran in 2006 – 2007. Preliminary results for the photon-beam asymmetry off bound protons [210] and polarisation observables in $K^0\Lambda$ and $K^0\Sigma^0$ production [153] have been presented. These analyses, however, are ongoing and have not been published yet.

To our knowledge, the only published $^2\mathrm{H}(\gamma, K)YN$ data set has been obtained at the Laboratory for Nuclear Science (LNS) at Tohoku University using the Neutral-Kaon Spectrometer (NKS) [211, 212]. The semi-inclusive neutral-kaon photoproduction cross section from deuterium was measured in two photon-energy bins close to threshold. The data are averaged over 100 MeV-wide energy bins and integrated over $0.9 < \cos\theta_K < 1$. The NKS spectrometer has since been upgraded to NKS2. In 2005 – 2006, new data has been collected with significantly higher count rates and an extended solid-angle coverage [213–215]. The NKS2 data comprises four angular bins in the forward hemisphere ($\Delta\cos\theta_K = 0.1$). In addition, semi-inclusive Λ-production cross sections have been extracted from the NKS2 data set. These data are presented as hyperon-momentum distributions in two angular bins in the forward hemisphere ($\Delta\cos\theta_Y = 0.05$) and a partial total cross section as function of the photon energy.

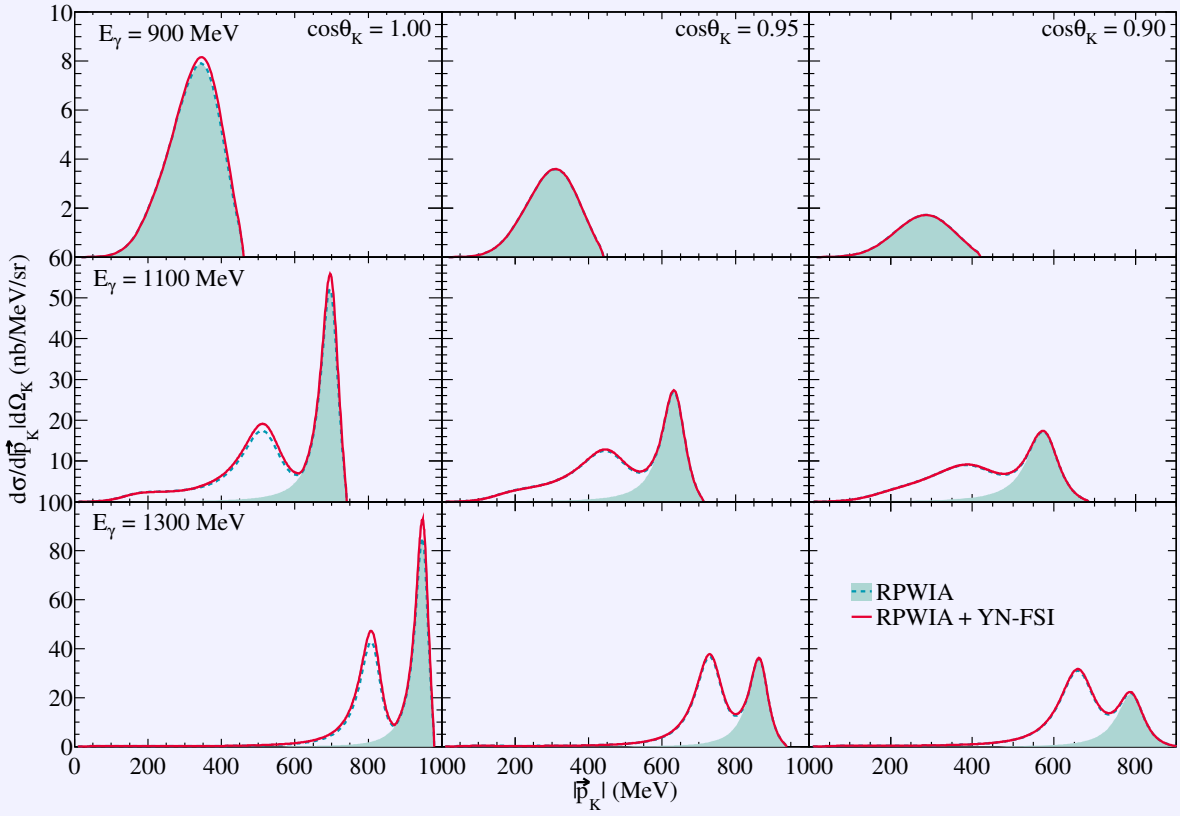

Figure 6.17 – The $^2\mathrm{H}(\gamma, K^+)YN$ differential cross section as function of the three-momentum of the outgoing kaon in the LAB frame. The results in the upper, middle and lower panels represent photon energies $E_\gamma = 900$, 1100 and 1300 MeV respectively. The results are obtained at three values for the kaon's scattering angle in the LAB (from left to right: $\cos\theta_K = 1$, 0.95 and 0.9). The dashed lines represent the RPWIA result with the shaded region indicating the contribution of the $^2\mathrm{H}(\gamma, K^+\Lambda)n$ channel. The full result, which includes the on-shell YN-FSI contribution, corresponds to the solid lines.

In Figures 6.18 and 6.19, our RPWIA results for neutral-kaon momentum distributions are compared to both the NKS and NKS2 data sets. The model calculations are performed at the centre of the photon-energy bin. As photon energies close to the Σ-production threshold are probed, the cross sections are predominantly uni-modal except in the highest energy bin at forward angles. The RPWIA predictions reproduce the shape of the data and the characteristic quasi-elastic peaks of semi-inclusive kaon production. At the lowest energy bin, the strength of the reaction is underpredicted by roughly a factor of two-to-three at all angles. Whereas the model calculations suggest the differential cross sections falls off when the angle between kaon and photon momentum grows, the LNS data in both angular bins have the same size. One notices that the resonant contributions to the elementary-production operator play an unsubstantial role. At $E_\gamma = 1050$ MeV, the size of the cross sections in the RPWIA is in line with the measurements and the reaction is still dominated by the Reggeized background. Yet, one notes that nucleon-resonance contributions are essential to reproduce the observed shoulder at $|\vec{p}_K| \approx 200$ MeV. These kinematics correspond to quasi-free Σ-production.

In Section 6.1, the error bars on experimental helicity amplitudes emerged as the chief source of theoretical uncertainties in our formalism. Because both elementary $K^0\Lambda$ and $K^0\Sigma^0$ production from the neutron contribute to the $^2\mathrm{H}(\gamma, K^0)YN$ cross section, one can expect a considerable impact. The shaded band in Figures 6.20 and 6.21 represents the range of cross sections obtained with

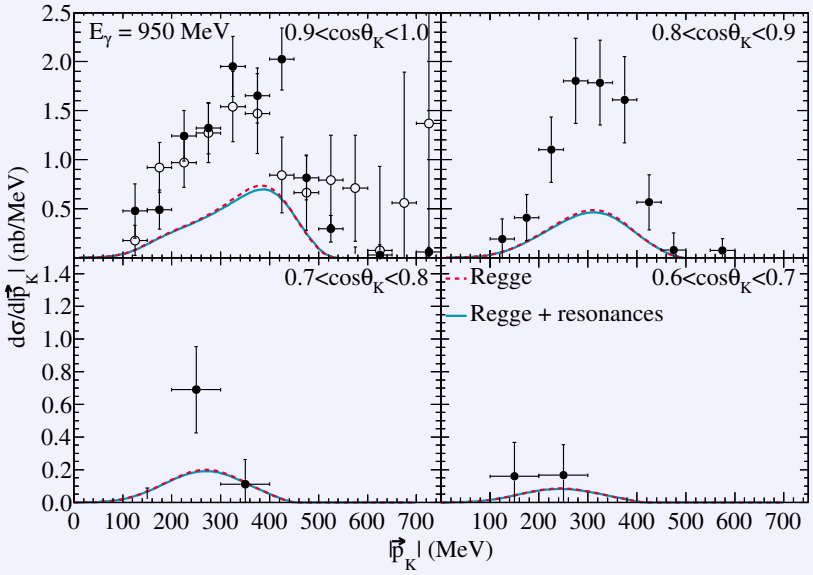

Figure 6.18 – The semi-inclusive $^2\mathrm{H}(\gamma, K^0)YN$ differential cross section as a function of the kaon momentum $|\vec{p}_K|$ integrated over four $\cos\theta_K$ bins. The data are from Refs. [211, 212] (○) and [215] (●), and are averaged over 900 MeV $< E_\gamma <$ 1000 MeV. The model results have been calculated at the bin centre $E_\gamma = 950$ MeV. The solid line shows the RPR model result in the RPWIA, whereas the dashed line singles out the contribution of the Reggeized background model.

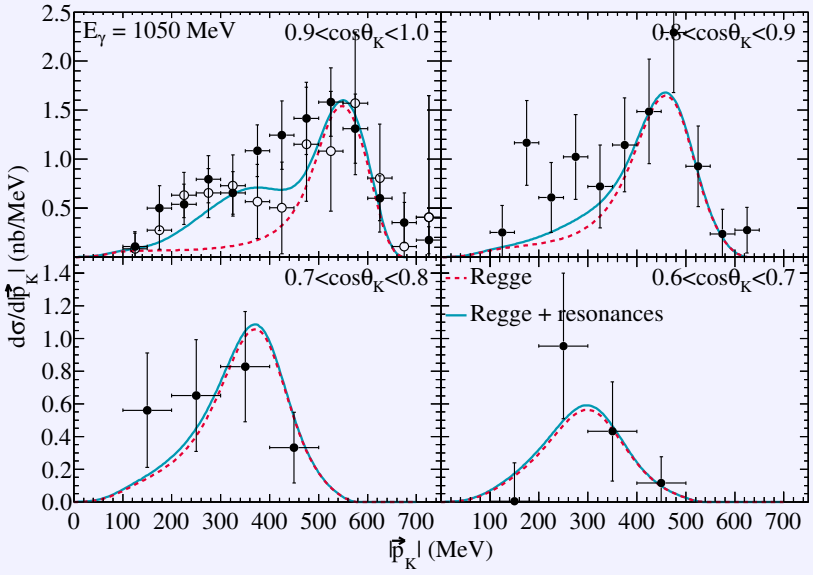

Figure 6.19 – As in Figure 6.18 for data averaged over 1000 MeV $< E_\gamma <$ 1100 MeV. The model results have been calculated at the bin centre $E_\gamma = 1050$ MeV.

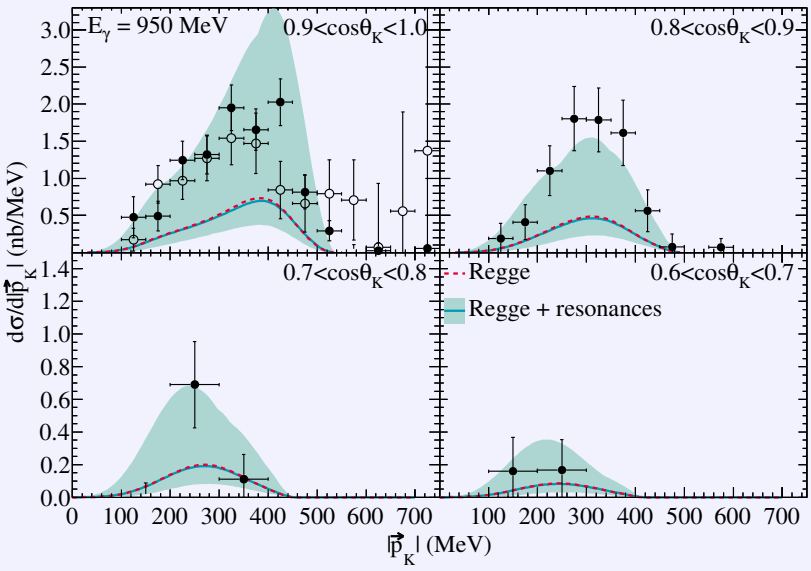

Figure 6.20 – The semi-inclusive $^2\mathrm{H}(\gamma, K^0)YN$ differential cross section as a function of the kaon momentum $|\vec{p}_K|$ integrated over four $\cos\theta_K$ bins. The data are from Refs. [211, 212] (○) and [215] (●), and are averaged over 900 MeV $< E_\gamma <$ 1000 MeV. The RPWIA results have been calculated at the bin centre $E_\gamma = 950$ MeV. The dashed curve indicates the Reggeized background model, whereas the full curve corresponds to the full RPR amplitude. The shaded area takes the uncertainties of the adopted helicity amplitudes into account.

the intervals of RPR-model coupling constants listed in Tables I.1 and I.2. The influence of the uncertainties is considerable. At $E_\gamma = 950$ MeV, where the RPR predictions do not agree with the data, the missing strength can be compensated by including the helicity-amplitude errors. One notices that the induced errors in the quasi-elastic Λ-production peak are large compared to those in the region of quasi-free Σ production. This can be understood if one considers the resonant content of the RPR model for Λ production. Two less-established resonances, i.e. $P_{13}(1900)$ and $D_{13}(1900)$, play a role and their photon-helicity couplings have not been determined experimentally. This forced us to introduce sizable estimates for the error bars on the ratios of their coupling constants. As such, our appraisal of the theoretical uncertainties is conservative and likely an overestimation.

The preliminary hyperon-momentum distributions for semi-inclusive Λ production are shown in Figure 6.22. These data have been obtained at two photon-energy bins (900 MeV $< E_\gamma <$ 1000 MeV and 1000 MeV $< E_\gamma <$ 1080 MeV) and are integrated over two angular bins in the forward-scattering hemisphere. The data are confronted with RPR model calculations using the RPWIA obtained for photon energies at the bin centre. The overall agreement between theory and experiment is good. The size and shape of the momentum distributions are nicely reproduced in both photon-energy bins. This is in contrast with the semi-inclusive kaon-production results at $E_\gamma = 950$ MeV presented in Figure 6.18, which underpredicted the data considerably. Charged-kaon production from the proton inside the deuteron accounts for the bulk of the cross section strength.

In Figure 6.23, a partial total $^2\mathrm{H}(\gamma, \Lambda)KN$ cross section is depicted over the full energy range of the LNS experiment. The data have been integrated over hyperon scattering angles in the range $0.9 \leq \cos\theta_Y \leq 1$. In the threshold region, where neutral-kaon production plays an insignificant role, the RPR model provides an excellent description of the NKS2 data. For $E_\gamma \gtrsim 950$ MeV, the relative contribution of the $^2\mathrm{H}(\gamma, K^0\Lambda)p$ channel builds up and the RPR predictions overshoot the data.

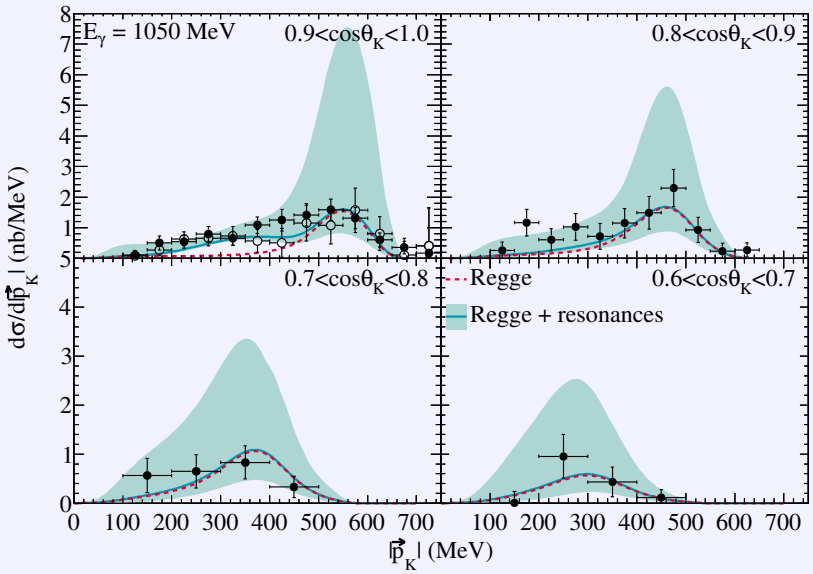

Figure 6.21 – As in Figure 6.20 for data averaged over 1000 MeV $< E_\gamma <$ 1100 MeV. The model results have been calculated at the bin centre $E_\gamma = 1050$ MeV.

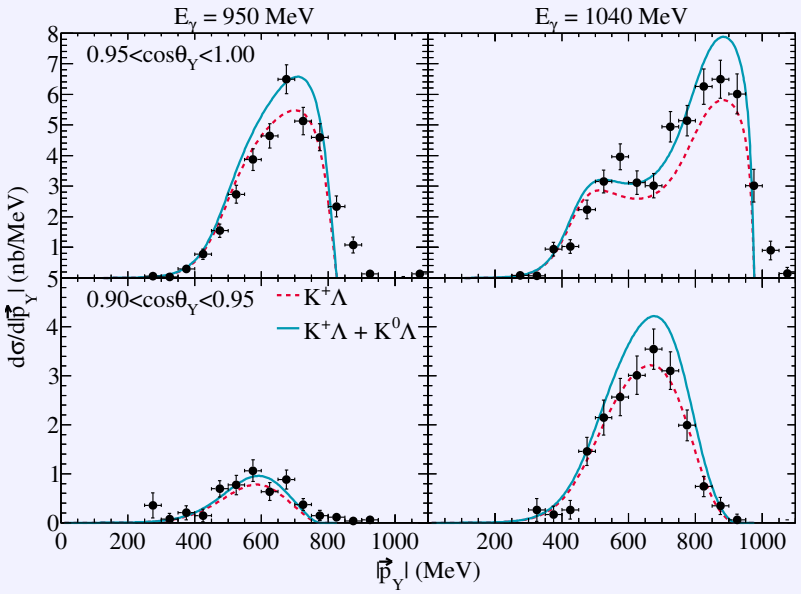

Figure 6.22 – The semi-inclusive ^{2}H$(\gamma,\Lambda)KN$ differential cross section as a function of the hyperon momentum $|\vec{p}_Y|$ integrated over two forward scattering-angle bins: $0.95 \leq \cos\theta_Y \leq 1$ (upper panels) and $0.9 \leq \cos\theta_Y \leq 0.95$ (lower panels). The data are from Ref. [215] and are averaged over $900 < E_\gamma$(MeV) $<$ 1000 (left panels) and $1000 < E_\gamma$(MeV) < 1080 (right panels). The theoretical results are calculated at the bin centres. The full line gives the RPWIA prediction using the RPR model, whereas the dashed line singles out the contribution of the ^{2}H$(\gamma, K^+\Lambda)n$ channel.

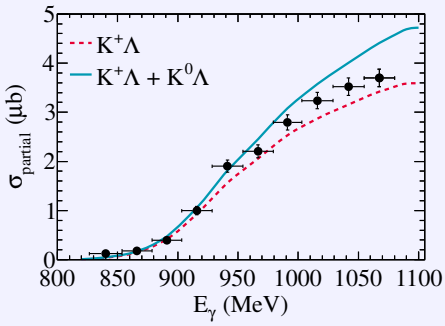

Figure 6.23 – The *total* $^2\mathrm{H}(\gamma,\Lambda)KN$ cross section for forward hyperon angles ($0.9 \leq \cos\theta_Y \leq 1$) as a function of the photon energy E_γ. The full line gives the RPWIA prediction using the RPR model, whereas the dashed line singles out the contribution of the $^2\mathrm{H}(\gamma,K^+\Lambda)n$ channel. Data are from Ref. [215].

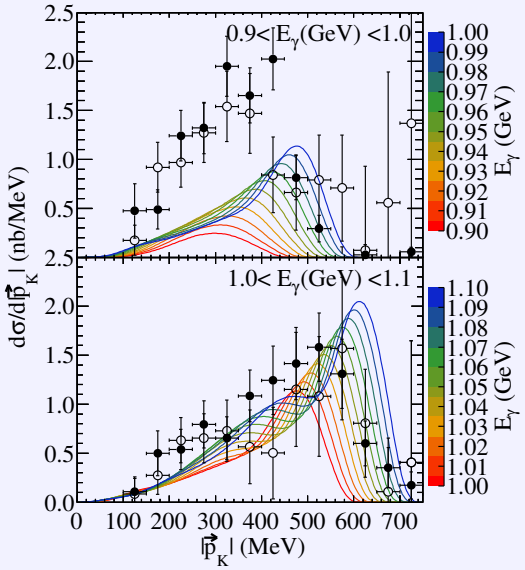

Figure 6.24 – The semi-inclusive $^2\mathrm{H}(\gamma,K^0)YN$ differential cross section as a function of the kaon momentum $|\vec{p}_K|$ integrated over forward scattering angles $0.9 < \cos\theta_K < 1$. The data are from Refs. [211, 212] (○) and [215] (●), and are averaged over two, 100 MeV-wide, photon-energy bins. The lines correspond to RPR calculations using the RPWIA performed in 10 MeV steps for 900 MeV $< E_\gamma <$ 1100 MeV.

So far, we have compared model predictions calculated at the centre of the photon-energy bins to the experimental results from LNS. These data are averaged over 100 MeV-wide bins. The energy range 900 MeV $\leq E_\gamma \leq$ 1100 MeV is near the kaon-production threshold. This implies that the shape of the cross section undergoes rapid changes. We illustrate this in Figure 6.24. Model calculations in the RPWIA are shown at the kinematics of the NKS data. The results are obtained over the full range of photon-beam energies in 10 MeV intervals. Within each energy bin, both the threshold value for the kaon momentum as well as the position of the quasi-elastic peak shift appreciably. Especially the onset of the Σ-production peak results in a non-linear evolution of the cross section. As a consequence, the effect of averaging substantially alters the aspect of the cross section and the data will be very sensitive to possible asymmetries in the detector's acceptance.

Bin-averaged and bin-centred RPWIA results are compared to the data in Figures 6.25 and 6.26. As anticipated, the averaging procedure smears the characteristic shape of the differential cross sections.

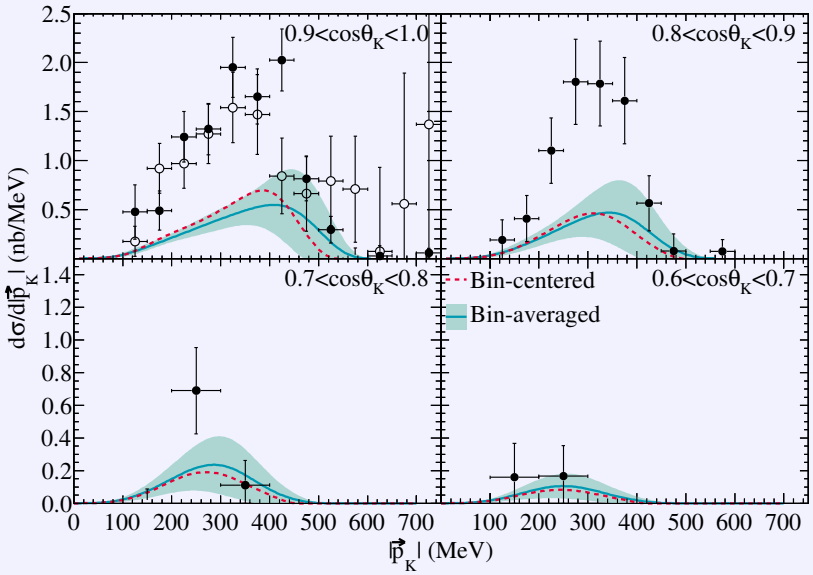

Figure 6.25 – The $|\vec{p}_K|$ dependence of the semi-inclusive $^2\mathrm{H}(\gamma, K^0)YN$ differential cross section integrated over four $\cos\theta_K$ bins. The data are from Refs. [211, 212] (○) and [215] (●), and are averaged over $900 < E_\gamma(\mathrm{MeV}) < 1000$. The results are obtained with the RPR model in the RPWIA. The dashed line shows calculations at the bin centre, whereas the full line and the shaded band indicate bin-averaged results with the corresponding averaging error.

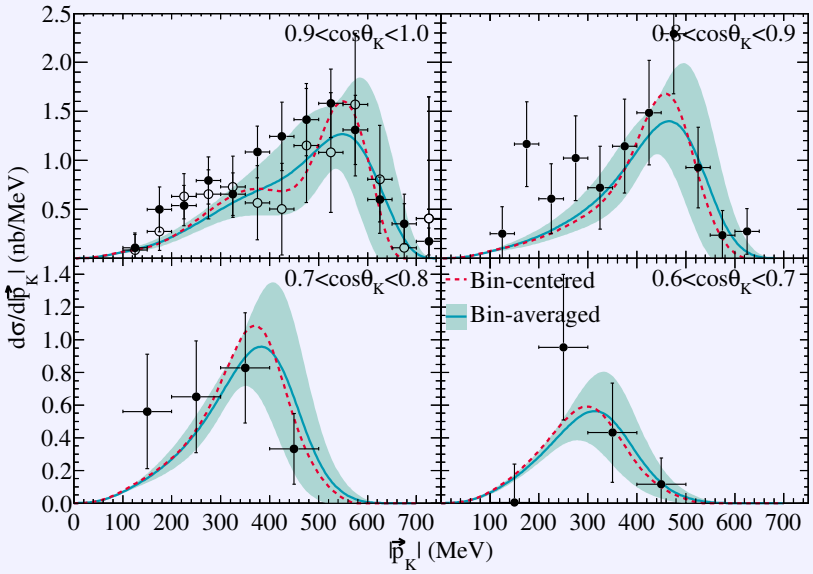

Figure 6.26 – As in Figure 6.25 for data averaged over $1000\,\mathrm{MeV} < E_\gamma < 1100\,\mathrm{MeV}$. The model results have been calculated at the bin centre $E_\gamma = 1050\,\mathrm{MeV}$.

Particularly at $E_\gamma = 1050\,\mathrm{MeV}$ and $0.9 \leq \cos\theta_K \leq 1.0$, the shoulder attributed to quasi-free Σ production is far less pronounced. At each value of $|\vec{p}_K|$, we have computed the standard deviation on the cross section. The latter are represented by the shaded area. The uncertainties related to bin averaging are appreciable and the relative effect can amount to 100%. This is similar in magnitude to the experimental error bars.

Finally, we consider the role of the YN-FSI diagram at the kinematics of the LNS experiment.

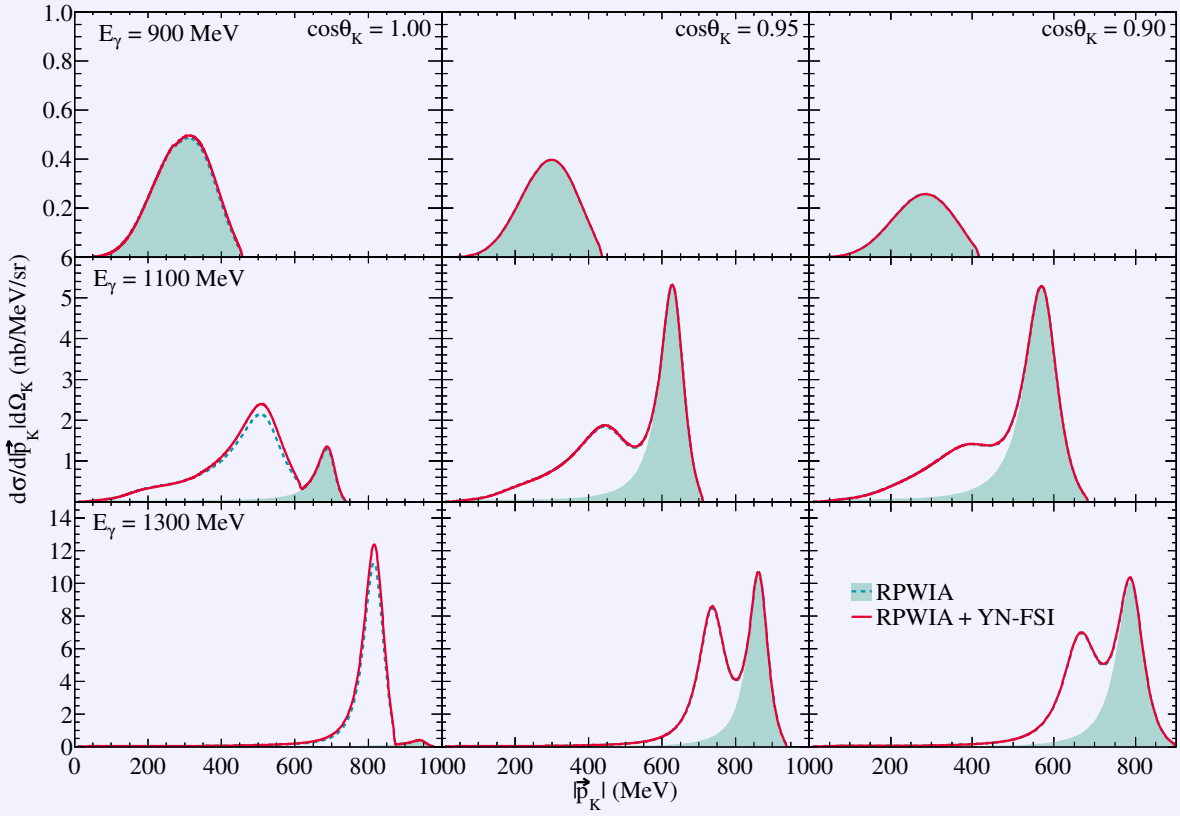

Figure 6.27 – The $^2\mathrm{H}(\gamma, K^0)YN$ differential cross section as a function of $|\vec{p}_K|$. The results in the upper, middle and lower panels represent photon energies $E_\gamma = 900$, 1100 and 1300 MeV respectively. The results are obtained at three values for $\cos\theta_K$ (from left to right: $\cos\theta_K = 1$, 0.95 and 0.9). The dashed lines represent the RPWIA result with the shaded region indicating the contribution of the $^2\mathrm{H}(\gamma, K^+\Lambda)n$ channel. The full result, which includes the on-shell YN-FSI contribution, corresponds to the solid lines.

In Figure 6.16, cross sections for neutral-kaon production are shown as a function of the kaon's scattering angle. The effect of the YN-FSI contribution is generally small and is most outspoken in a small angular range at extreme-forward angles. This is evident in Figure 6.27 which features the semi-inclusive cross section at forward angles. For $\cos\theta_K = 1$, the Σ peak dominates and YN-FSI effects result in an 25 % increase of the cross section. However, as soon as the kaon is no longer produced along the photon, Λ production has the upper hand and rescattering effects are minimal. Since the NKS and NKS2 data are integrated over angular bins that have a width of $\Delta\cos\theta_K = 0.1$, the overall YN-FSI contribution is unimportant. Our calculations point to an effect of at most 1–2 %.

6.4 Electroproduction data

Also for the $^2\mathrm{H}(e, e'K)YN$ reaction, few data are available. To our knowledge, a total of two data points have been published. These data have been obtained at Jefferson Lab's Hall-C [216] in a double-coincidence experiment. The incident-beam energy was fixed at 3245 MeV and scattered electrons where measured at an angle of 14.93°. The virtual photon has virtuality $Q^2 = 0.35\,\mathrm{GeV}^2$ and energy $E_\gamma = 1668$ MeV. Even though data was collected at different configurations for the kaon

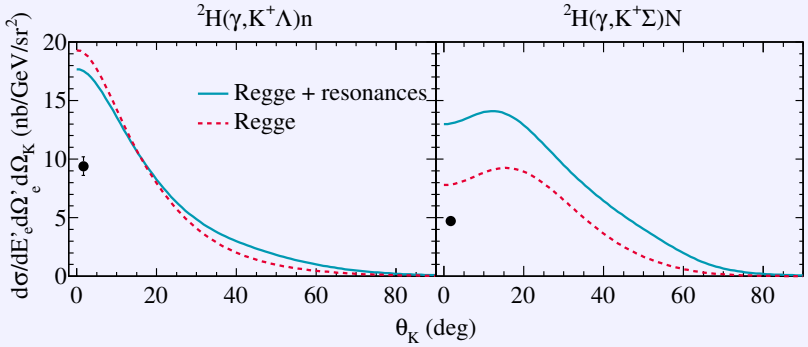

Figure 6.28 – Five-fold differential LAB cross sections for $^2\mathrm{H}(e,e'K^+\Lambda)n$ (left panel) and $^2\mathrm{H}(e,e'K^+\Sigma)N$ (right panel) as a function of θ_K. The incident-beam energy is fixed at 3245 MeV and the electron scatters at an angle 14.93°. The virtual photon has $Q^2 = 0.35\,\mathrm{GeV}^2$ and $E_\gamma = 1668\,\mathrm{MeV}$. The dashed curve shows the contribution of the Reggeized background, whereas the solid curve also includes the s-channel resonant contributions of the full RPR amplitude. Data from Ref. [216].

spectrometer, cross sections have only been published for a single value of the kaon scattering angle. These cross sections have been averaged over the azimuthal angle.

By fitting missing-mass distributions to data, Λ and Σ production have been separated. Owing to the small mass difference between the Σ^0 and Σ^- hyperons, only the total Σ strength could be determined via the missing-mass technique. Ref. [216] disentangles the Σ^0 and Σ^- contributions based on a dedicated phenomenological model developed in Ref. [217]. Inevitably, this introduces a critical model dependence in the published exclusive Σ-production results. Therefore we will only use the inclusive Σ-production cross sections.

In Figure 6.28, RPWIA predictions are confronted with the Hall-C data. The model calculations clearly overestimate the data. No experimental angular distributions have been published to verify the predicted θ_K-dependence of the cross section.

CHAPTER 7

Conclusions and outlook

Motivated by the desire to understand the structure of baryons in the confinement regime, the exploration of the nucleon's excitation spectrum has been a cornerstone of modern hadronic physics. Nucleon spectroscopy presents a unique opportunity to judge the validity of the constituent-quark paradigm. Pion-nucleon scattering is the conventional tool to chart the excited states of the nucleon. Yet strangeness production is highly complementary, because of its inherent sensitivity to the nucleon sea.

The Regge-plus-resonance formalism

The traditional approach to EM meson production is based on isobar models. For kaon production, however, one quickly runs into trouble because of the high threshold and the dominance of background terms. This calls for a description in terms of alternative degrees of freedom. Regge theory provides an efficient account of the reaction dynamics in the high-energy region, where partonic degrees of freedom dominate. We successfully model charged-kaon photoproduction at high energies through the exchange of $K^+(494)$ and $K^{*+}(892)$ Regge-trajectories. Extrapolating this amplitude into the resonance region, we find that it accounts for the general trends of the data. Applying the Regge model as a parametrisation of the troublesome background contributions, the coupling constants of the resonance-exchange diagrams can be determined independently. In this way, the analysis of the resonant and non-resonant content of strangeness production is effectively decoupled.

An RPR model including different resonance-exchange diagrams is optimised to the resonance-region data, while the three free parameters of the Regge model are held fixed. In the $K^+\Lambda$ channel, the set of established resonances found in the RPP turns out to be insufficient and a missing $D_{13}(1900)$ resonance is introduced. For $K^+\Sigma^0$ production, both established nucleon and Δ resonances are considered and a successful description of the data is achieved. Interestingly, in both $K^+\Lambda$ and $K^+\Sigma^0$ production, the two-star $P_{13}(1900)$ resonance emerges as a vital model ingredient. Since this state is not predicted by quark-diquark models, it represents strong evidence in favour of a picture

of the nucleon with three constituent quarks.

Using the most recent photo- and electroproduction data, the reliability of the RPR model can be evaluated. Some interesting extensions to the current RPR model are formulated. These aim at improving the description of the differential cross section at backward angles. In addition, it is also desirable to consider spin-5/2 resonances in the analysis of the resonant content of the reaction. The RPR framework has recently been updated in this direction and a re-analysis of the complete database is forthcoming. In spite of its limited number of adjustable parameters, the RPR-2007 model displays a remarkable ability to describe and predict the available $p(\gamma^{(*)}, K^+)\Lambda$ and $p(\gamma^{(*)}, K^+)\Sigma^0$ observables from threshold up to $E_\gamma = 16\,\text{GeV}$.

In order to gauge the predictive power of the RPR model, whose parameters are constrained by data obtained off proton targets, we extend the formalism to reactions with a neutron target or a neutral kaon in the final state. The conversion to neutron targets of kaon production models that include resonant diagrams requires knowledge of helicity amplitudes. Beyond the second resonance region, the latter are either unknown or poorly constrained by pion-production data. As a consequence, they put severe limits on the predictive power of both the RPR and isobar approaches. The Regge model, by contrast, offers an elegant and economical description of EM kaon production. Isospin symmetry suffices to anchor the neutron to the proton channel.

Applying the RPR formalism to neutral-kaon production fails to account for the available $p(\gamma, K^0)\Sigma^+$ data. Because the $K^0(494)$-exchange diagram does not contribute, a single trajectory remains in the Regge amplitude. We consider the option of adding an additional trajectory and identify the $K^*(1410)$-trajectory with a constant phase as the best solution. Since there are no data available at high energies to reliably anchor the parameters of this contribution, we opt for a more pragmatic approach. In the $N(\gamma, K^0)\Sigma$ channels, the EM coupling constant of the $K^*(892)$-exchange diagram is re-adjusted to the available data, resulting in a good description of the observables.

The usefulness of the RPR formalism is illustrated by considering K^- radiative capture in flight on the proton, which is related to kaon photoproduction through crossing symmetry. This reaction is ideally suited for studying the spectrum of excited hyperon states. Recently, the first differential-cross-section results for the $\gamma\Lambda$ and $\gamma\Sigma^0$ final states have been published. A theoretical analysis is performed with the RPR approach. The non-resonant contributions to the reaction amplitude can be parametrised by the Regge model that has been optimised against kaon-photoproduction data. Using the cross-section data, we explore the possible contributions of hyperon resonances listed in the RPP. The $\gamma\Sigma^0$ final state is dominated by hyperon-resonance exchange and hints at an important role for a resonance in the 1700 MeV mass region. In the $\gamma\Lambda$ final state, on the other hand, the non-resonant contributions account for half of the measured strength, and the data suggest the importance of a resonance in the mass region around 1550 MeV.

Strangeness production from the deuteron

In the final part of this work, we focus on EM strangeness production from the deuteron. By studying kaon production from this barely bound state of a proton and a neutron, one hopes to extract the elementary reaction from the neutron. To date, the strangeness-production database is heavily dominated by charged-kaon production from the proton. Measuring all six possible final states would in some sense constitute an *isospin-complete* experiment and would help constrain the

reaction dynamics.

We develop a covariant formalism for $^2\mathrm{H}(\gamma, KY)N$ based on the RIA using the RPR model as elementary-production operator. The leading contribution to the reaction amplitude stems from the RPWIA. The momentum distribution of the deuteron emerges as the dominant factor that dictates the angular and momentum dependence of the cross sections. Studied as a function of the momentum of the outgoing nucleon, one notices that the reaction strength falls off exponentially as the missing momentum increases and that the distribution is nearly isotropic. The semi-inclusive kaon-production cross section is dominated by those phase-space regions where the spectator nucleon is almost at rest.

We investigate the sensitivity of the computed cross sections to the various model ingredients. The details of the deuteron wave functions do not have a large impact on the final results, except at large missing momenta. A similar observation is made for the effect of off-shell extrapolations of the elementary-production operator. The variations induced by the poorly constrained helicity amplitudes, on the other hand, are large. We judge the extrapolation of the resonance information from proton to neutron targets to be the most important source of uncertainties.

Model predictions for semi-inclusive K^0 and Λ photoproduction are compared to experimental results obtained in the threshold region with the NKS and NKS2 spectrometers at LNS. Except at the lowest energy for $^2\mathrm{H}(\gamma, K^0)YN$, all predictions compare favourably to the data. The agreement of the RPR-model with the two published charged-kaon electroproduction data points is less satisfactory. The data is overpredicted by roughly a factor two to three. Additional measurements are clearly needed to further investigate the $^2\mathrm{H}(e, e'KY)N$ reaction.

The effectiveness of the deuteron as a neutron target is threatened by final-state interactions. We investigate the effect of a photoproduced hyperon which rescatters of the spectator nucleon. This contribution can be split up in an on-shell part, with all rescattering particles on mass shell, and an off-shell term. The latter involves a virtual hyperon and requires a computationally expensive principal-value integration. The effect of YN-FSI is important when the invariant mass of the hyperon-nucleon system is close to threshold. For semi-inclusive kaon production, rescattering contributes exclusively when the kaon is emitted along the direction of the incident photon. Since the YN-FSI-diagram is unimportant at low missing momenta, the quasi-free strangeness-production cross section can be effectively extracted when judicious cuts are applied on the momentum of the outgoing nucleon. Thus, the deuteron can be considered as a reliable effective neutron target.

From an alternative point of view, strangeness production from the deuteron can be thought of as a nuclear laboratory to study the hyperon-nucleon interaction. Such a program requires that one focuses on phase-space regions where YN-FSI dominate the reaction dynamics. Our model calculations indicate that this implies exclusive measurements at high missing momenta. The reliable extraction of information on the hyperon-nucleon force at these kinematics will however be challenging. At high missing momenta, the cross section is small and count rates will be low. Moreover, this region in phase space is most prone to theoretical uncertainties originating from the adopted deuteron wave function and the off-shell extrapolation of the elementary-production operator. Therefore, we conclude that in order to distill trustworthy information on the hyperon-nucleon interaction from strangeness-production data, the deuteron structure and the reaction dynamics need be investigated further.

Outlook

In this dissertation, we have studied strangeness production from the nucleon and the deuteron using the RPR formalism. This framework provides a unique approach to kaon production, and makes it possible to describe data in the resonance region with a small number of free parameters, while the correct high-energy limit is ensured. We have demonstrated the ability of the RPR formalism to predict results for strangeness production from the neutron, as well as neutral-kaon production. In the foreseeable future, new experimental information for the $N(\gamma, K^0)Y$ reaction channels will become available. These data will constitute an important test for the extensions to the RPR-model presented in Chapter 3.

For the transformation of the Regge-model amplitudes to neutral-kaon production reactions, we have made use of the limited database in the resonance region. The planned upgrade of the accelerator facility at Jefferson Lab offers the opportunity to measure strangeness production at photon energies well beyond the resonance region. These results would constitute invaluable input for the construction of more reliable Regge models, making it possible to constrain Regge-model amplitudes for all six strangeness final states in an energy region where resonant contributions have died out.

Our results for strangeness production from the deuteron rely chiefly on the elementary-production operator. In Section 2.4, we have anticipated a re-analysis of the current $N(\gamma, K)Y$ database in an upgraded RPR framework. This forthcoming model will mainly provide an improved account of the reaction mechanisms at backward angles. Applying this model in future deuteron calculations will lead to more reliable results.

Our primary motivation to study the ${}^2\mathrm{H}(\gamma, KY)N$ reaction stems from the prospect to extract information on quasi-free kaon-production from the neutron. Our YN-FSI results have provided evidence that the deuteron indeed constitutes a dependable neutron target. In order to further substantiate this claim, other possible rescattering contributions need to be considered. Especially the two-step process, where an intermediary pion is produced by the incoming photon, can play an important role, since the elementary pion-production cross section is nearly one order of magnitude larger than the kaon-production one. The two-step process can be calculated in an analogous way to the YN-FSI contribution, and requires models for the elementary pion-production operator and the $\pi N \to KY$ rescattering vertex. For the former, many reliable models that are constrained by a large database are available. Experimental information on the latter, on the other hand, is scant, and a successful evaluation of the two-step process will hinge on a reliable description of the $N(\pi, K)Y$ reaction.

APPENDIX A

Notations and conventions

If you obey all the rules, you miss all the fun.
— Katharine Hepburn

Throughout this document, we adopt the conventions used in the textbook of Gross [218]. Our conventions with regard to Lorentz transformations and rotations largely follow those of Leader's textbook on spin in particle physics [100]. For the benefit of a self-contained manuscript, our conventions and notations will be summarised in this appendix.

In this work, we assume *God-given* units [171], where

$$\hbar = c = 1\,. \tag{A.1}$$

In order to convert lengths and cross sections to SI units, the following conversion constants are useful [1]

$$\begin{aligned} \hbar c &= 197.3\ \text{MeV fm}\,, \\ (\hbar c)^2 &= 389.4\ \text{GeV}^2\ \mu\text{barn}\,. \end{aligned} \tag{A.2}$$

A.1 Four-vectors and tensors

A contravariant four-vector $\boldsymbol{x}$ is written as

$$x^\mu = (x^0, \vec{x}) = (x^0, x^i) = (x^0, x^1, x^2, x^3)\,, \tag{A.3}$$

where the Greek index μ runs from 0 to 3 and Roman indices run over spatial coordinates 1 to 3. The covariant four-vector is obtained by lowering the Lorentz index

$$x_\mu = g_{\mu\nu} x^\nu = (x^0, -\vec{x})\,. \tag{A.4}$$

In this expression, we tacitly assume summation over the duplicated indices and introduce the metric tensor

$$g_{\mu\nu} = g^{\mu\nu} = \begin{pmatrix} 1 & 0 & 0 & 0 \\ 0 & -1 & 0 & 0 \\ 0 & 0 & -1 & 0 \\ 0 & 0 & 0 & -1 \end{pmatrix} . \tag{A.5}$$

The symbol $\boldsymbol{p}$ is used to denote the energy-momentum four-vector. One has the Einstein relation for free particles

$$\boldsymbol{p}^2 = \boldsymbol{p} \cdot \boldsymbol{p} = p_\mu p^\mu = g_{\mu\nu} p^\mu p^\nu = (p^0)^2 - |\vec{p}|^2 = m^2 \geq 0 \,, \tag{A.6}$$

where m is the rest mass.

The totally antisymmetric tensor is defined according to

$$\epsilon^{\alpha\beta\gamma\delta} = \begin{cases} +1 & \text{for even permutations of (0,1,2,3)} \,, \\ -1 & \text{for odd permutations of (0,1,2,3)} \,, \\ 0 & \text{for repeated indices} \,. \end{cases} \tag{A.7}$$

A.2 Rotations and Lorentz transformations

Conventionally, transformations are considered either from the *active* or *passive* point of view. Here, we adopt a different convention. A transformation t denotes the *physical operation* of the transformation on the object on which it acts. The notation $t\boldsymbol{p}$ implies that $\boldsymbol{p}$ is physically boosted and/or rotated. In literature, this action corresponds to the *active* point of view. The transformation t of the axes of a reference frame $\mathcal{O}$ is referred to as $t\mathcal{O}$.

A rotation is completely specified by three real parameters. In this document we will adopt two different descriptions:

- in terms of Euler angles α, β and γ the rotation $r(\alpha, \beta, \gamma)$ is performed by successive rotations through angle γ ($0 \leq \alpha < 2\pi$) about the z axis, angle β ($0 \leq \beta \leq \pi$) about the y axis and finally angle α ($0 \leq \gamma < 2\pi$) about the z axis. Denoting by $r_i(\theta)$ ($i = x, y, z$) a rotation through angle θ about the i axis, we have

$$r(\alpha, \beta, \gamma) = r_z(\alpha) r_y(\beta) r_z(\gamma) \,. \tag{A.8}$$

- as a single rotation through the angle ω ($0 \leq \omega \leq \pi$) about the unit axis $\hat{\vec{n}}$ defined by the polar and azimuthal angles θ and ϕ. We use the notation $r(\omega; \theta, \phi)$ or $r(\vec{\omega})$ with $\vec{\omega} = \omega \hat{\vec{n}}$.

An arbitrary Lorentz boost $l(\vec{\beta})$ is equivalently fixed by three real parameters: the boost speed $|\vec{\beta}|$ and the azimuthal and polar angles of the boost direction $\hat{\vec{\beta}} \equiv \vec{\beta}/|\vec{\beta}|$. For a boost with velocity v along the x, y or z axis, we adopt the notation: $l_i(v)$ ($i = x, y, z$).

Any physical Lorentz transformation t can be decomposed as a rotation $r(\vec{\omega})$ followed by a pure Lorentz boost $l(\vec{\beta})$. For such a Lorentz transformation acting on a four-vector, we adopt the following standard notation

$$(t\boldsymbol{p})^\mu = [\Lambda(t)]^\mu{}_\nu \, p^\nu \,, \tag{A.9}$$

having

$$\Lambda(t) \equiv \Lambda(l(\vec{\beta}))\Lambda(r(\vec{\omega})) = \begin{pmatrix} \gamma & \gamma\beta_x & \gamma\beta_y & \gamma\beta_z \\ \gamma\beta_x & 1+\alpha\beta_x^2 & \alpha\beta_x\beta_y & \alpha\beta_x\beta_z \\ \gamma\beta_y & \alpha\beta_y\beta_x & 1+\alpha\beta_y^2 & \alpha\beta_y\beta_z \\ \gamma\beta_z & \alpha\beta_z\beta_x & \alpha\beta_z\beta_y & 1+\alpha\beta_z^2 \end{pmatrix} \begin{pmatrix} 1 & 0 & 0 & 0 \\ 0 & & & \\ 0 & & R_{ij} & \\ 0 & & & \end{pmatrix}, \tag{A.10}$$

where

$$\begin{aligned} \gamma &= \frac{1}{\sqrt{1-|\vec{\beta}|^2}}\,, \\ \alpha &= \frac{\gamma^2}{\gamma+1}\,, \end{aligned} \tag{A.11}$$

and

$$R_{ij} = \cos\omega\delta_{ij} + (1-\cos\omega)\hat{\vec{\omega}}_i\hat{\vec{\omega}}_j - \sin\omega\epsilon_{ijk}\hat{\vec{\omega}}_k\,, \tag{A.12}$$

with $i,j = 1,2,3$.

A Lorentz transformation t acting on the Dirac indices of spinors is denoted by $S(t)$. For a rotation $r(\vec{\omega})$, we have explicitly

$$S(r(\vec{\omega})) = \cos\frac{\omega}{2} - i\sin\frac{\omega}{2}\hat{\vec{\omega}}_i\gamma^5\gamma^0\gamma^i\,. \tag{A.13}$$

The representation of a boost $l(\vec{\beta})$ is given by

$$S(l(\vec{\beta})) = \cosh\frac{\xi}{2} + \sinh\frac{\xi}{2}\hat{\vec{\beta}}_i\gamma^0\gamma^i\,, \tag{A.14}$$

with ξ the rapidity and

$$\begin{aligned} \cosh\xi &= \frac{1}{\sqrt{1-|\vec{\beta}|^2}}\,, \\ \cosh\frac{\xi}{2} &= \sqrt{\frac{\cosh\xi+1}{2}}\,, \\ \sinh\frac{\xi}{2} &= \sqrt{\frac{\cosh\xi-1}{2}}\,. \end{aligned} \tag{A.15}$$

Finally, we introduce the Wigner rotation matrices $\mathfrak{D}^J(r)$ as the unitary $(2J+1)$-dimensional representation matrices of the rotation r. They obey the following property

$$\left[\mathfrak{D}^J_{mm'}(r)\right]^* = (-1)^{m-m'}\mathfrak{D}^J_{-m,-m'}(r)\,. \tag{A.16}$$

Describing the rotation in terms of Euler angles, the Wigner matrices are given by

$$\mathfrak{D}^J_{mm'}(\alpha,\beta,\gamma) = e^{-im\alpha}d^J_{mm'}(\beta)e^{-im'\gamma}\,, \tag{A.17}$$

where the non-trivial part is contained in the real-valued d-functions. The latter enjoy several symmetry properties

$$d^J_{mm'}(\beta) = d^J_{-m',-m}(\beta) = (-1)^{m-m'}d^J_{m'm}(\beta) = (-1)^{J+m}d^J_{m,-m'}(\pi-\beta) = d^J_{m'm}(-\beta)\,. \tag{A.18}$$

The d-functions used in this work are

$$\begin{aligned} d^{1/2}_{1/2,1/2}(\beta) &= \cos\frac{\beta}{2}\,, \\ d^{1/2}_{1/2,-1/2}(\beta) &= -\sin\frac{\beta}{2}\,, \\ d^{1}_{11}(\beta) &= \frac{1+\cos\beta}{2}\,, \\ d^{1}_{10}(\beta) &= -\frac{\sin\beta}{\sqrt{2}}\,, \\ d^{1}_{00}(\beta) &= \cos\beta\,. \end{aligned} \tag{A.19}$$

The Wigner rotation matrices for rotations in the representation $r(\vec{\omega})$ or $r(\omega;\theta,\phi)$ are defined as

$$\mathfrak{D}^{J}_{mm'}(\vec{\omega}) = \mathfrak{D}^{J}_{mm'}(\omega;\theta,\phi) = \langle Jm|\, e^{-i\vec{\omega}\cdot\hat{\vec{J}}}\,|Jm'\rangle\,, \tag{A.20}$$

with $\hat{\vec{J}} \equiv (\hat{J}_x, \hat{J}_y, \hat{J}_z)$ the angular momentum operators, which are the generators of rotations. The Wigner matrix for $J = 1/2$ is given by [219]

$$\mathfrak{D}^{1/2}(\omega;\theta,\phi) = \begin{pmatrix} \cos\frac{\omega}{2} - i\sin\frac{\omega}{2}\cos\theta & -\sin\frac{\omega}{2}\sin\theta e^{i\left(\phi+\frac{\pi}{2}\right)} \\ -\sin\frac{\omega}{2}\sin\theta e^{-i\left(\phi+\frac{\pi}{2}\right)} & \cos\frac{\omega}{2} + i\sin\frac{\omega}{2}\cos\theta \end{pmatrix}. \tag{A.21}$$

A.3 Pauli and Dirac matrices

The Pauli sigma matrices are given by

$$\sigma^1 = \begin{pmatrix} 0 & 1 \\ 1 & 0 \end{pmatrix} \quad , \quad \sigma^2 = \begin{pmatrix} 0 & -i \\ i & 0 \end{pmatrix} \quad , \quad \sigma^3 = \begin{pmatrix} 1 & 0 \\ 0 & -1 \end{pmatrix}, \tag{A.22}$$

and obey the relation

$$\sigma^i\sigma^j = i\epsilon_{ijk}\sigma^k\,, \tag{A.23}$$

where we have introduced the antisymmetric tensor

$$\epsilon_{123} = \epsilon_{231} = \epsilon_{312} = 1 \quad \text{and} \quad \epsilon_{jik} = -\epsilon_{ijk}\,. \tag{A.24}$$

The Pauli matrices fulfil the following commutation and anticommutation relations

$$\begin{aligned} [\sigma^i, \sigma^j] &= 2i\epsilon_{ijk}\sigma^k\,, \\ \{\sigma^i, \sigma^j\} &= 2\delta_{ij}\,. \end{aligned} \tag{A.25}$$

Dirac or gamma matrices are defined as the set of $n \times n$ matrices γ^μ that generate the Clifford algebra defined by the anticommutation relation

$$\{\gamma^\mu, \gamma^\nu\} \equiv \gamma^\mu\gamma^\nu + \gamma^\nu\gamma^\mu = 2g^{\mu\nu} \times \mathbb{1}_n\,, \tag{A.26}$$

with $\mathbb{1}_n$ the n-dimensional unity matrix. In four-dimensional Minkowski space, several representations of the Dirac matrices exist. We adopt the *Dirac* representation which, in terms of Pauli matrices, gives

$$\gamma^0 = \begin{pmatrix} \mathbb{1}_2 & 0 \\ 0 & -\mathbb{1}_2 \end{pmatrix} \quad \text{and} \quad \gamma^i = \begin{pmatrix} 0 & \sigma^i \\ -\sigma^i & 0 \end{pmatrix}, \tag{A.27}$$

for $i = 1, 2, 3$. Several interesting matrices can be constructed from these γ matrices. We define the traceless product

$$\gamma^5 = i\gamma^0\gamma^1\gamma^2\gamma^3\,, \tag{A.28}$$

the traceless antisymmetric combination

$$\sigma^{\mu\nu} = \frac{i}{2}[\gamma^\mu, \gamma^\nu]\,, \tag{A.29}$$

and the charge conjugation matrix

$$\mathcal{C} = -i\gamma^0\gamma^2\,. \tag{A.30}$$

A.4 Dirac spinors

The positive- and negative-energy four-component spinors $u(\vec{p}; m_s)$ and $v(\vec{p}; m_s)$ of an on-mass-shell particle with four-momentum $\boldsymbol{p} = (E_p, \vec{p})$ and mass $m = \sqrt{p^\mu p_\mu}$ are solutions to the Dirac equation

$$0 = \left(\not{\boldsymbol{p}} - m\right) u(\vec{p}; m_s) = \left(\not{\boldsymbol{p}} + m\right) v(\vec{p}; m_s)\,, \tag{A.31}$$

where we have adopted Feynman's notation

$$\not{\boldsymbol{A}} \equiv A_\mu \gamma^\mu\,. \tag{A.32}$$

Defining the conjugate spinor $\overline{u}(\vec{p}; m_s) \equiv u^\dagger(\vec{p}; m_s)\gamma^0$, and imposing the normalisations

$$\overline{u}(\vec{p}; m_s)u(\vec{p}; m'_s) = 2m\delta_{m_s m'_s} \quad , \quad \overline{v}(\vec{p}; m_s)v(\vec{p}; m'_s) = -2m\delta_{m_s m'_s}\,, \tag{A.33}$$

the spinors read

$$\begin{aligned} u(\vec{p}; m_s) &= \sqrt{E_p + m}\begin{pmatrix} \mathbb{1}_2 \\ \frac{\vec{\sigma}\cdot\vec{p}}{E_p+m} \end{pmatrix}\chi_{m_s}\,, \\ v(\vec{p}; m_s) &= \sqrt{E_p + m}\begin{pmatrix} \frac{\vec{\sigma}\cdot\vec{p}}{E_p+m} \\ \mathbb{1}_2 \end{pmatrix}\eta_{m_s}\,. \end{aligned} \tag{A.34}$$

The two-component spinors χ_{m_s} and η_{m_s} are orthogonal and normalised so that

$$\chi^\dagger_{m_s}\chi_{m'_s} = \eta^\dagger_{m_s}\eta_{m'_s} = \delta_{m_s m'_s}\,. \tag{A.35}$$

Associating m_s with the physical spin component of the fermion along the z axis, one can adopt the following representation

$$\chi_{+1/2}(\theta = 0, \phi = 0) = \begin{pmatrix} 1 \\ 0 \end{pmatrix} \quad , \quad \chi_{-1/2}(\theta = 0, \phi = 0) = \begin{pmatrix} 0 \\ 1 \end{pmatrix}\,. \tag{A.36}$$

A spinor $u(\vec{p}; m_s, \theta, \phi)$ with spin-projection m_s along an axis fixed by (θ, ϕ), can be obtained by rotating the spinor $u(\vec{p}; m'_s) \equiv u(\vec{p}; m'_s, 0, 0)$ with the Wigner matrices defined in (A.17), i.e.

$$u(\vec{p}; m_s, \theta, \phi) = \mathfrak{D}^{1/2}_{m'_s m_s}(\phi, \theta, -\phi)u(\vec{p}; m'_s)\,. \tag{A.37}$$

Explicitly, the two-component spinors are given by

$$\chi_{+1/2}(\theta,\phi) = \begin{pmatrix} \cos\frac{\theta}{2} \\ e^{i\phi}\sin\frac{\theta}{2} \end{pmatrix} \quad , \quad \chi_{-1/2}(\theta,\phi) = \begin{pmatrix} -e^{-i\phi}\sin\frac{\theta}{2} \\ \cos\frac{\theta}{2} \end{pmatrix} . \tag{A.38}$$

The two-component spinors for particle and antiparticle states are related to each other up to an arbitrary phase. We define the following phase convention

$$\eta_{m_s} = \chi_{-m_s} . \tag{A.39}$$

The u and v spinors are then related by charge conjugation as follows

$$C\overline{v}^T(\vec{p};m_s) = (2m_s)\, u(\vec{p};m_s) \quad , \quad C\overline{u}^T(\vec{p};m_s) = (2m_s)\, v(\vec{p};m_s) . \tag{A.40}$$

One can define projection operators for positive- and negative-energy states as

$$\begin{aligned} \Lambda_+(\vec{p}) &= \not{\boldsymbol{p}} + m , \\ \Lambda_-(\vec{p}) &= m - \not{\boldsymbol{p}} , \end{aligned} \tag{A.41}$$

or in terms of spinor components

$$\begin{aligned} [\Lambda_+(\vec{p})]_{ab} &= \sum_{m_s} u_a(\vec{p};m_s)\overline{u}_b(\vec{p};m_s) , \\ [\Lambda_-(\vec{p})]_{ab} &= -\sum_{m_s} v_a(\vec{p};m_s)\overline{v}_b(\vec{p};m_s) . \end{aligned} \tag{A.42}$$

This allows one to write the completeness relation

$$[\Lambda_+(\vec{p}) + \Lambda_-(\vec{p})]_{ab} = 2m\,\delta_{ab} . \tag{A.43}$$

Finally, the propagator of a Dirac particle of mass m and four-momentum $\boldsymbol{p}$ is given by

$$G_{\frac{1}{2}}(\boldsymbol{p},m) = \frac{\not{\boldsymbol{p}} + m}{\boldsymbol{p}^2 - m^2 + i\epsilon} , \tag{A.44}$$

and has the following useful decomposition

$$G_{\frac{1}{2}}(\boldsymbol{p},m) = \frac{1}{2E_p}\left(\frac{\Lambda_+(\vec{p})}{p^0 - E_p + i\epsilon} - \frac{\Lambda_-(-\vec{p})}{p^0 + E_p - i\epsilon}\right) , \tag{A.45}$$

with $E_p = \sqrt{|\vec{p}|^2 + m^2}$.

APPENDIX B

Biquaternions

And here there dawned on me the notion that we must admit,in some sense,
a fourth dimension of space for the purpose of calculating with triples...
An electric circuit seemed to close, and a spark flashed forth.
— W. R. Hamilton

It is well known that an arbitrary complex number has a unique representation on the two-dimensional plane. By virtue of Euler's formula, one has

$$x + iy = r\cos\phi + ir\sin\phi = re^{i\phi}\,, \tag{B.1}$$

where r and ϕ are the modulus and phase respectively. Since $e^{i\phi}e^{i\phi'} = e^{i(\phi+\phi')}$, we see intuitively that complex numbers with unit norm form a representation of the rotation group in two dimensions, denoted by O(2).

The number system of quaternions $\mathbb{H}$ was introduced by W. R. Hamilton in 1843 in an attempt to extend the concept of complex numbers to three dimensions. A set of three numbers turned out to be insufficient to form an algebra. The breakthrough occurred when Hamilton decided to abandon the commutative law of multiplications. He introduced two additional *imaginary* units j and k, obeying the rules

$$i^2 = j^2 = k^2 = ijk = -1\,. \tag{B.2}$$

A quaternion Q is represented by

$$Q \equiv q_0 + iq_1 + jq_2 + kq_3\,, \tag{B.3}$$

with q_0, q_1, q_2 and q_3 real numbers. Later, Hamilton extended the notion of quaternions by allowing the four components to be complex numbers. He dubbed these objects biquaternions.

It is not our intention to give a extensive review on biquaternions and their role in number theory and physics. We will restrict ourselves to providing their definition and some of their basic properties in Section B.1. In this thesis, biquaternions will prove to be a useful alternate representation of the Lorentz group. To this end, the relevant formulae connecting biquaterions to rotations and Lorentz boosts will be presented in Section B.2

B.1 Definition

We adopt a number of different notations for a biquaternion Q

$$Q \equiv \sum_{i=0}^{3} q_i \mathsf{e}_i \equiv (q_0, q_1, q_2, q_3) \equiv (q_0, \vec{q}) \,, \tag{B.4}$$

where $q_i \in \mathbb{C}$. The imaginary units of the biquaternions are denoted by e_i $(i = 1, 2, 3)$ and their multiplication is defined as

$$\mathsf{e}_i \mathsf{e}_j = -\delta_{ij} \mathsf{e}_0 + \epsilon_{ijk} \mathsf{e}_k \,, \tag{B.5}$$

for $i, j = 1, 2, 3$. Here, we have defined $\mathsf{e}_0 = 1$.

Biquaternions are added, subtracted and multiplied with scalars according to the usual laws of arithmetic. Due to the property (B.5) of the imaginary units, they obey the following non-commutative multiplication law

$$QQ' = (q_0 q'_0 - \vec{q} \cdot \vec{q}', q_0 \vec{q}' + q'_0 \vec{q} + \vec{q} \times \vec{q}') \,, \tag{B.6}$$

with $(\square \cdot \square)$ and $(\square \times \square)$ the usual scalar and vector product of three-vectors.

We define biquaternion conjugation

$$\overline{Q} = (q_0, -\vec{q}) \,, \tag{B.7}$$

as well as complex conjugation

$$Q^* = (q_0^*, \vec{q}^*) \,. \tag{B.8}$$

In addition, hermitian conjugation is defined by

$$Q^\dagger = \overline{Q^*} \,. \tag{B.9}$$

In general, the norm $\mathcal{N}(Q)$ of a biquaternion is a complex number

$$\mathcal{N}(Q) = Q\overline{Q} = \overline{Q}Q = q_0^2 + q_1^2 + q_2^2 + q_3^2 \,, \tag{B.10}$$

and obeys the rule

$$\mathcal{N}(QQ') = \mathcal{N}(Q)\mathcal{N}(Q') \,. \tag{B.11}$$

For biquaternions of non-zero norm, one can define an inverse

$$Q^{-1} = \frac{1}{\mathcal{N}(Q)} \overline{Q} \,. \tag{B.12}$$

B.2 Representation of the Lorentz group

In a biquaternion representation, a four-vector $\boldsymbol{p}$ reads

$$Q(\boldsymbol{p}) = (p^0, i\vec{p}) \,, \tag{B.13}$$

in which case the norm of the biquaternion is equal to the four-vector's length

$$\mathcal{N}(Q(\boldsymbol{p})) = \boldsymbol{p}^2 \,. \tag{B.14}$$

The biquaternion representation of a general Lorentz transformation t acting on a four-vector is defined by

$$Q(t\boldsymbol{p}) = Q(t)Q(\boldsymbol{p})Q(t)^{\dagger}\,. \tag{B.15}$$

It is easily shown that the four-vector's length is invariant as long as $\mathcal{N}(Q(t)) = 1$. Therefore, biquaternions of unit norm form a representation of the Lorentz group. Multiple Lorentz transformations can be chained by multiplying them from the left.

A boost in the direction $\hat{\vec{\beta}}$ with rapidity ξ (see Eq. (A.15)) is represented as

$$Q(l(\vec{\beta})) = (\cosh\frac{\xi}{2}, i\hat{\vec{\beta}}\sinh\frac{\xi}{2})\,, \tag{B.16}$$

whereas a rotation through the angle $|\vec{\omega}|$ about the unit axis $\hat{\vec{\omega}}$ can be accomplished by the following operator

$$Q(r(\vec{\omega})) = (\cos\frac{\omega}{2}, \hat{\vec{\omega}}\sin\frac{\omega}{2})\,. \tag{B.17}$$

Remark that the biquaternion representation of a rotation is expressed in terms of half of the rotation angle ω. This is an important observation with regard to the rotation of (helicity) spinors, a subject that we will discuss in Section C.2. Clearly, two distinct quaternions represent the same rotation. This is reminiscent of the group SU(2) being a surjective homomorphism with regard to the rotation group SO(3). Indeed, quaternions of unit norm are isomorphic to the group SU(2).

Finally, we wish to point out a useful feature of the biquaternion representation of the Lorentz group. A Lorentz transformation t can always be decomposed as a rotation r that is followed by a Lorentz boost l. Given the matrix representation (A.10) of a Lorentz transformation, it is difficult to uniquely determine r and l. Starting from the biquaternion representation $Q(t)$, however, a straightforward recipe exists. Defining two quaternions $\Re\left[Q(t)\right]$ and $\Im\left[Q(t)\right]$ as the real and imaginary part of $Q(t)$, i.e.

$$\begin{aligned}\Re\left[Q(t)\right] &= \sum_{i=0}^{3}\Re[Q(t)_i]\mathsf{e}_i\,,\\ \Im\left[Q(t)\right] &= \sum_{i=0}^{3}\Im[Q(t)_i]\mathsf{e}_i\,,\end{aligned} \tag{B.18}$$

we have

$$\begin{aligned}Q(r) &= \frac{1}{\mu}\Re\left[Q(t)\right]\,,\\ Q(l) &= (\mu, -i\frac{1}{\mu}\Re\left[Q(t)\right]\overline{\Im\left[Q(t)\right]})\,,\end{aligned} \tag{B.19}$$

with

$$\mu = \sqrt{\Re\left[Q(t)\right]\overline{\Re\left[Q(t)\right]}}\,. \tag{B.20}$$

APPENDIX C

Helicity spinors

In Section A.4, we have introduced the four-component Dirac-spinor solutions $u(\vec{p}; m_s, \theta, \phi)$ and $v(\vec{p}; m_s, \theta, \phi)$ to the free Dirac equation. In this representation, the spin quantisation axis needs to be specified in a particular frame, and since this axis is a three-vector, it cannot be readily transformed to another frame. Suppose the state of a particle with momentum $\boldsymbol{p}$ is given by $u(\vec{p}; m_s)$ in the frame $\mathcal{O}$. Say that we wish to express this state in a different frame $\mathcal{O}' = l^{-1}\mathcal{O}$. With the spinor representation of Section A.4, one finds $u(l\vec{p}; m_s')$. However, it remains absolutely unclear what the corresponding spin projection m_s' is in $\mathcal{O}'$. The helicity formalism, which we will introduce hereafter, provides an elegant solution to this problem.

C.1 Definition

Our discussion of helicity states applies to particles as well as antiparticles. For this reason, we introduce the notation

$$|\boldsymbol{p}; m_s, \theta, \phi\rangle \ , \tag{C.1}$$

to describe the state of a (anti)particle with four-momentum $\boldsymbol{p}$ and spin projection m_s along an axis fixed by the polar angle θ and azimuthal angle ϕ. For each particle of mass m and three-momentum $\vec{p}$ in some frame $\mathcal{O}$, we can define a so-called helicity transformation,

$$h(\vec{p}) = r(\phi_p, \theta_p, 0) l_z(v) \, , \tag{C.2}$$

where θ_p and ϕ_p are the polar and azimuthal angle of the three-momentum $\vec{p}$ respectively, and

$$v = \frac{|\vec{p}|}{\sqrt{|\vec{p}|^2 + m^2}} \, . \tag{C.3}$$

This helicity transformation allows to associate a helicity rest-frame

$$\mathcal{O}_{\boldsymbol{p}} = h(\vec{p})\mathcal{O} \, , \tag{C.4}$$

with each particle. In its helicity rest-frame, a particle is at rest

$$h^{-1}(\vec{p})\boldsymbol{p} = \mathring{\boldsymbol{p}} \equiv (m, \vec{0})\,. \tag{C.5}$$

Using the helicity transformation, we define the helicity state $|\boldsymbol{p}, \lambda\rangle$ for a particle with four-momentum $\boldsymbol{p}$ in some frame $\mathcal{O}$ as

$$|\boldsymbol{p}, \lambda\rangle = S(h(\vec{p}))\,|\mathring{\boldsymbol{p}}; \lambda\rangle\ , \tag{C.6}$$

Thus, λ can be regarded as the z-component of the particle's spin in its helicity rest-frame $\mathcal{O}_{\boldsymbol{p}}$. Moreover, the state $|\boldsymbol{p}, \lambda\rangle$ is an eigenstate of the helicity operator, i.e.

$$\frac{\hat{\vec{J}} \cdot \hat{\vec{p}}}{|\vec{p}|}\,|\boldsymbol{p}, \lambda\rangle = \lambda\,|\boldsymbol{p}, \lambda\rangle\ , \tag{C.7}$$

where $\hat{\vec{J}}$ is the total angular momentum operator.

Before proceeding, a word of caution is in order. Our definition (C.6) for helicity states differs from those in the seminal paper of Jacob and Wick [220] in two respects. First, they employ a more complex rotation in their expression for the helicity transformation. In addition, a distinction is made between the states for different particles based on their role in a reaction, e.g. beam or target. In accordance with Ref. [100], we have chosen to treat all particles on an equal footing. These differences in conventions result in different phases for our helicity states.

Adhering to our choices for Dirac matrices and antiparticle two-component spinors described in Appendix A, the helicity spinors for particles of mass m with three-momentum $\vec{p}$ are given explicitly by

$$\begin{aligned} u(\vec{p}, \lambda = \pm\frac{1}{2}) &= \frac{1}{\sqrt{E_p + m}} \begin{pmatrix} E_p + m \\ 2\lambda|\vec{p}| \end{pmatrix} \xi_\lambda(\theta_p, \phi_p)\,, \\ v(\vec{p}, \lambda = \pm\frac{1}{2}) &= \frac{1}{\sqrt{E_p + m}} \begin{pmatrix} -2\lambda|\vec{p}| \\ E_p + m \end{pmatrix} \xi_{-\lambda}(\theta_p, \phi_p)\,, \end{aligned} \tag{C.8}$$

where θ_p and ϕ_p are the polar and azimuthal angle of the three-momentum $\vec{p}$ respectively. The two-component spinors read

$$\xi_{+1/2}(\theta_p, \phi_p) = \begin{pmatrix} e^{-i\phi_p/2}\cos\theta_p/2 \\ e^{i\phi_p/2}\sin\theta_p/2 \end{pmatrix} \quad , \quad \xi_{-1/2}(\theta_p, \phi_p) = \begin{pmatrix} -e^{-i\phi_p/2}\sin\theta_p/2 \\ e^{i\phi_p/2}\cos\theta_p/2 \end{pmatrix}\,. \tag{C.9}$$

C.2 Lorentz transformations

Suppose a particle with momentum $\boldsymbol{p}$ and helicity λ is described in some frame $\mathcal{O}$ by the state $|\boldsymbol{p}, \lambda\rangle$. Let $\mathcal{O}' = t^{-1}\mathcal{O}$ be a second reference frame obtained by carrying out a physical Lorentz transformation t^{-1}. The momentum for the particle in this new frame is $\boldsymbol{p}' = t\boldsymbol{p}$ and we can express the state as

$$|\boldsymbol{p}, \lambda\rangle_{\mathcal{O}'} = S(t)\,|\boldsymbol{p}, \lambda\rangle\ . \tag{C.10}$$

Invoking our definition for helicity states (C.6) and inserting the unit operator $\mathbb{1} = h(\vec{p}')h^{-1}(\vec{p}')$, we find

$$|\boldsymbol{p}, \lambda\rangle_{\mathcal{O}'} = S(h(\vec{p}'))S(r(t, \vec{p}))\,|\mathring{\boldsymbol{p}}; \lambda\rangle\ , \tag{C.11}$$

where we have introduced the transformation

$$r(t,\vec{p}) = h^{-1}(\vec{p}\,')\, t\, h(\vec{p})\,, \tag{C.12}$$

commonly referred to as the Wick helicity rotation. As its name suggests this transformation always represents a rotation, irrespective of the transformation t. One easily sees that $r(t,\vec{p})$ is the rotation that connects the two helicity rest-frames $\mathcal{O}_{\boldsymbol{p}}$ and $\mathcal{O}_{\boldsymbol{p}'}$, i.e.

$$\mathcal{O}_{\boldsymbol{p}} = r(t,\vec{p})\mathcal{O}_{\boldsymbol{p}'}\,. \tag{C.13}$$

Using the Wigner rotation matrices defined in Section A.2, one can directly apply the Wick rotation in Eq. (C.11). We find

$$|\boldsymbol{p},\lambda\rangle_{\mathcal{O}'} = S(h(\vec{p}\,'))\mathfrak{D}^{1/2}_{\lambda'\lambda}(r(t,\vec{p}))\,|\mathring{\boldsymbol{p}};\lambda\rangle\ . \tag{C.14}$$

As the $\mathfrak{D}^{1/2}_{\lambda'\lambda}$ are scalars, the helicity transformation can act directly on the state on the right-hand side. Using the definition for helicity states, we obtain our final, elegant result

$$|\boldsymbol{p},\lambda\rangle_{\mathcal{O}'} = \mathfrak{D}^{1/2}_{\lambda'\lambda}(r(t,\vec{p}))\,\big|\boldsymbol{p}',\lambda'\big\rangle\ . \tag{C.15}$$

This proves that it is straightforward to express helicity states with a helicity defined in a particular frame in any other frame. It suffices to work out the Wick rotation (C.12) for the Lorentz transformation connecting both frames and to compute the appropriate elements of the Wigner rotation matrix. The biquaternion representation of the Lorentz group, introduced in Appendix B, is particularly well suited to address this issue. By virtue of Eq. (B.19), one can easily extract the axis of rotation and rotation angle. In addition, the unit-norm quaternions are isomorphic to the group SU(2). It is well known that spinors only transform up to a sign under the rotation group SO(3). The isomorphism to SU(2), in conjunction with the expression (A.21) for the Wigner matrices as a function of $\omega/2$, allows one to correctly transform the helicity spinors.

APPENDIX D

Feynman rules

If I could explain it to the average person,
I wouldn't have been worth the Nobel Prize.
— Richard Feynman

This appendix summarises the rules and other ingredients needed to compute cross sections and decay rates. First, the formulae for the observables are given in terms of the transition amplitude. In the next section, we review the rules needed to construct these transition amplitudes from given Feynman diagrams. For the description of the elementary kaon-production reaction, we adopt an effective field-theoretical description in this work. Section D.3 lists the relevant Lagrangians and propagators which are required to calculate $N(\gamma^*, K)Y$ transition amplitudes.

D.1 Cross sections and decay rates

When the transition amplitude $\mathcal{T}$ for the scattering process $A + B \to 1 + 2 + \ldots n$ is known, the differential cross section is given by

$$d\sigma = \frac{1}{|\vec{v}_A - \vec{v}_B|} \frac{1}{2E_A 2E_B} \overline{\sum} |\mathcal{T}|^2 \left(\prod_{i=1}^{n} \frac{d^3\vec{p}_i}{2E_i(2\pi)^3} \right) (2\pi)^4 \delta^{(4)}(\boldsymbol{p}_A + \boldsymbol{p}_B - \sum_{i=1}^{n} \boldsymbol{p}_i) \,, \tag{D.1}$$

where $\vec{v}_i = \frac{\vec{p}_i}{E_i}$ are the velocities of the incident particles. With $\overline{\sum}$ we denote summing (averaging) over final- (initial-) states.

The differential decay rate for a particle of mass m at rest reads

$$d\Gamma = \frac{1}{2m} \overline{\sum} |\mathcal{T}|^2 \left(\prod_{i=1}^{n} \frac{d^3\vec{p}_i}{2E_i(2\pi)^3} \right) (2\pi)^4 \delta^{(4)}(\boldsymbol{p} - \sum_{i=1}^{n} \boldsymbol{p}_i) \,. \tag{D.2}$$

D.2 Transition amplitude

The Lorentz-invariant transition amplitude $\mathcal{T}$ is a sum of a comprehensive and adequate set of Feynman diagrams. Each diagram is translated to a numerical value by following a strict set of rules:

- Each amplitude requires a factor of i.
- At each interaction vertex an appropriate operator is to be inserted. Each vertex implies an energy-momentum conserving delta function.
- Each internal line is to be substituted by a propagator.
- Incoming and outgoing lines should be replaced by the free fields which they represent.
- Internal four-momenta $\boldsymbol{p}$ that are not fixed by energy-momentum conservation are integrated over as follows

$$\int \frac{d^4\boldsymbol{p}}{(2\pi)^4}\,.$$

- Every closed fermion loop results in an additional minus-sign.

The precise form of the propagators and the operators at the interaction vertices is the subject of the next section.

D.3 Effective fields and interactions

In order to translate the Feynman diagrams to transition amplitudes, expressions for propagators and interaction vertices are required. The latter are derived from an interaction Lagrangian applying a set of rules:

- Gradient operators acting on an incoming (outgoing) field Ψ ($\Psi^\dagger$) with four-momentum $\boldsymbol{p}$ are substituted as follows

$$\begin{aligned} \partial_\mu \Psi &\to -ip_\mu \Psi\,, \\ \partial_\mu \Psi^\dagger &\to ip_\mu \Psi^\dagger\,. \end{aligned} \tag{D.3}$$

- The Lagrangian is multiplied with the imaginary unit i.
- All external fields are removed, revealing the bare interaction vertex.

D.3.1 Propagators

Internal lines representing a spin-0, spin-1/2, spin-1 or spin-3/2 particle with four-momentum $\boldsymbol{p}$, mass m and width Γ are replaced with the following propagators,

$$\begin{aligned} G_0(\boldsymbol{p}) &= \frac{1}{\boldsymbol{p}^2 - m^2 + im\Gamma}\,, \\ G_{\frac{1}{2}}(\boldsymbol{p}) &= \frac{\not{\boldsymbol{p}} + m}{\boldsymbol{p}^2 - m^2 + im\Gamma}\,, \\ G_1^{\mu\nu}(\boldsymbol{p}) &= \frac{1}{\boldsymbol{p}^2 - m^2 + im\Gamma}\left(-g^{\mu\nu} + \frac{p^\mu p^\nu}{m^2}\right)\,, \\ G_{\frac{3}{2}}^{\mu\nu}(\boldsymbol{p}) &= \frac{1}{\boldsymbol{p}^2 - m^2 + im\Gamma}\left(g^{\mu\nu} - \frac{1}{3}\gamma^\mu\gamma^\nu - \frac{2p^\mu p^\nu}{3m^2} - \frac{\gamma^\mu p^\nu - \gamma^\nu p^\mu}{3m}\right)\,. \end{aligned} \tag{D.4}$$

D.3.2 Effective Lagrangians

In this paragraph, we list our choices with regard to the interaction Lagrangians relevant to this work. In case of electroproduction, the photon field is virtual and a form factor should be inserted at every EM coupling constant.

For the photon field A^μ and vector-meson field V^μ, we define an antisymmetric tensor

$$\begin{aligned} F^{\mu\nu} &= \partial^\nu A^\mu - \partial^\mu A^\nu\,, \\ V^{\mu\nu} &= \partial^\nu V^\mu - \partial^\mu V^\nu\,. \end{aligned} \tag{D.5}$$

For convenience of notation, two functions are introduced that take a different value depending on the parity of the exchanged particle

$$\begin{aligned} \Gamma &= \begin{cases} 1 & (P=-1) \\ \gamma^5 & (P=+1) \end{cases}\,, \\ \Gamma' &= \begin{cases} \gamma^5 & (P=-1) \\ 1 & (P=+1) \end{cases}\,. \end{aligned} \tag{D.6}$$

Born terms The EM interaction Lagrangian for a photon field A^μ coupling to a ground state nucleon N, kaon K or hyperon Y is given by

$$\mathcal{L}_{\gamma NN} = -e\overline{N}\gamma_\mu N A^\mu + \frac{e\kappa_N}{4m_p}\overline{N}\sigma_{\mu\nu}NF^{\mu\nu}\,, \tag{D.7}$$

$$\mathcal{L}_{\gamma KK} = -ie\left(K^\dagger\partial_\mu K - K\partial_\mu K^\dagger\right)A^\mu\,, \tag{D.8}$$

$$\mathcal{L}_{\gamma YY} = -e\overline{Y}\gamma_\mu Y A^\mu + \frac{e\kappa_Y}{4m_p}\overline{Y}\sigma_{\mu\nu}YF^{\mu\nu}\,, \tag{D.9}$$

When the kaon is neutral, the photon doesn't couple to it. For neutral nucleons and hyperons, the first term in Eqs. (D.7) and (D.9) vanishes.

For the strong KYN-vertex, a pseudoscalar coupling is adopted

$$\mathcal{L}_{KYN} = -ig_{KYN}K^\dagger\overline{Y}\gamma_5 N + h.c.\,. \tag{D.10}$$

Vector-meson exchange For the EM interaction Lagrangian of the γKK^*-vertex, we make a distinction between positive-parity vector mesons

$$\mathcal{L}_{\gamma KK_1} = i\frac{e\kappa_{K_1K}}{M}\left(\partial_\mu A_\nu \partial^\mu V^\nu - \partial_\mu A_\nu \partial^\nu V^\mu\right) K \,. \tag{D.11}$$

and negative-parity vector mesons

$$\mathcal{L}_{\gamma KK^*} = \frac{e\kappa_{K^*K}}{4M}\epsilon^{\mu\nu\lambda\sigma} F_{\mu\nu} V_{\lambda\sigma} K + h.c. \,, \tag{D.12}$$

Conventionally, the normalisation is fixed at $M = 1\,\mathrm{GeV}$.

In the strong-interaction vertex one has

$$\mathcal{L}_{K^*YN} = -g^v_{K^*_{YN}}\overline{Y}\Gamma_\mu N V^\mu + \frac{g^t_{K^*_{YN}}}{2\left(m_\Lambda + m_p\right)}\overline{Y}\sigma_{\mu\nu}V^{\mu\nu}\Gamma N + h.c. \,. \tag{D.13}$$

Spin-1/2 resonance exchange The EM interaction Lagrangian for spin-1/2 resonances reads

$$\mathcal{L}_{\gamma NN^*} = \frac{e\kappa_{N^*N}}{4m_p}\overline{R}\Gamma'\sigma_{\mu\nu}NF^{\mu\nu} + h.c. \,. \tag{D.14}$$

At the strong vertex, the interaction Lagrangian is given by

$$\mathcal{L}_{KYN^*} = -ig_{KYN^*}K^\dagger\overline{Y}\Gamma R + h.c. \,. \tag{D.15}$$

Spin-3/2 resonance exchange The EM interaction of a spin-3/2 resonance, described by a Rarita-Schwinger field R^μ, is given by the following effective Lagrangian

$$\mathcal{L}_{\gamma pN^*} = i\frac{e\kappa^{(1)}_{N^*N}}{2m_p}\overline{R}^\mu\theta_{\mu\nu}\left(Y\right)\Gamma\gamma_\lambda N F^{\lambda\nu} - \frac{e\kappa^{(2)}_{N^*N}}{4m_p^2}\overline{R}^\mu\theta_{\mu\nu}\left(X\right)\Gamma\left(\partial_\lambda N\right)F^{\nu\lambda} + h.c. \,. \tag{D.16}$$

At the strong-interaction we take

$$\mathcal{L}_{KYN^*} = \frac{g_{KYN^*}}{M_{K^+}}\overline{R}^\mu\theta_{\mu\nu}\left(Z\right)\Gamma' Y\left(\partial^\nu K\right) + h.c. \,. \tag{D.17}$$

In both the EM- and strong-interaction vertices, the tensor

$$\theta_{\mu\nu}(z) = g_{\mu\nu} - \left(z + \frac{1}{2}\right)\gamma_\mu\gamma_\nu \,, \tag{D.18}$$

features. The coupling constant z is called an *off-shell* parameter.

D.3.3 $N(\gamma, K)Y$ transition amplitudes

After having introduced our choice of effective interaction Lagrangians, we now list the formulae for the different contributions to the transition amplitude for kaon photoproduction. The relevant Feynman diagrams are drawn in Figure 1.2. In Chapters 2 and 3, a RPR-model optimised to the available photoproduction data is presented. The fitted coupling constants of this model are tabulated in Appendix I.

Born s-channel

$$\mathcal{T}_{\text{Born-}s} = e g_{KYN} \overline{u}_Y \gamma_5 \frac{\not{p}_\gamma + \not{p}_N + m_N}{s_{KY} - m_N^2} \left(\gamma^\mu + \frac{\kappa_N}{2m_N} i\sigma^{\mu\nu} k_\nu \right) u_N \varepsilon_\mu \,. \tag{D.19}$$

Born t-channel

$$\mathcal{T}_{\text{Born-}t} = e g_{KYN} \overline{u}_Y \left(2p_K^\mu - p_\gamma^\mu \right) \frac{1}{t - m_K^2} \gamma_5 u_N \varepsilon_\mu \,. \tag{D.20}$$

Born u-channel

$$\mathcal{T}_{\text{Born-}u} = e g_{KYN} \overline{u}_Y \left(\gamma^\mu + \frac{\kappa_Y}{2m_N} i\sigma^{\mu\nu} k_\nu \right) \frac{\not{p}_Y - \not{p}_\gamma + m_Y}{u - m_Y^2} \gamma_5 u_N \varepsilon_\mu \,. \tag{D.21}$$

Positive-parity vector-meson exchange

$$\begin{aligned} \mathcal{T}_{K_1} =& \frac{e}{M} \overline{u}_Y \left[p_\gamma^\lambda \left(p_K^\mu - p_\gamma^\mu \right) - g^{\mu\lambda} \boldsymbol{p}_\gamma \cdot \left(\boldsymbol{p}_K - \boldsymbol{p}_\gamma \right) \right] \frac{1}{t - m_{K_1}^2 + i m_{K_1} \Gamma_{K_1}} \\ & \times \left[G_{K_1}^v \gamma_\lambda + \frac{G_{K_1}^t}{m_\Lambda + m_p} i\sigma_{\lambda\xi} \left(p_Y^\xi - p_N^\xi \right) \right] \gamma_5 u_N \varepsilon_\mu \,. \end{aligned} \tag{D.22}$$

Negative-parity vector-meson exchange

$$\begin{aligned} \mathcal{T}_{K^*} =& \frac{e}{M} \overline{u}_Y i\epsilon_{\mu\nu\alpha\beta} \, p_\gamma^\nu p_K^\beta \frac{g^{\alpha\lambda}}{t - m_{K^*}^2 + i m_{K^*} \Gamma_{K^*}} \\ & \times \left[G_{K^*}^v \gamma_\lambda + \frac{G_{K^*}^t}{m_\Lambda + m_p} i\sigma_{\lambda\xi} \left(p_Y^\xi - p_N^\xi \right) \right] u_N \varepsilon^\mu \,. \end{aligned} \tag{D.23}$$

Spin-1/2 nucleon-resonance exchange

$$\mathcal{T}_{N^*} = e \frac{G_{N^*}}{2m_p} \overline{u}_Y \Gamma \frac{\not{p}_N + \not{p}_\gamma + m_{N^*}}{s_{KY} - m_{N^*}^2 + i m_{N^*} \Gamma_{N^*}} i\sigma_{\mu\nu} p_\gamma^\nu \Gamma' u_N \varepsilon^\mu \,. \tag{D.24}$$

Spin-1/2 hyperon-resonance exchange

$$\mathcal{T}_{Y^*} = e \frac{G_{Y^*}}{2m_p} \overline{u}_Y \Gamma' i\sigma_{\mu\nu} p_\gamma^\nu \frac{\not{p}_Y - \not{p}_\gamma + m_{Y^*}}{u - m_{Y^*}^2 + i M_{Y^*} \Gamma_{Y^*}} \Gamma u_N \varepsilon^\mu \,. \tag{D.25}$$

Spin-3/2 nucleon-resonance exchange

$$\begin{aligned} \mathcal{T}_{N^*} =& \frac{e}{2m_p m_{K^+}} \overline{u}_Y \Gamma' p_K^\alpha \theta_{\alpha\beta}(Z) \, G_{\frac{3}{2}}^{\beta\eta} \left(\boldsymbol{p}_\gamma + \boldsymbol{p}_N \right) \\ & \times \left[G_{N^*}^{(1)} \theta_{\eta\nu}(Y) \, \gamma_\mu - \; G_{N^*}^{(2)} \theta_{\eta\nu}(X) \, p_{N,\mu} \right] \left(p_\gamma^\nu \varepsilon^\mu - p_\gamma^\mu \varepsilon^\nu \right) \Gamma u_N \,. \end{aligned} \tag{D.26}$$

Spin-3/2 hyperon-resonance exchange

$$\begin{aligned} \mathcal{T}_{Y^*} =& \frac{e}{2m_p m_{K^+}} \overline{u}_Y \Gamma \left(p_\gamma^\nu \varepsilon^\mu - p_\gamma^\mu \varepsilon^\nu \right) \left[G_{Y^*}^{(1)} \gamma_\mu \theta_{\nu\eta}(Y) - \; G_{Y^*}^{(2)} p_{Y,\mu} \theta_{\nu\eta}(X) \right] \\ & \times G_{\frac{3}{2}}^{\eta\alpha} \left(\boldsymbol{p}_Y - \boldsymbol{p}_\gamma \right) \theta_{\alpha\beta}(Z) \, p_K^\beta \Gamma' u_N \,. \end{aligned} \tag{D.27}$$

APPENDIX E

Lorentz-invariant cross sections

The differential cross section for the reaction ${}^2\mathrm{H}(\gamma^{(*)}, KY)N$ is given by

$$d\sigma = \frac{1}{2\sqrt{\lambda(s,-Q^2,m_D^2)}}|\mathcal{T}|^2(2\pi)^4\delta^{(4)}(\boldsymbol{p}_\gamma + \boldsymbol{p}_D - \boldsymbol{p}_K - \boldsymbol{p}_Y - \boldsymbol{p}_N)\frac{d^3\vec{p}_K}{2E_K(2\pi)^3}\frac{d^3\vec{p}_Y}{2E_Y(2\pi)^3}\frac{d^3\vec{p}_N}{2E_N(2\pi)^3}\,, \tag{E.1}$$

with $s = (\boldsymbol{p}_\gamma + \boldsymbol{p}_D)^2$ and

$$\lambda(x,y,z) \equiv x^2 + y^2 + z^2 - 2xy - 2xz - 2yz\,, \tag{E.2}$$

the triangle function [221], which is totally symmetric in each of its arguments. Even though the differential cross section is a Lorentz invariant, cross sections are often presented as a function of kinematical variables expressed in a particular frame.

In this Appendix, we derive expressions that are frame independent. In order to do so, the three-body phase space needs to be expressed in terms of independent Lorentz-invariant quantities (see Eq. (5.11a) for definitions). This is a non-trivial problem and has been dealt with in Ref. [170] for the general case of n particles. After integrating out the momentum-conserving delta function, one finds that Eq. (E.1) reduces to

$$d\sigma = \frac{1}{(4\pi)^4\lambda(s,-Q^2,m_D^2)}|\mathcal{T}|^2\frac{1}{\sqrt{-\Delta_4}}ds_{KY}ds_{YN}dt_{\gamma K}dt_{DN}\,. \tag{E.3}$$

Here we have introduced the symmetric Gram determinant

$$\begin{aligned} 16\Delta_4 &= \begin{vmatrix} -Q^2 & \boldsymbol{p}_\gamma\cdot\boldsymbol{p}_D & \boldsymbol{p}_\gamma\cdot\boldsymbol{p}_K & \boldsymbol{p}_\gamma\cdot\boldsymbol{p}_N \\ & 2m_D^2 & \boldsymbol{p}_D\cdot\boldsymbol{p}_K & \boldsymbol{p}_D\cdot\boldsymbol{p}_N \\ & & 2m_K^2 & \boldsymbol{p}_K\cdot\boldsymbol{p}_N \\ & & & 2m_N^2 \end{vmatrix} \\ &= \begin{vmatrix} -Q^2 & s+Q^2-m_D^2 & -t_{\gamma K}-Q^2+m_K^2 & s-s_{KY}+t_{DN}-m_D^2 \\ & 2m_D^2 & s-s_{YN}+t_{\gamma K}+Q^2 & -t_{DN}+m_D^2+m_N^2 \\ & & 2m_K^2 & s-s_{KY}-s_{YN}+m_Y^2 \\ & & & 2m_N^2 \end{vmatrix}. \end{aligned} \tag{E.4}$$

An explicit form for the Gram determinant can be found in Ref. [222]. It is a second-degree polynomial in any of the invariants s, s_{KY}, s_{YN}, $t_{\gamma K}$ and t_{DN}. Conveniently, the ranges of physical values for these Lorentz-invariant variables coincide with the region $\Delta_4 \leq 0$.

The four-fold differential cross section defined in (E.3) is of limited use. By integrating over a selection of invariants, different potentially interesting semi-inclusive observables can be defined. We will present two famous distributions: the Dalitz [223] and Chew-Low [224] plots.

E.1 Dalitz cross section

The Dalitz plotting technique involves studying the cross section as a function of the invariant mass of two pairs of final-state particles, e.g. s_{KY} and s_{YN}. This implies that the expression (E.3) needs to be integrated over $t_{\gamma K}$ and t_{DN} for a fixed s, s_{KY} and s_{YN}. The physical regions for the the latter variables are given by

$$\begin{aligned} (m_K + m_Y)^2 \leq & s_{KY} \leq (\sqrt{s} - m_N)^2 \,, \\ (m_Y + m_N)^2 \leq & s_{YN} \leq (\sqrt{s} - m_K)^2 \,. \end{aligned} \tag{E.5}$$

For a given s_{KY}, the energies of the hyperon and nucleon can be readily determined in the kaon-hyperon rest frame

$$\begin{aligned} E_Y^* &= \frac{s_{KY} + Q^2 - m_K^2 + m_Y^2}{2\sqrt{s_{KY}}} \,, \\ E_N^* &= \frac{s - s_{KY} - m_N^2}{2\sqrt{s_{KY}}} \,. \end{aligned} \tag{E.6}$$

The upper and lower values of s_{YN} are reached when the hyperon's three-momentum is (anti-)parallel to the nucleon's, i.e.

$$s_{YN}^{\min/\max} = (E_Y^* + E_N^*)^2 - \left(\sqrt{E_Y^{*2} - m_Y^2} \pm \sqrt{E_N^{*2} - m_N^2} \right)^2 \,. \tag{E.7}$$

In order to integrate over the momentum transfers $t_{\gamma K}$ and t_{DN} in (E.3), we require the integration limits for fixed values of s, s_{KY} and s_{YN}. To integrate over t_{DN}, we determine the roots of

$$16\Delta_4 = \mathsf{A} t_{DN}^2 + 2\mathsf{B} t_{DN} + \mathsf{C} = 0 \,, \tag{E.8}$$

where

$$\begin{aligned} \mathsf{A} &= \lambda(s, s_{YN}, m_K^2) \,, \\ \mathsf{B} &= s s_{KY} t_{\gamma K} + s s_{YN} t_{\gamma K} + s s_{KY} s_{YN} + s_{KY} s_{YN} t_{\gamma K} - s^2 t_{\gamma K} - s_{KY} s_{YN}^2 \\ &\quad + m_D^2 m_K^2 m_Y^2 - 2 m_D^2 m_K^2 m_N^2 - m_K^4 m_N^2 - m_K^4 m_D^2 + s_{KY} s_{YN} m_D^2 - s^2 m_Y^2 \\ &\quad - s_{YN} m_D^2 m_Y^2 + s t_{\gamma K} m_N^2 + s s_{YN} m_Y^2 + s m_K^2 m_N^2 - Q^2 s m_Y^2 - Q^2 m_K^2 m_N^2 \\ &\quad - Q^2 s_{YN} m_Y^2 + 2 Q^2 s_{KY} s_{YN} - 2 s t_{\gamma K} m_Y^2 + s_{YN} m_K^2 m_N^2 + t_{\gamma K} m_K^2 m_N^2 \\ &\quad + s m_D^2 m_K^2 + s_{KY} m_D^2 m_K^2 + s_{YN} m_D^2 m_K^2 s_{YN} - Q^2 s s_{YN} + Q^2 s m_N^2 \\ &\quad - s_{YN} t_{\gamma K} m_N^2 - s s_{KY} m_D^2 + s m_D^2 m_Y^2 + Q^2 s_{YN}^2 + s m_K^2 m_Y^2 - 2 s s_{YN} m_K^2 \\ &\quad + Q^2 m_K^2 m_Y^2 - Q^2 s_{YN} m_K^2 + s_{KY} s_{YN} m_K^2 - s_{KY} t_{\gamma K} m_K^2 + s t_{\gamma K} m_K^2 \end{aligned} \tag{E.9}$$

and the discriminant is given by

$$4\mathsf{B}^2 - 4\mathsf{AC} = 16G(s_{KY}, s_{YN}, s, m_Y^2, m_K^2, m_N^2)G(s, t_{\gamma K}, s_{YN}, -Q^2, m_D^2, m_K^2)\,. \tag{E.10}$$

In the previous step, we have defined the useful function

$$\begin{aligned} G(x,y,z,u,v,w) \equiv\; & x^2y + xy^2 + z^2u + zu^2 + v^2w + vw^2 + xzw + xuv + yzv + yuw \\ & - xy(z+u+v+w) - zu(x+y+v+w) - vw(x+y+z+u)\,. \end{aligned} \tag{E.11}$$

As it as a second-order polynomial in y, it can be rewritten as

$$G(x,y,z,u,v,w) = x(y-y_-)(y-y_+)\,, \tag{E.12}$$

with

$$y_\pm = u + w + \frac{1}{2x}(x-v+u)(z-x-w) \pm \frac{1}{2x}\sqrt{\lambda(x,u,v)\lambda(x,z,w)}\,. \tag{E.13}$$

The roots of the constraint $\Delta_4 = 0$ determine the integration limits for t_{DN}

$$t_{DN}^{\max/\min} = \frac{-\mathsf{B} \pm 2\sqrt{G(s_{KY}, s_{YN}, s, m_Y^2, m_K^2, m_N^2)G(s, t_{\gamma K}, s_{YN}, -Q^2, m_D^2, m_K^2)}}{\lambda(s, s_{YN}, m_K^2)}\,, \tag{E.14}$$

under the condition that the discriminant (E.10) is not negative. Solving the first factor for s_{YN} with the help of (E.13), it can be easily shown that the roots of

$$G(s_{KY}, s_{YN}, s, m_Y^2, m_K^2, m_N^2)\,, \tag{E.15}$$

correspond to the limits we have defined in Eq. (E.7). Since Eq. (E.15) is positive within these bounds, this implies that the second G function in the discriminant (E.10) should be negative. This condition results in integrations limits for $t_{\gamma K}$, i.e.

$$t_{\gamma K}^{\max/\min} = -Q^2 + m_K^2 + \frac{1}{2s}(s - Q^2 - m_D^2)(s_{YN} - s - m_K^2) \pm \frac{1}{2s}\sqrt{\lambda(s, -Q^2, m_D^2)\lambda(s, s_{YN}, m_K^2)}\,. \tag{E.16}$$

The product of triangle functions under the square-root sign is always positive given the physical region for s_{YN} defined in (E.5)

Collecting the above results, we obtain our final result for the Dalitz cross section

$$\frac{d\sigma}{dW_{KY}dW_{YN}} = \frac{4W_{KY}W_{YN}}{(4\pi)^4\lambda(s,-Q^2,m_D^2)} \int_{t_{\gamma K}^{\min}}^{t_{\gamma K}^{\max}} dt_{\gamma K} \int_{t_{DN}^{\min}}^{t_{DN}^{\max}} dt_{DN} \frac{|\mathcal{T}|^2}{\sqrt{-\Delta_4}}\,. \tag{E.17}$$

E.2 Chew-Low cross section

A Chew-Low plot represents a scatter plot as a function of one invariant mass in conjunction with a transferred momentum. For the reaction at hand, it is relevant to consider cross sections in terms of the invariant mass of the hyperon-nucleon system and the momentum transferred from photon to kaon. This implies that the differential cross section needs to be integrated over s_{KY} and t_{DN}. If one adopts the exact same approach as in the preceding section, the Chew-Low cross section becomes

$$\frac{d\sigma}{dW_{YN}dt_{\gamma K}} = \frac{2W_{YN}}{(4\pi)^4\lambda(s,-Q^2,m_D^2)} \int_{s_{KY}^{\min}}^{s_{KY}^{\max}} ds_{KY} \int_{t_{DN}^{\min}}^{t_{DN}^{\max}} dt_{DN} \frac{|\mathcal{T}|^2}{\sqrt{-\Delta_4}}\,. \tag{E.18}$$

For fixed values of s_{YN} and $t_{\gamma K}$ within their physical bound given by (E.5) and (E.16) respectively, the integration limits for t_{DN} are the same as in Eq. (E.14). The limits on s_{KY} are imposed by the roots of the factor in the discriminant (E.10). Since

$$G(s_{KY}, s_{YN}, s, m_Y^2, m_K^2, m_N^2) = G(s_{YN}, s_{KY}, s, m_Y^2, m_N^2, m_K^2)\,, \tag{E.19}$$

we can make use of (E.13) to find

$$\begin{aligned} s_{KY}^{\max/\min} = {} & m_K^2 + m_Y^2 + \frac{1}{2s_{YN}}(s_{YN} + m_Y^2 - m_N^2)(s - s_{YN} - m_K^2) \\ & \pm \frac{1}{2s_{YN}}\sqrt{\lambda(s_{YN}, m_Y^2, m_N^2)\lambda(s, s_{YN}, m_K^2)}\,. \end{aligned} \tag{E.20}$$

APPENDIX F

Density matrix

Scattering experiments that make use of polarised beams and/or targets deal with quantum-mechanical particles without a definite polarisation in the classical sense. Indeed, for incoherent mixtures of particles, only statements about the average properties of the statistical ensemble are meaningful. The density-matrix formalism is a convenient tool to account for the polarisation properties of the initial and final particles when addressing cross sections [225]. In this appendix, this formalism is sketched. After introducing the density matrix and some of its basic properties in Section F.1, we discuss the most general decomposition of the density matrix for an ensemble of spin-1/2 particles, spin-1 particles and photons.

F.1 Definition

For a particle of spin s, one defines a complete set of normalised basis states $|s; m_s\rangle$ with $m_s = -s, \ldots, s$. A *pure* quantum-mechanical spin state $|\Psi_\alpha\rangle$ can be decomposed as

$$|\Psi_\alpha\rangle = \sum_{m_s=-s}^{s} c^\alpha_{m_s} |s; m_s\rangle \ . \tag{F.1}$$

The expectation value of an observable $\hat{\Omega}$ is defined by

$$\begin{aligned} \langle\Omega\rangle &= \langle\Psi_\alpha| \hat{\Omega} |\Psi_\alpha\rangle \\ &= \sum_{m_s, m'_s} c^{\alpha *}_{m_s} \Omega_{m_s m'_s} c^\alpha_{m'_s} \ , \end{aligned} \tag{F.2}$$

where we have introduced a matrix notation for the operator $\hat{\Omega}$ in the basis $\{|s; m_s\rangle\}$, i.e.

$$\Omega_{m_s m'_s} = \langle s; m_s| \hat{\Omega} |s; m'_s\rangle \ . \tag{F.3}$$

A statistical ensemble of spin-s particles does not need to be in a pure state and is described by an incoherent sum of pure states

$$\sum_\alpha p_\alpha \left|\Psi_\alpha\right\rangle \,, \tag{F.4}$$

with $p_\alpha \in \mathbb{R}$ the statistical weight of each state in the ensemble such that $\sum_\alpha p_\alpha = 1$. The mean value of the observable $\hat{\Omega}$ over the entire ensemble then reads

$$\begin{aligned} \overline{\langle\Omega\rangle} &= \sum_\alpha p_\alpha \left\langle\Psi_\alpha\right| \hat{\Omega} \left|\Psi_\alpha\right\rangle \,, \\ &= \mathrm{Tr}\left(\Omega\rho\right) \,, \end{aligned} \tag{F.5}$$

where we have introduced the spin density matrix

$$\rho_{ij} = \sum_\alpha p_\alpha c_i^\alpha c_j^{\alpha *} \,. \tag{F.6}$$

The density matrix obeys a number of properties, which we shall not prove here (see Ref. [100] for an introduction). We only mention that ρ is a hermitian matrix with unit trace.

In this work we deal with spin-1/2 and spin-1 particles. Therefore we investigate the density matrix for those systems.

F.2 Spin-1/2 system

After selecting a quantisation axis, a spin-1/2 particle can occupy two basis states (up or down). This implies the density matrix of a spin-1/2 system will be a 2x2-matrix. A hermitian matrix with dimension two and unit trace can be decomposed as [225]

$$\rho^{(1/2)} = \frac{1}{2}\left(\mathbb{1}_2 + p_x\sigma^1 + p_y\sigma^2 + p_z\sigma^3\right) = \frac{1}{2}\begin{pmatrix} 1+p_z & p_x - ip_y \\ p_x + ip_y & 1-p_z \end{pmatrix} \,, \tag{F.7}$$

where σ^i are the Pauli matrices of Eq. (A.22). The interpretation of the coefficients p_i becomes clear upon considering the expectation value of the spin-1/2 angular-momentum operators $S_i = \frac{1}{2}\sigma_i$

$$\langle S_i\rangle = \mathrm{Tr}\left(S_i\rho^{(1/2)}\right) = \frac{p_i}{2} \,, \tag{F.8}$$

where we made use of ($\sigma_0 \equiv \mathbb{1}_2$)

$$\mathrm{Tr}(\sigma_i\sigma_j) = 2\delta_{ij} \,. \tag{F.9}$$

The three-vector $\vec{p} = (p_x, p_y, p_z)$ can be interpreted as the spin-polarisation vector for the ensemble of spin-1/2 particles.

F.3 Spin-1 system

The spin structure of a spin-1 particle is more involved. The density matrix $\rho^{(1)}$ is a hermitian 3x3-matrix with unit trace. In literature, they are either expressed in terms of rectangular operators [225] or spherical tensor operators [226]. For completeness we will present both and show how they are related to each other.

The spin-1 angular-momentum operators can be defined as [225]

$$S_x = \frac{1}{\sqrt{2}}\begin{pmatrix} 0 & 1 & 0 \\ 1 & 0 & 1 \\ 0 & 1 & 0 \end{pmatrix}, \quad S_y = \frac{1}{\sqrt{2}}\begin{pmatrix} 0 & -i & 0 \\ i & 0 & -i \\ 0 & i & 0 \end{pmatrix}, \quad S_z = \begin{pmatrix} 1 & 0 & 0 \\ 0 & 0 & 0 \\ 0 & 0 & -1 \end{pmatrix}. \tag{F.10}$$

With these operators one defines six traceless symmetric rank-two tensors

$$\mathcal{P}_{ij} = \frac{3}{2}\left(S_i S_j + S_j S_i\right) - 2\delta_{ij}\mathbb{1}_3 \,. \tag{F.11}$$

This leaves us with an over-complete set of operators which span the space of traceless hermitian 3x3-matrices

$$\begin{aligned}
\mathcal{P}_x &= \tfrac{1}{\sqrt{2}}\begin{pmatrix} 0 & 1 & 0 \\ 1 & 0 & 1 \\ 0 & 1 & 0 \end{pmatrix}, & \mathcal{P}_y &= \tfrac{1}{\sqrt{2}}\begin{pmatrix} 0 & -i & 0 \\ i & 0 & -i \\ 0 & i & 0 \end{pmatrix}, & \mathcal{P}_z &= \begin{pmatrix} 1 & 0 & 0 \\ 0 & 0 & 0 \\ 0 & 0 & -1 \end{pmatrix}, \\
\mathcal{P}_{xy} &= \tfrac{3i}{2}\begin{pmatrix} 0 & 0 & -1 \\ 0 & 0 & 0 \\ 1 & 0 & 0 \end{pmatrix}, & \mathcal{P}_{xz} &= \tfrac{3}{2\sqrt{2}}\begin{pmatrix} 0 & 1 & 0 \\ 1 & 0 & -1 \\ 0 & -1 & 0 \end{pmatrix}, & \mathcal{P}_{yz} &= \tfrac{3i}{2\sqrt{2}}\begin{pmatrix} 0 & -1 & 0 \\ 1 & 0 & 1 \\ 0 & -1 & 0 \end{pmatrix}, \\
\mathcal{P}_{xx} &= \tfrac{1}{2}\begin{pmatrix} -1 & 0 & 3 \\ 0 & 2 & 0 \\ 3 & 0 & -1 \end{pmatrix}, & \mathcal{P}_{yy} &= \tfrac{1}{2}\begin{pmatrix} -1 & 0 & -3 \\ 0 & 2 & 0 \\ -3 & 0 & -1 \end{pmatrix}, & \mathcal{P}_{zz} &= \begin{pmatrix} 1 & 0 & 0 \\ 0 & -2 & 0 \\ 0 & 0 & 1 \end{pmatrix}.
\end{aligned} \tag{F.12}$$

The redundancy can be eliminated using the following relation

$$\mathcal{P}_{xx} + \mathcal{P}_{yy} + \mathcal{P}_{zz} = \begin{pmatrix} 0 & 0 & 0 \\ 0 & 0 & 0 \\ 0 & 0 & 0 \end{pmatrix}. \tag{F.13}$$

Finally, we wish to impose a normalisation condition. Extending the normalisation of the spin-1/2 spin operators (F.9), we take the conventional [225]

$$\mathrm{Tr}(\Omega_i \Omega_j) = 3\delta_{ij} \,. \tag{F.14}$$

This leads to the following set of normalised rectangular operators Ω_i

$$\left\{\mathbb{1}_3, \sqrt{\frac{3}{2}}\mathcal{P}_x, \sqrt{\frac{3}{2}}\mathcal{P}_y, \sqrt{\frac{3}{2}}\mathcal{P}_z, \sqrt{\frac{2}{3}}\mathcal{P}_{xy}, \sqrt{\frac{2}{3}}\mathcal{P}_{xz}, \sqrt{\frac{2}{3}}\mathcal{P}_{yz}, \sqrt{\frac{1}{6}}\left(\mathcal{P}_{xx} - \mathcal{P}_{yy}\right), \sqrt{\frac{1}{2}}\mathcal{P}_{zz}\right\}, \tag{F.15}$$

which allow to decompose the density matrix of a spin-1 system

$$\begin{aligned}
\rho^{(1)} = \frac{1}{3}\Bigg(\mathbb{1}_3 &+ \frac{3}{2}\left(p_x\mathcal{P}_x + p_y\mathcal{P}_y + p_z\mathcal{P}_z\right) + \frac{2}{3}\left(p_{xy}\mathcal{P}_{xy} + p_{xz}\mathcal{P}_{xz} + p_{yz}\mathcal{P}_{yz}\right) \\
&+ \frac{1}{6}\left(p_{xx} - p_{yy}\right)\left(\mathcal{P}_{xx} - \mathcal{P}_{yy}\right) + \frac{1}{2}p_{zz}\mathcal{P}_{zz}\Bigg) \,.
\end{aligned} \tag{F.16}$$

In analogy to the spin-1/2 case, the coefficients can be interpreted as polarisation probabilities for the ensemble. For a spin-1 system, one has three vector polarisations p_i, and five tensor polarisations p_{ij}. These quantities are bounded by [225]

$$\begin{aligned}
-1 \leq p_i &\leq 1 \,, \\
-\frac{3}{2} \leq p_{ij} &\leq \frac{3}{2} \,, \\
-2 \leq p_{ii} &\leq 1 \,.
\end{aligned} \tag{F.17}$$

As mentioned previously, the decomposition (F.16) is not unique. Some authors prefer to expand the density matrix in terms of spherical tensor operators τ^I_M of rank I with their corresponding orientation parameters P_{IM} [226, 227]

$$\rho^{(1)} = \frac{1}{3}\sum_{IM}(-1)^M \tau^I_M P_{I-M}\,. \tag{F.18}$$

The operators τ^I are defined through their reduced matrix elements

$$\langle 1 \| \tau^I \| 1 \rangle = \sqrt{3}\sqrt{2I+1}\,, \tag{F.19}$$

allowing us to write the density matrix as function of 3j-symbols [226]

$$\begin{aligned}\rho^{(1)}_{mm'} &= \frac{1}{3}\sum_{IM}(-1)^M \langle 1m|\, \tau^I_M \,|1m'\rangle\, P_{I-M} \\ &= \frac{1}{\sqrt{3}}\sum_{IM}(-1)^{1+m'}\sqrt{2I+1}\begin{pmatrix} 1 & 1 & I \\ m' & -m & -M \end{pmatrix} P_{IM}\,,\end{aligned} \tag{F.20}$$

or explicitly,

$$\rho^{(1)} = \frac{1}{3}\begin{pmatrix} 1+\sqrt{\frac{3}{2}}P_{10}+\frac{1}{\sqrt{2}}P_{20} & \sqrt{\frac{3}{2}}P_{1-1}+\sqrt{\frac{3}{2}}P_{2-1} & \sqrt{3}P_{2-2} \\ -\sqrt{\frac{3}{2}}P_{11}-\sqrt{\frac{3}{2}}P_{21} & 1-\sqrt{2}P_{20} & \sqrt{\frac{3}{2}}P_{1-1}-\sqrt{\frac{3}{2}}P_{2-1} \\ \sqrt{3}P_{22} & -\sqrt{\frac{3}{2}}P_{11}+\sqrt{\frac{3}{2}}P_{21} & 1-\sqrt{\frac{3}{2}}P_{10}+\frac{1}{\sqrt{2}}P_{20} \end{pmatrix}. \tag{F.21}$$

Equating (F.16) and (F.21), allows to establish a relation between the expectation values of spherical and rectangular operators

$$P_{10} = \sqrt{\frac{3}{2}}P_z\,, \tag{F.22a}$$

$$P_{1\pm1} = \mp\frac{\sqrt{3}}{2}\left(P_x \pm iP_y\right), \tag{F.22b}$$

$$P_{20} = \frac{1}{\sqrt{2}}P_{zz}\,, \tag{F.22c}$$

$$P_{2\pm1} = \mp\frac{1}{\sqrt{3}}\left(P_{xz} \pm iP_{yz}\right), \tag{F.22d}$$

$$P_{2\pm2} = \frac{1}{2\sqrt{3}}\left(P_{xx} - P_{yy} \pm 2iP_{xy}\right). \tag{F.22e}$$

Using the following property of the spherical tensor operators and their expectation values,

$$\left(\tau^I_M\right)^\dagger = (-1)^M \tau^I_{-M} \quad \text{and} \quad P^*_{IM} = (-1)^M P_{I-M}\,, \tag{F.23}$$

we find the inverse relations

$$\begin{aligned} P_x &= -\tfrac{2}{\sqrt{3}}\Re(P_{11}), & P_y &= -\tfrac{2}{\sqrt{3}}\Im(P_{11}), & P_z &= \sqrt{\tfrac{2}{3}}P_{10}, \\ P_{xy} &= \sqrt{3}\Im(P_{22}), & P_{xz} &= -\sqrt{3}\Re(P_{21}), & P_{yz} &= -\sqrt{3}\Im(P_{21}), \\ P_{xx} &= \sqrt{3}\Re(P_{22}) - \tfrac{1}{\sqrt{2}}P_{20}, & P_{yy} &= -\sqrt{3}\Re(P_{22}) - \tfrac{1}{\sqrt{2}}P_{20}, & P_{zz} &= \sqrt{2}P_{20}. \end{aligned} \tag{F.24}$$

When polarised spin-1 particles are used as target in an actual experiment, the density matrix will be diagonal with respect to a quantisation axis $\vec{d}$ defined by the polar and azimuthal angles θ_d and ϕ_d [227],

$$\rho^{(1)}_{mm'}(\vec{d}) = p_m \delta_{mm'} \,. \tag{F.25}$$

Using the decomposition of the density matrix (F.21) and the orthogonality relation for 3j-symbols

$$\sum_{m_1 m_2} (2j_3+1) \begin{pmatrix} j_1 & j_2 & j_3 \\ m_1 & m_2 & m_3 \end{pmatrix} \begin{pmatrix} j_1 & j_2 & j'_3 \\ m_1 & m_2 & m'_3 \end{pmatrix} = \delta_{j_3 j'_3} \delta_{m_3 m'_3} \,, \tag{F.26}$$

we can relate the orientation parameters to the diagonal elements

$$P_{IM}(\vec{d}) = \delta_{M0} \sqrt{3} \sum_m (-1)^{1-m} \sqrt{2I+1} p_m \begin{pmatrix} 1 & 1 & I \\ m & -m & 0 \end{pmatrix} \,, \tag{F.27}$$

which yields $P_{IM}(\vec{d}) = \delta_{M0} P_I$, with

$$\begin{aligned} P_0 &= 1 \,, \\ P_1 &= \sqrt{\frac{3}{2}} \left(p_1 - p_{-1}\right) \,, \\ P_2 &= \frac{1}{\sqrt{2}} \left(1 - 3p_0\right) \,. \end{aligned} \tag{F.28}$$

Owing to the elegant properties of the spherical tensor operators under rotation, we can easily express the density matrix of a spin-1 particle oriented along $\vec{d}$, in a reference frame with the quantisation axis along the z axis,

$$\rho^{(1)}_{mm'}(\vec{z}) = \frac{(-1)^{1-m}}{\sqrt{3}} \sum_{IM} \sqrt{2I+1} \begin{pmatrix} 1 & 1 & I \\ m' & -m & M \end{pmatrix} e^{-iM\phi_d} d^I_{M0}(\theta_d) P_I \,, \tag{F.29}$$

where $d^j_{mm'}(\theta)$ are Wigner's small rotation matrices.

F.4 Photons

Although the photon is a spin-1 particle, it has only two polarisation states. Therefore, the photon density matrix has a structure analogous to that of an ensemble of spin-1/2 particles

$$\rho^{(\gamma)} = \frac{1}{2} \left(\mathbb{1}_2 + P^{(\gamma)}_l \sigma_x + P^{(\gamma)}_t \sigma_y + P^{(\gamma)}_c \sigma_z \right) \,, \tag{F.30}$$

with respect to the circular polarisation basis $\{|+\rangle, |-\rangle\}$. We added the superscript γ to the coefficients $P^{(\gamma)}_i$ to emphasise that their physical interpretation is very different from those for the spin-1/2 case. Using the definition (F.6), we can write down density matrices for some explicit cases,

where the photon ensemble is in a pure state

$$\begin{array}{lcllcl}
|RC\rangle & = & |+\rangle & \Rightarrow & \rho_{RC}^{(\gamma)} & = & \frac{1}{2}\left(\mathbb{1}_2 + \sigma_z\right) , \\
|LC\rangle & = & |-\rangle & \Rightarrow & \rho_{LC}^{(\gamma)} & = & \frac{1}{2}\left(\mathbb{1}_2 - \sigma_z\right) , \\
|Lx\rangle & = & \frac{1}{\sqrt{2}}(|+\rangle - |-\rangle) & \Rightarrow & \rho_{Lx}^{(\gamma)} & = & \frac{1}{2}\left(\mathbb{1}_2 - \sigma_x\right) , \\
|Ly\rangle & = & \frac{i}{\sqrt{2}}(|+\rangle + |-\rangle) & \Rightarrow & \rho_{Ly}^{(\gamma)} & = & \frac{1}{2}\left(\mathbb{1}_2 + \sigma_x\right) , \\
|Tx\rangle & = & \frac{1}{\sqrt{2}}(|Lx\rangle - |Ly\rangle) & \Rightarrow & \rho_{Tx}^{(\gamma)} & = & \frac{1}{2}\left(\mathbb{1}_2 - \sigma_y\right) , \\
|Ty\rangle & = & \frac{1}{\sqrt{2}}(|Lx\rangle + |Ly\rangle) & \Rightarrow & \rho_{Ty}^{(\gamma)} & = & \frac{1}{2}\left(\mathbb{1}_2 + \sigma_y\right) .
\end{array} \tag{F.31}$$

From these equations it is clear why the polarisation coefficients are labelled c, l and t. The quantity $P_c^{(\gamma)}$ can be interpreted as the degree of circular polarisation, with $P_c^{(\gamma)} > 0$ (< 0) indicating right-(left-)handed orientation. The coefficient $P_l^{(\gamma)}$ expresses the amount of linear polarisation along the y ($P_l^{(\gamma)} > 0$) or x ($P_l^{(\gamma)} < 0$) axis, whereas $P_t^{(\gamma)} > 0$ (< 0) quantifies linear polarisation along the y (x) axis rotated $-\frac{\pi}{4}$ about the z axis.

APPENDIX G

Parametrisations of the deuteron wave function

In Section 5.5, we have dealt with the deuteron. After discussing the covariant *Dnp*-vertex, we introduced the non-relativistic and relativistic wave functions. In this dissertation, we use the deuteron wave functions obtained with a number of different NN potentials. For all but one of these wave functions, convenient parametrisations exist.

In Section G.1 of this appendix, we discuss a parametrisation for the non-relativistic Paris and CD-Bonn wave functions. Sections G.2 and G.3 are devoted to the parametrisations used in the Gross formalism. To our knowledge, no parametrisation for the deuteron wave functions obtained with the Nijmegen potential is available. The latter wave functions can be found on-line in a tabulated format [228].

G.1 Non-relativistic wave-function parametrisation

Realistic NN potentials, such as the Paris potential [229] and the charge-dependent Bonn potential [179], are often expressed as a discrete superposition of Yukawa terms. This naturally leads one to the following algebraic parametrisation of the deuteron wave functions in configuration space

$$\begin{aligned} u(r) &= \sum_{i=1}^{n} C_i \, e^{-m_i r} \,, \\ w(r) &= \sum_{i=1}^{n} D_i \, e^{-m_i r} \left(1 + \frac{3}{m_i r} + \frac{3}{m_i^2 r^2} \right) \,, \end{aligned} \tag{G.1}$$

with $m_i = \alpha + (i-1) m_0$. In the limit $r \to 0$, the radial wave functions satisfy the boundary conditions

$$u(r) \to r \quad \text{and} \quad w(r) \to r^3 \,. \tag{G.2}$$

Table G.1 – Expansion coefficients of the parametrised radial deuteron wave functions (G.1) corresponding with the Paris potential [229] and the CD-Bonn potential [179].

	Paris ($n = 13$)		CD-Bonn ($n = 11$)	
i	C_i (fm$^{-1/2}$)	D_i (fm$^{-1/2}$)	C_i (fm$^{-1/2}$)	D_i (fm$^{-1/2}$)
1	$0.88688076 \cdot 10^{+0}$	$0.23135193 \cdot 10^{-1}$	$0.88472985 \cdot 10^{+0}$	$0.22623762 \cdot 10^{-1}$
2	$-0.34717093 \cdot 10^{+0}$	$-0.85604572 \cdot 10^{+0}$	$-0.26408759 \cdot 10^{+0}$	$-0.50471056 \cdot 10^{+0}$
3	$-0.30502380 \cdot 10^{+1}$	$0.56068193 \cdot 10^{+1}$	$-0.44114404 \cdot 10^{-1}$	$0.56278897 \cdot 10^{+0}$
4	$0.56207766 \cdot 10^{+2}$	$-0.69462922 \cdot 10^{+2}$	$-0.14397512 \cdot 10^{+2}$	$-0.16079764 \cdot 10^{+2}$
5	$-0.74957334 \cdot 10^{+3}$	$0.41631118 \cdot 10^{+3}$	$0.85591256 \cdot 10^{+2}$	$0.11126803 \cdot 10^{+3}$
6	$0.53365279 \cdot 10^{+4}$	$-0.12546621 \cdot 10^{+4}$	$-0.31876761 \cdot 10^{+3}$	$-0.44667490 \cdot 10^{+3}$
7	$-0.22706863 \cdot 10^{+5}$	$0.12387830 \cdot 10^{+4}$	$0.70336701 \cdot 10^{+3}$	$0.10985907 \cdot 10^{+4}$
8	$0.60434469 \cdot 10^{+5}$	$0.33739172 \cdot 10^{+4}$	$-0.90049586 \cdot 10^{+3}$	$-0.16114995 \cdot 10^{+4}$
9	$-0.10292058 \cdot 10^{+6}$	$-0.13041151 \cdot 10^{+5}$	$0.66145441 \cdot 10^{+3}$	see (G.3b)
10	$0.11223357 \cdot 10^{+6}$	$0.19512524 \cdot 10^{+5}$	$-0.25958894 \cdot 10^{+3}$	see (G.3b)
11	$-0.75925226 \cdot 10^{+5}$	see (G.3b)	see (G.3a)	see (G.3b)
12	$0.29059715 \cdot 10^{+5}$	see (G.3b)		
13	see (G.3a)	see (G.3b)		
α	0.23162461 fm^{-1}		0.2315380 fm^{-1}	
m_0	1.0 fm^{-1}		0.9 fm^{-1}	

This gives rise to the following constraints for the coefficients of Eq. (G.1)

$$0 = \sum_{i=1}^{n} C_i \,, \tag{G.3a}$$

$$0 = \sum_{i=1}^{n} D_i = \sum_{i=1}^{n} D_i m_i^2 = \sum_{i=1}^{n} \frac{D_i}{m_i^2} \,. \tag{G.3b}$$

In table G.1, we have listed the coefficients C_i, D_i, α and m_0 for the Paris and CD-Bonn wave functions.

Using (H.2), it is straightforward to find the parametrised radial wave functions in momentum space

$$\begin{aligned} u(p) &= \sqrt{\frac{2}{\pi}} \sum_{i=1}^{n} \frac{C_i}{p^2 + m_i^2} \,, \\ w(p) &= \sqrt{\frac{2}{\pi}} \sum_{i=1}^{n} \frac{-D_i}{p^2 + m_i^2} \,, \end{aligned} \tag{G.4}$$

where we have made use of the boundary conditions in (G.3b).

G.2 Relativistic wave-function parametrisation I

Buck and Gross developed an analytical form for their relativistic wave functions [230] which is in line with the parametrisation of Eq. (G.1)

$$\phi_i(q) = \sum_{n=1}^{N} b_{i,n} G_L^n(q) \quad \text{with} \quad i = {}^3S_1, {}^3D_1, {}^3P_1, {}^1P_1 \,, \tag{G.5}$$

with L the angular momentum of the state. This parametrisation is valid both in configuration as in momentum space, visualised by the q dependence. As their non-relativistic counterparts, these wave functions obey the boundary conditions (G.2). These conditions can be met by the following choice

$$G_L^n(q) = f_{L,n}(q) - \sum_{i=1}^{N+2} K_{L,i}^n f_{L,N+i}(q) \,, \tag{G.6}$$

with

$$\begin{aligned} K_{L,i}^n &= \left(\frac{M_{L,N+i}}{M_{L,n}}\right)^L \prod_{\substack{j=1 \\ j\neq i}}^{L+2} \frac{M_{L,N+j}^2 - M_{L,n}^2}{M_{L,N+j}^2 - M_{L,N+i}^2} \,, \\ M_{L,i} &= \alpha_L + (i+1) m_{L,0} \,. \end{aligned} \tag{G.7}$$

In analogy with the non-relativistic parametrisation we have

$$\begin{aligned} f_{0,n}(r) &= e^{-M_{0,n} r} \,, \\ f_{1,n}(r) &= e^{-M_{1,n} r} \left(1 + \frac{1}{M_{1,n} r}\right) \,, \\ f_{2,n}(r) &= e^{-M_{2,n} r} \left(1 + \frac{3}{M_{2,n} r} + \frac{3}{M_{2,n}^2 r^2}\right) \,, \end{aligned} \tag{G.8}$$

in configuration space and

$$\begin{aligned} f_{0,n}(p) &= \sqrt{\frac{2}{\pi}} \frac{1}{p^2 + M_{0,n}^2} \,, \\ f_{1,n}(p) &= \sqrt{\frac{2}{\pi}} \left(\frac{p}{M_{1,n}}\right) \frac{1}{p^2 + M_{1,n}^2} \,, \\ f_{2,n}(p) &= \sqrt{\frac{2}{\pi}} \left(\frac{p}{M_{2,n}}\right)^2 \frac{1}{p^2 + M_{2,n}^2} \,, \end{aligned} \tag{G.9}$$

in momentum space.

In table G.2 we have listed the expansion coefficients [231] for the relativistic wave function labelled IIb in Ref. [181].

G.3 Relativistic wave-function parametrisation II

In Ref. [182], Gross and Stadler have introduced a parametrisation for the deuteron wave functions that are obtained from the OBE potential presented in Ref. [183]. The different components are

Table G.2 – Expansion coefficients of the relativistic deuteron wave function labelled IIb in Ref. [181] to be used with the wave-function parametrisation of Section G.2. The coefficients α_L and $b_{i,n}$ have dimensions MeV and $\text{MeV}^{1/2}$ respectively. The parameter $m_{L,0}$ is fixed at 138 MeV for all states.

	$^3S_1$	$^3D_1$	$^3P_1$	$^1P_1$
α_L	$0.45702000 \cdot 10^{+2}$	$0.45702000 \cdot 10^{+2}$	$0.13800000 \cdot 10^{+3}$	$0.13800000 \cdot 10^{+3}$
$b_{i,1}$	$1.23473909 \cdot 10^{+1}$	$3.04445499 \cdot 10^{-1}$	$3.58649195 \cdot 10^{-2}$	$9.01574296 \cdot 10^{-3}$
$b_{i,2}$	$-9.79182548 \cdot 10^{-1}$	$-2.28389143 \cdot 10^{+0}$	$-1.11941519 \cdot 10^{+0}$	$-5.62298514 \cdot 10^{-1}$
$b_{i,3}$	$-1.33149654 \cdot 10^{+1}$	$-1.25535880 \cdot 10^{+1}$	$1.24100281 \cdot 10^{+0}$	$5.90732942 \cdot 10^{+0}$
$b_{i,4}$	$2.03598985 \cdot 10^{+1}$	$4.75484843 \cdot 10^{+0}$	$3.01054706 \cdot 10^{+1}$	$-1.88499536 \cdot 10^{+1}$
$b_{i,5}$	$-5.49883687 \cdot 10^{+1}$	$3.44785873 \cdot 10^{+0}$	$-5.39212864 \cdot 10^{+1}$	$7.36252577 \cdot 10^{+0}$
$b_{i,6}$	$-3.35208211 \cdot 10^{+1}$	$1.06337512 \cdot 10^{+0}$	$-2.96869223 \cdot 10^{+1}$	$1.35240434 \cdot 10^{+1}$
$b_{i,7}$	$1.42816421 \cdot 10^{+1}$	$-7.15449045 \cdot 10^{-3}$	$2.39138486 \cdot 10^{+1}$	$7.26850340 \cdot 10^{+0}$
$b_{i,8}$	$4.58613894 \cdot 10^{+1}$	$-2.60000217 \cdot 10^{-1}$	$5.34140258 \cdot 10^{+1}$	$5.58906563 \cdot 10^{-1}$
$b_{i,9}$	$5.36566194 \cdot 10^{+1}$	$-2.11957448 \cdot 10^{-1}$	$5.34280647 \cdot 10^{+1}$	$-2.62991867 \cdot 10^{+0}$
$b_{i,10}$	$4.42571196 \cdot 10^{+1}$	$-1.11702589 \cdot 10^{-1}$	$3.71934963 \cdot 10^{+1}$	$-2.81893558 \cdot 10^{+0}$
$b_{i,11}$	$2.71001008 \cdot 10^{+1}$	$-4.10060436 \cdot 10^{-2}$	$1.84515566 \cdot 10^{+1}$	$-1.67873493 \cdot 10^{+0}$
$b_{i,12}$	$1.03563424 \cdot 10^{+1}$	$-8.54424870 \cdot 10^{-3}$	$5.34193503 \cdot 10^{+0}$	$-5.38676867 \cdot 10^{-1}$

expanded like in Eq. (G.5). In momentum space, the expansion functions are given by

$$G_L^n(p) = \sqrt{\frac{2}{\pi}} \frac{p^L M_{L,n-2}^2 M_{L,n-1}^{2n_L-L}}{\left(M_{L,n-2}^2 + p^2\right)\left(M_{L,n-1}^2 + p^2\right)}\,, \tag{G.10}$$

for $n = 1, \ldots, (N-1)$, with $M_{L,i}$ defined in Eq. (G.7). The final expansion function, labelled the tail wave function, ensures a correct falloff as $p \to \infty$ and is defined as

$$G_L^N(p) = \sqrt{\frac{2}{\pi}} \frac{p^L M_{L,N-1}^{2n_L+1-L}}{\left(M_{L,N-1}^2 + p^2\right)^{n_L+1/2}}\,. \tag{G.11}$$

The expansion functions in configuration space are more involved. For the terms $n < N$, we have

$$G_0^n(r) = \frac{M_{0,n-2}^2 M_{0,n-1}^4}{\left(M_{0,n-1}^2 - M_{0,n-2}^2\right)^2} \left\{ e^{-rM_{0,n-2}} - e^{-rM_{0,n-1}} \left[1 + \frac{r}{2} M_{0,n-1} \left(1 - \frac{M_{0,n-2}^2}{M_{0,n-1}^2} \right) \right] \right\}, \tag{G.12}$$

$$\begin{aligned} G_1^n(r) = \frac{M_{1,n-2}^2 M_{1,n-1}^4}{\left(M_{1,n-1}^2 - M_{1,n-2}^2\right)^2} \Bigg\{ & \frac{M_{1,n-2}}{M_{1,n-1}} e^{-rM_{1,n-2}} \left[1 + \frac{1}{rM_{1,n-2}} \right] \\ & - e^{-rM_{1,n-1}} \left[1 + \frac{1}{rM_{1,n-1}} + \frac{rM_{1,n-1}}{2} \left(1 - \frac{M_{1,n-2}^2}{M_{1,n-1}^2} \right) \right] \Bigg\}, \end{aligned} \tag{G.13}$$

$$G_2^i(r) = \frac{M_{2,n-2}^2 M_{2,n-1}^6}{\left(M_{2,n-1}^2 - M_{2,n-2}^2\right)^3} \left\{ \frac{M_{2,n-2}^2}{M_{2,n-1}^2} e^{-rM_{2,n-2}} \left[1 + \frac{3}{rM_{2,n-2}} + \frac{3}{r^2 M_{2,n-2}^2} \right] \right.$$
$$- e^{-rM_{2,n-1}} \left[1 + \frac{3}{rM_{2,n-1}} + \frac{3}{r^2 M_{2,n-1}^2} + \frac{1 + rM_{2,n-1}}{2} \left(1 - \frac{M_{2,n-2}^2}{M_{2,n-1}^2} \right) \right.$$
$$\left. \left. + \frac{r^2 M_{2,n-1}^2}{8} \left(1 - \frac{M_{2,n-2}^2}{M_{2,n-1}^2} \right)^2 \right] \right\} . \quad \text{(G.14)}$$

Finally, the tail wave functions in configuration space read

$$\begin{aligned} G_0^N(r) &= \frac{2r^2}{3\pi} M_{0,N-1}^4 K_1(rM_{0,N-1}) , \\ G_1^N(r) &= \frac{2r^2}{3\pi} M_{1,N-1}^4 K_0(rM_{1,N-1}) , \\ G_2^N(r) &= \frac{2r^3}{15\pi} M_{2,N-1}^5 K_0(rM_{2,N-1}) , \end{aligned} \quad \text{(G.15)}$$

where

$$K_n(z) = \frac{z^n}{(2n-1)!!} \int_1^\infty dt e^{-zt} (t^2 - 1)^{n - \frac{1}{2}} , \quad \text{(G.16)}$$

are the modified Bessel functions of the second kind.

In table G.3, we have listed the expansion coefficients for the wave functions obtained with the WJC-1 model of Ref. [183]. As was pointed out in Ref. [182], the CST wave functions obey the following normalisation condition

$$1 = \int_0^\infty dp p^2 \left[u^2(p) + w^2(p) + v_t^2(p) + v_s^2(p) + \left\langle \frac{dV}{dm_D} \right\rangle \right] . \quad \text{(G.17)}$$

The last term, which does not feature in the conventional normalisation of the deuteron wave function, is of the order of a few percent. Therefore, the authors put forward a *scaled* wave function that conforms to the conventional normalisation condition and recommend it for use in EM calculations based on the RIA. When we refer to the WJC-1 wave function in this work, we will always allude to this *scaled* wave function.

Table G.3 – Expansion coefficients of the relativistic deuteron wave function labelled WJC-1 in Ref. [183] to be used with the wave-function parametrisation of Section G.3. The parameters α_L and $m_{L,0}$ are given in MeV. The coefficients $b_{i,n}$ have dimensions $\mathrm{GeV}^{-3/2}$. The *tail* mass $M_{L,N-1}$ is not given by Eq. (G.7), but is fixed at 2 GeV instead.

	$^3S_1$	$^3D_1$	$^3P_1$	$^1P_1$
N	17	16	12	12
n_L	2	3	2	2
α_L	45.716	45.716	488.000	633.000
$m_{L,0}$	75.000	80.000	109.090	109.090
$b_{i,1}$	134.963	23.813	−27.120	−78.763
$b_{i,2}$	52.871	32.709	233.155	688.895
$b_{i,3}$	−217.709	−111.381	−998.893	−2910.298
$b_{i,4}$	1876.699	844.861	2679.013	7690.084
$b_{i,5}$	−11369.449	−4376.965	−4894.348	−13861.596
$b_{i,6}$	49427.176	16489.297	6277.553	17571.825
$b_{i,7}$	−156695.247	−45122.587	−5674.481	−15720.926
$b_{i,8}$	369322.468	91061.493	3550.952	9747.293
$b_{i,9}$	−655367.189	−136672.748	−1467.429	−3994.747
$b_{i,10}$	879178.453	152411.033	360.796	975.086
$b_{i,11}$	−887103.150	−124633.670	−40.010	−107.489
$b_{i,12}$	662786.733	72617.712	$-498 \cdot 10^{-7}$	$-394 \cdot 10^{-7}$
$b_{i,13}$	−355720.583	−28549.974		
$b_{i,14}$	129738.381	6790.953		
$b_{i,15}$	−28805.739	−738.436		
$b_{i,16}$	2939.797	$-100 \cdot 10^{-6}$		
$b_{i,17}$	$-125 \cdot 10^{-6}$			

APPENDIX H

Connecting (non-)relativistic wave functions with the covariant Dnp-vertex

In Section 5.5, we introduced the covariant *Dnp*-vertex (5.82). This vertex is the most general structure that describes the breakup of a deuteron into two nucleons, with the second nucleon on its mass-shell. It is given in terms of four Lorentz-invariant form factors.

In Eq. (5.85) we defined two energy-projected wave functions in terms of the covariant *Dnp*-vertex, and in paragraphs 5.5.2 and 5.5.3 we have argued that these wave functions can be linked to the well-known (non-)relativistic wave-function decompositions in the ${}^{2S+1}L_J$ basis. In this appendix, we will prove this correspondence explicitly. In addition, we will deduce a connection between the form factors and the wave functions.

First, we require the deuteron's wave functions given by Eqs. (5.88) and (5.92) in momentum space. This is readily achieved by taking the Fourier transform (5.87). We obtain

$$\begin{aligned}
\Psi^{++}(\vec{p};\lambda_D) &= u(|\vec{p}|)\chi_{1\lambda_D}Y_{00}(\hat{\vec{p}}) - w(|\vec{p}|)\sum_{m_S}\langle 2,\lambda_D\text{-}m_S;1,m_S|\,1,\lambda_D\rangle\,\chi_{1m_S}Y_{2,\lambda_D\text{-}m_S}(\hat{\vec{p}})\,,\\
\Psi^{-+}(\vec{p};\lambda_D) &= -v_s(|\vec{p}|)\chi_{00}Y_{1\lambda_D}(\hat{\vec{p}}) - v_t(|\vec{p}|)\sum_{m_S}\langle 1,\lambda_D\text{-}m_S;1,m_S|\,1,\lambda_D\rangle\,\chi_{1m_S}Y_{1,\lambda_D\text{-}m_S}(\hat{\vec{p}})\,.
\end{aligned} \tag{H.1}$$

Herein, we have defined

$$\phi_i(p) = \sqrt{\frac{2}{\pi}}\int_0^\infty dr r\phi_i(r)j_L(pr)\,, \tag{H.2}$$

with ϕ_i $(i=1,2,3,4)$ a shorthand notation for the u, w, v_s and v_t wave functions in configuration and momentum space. The functions $j_L(x)$ are spherical Bessel functions of the first kind.

The wave functions in (H.1) are expressed in the direct-product representation $\frac{1}{2}\otimes\frac{1}{2}$ of the spins of both nucleons. Introducing the notation $\vec{\sigma}_i\chi_{Sm_S}$ $(i=1,2)$ for the Pauli matrices acting in the spin-space of particle i, one can easily prove identities such as

$$\vec{\sigma}_1\cdot\vec{\sigma}_2\;\chi_{Sm_S} = \chi_{Sm_S}\,. \tag{H.3}$$

After some manipulations, one can rewrite the wave functions as

$$\begin{aligned}\Psi^{++}(\vec{p};\lambda_D) &= \frac{1}{\sqrt{4\pi}}\left[u(|\vec{p}|)\vec{\sigma}_1\cdot\vec{\sigma}_2 - \frac{w(|\vec{p}|)}{\sqrt{8}}(3\vec{\sigma}_1\cdot\hat{\vec{p}}\,\vec{\sigma}_2\cdot\hat{\vec{p}} - \vec{\sigma}_1\cdot\vec{\sigma}_2)\right]\chi_{1\lambda_D}\,,\\ \Psi^{-+}(\vec{p};\lambda_D) &= -\sqrt{\frac{3}{4\pi}}\left[\frac{v_s(|\vec{p}|)}{2}(\vec{\sigma}_1-\vec{\sigma}_2)\cdot\hat{\vec{p}} - \frac{v_t(|\vec{p}|)}{2\sqrt{2}}(\vec{\sigma}_1+\vec{\sigma}_2)\cdot\hat{\vec{p}}\right]\chi_{1\lambda_D}\,.\end{aligned} \tag{H.4}$$

In order to make a direct connection with the energy-projected wave functions (5.85) defined in terms of the covariant *Dnp*-vertex, we will first rewrite (H.4) in matrix representation, where

$$\begin{aligned}|+\rangle_1|+\rangle_2 &\equiv \begin{pmatrix}1&0\\0&0\end{pmatrix}\,, \quad |+\rangle_1|-\rangle_2 \equiv \begin{pmatrix}0&1\\0&0\end{pmatrix}\,,\\ |-\rangle_1|+\rangle_2 &\equiv \begin{pmatrix}0&0\\1&0\end{pmatrix}\,, \quad |-\rangle_1|-\rangle_2 \equiv \begin{pmatrix}0&0\\0&1\end{pmatrix}\,.\end{aligned} \tag{H.5}$$

In this representation, the coupled-spin wave functions can conveniently be expressed as

$$\chi_{1m} \equiv \left(\vec{\sigma}\cdot\vec{\xi}^m\,\frac{i\sigma_y}{\sqrt{2}}\right)\Big|_{\lambda_2\lambda_1}\,, \tag{H.6}$$

where we have taken the deuteron's polarisation vectors as defined in Eq. (5.79). The indices λ_1 and λ_2 are the spin-projections of particles 1 and 2 along the z axis. For a general operator A_1 (B_2) acting in the spin-space of particle 1 (2), one can prove the following equivalence

$$A_1B_2\chi_{1m} \equiv \left(B\,\vec{\sigma}\cdot\vec{\xi}^m\,\tilde{A}\frac{i\sigma_y}{\sqrt{2}}\right)\Big|_{\lambda_2\lambda_1}\,, \tag{H.7}$$

with $\tilde{A} = \sigma_2 A^T \sigma_2$. After putting this relation to use, we find an expression for the wave functions in matrix representation

$$\begin{aligned}\Psi^{++}_{\lambda_1\lambda_2}(\vec{p};\lambda_D) &\equiv \frac{1}{\sqrt{4\pi}}\left[u(|\vec{p}|)\vec{\sigma}\cdot\vec{\xi}^{\lambda_D} + \frac{w(|\vec{p}|)}{\sqrt{2}}(3\hat{\vec{p}}\cdot\vec{\xi}^{\lambda_D}\vec{\sigma}\cdot\hat{\vec{p}} - \vec{\sigma}\cdot\vec{\xi}^{\lambda_D})\right]\frac{i\sigma_y}{\sqrt{2}}\Big|_{\lambda_2\lambda_1}\,,\\ \Psi^{-+}_{\lambda_1\lambda_2}(\vec{p};\lambda_D) &\equiv \sqrt{\frac{3}{4\pi}}\left[v_s(|\vec{p}|)\hat{\vec{p}}\cdot\vec{\xi}^{\lambda_D} + \frac{v_t(|\vec{p}|)}{\sqrt{2}}(\vec{\sigma}\cdot\hat{\vec{p}}\vec{\sigma}\cdot\vec{\xi}^{\lambda_D} - \hat{\vec{p}}\cdot\vec{\xi}^{\lambda_D})\right]\frac{i\sigma_y}{\sqrt{2}}\Big|_{\lambda_2\lambda_1}\,.\end{aligned} \tag{H.8}$$

Note that the v_s-term is antisymmetric in the indices, whereas the other terms are symmetric.

In order to link the form factors of the covariant *Dnp*-vertex with the deuteron wave functions, we need to rewrite the energy-projected wave functions defined in terms of the *Dnp*-vertex in matrix representation. Adopting the conventions for positive- and negative-energy Dirac spinors given in Section A.4, we are able to work out the deuteron wave functions as given in Eq. (5.85). After a tedious calculation, one obtains

$$\begin{aligned}\Psi^{++}_{\lambda_1\lambda_2}(\vec{p};\lambda_D) &= \frac{(-1)^{\frac{1}{2}-\lambda_2}}{\sqrt{(2\pi)^3 2m_D}2E_p(2E_p-m_D)}\\ &\times\xi^\dagger_{\lambda_1}\Bigg\{\vec{\sigma}\cdot\vec{\xi}^{\lambda_D}\frac{2}{3}\left[H(|\vec{p}|)\frac{(2E_p-m_D)(2m_N+E_p)}{m_N} - F(|\vec{p}|)(2E_p+m_N) - G(|\vec{p}|)\frac{|\vec{p}|^2}{m_N}\right]\\ &+(3\hat{\vec{p}}\cdot\vec{\xi}^{\lambda_D}\vec{\sigma}\cdot\hat{\vec{p}} - \vec{\sigma}\cdot\vec{\xi}^{\lambda_D})\frac{2}{3}\left[F(|\vec{p}|)(E_p-m_N) + H(|\vec{p}|)\frac{(2E_p-m_D)(E_p-m_N)}{m_N} - G(|\vec{p}|)\frac{|\vec{p}|^2}{m_N}\right]\Bigg\}\eta_{\lambda_2}\,,\end{aligned} \tag{H.9}$$

$$\Psi^{-+}_{\lambda_1\lambda_2}(\vec{p};\lambda_D) = \frac{-(-1)^{\frac{1}{2}-\lambda_2}}{\sqrt{(2\pi)^3 2m_D}2E_p m_D} \times \eta^{\dagger}_{-\lambda_1}\left\{2\vec{p}\cdot\vec{\xi}^{\lambda_D}\left(F(|\vec{p}|)-G(|\vec{p}|)+I(|\vec{p}|)\frac{m_D E_p}{m_N^2}\right)+2(\vec{\sigma}\cdot\vec{p}\vec{\sigma}\cdot\vec{\xi}^{\lambda_D}-\hat{\vec{p}}\cdot\vec{\xi}^{\lambda_D})H(|\vec{p}|)\frac{m_D}{m_N}\right\}\eta_{\lambda_2}\,. \tag{H.10}$$

Through an explicit computation, it is elementary to prove the following properties for two-component Pauli spinors

$$\begin{aligned}(-1)^{\frac{1}{2}-\lambda'}\,\xi^{\dagger}_{\lambda}\eta_{\lambda'} &= -i\,\sigma_y|_{\lambda\lambda'}\,,\\ (-1)^{\frac{1}{2}-\lambda'}\,\xi^{\dagger}_{\lambda}\vec{\sigma}\eta_{\lambda'} &= -i\,\vec{\sigma}\sigma_y|_{\lambda\lambda'}\,,\end{aligned} \tag{H.11}$$

and since any complex 2x2-matrix A can be decomposed as $A = A_0\mathbb{1} + \sum_i A_i\sigma_i$, we have in general

$$(-1)^{\frac{1}{2}-\lambda'}\,\xi^{\dagger}_{\lambda}A\eta_{\lambda'} = -i\,A\sigma_y|_{\lambda\lambda'}\,. \tag{H.12}$$

Applying this to our previous expression for the deuteron wave function, a direct comparison can be made with Eq. (H.8). In this way, we obtain the deuteron wave functions u, w, v_s and v_t as a function of the *Dnp*-vertex form factors. After inverting these relations, we reach our final result

$$\begin{aligned}F(|\vec{p}|) &= \pi\sqrt{2m_D}(2E_p-m_D)\left[u(|\vec{p}|)-\frac{1}{\sqrt{2}}w(|\vec{p}|)+\sqrt{\frac{3}{2}}\frac{m_N}{|\vec{p}|}v_t(|\vec{p}|)\right]\,,\\ G(|\vec{p}|) &= \pi\sqrt{2m_D}(2E_p-m_D)\left[\frac{m_N u(|\vec{p}|)}{E_p+m_N}+\frac{m_N(2E_p+m_N)}{|\vec{p}|^2}\frac{w(|\vec{p}|)}{\sqrt{2}}+\sqrt{\frac{3}{2}}\frac{m_N}{|\vec{p}|}v_t(|\vec{p}|)\right]\,,\\ H(|\vec{p}|) &= \pi\sqrt{2m_D}\sqrt{\frac{3}{2}}\frac{E_p m_N}{|\vec{p}|}v_t(|\vec{p}|)\,,\\ I(|\vec{p}|) &= -\pi\sqrt{2m_D}\frac{m_N^2}{m_D}\left[(2E_p-m_D)\left(\frac{u(|\vec{p}|)}{E_p+m_N}-\frac{E_p+2m_N}{|\vec{p}|^2}\frac{w(|\vec{p}|)}{\sqrt{2}}\right)+\frac{\sqrt{3}m_D}{|\vec{p}|}v_s(|\vec{p}|)\right]\,.\end{aligned} \tag{H.13}$$

APPENDIX I

Parameters of the Regge-plus-resonance model

Essentially, all models are wrong, but some are useful.
— George E. P. Box

The RPR formalism was introduced in Chapter 2. It consists of non-resonant contributions that are parametrised as Regge-trajectory exchange in the t-channel and the exchange of a selection of nucleon and Δ resonances in the s-channel. Expressions for the different contributions to the transition amplitude are given in Paragraph D.3.3. In this appendix, we summarise the coupling constants that feature in these amplitudes.

The parameters for the Λ-production RPR model are given in Table I.1. This model has been published in Refs. [39, 69]. Table I.2 lists the coupling constants of the RPR model for the Σ-production channels discussed in Refs. [40, 69].

In Chapter 3, we develop a formalism which permits to derive the coupling constants for the reaction channels with a neutron target and/or a neutral kaon in the final state from those for $p(\gamma, K^+)\Lambda$ and $p(\gamma, K^+)\Sigma^0$. The EM coupling constants of resonance-exchange diagrams have error bars due to the experimental uncertainties related to photocoupling helicity amplitudes. We have adopted the helicity amplitude labelled SM95 in Table 3.1.

Table I.1 – Coupling constants of the RPR-2007 model optimised for $K\Lambda$ production. The cutoff mass for the Gaussian form factor at the strong-interaction vertices of the resonance-exchange diagrams is fixed at $\Lambda = 1636.53\,\mathrm{MeV}$.

		$p(\gamma, K^+)\Lambda$	$n(\gamma, K^0)\Lambda$
Born	$g_{K\Lambda N}$	$-1.064 \cdot 10^{+1}$	—
$K^*(892)$	$G^v_{K^*}$	$1.082 \cdot 10^{+1}$	$-1.655 \cdot 10^{+1}$
	$G^t_{K^*}$	$-2.906 \cdot 10^{+1}$	$4.446 \cdot 10^{+1}$
$S_{11}(1650)$	G_{N^*}	$-2.251 \cdot 10^{-2}$	$4.951 \pm 1.575 \cdot 10^{-3}$
$P_{11}(1710)$	G_{N^*}	$-2.348 \cdot 10^{-1}$	$0.681 \pm 5.235 \cdot 10^{-1}$
$P_{13}(1720)$	$G^{(1)}_{N^*}$	$3.842 \cdot 10^{-2}$	$-1.460 \pm 7.685 \cdot 10^{-2}$
	$G^{(2)}_{N^*}$	$-1.812 \cdot 10^{-2}$	$0.906 \pm 1.957 \cdot 10^{-2}$
	X	$1.437 \cdot 10^{+2}$	$1.437 \cdot 10^{+2}$
	Y	$5.696 \cdot 10^{+1}$	$5.696 \cdot 10^{+1}$
	Z	$-3.117 \cdot 10^{-1}$	$-3.117 \cdot 10^{-1}$
$P_{13}(1900)$	$G^{(1)}_{N^*}$	$-7.499 \cdot 10^{-1}$	$0.000 \pm 1.500 \cdot 10^{+0}$
	$G^{(2)}_{N^*}$	$3.377 \cdot 10^{-1}$	$0.000 \pm 6.754 \cdot 10^{-1}$
	X	$-1.770 \cdot 10^{+1}$	$-1.770 \cdot 10^{+1}$
	Y	$2.588 \cdot 10^{+0}$	$2.588 \cdot 10^{+0}$
	Z	$-8.878 \cdot 10^{-1}$	$-8.878 \cdot 10^{-1}$
$D_{13}(1900)$	$G^{(1)}_{N^*}$	$1.115 \cdot 10^{+0}$	$0.000 \pm 2.230 \cdot 10^{+0}$
	$G^{(2)}_{N^*}$	$5.105 \cdot 10^{-1}$	$0.000 \pm 1.021 \cdot 10^{+0}$
	X	$4.031 \cdot 10^{+1}$	$4.031 \cdot 10^{+1}$
	Y	$-1.399 \cdot 10^{+1}$	$-1.399 \cdot 10^{+1}$
	Z	$-3.969 \cdot 10^{-2}$	$-3.969 \cdot 10^{-2}$

Table I.2 – Coupling constants of the RPR-2007 model optimised for $K\Sigma$ production. The cutoff mass for the Gaussian form factor at the strong-interaction vertices of the resonance-exchange diagrams is fixed at $\Lambda = 1593.37\,\mathrm{MeV}$.

		$p(\gamma, K^+)\Sigma^0$	$p(\gamma, K^0)\Sigma^+$	$n(\gamma, K^0)\Sigma^0$	$n(\gamma, K^+)\Sigma^-$
Born	$g_{K\Sigma N}$	$4.606 \cdot 10^{+0}$	—	—	$6.514 \cdot 10^{+0}$
$K^*(892)$	$G^v_{K^*}$	$1.454 \cdot 10^{+1}$	$1.110 \cdot 10^{+0}$	$-7.852 \cdot 10^{-1}$	$2.056 \cdot 10^{+1}$
	$G^t_{K^*}$	$-2.725 \cdot 10^{+1}$	$-2.081 \cdot 10^{+0}$	$1.472 \cdot 10^{+0}$	$-3.854 \cdot 10^{+1}$
$S_{11}(1650)$	G_{N^*}	$-1.391 \cdot 10^{-1}$	$-1.967 \cdot 10^{-1}$	$-3.060 \pm 0.974 \cdot 10^{-2}$	$4.328 \pm 1.377 \cdot 10^{-2}$
$D_{33}(1700)$	$G^{(1)}_{N^*}$	$-2.463 \cdot 10^{+0}$	$1.741 \cdot 10^{+0}$	$-2.463 \cdot 10^{+0}$	$-1.741 \cdot 10^{+0}$
	$G^{(2)}_{N^*}$	$-2.057 \cdot 10^{+0}$	$1.455 \cdot 10^{+0}$	$-2.057 \cdot 10^{+0}$	$-1.455 \cdot 10^{+0}$
	X	$-4.999 \cdot 10^{+0}$	$-4.999 \cdot 10^{+0}$	$-4.999 \cdot 10^{+0}$	$-4.999 \cdot 10^{+0}$
	Y	$-4.521 \cdot 10^{+0}$	$-4.521 \cdot 10^{+0}$	$-4.521 \cdot 10^{+0}$	$-4.521 \cdot 10^{+0}$
	Z	$-1.577 \cdot 10^{-1}$	$-1.577 \cdot 10^{-1}$	$-1.577 \cdot 10^{-1}$	$-1.577 \cdot 10^{-1}$
$P_{11}(1710)$	G_{N^*}	$1.744 \cdot 10^{-1}$	$2.466 \cdot 10^{-1}$	$0.506 \pm 3.888 \cdot 10^{-1}$	$-0.715 \pm 5.499 \cdot 10^{-1}$
$P_{13}(1720)$	$G^{(1)}_{N^*}$	$1.839 \cdot 10^{-1}$	$2.600 \cdot 10^{-1}$	$0.699 \pm 3.677 \cdot 10^{-1}$	$-0.988 \pm 5.201 \cdot 10^{-1}$
	$G^{(2)}_{N^*}$	$5.689 \cdot 10^{-2}$	$8.045 \cdot 10^{-2}$	$2.844 \pm 6.144 \cdot 10^{-2}$	$-4.022 \pm 8.689 \cdot 10^{-2}$
	X	$-6.114 \cdot 10^{+0}$	$-6.114 \cdot 10^{+0}$	$-6.114 \cdot 10^{+0}$	$-6.114 \cdot 10^{+0}$
	Y	$-4.490 \cdot 10^{-1}$	$-4.490 \cdot 10^{-1}$	$-4.490 \cdot 10^{-1}$	$-4.490 \cdot 10^{-1}$
	Z	$3.276 \cdot 10^{+0}$	$3.276 \cdot 10^{+0}$	$3.276 \cdot 10^{+0}$	$3.276 \cdot 10^{+0}$
$P_{13}(1900)$	$G^{(1)}_{N^*}$	$9.811 \cdot 10^{-1}$	$1.387 \cdot 10^{+0}$	$0.000 \pm 1.962 \cdot 10^{+0}$	$0.000 \pm 2.775 \cdot 10^{+0}$
	$G^{(2)}_{N^*}$	$1.890 \cdot 10^{+0}$	$2.674 \cdot 10^{+0}$	$0.000 \pm 3.781 \cdot 10^{+0}$	$0.000 \pm 5.347 \cdot 10^{+0}$
	X	$4.465 \cdot 10^{+0}$	$4.465 \cdot 10^{+0}$	$4.465 \cdot 10^{+0}$	$4.465 \cdot 10^{+0}$
	Y	$-3.495 \cdot 10^{+0}$	$-3.495 \cdot 10^{+0}$	$-3.495 \cdot 10^{+0}$	$-3.495 \cdot 10^{+0}$
	Z	$-2.442 \cdot 10^{-1}$	$-2.442 \cdot 10^{-1}$	$-2.442 \cdot 10^{-1}$	$-2.442 \cdot 10^{-1}$
$S_{31}(1900)$	G_{N^*}	$3.236 \cdot 10^{-1}$	$-2.288 \cdot 10^{-1}$	$3.236 \cdot 10^{-1}$	$2.288 \cdot 10^{-1}$
$P_{31}(1910)$	G_{N^*}	$-2.597 \cdot 10^{-1}$	$1.836 \cdot 10^{-1}$	$-2.597 \cdot 10^{-1}$	$-1.836 \cdot 10^{-1}$
$P_{33}(1920)$	$G^{(1)}_{N^*}$	$4.709 \cdot 10^{-1}$	$-3.329 \cdot 10^{-1}$	$4.709 \cdot 10^{-1}$	$3.329 \cdot 10^{-1}$
	$G^{(2)}_{N^*}$	$4.589 \cdot 10^{-1}$	$-3.245 \cdot 10^{-1}$	$4.589 \cdot 10^{-1}$	$3.245 \cdot 10^{-1}$
	X	$8.031 \cdot 10^{+0}$	$8.031 \cdot 10^{+0}$	$8.031 \cdot 10^{+0}$	$8.031 \cdot 10^{+0}$
	Y	$2.416 \cdot 10^{+0}$	$2.416 \cdot 10^{+0}$	$2.416 \cdot 10^{+0}$	$2.416 \cdot 10^{+0}$
	Z	$-5.272 \cdot 10^{-1}$	$-5.272 \cdot 10^{-1}$	$-5.272 \cdot 10^{-1}$	$-5.272 \cdot 10^{-1}$

APPENDIX J

Experimental data

Facts are meaningless.
You could use facts to prove anything that's even remotely true.
— Homer Simpson

In this appendix, an overview is given of the published datasets for kaon photoproduction from the nucleon.

In Tables J.1 and J.2, the experimental data for the $p(\gamma, K^+)\Lambda$ and $p(\gamma, K^+)\Sigma^0$ reactions is given. The datasets used in Refs. [39, 40] to optimise the RPR-2007 model are marked in the rightmost column. The fitted coupling constants are listed in Appendix I.

The $p(\gamma, K^0)\Sigma^+$ reaction data is enumerated in Table J.3. The last column marks the datasets used in Section 3.3 to optimise the $K^{*0}(892)$'s EM coupling constant and explore the possibility of a third Regge trajectory.

Table J.4 provides an overview of the published experimental data for the $n(\gamma, K^+)\Sigma^-$ reaction. To date, no results have been published for the $n(\gamma, K^0)\Lambda$ and $n(\gamma, K^0)\Sigma^0$ reactions.

Table J.1 – List of published experimental data for the reaction $p(\gamma, K^+)\Lambda$ in chronological order per observable. The datasets used to determine the RPR-2007 model are marked in the last column.

Observable	Year	Experiment	Reference	# data points	Fitted
σ	1998	SAPHIR	Tran *et al.* [124]	24	
	2004	SAPHIR	Glander *et al.* [125]	36	
	2006	CLAS	Bradford *et al.* [119]	78	
$\frac{d\sigma}{d\Omega}$	1969	SLAC	Boyarski *et al.* [113]	56	✓
	1998	SAPHIR	Tran *et al.* [124]	90	
	2004	SAPHIR	Glander *et al.* [125]	720	
	2004	CLAS	McNabb *et al.* [121]	920	
	2006	CLAS	Bradford *et al.* [119]	1377	✓
	2006	LEPS	Sumihama *et al.* [135]	54	
	2007	LEPS	Hicks *et al.* [132]	12	
	2010	CLAS	McCracken *et al.* [123]	2066	
Σ	1979	SLAC	Quinn *et al.* [114]	9	✓
	2003	LEPS	Zegers *et al.* [122]	45	✓
	2006	LEPS	Sumihama *et al.* [135]	54	
	2007	LEPS	Hicks *et al.* [132]	4	
	2007	GRAAL	Lleres *et al.* [120]	66	✓
P	1972	DESY	Vogel *et al.* [115]	7	✓
	1998	SAPHIR	Tran *et al.* [124]	12	
	2004	SAPHIR	Glander *et al.* [125]	30	
	2004	CLAS	McNabb *et al.* [121]	233	✓
	2007	GRAAL	Lleres *et al.* [120]	66	✓
	2010	CLAS	McCracken *et al.* [123]	1707	
T	1978	BONN	Althoff *et al.* [142]	3	✓
	2008	GRAAL	Lleres *et al.* [141]	66	
C_x, C_z	2007	CLAS	Bradford *et al.* [140]	320	
$O_{x'}, O_{z'}$	2008	GRAAL	Lleres *et al.* [141]	66	

Table J.2 – List of published experimental data for the reaction $p(\gamma, K^+)\Sigma^0$ in chronological order per observable. The datasets used to determine the RPR-2007 model are marked in the last column.

Observable	Year	Experiment	Reference	# data points	Fitted
σ	1998	SAPHIR	Tran *et al.* [124]	21	
	2004	SAPHIR	Glander *et al.* [125]	33	
	2006	CLAS	Bradford *et al.* [119]	72	
$\frac{d\sigma}{d\Omega}$	1969	SLAC	Boyarski *et al.* [113]	48	✓
	1998	SAPHIR	Tran *et al.* [124]	70	
	2004	SAPHIR	Glander *et al.* [125]	660	
	2004	CLAS	McNabb *et al.* [121]	782	
	2006	CLAS	Bradford *et al.* [119]	1280	✓
	2006	LEPS	Sumihama *et al.* [135]	54	
	2006	LEPS	Kohri *et al.* [134]	73	
	2010	CLAS	Dey *et al.* [130]	2089	
Σ	1979	SLAC	Quinn *et al.* [114]	9	✓
	2003	LEPS	Zegers *et al.* [122]	45	✓
	2006	LEPS	Sumihama *et al.* [135]	54	
	2006	LEPS	Kohri *et al.* [134]	35	
	2007	GRAAL	Lleres *et al.* [120]	42	✓
P	1998	SAPHIR	Tran *et al.* [124]	12	
	2004	SAPHIR	Glander *et al.* [125]	16	
	2004	CLAS	McNabb *et al.* [121]	98	✓
	2007	GRAAL	Lleres *et al.* [120]	8	✓
	2010	CLAS	Dey *et al.* [130]	455	
C_x, C_z	2007	CLAS	Bradford *et al.* [140]	190	

Table J.3 – List of published experimental data for the reaction $p(\gamma, K^0)\Sigma^+$ in chronological order per observable. The datasets used in Section 3.3 for fitting are marked in the last column.

Observable	Year	Experiment	Reference	# data points	Fitted
σ	1999	SAPHIR	Goers *et al.* [232]	5	
	2005	SAPHIR	Lawall *et al.* [154]	12	
	2008	CB/ELSA-TAPS	Castelijns *et al.* [155]	12	
$\frac{d\sigma}{d\Omega}$	1999	SAPHIR	Goers *et al.* [232]	18	
	2003	CLAS	Carnahan [157]	48	✓
	2005	SAPHIR	Lawall *et al.* [154]	120	✓
	2008	CB/ELSA-TAPS	Castelijns *et al.* [155]	72	✓
P	1999	SAPHIR	Goers *et al.* [232]	4	
	2005	SAPHIR	Lawall *et al.* [154]	10	
	2008	CB/ELSA-TAPS	Castelijns *et al.* [155]	72	✓

Table J.4 – List of published experimental data for the reaction $n(\gamma, K^+)\Sigma^-$ in chronological order per observable.

Observable	Year	Experiment	Reference	# data points
$\frac{d\sigma}{d\Omega}$	2006	LEPS	Kohri *et al.* [134]	72
	2010	CLAS	Anefalos Pereira *et al.* [151]	388
Σ	2006	LEPS	Kohri *et al.* [134]	36

APPENDIX K

Hyperon-nucleon interaction

This appendix deals with the hyperon-nucleon interaction. In the first section, we sketch the kinematics of the hyperon-nucleon scattering reaction. Section K.2 introduces the transition matrix elements that are required for the calculation of the YN-FSI contribution to EM kaon production from the deuteron (see Section 5.6.3). They will be expressed in terms of the helicity amplitudes of the hyperon-nucleon scattering process. The latter can be obtained within the context of non-relativistic hyperon-nucleon potential models. The issue of the off-shell extrapolation of the scattering amplitude is the subject of Section K.3. In the final section, we will briefly present the Jülich model whose scattering amplitudes will be adopted in this dissertation.

K.1 Kinematics

Throughout this appendix, we will consider the following (in)elastic scattering reaction

$$Y' + N' \to Y + N \,, \tag{K.1}$$

where we label the incoming hyperon and nucleon with primes. This notation is somewhat uncommon, but simplifies the comparison with Section 5.6, where we present the YN-FSI contribution to kaon production from the deuteron.

The kinematics of the scattering process are fixed by specifying the invariant mass W_{YN} and the hyperon's scattering angle $\theta^*_{YY'}$ in the YN-CM frame. The latter is given by

$$\cos\theta^*_{YY'} = \frac{\vec{p}^{\,*}_{Y} \cdot \vec{p}^{\,*}_{Y'}}{|\vec{p}^{\,*}_{Y}||\vec{p}^{\,*}_{Y'}|} \,. \tag{K.2}$$

As was pointed out in Paragraph 5.6.3, the hyperon-nucleon rescattering diagram is most readily obtained in the YN-CM frame using the primed reference frame that was introduced in Eq. (5.3). Four-momenta in this frame are denoted with an asterisk, i.e. $\boldsymbol{p}^*_i$. The elementary scattering reaction,

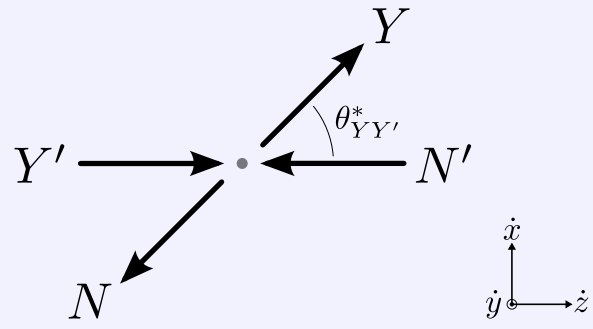

Figure K.1 – Orientation of the dotted reference frame $(\dot{x}, \dot{y}, \dot{z})$ for the $Y'N' \to YN$ reaction in the YN-CM frame.

on the other hand, is typically described in a reference frame $(\dot{x}, \dot{y}, \dot{z})$ that has its $\dot{z}$ axis along the incoming hyperon and the $\dot{y}$ axis perpendicular to the reaction plane. This *dotted* frame is illustrated in figure K.1 and is defined through

$$\dot{\vec{z}} = \frac{\vec{p}^{\,*}_{Y'}}{|\vec{p}^{\,*}_{Y'}|}\,, \qquad \dot{\vec{y}} = \frac{\vec{p}^{\,*}_{Y'} \times \vec{p}^{\,*}_{Y}}{|\vec{p}^{\,*}_{Y'} \times \vec{p}^{\,*}_{Y}|}\,, \qquad \dot{\vec{x}} = \dot{\vec{y}} \times \dot{\vec{z}}\,. \tag{K.3}$$

The four-vectors of the particles participating in reaction (K.1) are represented in the dotted reference frame as

$$\dot{\boldsymbol{p}}^{\,*}_i = \mathsf{r}\boldsymbol{p}^{\,*}_i\,, \tag{K.4}$$

with r the rotation that connects both frames. It consists of rotations about the z and y axis that bring the momentum of the incoming hyperon along the z axis and is followed by an additional rotation about the z axis that moves the outgoing particles in the xz plane. Caution is needed to ensure that the momentum of the outgoing hyperon lies along the positive x axis. Explicitly, we have

$$\mathsf{r} = r_z(\theta_\mathsf{r}) r_y(-\theta^*_{Y'}) r_z(-\phi^*_{Y'})\,, \tag{K.5}$$

with

$$\theta_\mathsf{r} = \frac{\pi}{2} - 2\arctan\left(\frac{\sqrt{1-\cos^2\theta^*_{YY'}} - \sin\theta^*_Y\left(\sin\phi^*_{Y'}\cos\phi^*_Y - \cos\phi^*_{Y'}\sin\phi^*_Y\right)}{\cos\theta^*_{Y'}\sin\theta^*_Y\left(\cos\phi^*_{Y'}\cos\phi^*_Y + \sin\phi^*_{Y'}\sin\phi^*_Y\right) - \sin\theta^*_{Y'}\cos\theta^*_Y}\right)\,, \tag{K.6}$$

for $\cos\theta^*_{YY'} \neq 1$. When $\cos\theta^*_{YY'} = 1$, θ_r is arbitrary. In case the argument of the arctangent is singular, $\theta_\mathsf{r} = \pm\pi/2$, where the positive (negative) sign occurs for a positive (negative) nominator.

K.2 Transition amplitudes

In Paragraph 5.6.3, expressions are derived for the YN-FSI contribution to the kaon-production transition amplitude. There, the hyperon-nucleon rescattering diagram is written in terms of

$$\begin{aligned}\langle \boldsymbol{p}_Y, \lambda_Y; \boldsymbol{p}_N, \lambda_N | \hat{\mathrm{J}}_{\mathrm{YN}} | \boldsymbol{p}_{Y'}, \lambda_{Y'}; \boldsymbol{p}_{N'}, \lambda_{N'} \rangle &\overset{\text{YN-CM}}{=} \\ \overline{u}_a(\vec{p}^{\,*}_Y, \lambda_Y)\overline{u}_b(\vec{p}^{\,*}_N, \lambda_N)\, \Gamma^{\mathrm{YN}}_{ab;cd}\, u_c(\vec{p}^{\,*}_{Y'}, \lambda_{Y'}) u_d(\vec{p}^{\,*}_{N'}, \lambda_{N'})\,,\end{aligned} \tag{K.7}$$

where the elementary rescattering vertex Γ^{YN} is sandwiched between spinors for the incoming and outgoing particles. This transition amplitude is to be evaluated in the YN-CM frame with its helicities

defined in the primed reference frame. In the previous section, we introduced dotted coordinates as the most natural reference frame for the description of the elementary hyperon-nucleon scattering process. In that frame, the hyperon-nucleon vertex operator reads

$$\dot{\Gamma}^{\mathrm{YN}}_{ab;cd} = S_{ae}(\mathsf{r}) S_{bf}(\mathsf{r})\, \Gamma^{\mathrm{YN}}_{ef;gh}\, S_{gc}(\mathsf{r}^{-1}) S_{hd}(\mathsf{r}^{-1})\,, \tag{K.8}$$

where

$$S(t^{-1}) = \gamma^0 S^\dagger(t) \gamma^0\,, \tag{K.9}$$

is the representation of the inverse transformation t^{-1} in Dirac space [218]. After inserting the unity operator several times in Eq. (K.7) and applying the transformation rule for helicity spinors provided in Paragraph C.2, we obtain for the transition amplitude

$$\begin{aligned}\langle \boldsymbol{p}_Y, \lambda_Y; \boldsymbol{p}_N, \lambda_N |\, \hat{\mathrm{J}}_{\mathrm{YN}}\, | \boldsymbol{p}_{Y'}, \lambda_{Y'}; \boldsymbol{p}_{N'}, \lambda_{N'} \rangle = \sum_{\mu_{Y'}, \mu_{N'}, \mu_Y, \mu_N} \Big[\mathfrak{D}^{1/2}_{\mu_Y, \lambda_Y} \left(r(\mathsf{r}, \vec{p}^{\,*}_Y) \right) \Big]^* \\ \times \Big[\mathfrak{D}^{1/2}_{\mu_N, \lambda_N} \left(r(\mathsf{r}, \vec{p}^{\,*}_N) \right) \Big]^* \mathfrak{D}^{1/2}_{\mu_{Y'}, \lambda_{Y'}} \left(r(\mathsf{r}, \vec{p}^{\,*}_{Y'}) \right) \mathfrak{D}^{1/2}_{\mu_{N'}, \lambda_{N'}} \left(r(\mathsf{r}, \vec{p}^{\,*}_{N'}) \right) \mathcal{T}^{\mathrm{YN}}_{\mu_Y, \mu_N; \mu_{Y'}, \mu_{N'}}\,,\end{aligned} \tag{K.10}$$

where we have introduced helicity amplitudes

$$\mathcal{T}^{\mathrm{YN}}_{\lambda_Y, \lambda_N; \lambda_{Y'}, \lambda_{N'}} = \overline{u}_a(\dot{\vec{p}}^{\,*}_Y, \lambda_Y) \overline{u}_b(\dot{\vec{p}}^{\,*}_N, \lambda_N)\, \dot{\Gamma}^{\mathrm{YN}}_{ab;cd}\, u_c(\dot{\vec{p}}^{\,*}_{Y'}, \lambda_{Y'}) u_d(\dot{\vec{p}}^{\,*}_{N'}, \lambda_{N'})\,, \tag{K.11}$$

for the hyperon-nucleon scattering reaction with the helicities defined in the dotted reference frame. With the help of the explicit form of the rotation r and the definition of the helicity transformation given in Eq. (C.2), the different Wick rotations can be worked out. One finds

$$r(\mathsf{r}, \vec{p}^{\,*}_i) = r_z(\Phi_i)\,, \tag{K.12}$$

for $i = Y', N', Y, N$. Since the Wigner rotation matrix is diagonal for rotations about the z axis (see Section A.2), this implies that the rotation r conserves the helicities and merely introduces an additional phase. We wish to stress the importance of using the quaternion representation of the rotation group introduced in Appendix B. Since we are rotating spinors, the isomorphism between this representation and SU(2) is crucial to obtain the correct phases. In the most general case, no elegant closed form exists for the rotation angles Φ_i. However, they can easily be found numerically. The phase for the incoming hyperon is the noted exception. It simply reads

$$\Phi_{Y'} = \theta_{\mathsf{r}}\,. \tag{K.13}$$

Introducing the Wick rotations into the Wigner rotation matrices of Eq. (K.10), we obtain

$$\langle \boldsymbol{p}_Y, \lambda_Y; \boldsymbol{p}_N, \lambda_N |\, \hat{\mathrm{J}}_{\mathrm{YN}}\, | \boldsymbol{p}_{Y'}, \lambda_{Y'}; \boldsymbol{p}_{N'}, \lambda_{N'} \rangle = e^{-i(\lambda_{Y'}\theta_{\mathsf{r}} + \lambda_{N'}\Phi_{N'} - \lambda_Y \Phi_Y - \lambda_N \Phi_N)}\, \mathcal{T}^{\mathrm{YN}}_{\lambda_Y, \lambda_N; \lambda_{Y'}, \lambda_{N'}}\,. \tag{K.14}$$

K.3 Off-shell scattering

In the previous section, we have focused on the frame-dependence of the helicities that feature in the transition amplitude for hyperon-nucleon scattering. A second important aspect of the amplitude is the kinematics at which it is to be evaluated. In Section K.1, we have noted that the elementary scattering process depends on the variables W_{YN} and $\theta^*_{YY'}$. However, when the rescattering vertex is inserted in a loop diagram such as the YN-FSI contribution considered in Paragraph 5.6.3, this no

longer holds true. Because of the deuteron's binding energy and the energy-momentum conserving delta functions at the different interaction vertices, the rescattering hyperon is generally off its mass shell, i.e.

$$\boldsymbol{p}_{Y'}^2 \neq m_{Y'}^2 \,. \tag{K.15}$$

The hyperon-nucleon scattering vertex operator Γ^{YN} has, to our knowledge, not been considered in a covariant field-theoretical framework. A number of hyperon-nucleon potential models are available on the other hand [199–201], and the question arises how the scattering amplitude with one off-mass-shell leg can be obtained within the context of non-relativistic scattering theory.

Potential models construct a phenomenological potential that serves as a kernel to solve a Lippmann-Schwinger equation. In doing so, one obtains a half-off-energy-shell amplitude

$$\mathcal{T}^{\mathrm{YN}}_{\lambda_Y,\lambda_N;\lambda_{Y'},\lambda_{N'}}(W,\theta^*_{YY'};W') \,, \tag{K.16}$$

with W' and W the invariant masses of the initial and final state respectively. As one can have $W' \neq W$, the $\Sigma N \to \Lambda N$ transitions can occur below the physical threshold of the initial hyperon-nucleon state, for example. In the limit of physical scattering, one has $W' \to W$ and the half-off-shell amplitude converges to the on-shell amplitude

$$\mathcal{T}^{\mathrm{YN}}_{\lambda_Y,\lambda_N;\lambda_{Y'},\lambda_{N'}}(W,\theta^*_{YY'}) \equiv \mathcal{T}^{\mathrm{YN}}_{\lambda_Y,\lambda_N;\lambda_{Y'},\lambda_{N'}}(W,\theta^*_{YY'};W) \,. \tag{K.17}$$

It can be shown that off-energy-shell amplitudes in non-relativistic scattering theory and amplitudes with off-mass-shell legs from relativistic quantum field theory have the same on-shell limit [233]. The off-shell extrapolations, however, are not unique. When the hyperon-nucleon transition amplitude with one leg off-mass-shell is needed in the off-shell contribution to the YN-FSI diagram (see Eq. (5.131)), we will consider the following half off-energy-shell amplitude

$$\mathcal{T}^{\mathrm{YN}}_{\lambda_Y,\lambda_N;\lambda_{Y'},\lambda_{N'}}(W_{YN},\theta^*_{YY'};\widetilde{W}_{Y'N'}) \,, \tag{K.18}$$

with

$$\widetilde{W}_{Y'N'} = \sqrt{|\vec{p}^{\,*}_{Y'}|^2 + m_{Y'}^2} + \sqrt{|\vec{p}^{\,*}_{Y'}|^2 + m_{N'}^2} \,. \tag{K.19}$$

In the limit that the rescattering hyperon Y' inside the loop is on its mass shell, one has

$$\widetilde{W}_{Y'N'} \to W_{YN} \,, \tag{K.20}$$

and the half off-energy-shell amplitude converges to the on-shell amplitude.

K.4 Jülich model

In Section 6.2, the effect of the YN-FSI contribution to the dynamics of strangeness production from the deuteron is investigated. As input, we adopt the hyperon-nucleon transition amplitudes as calculated within the Jülich model, which is discussed at length in Ref. [199].

The different elastic and inelastic hyperon-nucleon scattering reactions can be grouped in four charge channels

$$q = +2: \quad \Sigma^+ p \to \Sigma^+ p \,, \tag{K.21}$$

$$q = +1: \quad \Lambda p, \Sigma^+ n, \Sigma^0 p \to \Lambda p, \Sigma^+ n, \Sigma^0 p \,, \tag{K.22}$$

$$q = 0: \quad \Lambda n, \Sigma^0 n, \Sigma^- p \to \Lambda n, \Sigma^0 n, \Sigma^- p \,, \tag{K.23}$$

$$q = -1: \quad \Sigma^- n \to \Sigma^- n \,. \tag{K.24}$$

Table K.1 – Coefficients of the isospin decomposition of the hyperon-nucleon amplitudes in the particle basis. $\langle YN|\,T^{1/2}\,|YN\rangle$ and $\langle \Sigma N|\,T^{3/2}\,|\Sigma N\rangle$ are the isospin $I=1/2$ and $I=3/2$ amplitudes respectively.

	$\langle \Lambda N\vert\, T^{1/2}\,\vert \Lambda N\rangle$	$\langle \Sigma N\vert\, T^{1/2}\,\vert \Sigma N\rangle$	$\langle \Sigma N\vert\, T^{3/2}\,\vert \Sigma N\rangle$	$\langle \Lambda N\vert\, T^{1/2}\,\vert \Sigma N\rangle$
$\langle \Lambda p\vert T\vert \Lambda p\rangle$	1	0	0	0
$\langle \Lambda p\vert T\vert \Sigma^+ n\rangle$	0	0	0	$-\sqrt{\frac{2}{3}}$
$\langle \Lambda p\vert T\vert \Sigma^0 p\rangle$	0	0	0	$-\sqrt{\frac{1}{3}}$
$\langle \Lambda n\vert T\vert \Lambda n\rangle$	1	0	0	0
$\langle \Lambda n\vert T\vert \Sigma^0 n\rangle$	0	0	0	$\sqrt{\frac{1}{3}}$
$\langle \Lambda n\vert T\vert \Sigma^- p\rangle$	0	0	0	$-\sqrt{\frac{2}{3}}$
$\langle \Sigma^+ p\vert T\vert \Sigma^+ p\rangle$	0	0	1	0
$\langle \Sigma^+ n\vert T\vert \Sigma^+ n\rangle$	0	$\frac{2}{3}$	$\frac{1}{3}$	0
$\langle \Sigma^+ n\vert T\vert \Sigma^0 p\rangle$	0	$-\frac{\sqrt{2}}{3}$	$-\frac{\sqrt{2}}{3}$	0
$\langle \Sigma^0 p\vert T\vert \Sigma^0 p\rangle$	0	$\frac{1}{3}$	$\frac{2}{3}$	0
$\langle \Sigma^0 n\vert T\vert \Sigma^0 n\rangle$	0	$\frac{1}{3}$	$\frac{2}{3}$	0
$\langle \Sigma^0 n\vert T\vert \Sigma^- p\rangle$	0	$-\frac{\sqrt{2}}{3}$	$\frac{\sqrt{2}}{3}$	0
$\langle \Sigma^- p\vert T\vert \Sigma^- p\rangle$	0	$\frac{2}{3}$	$\frac{1}{3}$	0
$\langle \Sigma^- n\vert T\vert \Sigma^- n\rangle$	0	0	1	0

In the Jülich-model, however, the helicity amplitudes are obtained in the isospin basis [234]. For hyperon-nucleon scattering, there are only two isospin channels

$$I=\frac{1}{2}: \qquad \Lambda N, \Sigma N \to \Lambda N, \Sigma N\,, \tag{K.25}$$

$$I=\frac{3}{2}: \qquad \Sigma N \to \Sigma N\,. \tag{K.26}$$

In order to go from the isospin basis to the particle basis, we calculate the isospin decomposition of the amplitudes using the states defined in Eq. (3.7). The different coefficients are listed Table K.1.

For every isospin transition and each point in phase space, there are a total of sixteen helicity amplitudes. Parity invariance of the strong interaction, however, yields [100]

$$\mathcal{T}^{\mathrm{YN}}_{\lambda_Y,\lambda_N;\lambda_{Y'},\lambda_{N'}} = (-1)^{\lambda_{Y'}-\lambda_{N'}-\lambda_Y+\lambda_N}\mathcal{T}^{\mathrm{YN}}_{-\lambda_Y,-\lambda_N;-\lambda_{Y'},-\lambda_{N'}}\,, \tag{K.27}$$

which allows to reduce the number of independent amplitude by a factor of two. We define

$$\begin{aligned}
\mathcal{T}^{\mathrm{YN}}_1 &= \mathcal{T}^{\mathrm{YN}}_{++;++}\,, & \mathcal{T}^{\mathrm{YN}}_2 &= \mathcal{T}^{\mathrm{YN}}_{++;--}\,,\\
\mathcal{T}^{\mathrm{YN}}_3 &= \mathcal{T}^{\mathrm{YN}}_{+-;+-}\,, & \mathcal{T}^{\mathrm{YN}}_4 &= \mathcal{T}^{\mathrm{YN}}_{+-;-+}\,,\\
\mathcal{T}^{\mathrm{YN}}_5 &= \mathcal{T}^{\mathrm{YN}}_{++;+-}\,, & \mathcal{T}^{\mathrm{YN}}_6 &= \mathcal{T}^{\mathrm{YN}}_{+-;++}\,,\\
\mathcal{T}^{\mathrm{YN}}_7 &= \mathcal{T}^{\mathrm{YN}}_{++;-+}\,, & \mathcal{T}^{\mathrm{YN}}_8 &= \mathcal{T}^{\mathrm{YN}}_{-+;++}\,,
\end{aligned} \tag{K.28}$$

where $\pm$ is shorthand notation for the helicities $\lambda=\pm\frac{1}{2}$. In case of elastic scattering, the amplitudes also obey time-reversal invariance [100]

$$\mathcal{T}^{\mathrm{YN}}_{\lambda_Y,\lambda_N;\lambda_{Y'},\lambda_{N'}} = (-1)^{\lambda_{Y'}-\lambda_{N'}-\lambda_Y+\lambda_N}\mathcal{T}^{\mathrm{YN}}_{\lambda_{Y'},\lambda_{N'};\lambda_Y,\lambda_N}\,, \tag{K.29}$$

and one has

$$\mathcal{T}_5^{\rm YN} = -\mathcal{T}_6^{\rm YN}\,, \quad \text{and} \quad \mathcal{T}_7^{\rm YN} = -\mathcal{T}_8^{\rm YN}\,. \tag{K.30}$$

The mass differences between the different hyperons is relatively small, i.e. of the order of $\approx 78\,\text{MeV}$. This implies the ΛN and ΣN channels will be strongly coupled. Therefore, a non-relativistic CC Lippmann-Schwinger equation is solved in momentum space in order to obtain the scattering amplitude. This is most readily done with partial-wave decomposed amplitudes in the JLS-basis

$$\mathcal{T}^{{\rm YN},JM}_{L,S;L',S'} \equiv \langle JM;LS|\,\mathcal{T}^{\rm YN}\,|JM;L'S'\rangle\,. \tag{K.31}$$

More details can be found in Ref. [193].

Since we require helicity amplitudes as input for our formalism, the amplitudes in the JLS-basis need to be converted. This can be achieved by inverting Eqs. (B.13) and (B.14) of Ref. [193]. After some algebra, one obtains relations for the partial-wave helicity amplitudes

$$\begin{aligned}
\mathcal{T}_{1,2}^{\rm YN,J} &= \pm\frac{1}{2}\mathcal{T}^{{\rm YN},JM}_{J,0;J,0} + \frac{1}{2}\frac{J+1}{2J+1}\mathcal{T}^{{\rm YN},JM}_{J+1,1;J+1,1} + \frac{1}{2}\frac{J}{2J+1}\mathcal{T}^{{\rm YN},JM}_{J-1,1;J-1,1} \\
&\quad - \frac{1}{2}\frac{\sqrt{J(J+1)}}{2J+1}\left(\mathcal{T}^{{\rm YN},JM}_{J+1,1;J-1,1} + \mathcal{T}^{{\rm YN},JM}_{J-1,1;J+1,1}\right)\,, \qquad \text{(K.32)}\\
\mathcal{T}_{3,4}^{\rm YN,J} &= \pm\frac{1}{2}\mathcal{T}^{{\rm YN},JM}_{J,1;J,1} + \frac{1}{2}\frac{J}{2J+1}\mathcal{T}^{{\rm YN},JM}_{J+1,1;J+1,1} + \frac{1}{2}\frac{J+1}{2J+1}\mathcal{T}^{{\rm YN},JM}_{J-1,1;J-1,1} \\
&\quad + \frac{1}{2}\frac{\sqrt{J(J+1)}}{2J+1}\left(\mathcal{T}^{{\rm YN},JM}_{J+1,1;J-1,1} + \mathcal{T}^{{\rm YN},JM}_{J-1,1;J+1,1}\right)\,, \qquad \text{(K.33)}\\
\mathcal{T}_{5,7}^{\rm YN,J} &= \mp\frac{1}{2}\mathcal{T}^{{\rm YN},JM}_{J,0;J,1} + \frac{1}{2}\frac{J}{2J+1}\mathcal{T}^{{\rm YN},JM}_{J+1,1;J-1,1} - \frac{1}{2}\frac{J+1}{2J+1}\mathcal{T}^{{\rm YN},JM}_{J-1,1;J+1,1} \\
&\quad - \frac{1}{2}\frac{\sqrt{J(J+1)}}{2J+1}\left(\mathcal{T}^{{\rm YN},JM}_{J+1,1;J+1,1} - \mathcal{T}^{{\rm YN},JM}_{J-1,1;J-1,1}\right)\,, \qquad \text{(K.34)}\\
\mathcal{T}_{6,8}^{\rm YN,J} &= \mp\frac{1}{2}\mathcal{T}^{{\rm YN},JM}_{J,1;J,0} - \frac{1}{2}\frac{J+1}{2J+1}\mathcal{T}^{{\rm YN},JM}_{J+1,1;J-1,1} + \frac{1}{2}\frac{J}{2J+1}\mathcal{T}^{{\rm YN},JM}_{J-1,1;J+1,1} \\
&\quad - \frac{1}{2}\frac{\sqrt{J(J+1)}}{2J+1}\left(\mathcal{T}^{{\rm YN},JM}_{J+1,1;J+1,1} - \mathcal{T}^{{\rm YN},JM}_{J-1,1;J-1,1}\right)\,. \qquad \text{(K.35)}
\end{aligned}$$

Finally, the partial-wave helicity amplitudes need to be recomposed

$$\begin{aligned}
\mathcal{T}_1^{\rm YN} &= \sum_J (2J+1)\mathcal{T}_1^{{\rm YN},J} d^J_{0,0}(\theta^*_{YY'})\,, & \mathcal{T}_2^{\rm YN} &= \sum_J (2J+1)\mathcal{T}_2^{{\rm YN},J} d^J_{0,0}(\theta^*_{YY'})\,,\\
\mathcal{T}_3^{\rm YN} &= \sum_J (2J+1)\mathcal{T}_3^{{\rm YN},J} d^J_{1,1}(\theta^*_{YY'})\,, & \mathcal{T}_4^{\rm YN} &= \sum_J (2J+1)\mathcal{T}_4^{{\rm YN},J} d^J_{-1,1}(\theta^*_{YY'})\,,\\
\mathcal{T}_5^{\rm YN} &= \sum_J (2J+1)\mathcal{T}_5^{{\rm YN},J} d^J_{1,0}(\theta^*_{YY'})\,, & \mathcal{T}_6^{\rm YN} &= -\sum_J (2J+1)\mathcal{T}_6^{{\rm YN},J} d^J_{1,0}(\theta^*_{YY'})\,,\\
\mathcal{T}_7^{\rm YN} &= -\sum_J (2J+1)\mathcal{T}_7^{{\rm YN},J} d^J_{1,0}(\theta^*_{YY'})\,, & \mathcal{T}_8^{\rm YN} &= \sum_J (2J+1)\mathcal{T}_8^{{\rm YN},J} d^J_{1,0}(\theta^*_{YY'})\,.
\end{aligned} \tag{K.36}$$

In our calculations, we have considered partial waves up to $J = 5$.

Samenvatting

Nederlands is geen taal,
maar een verkoudheid
— Jacques Brel

Inleiding

Vooraleer een fenomeen doorgerekend kan worden, dient men er allereerst de relevante vrijheidsgraden van te bepalen. Dit lijkt triviaal, maar het antwoord ligt vaak niet voor de hand en vereist het een grondige kennis van de materie.

De hadronenfysica confronteert ons met een weelde aan fenomenen. Enerzijds is er het deuteron, een proton-neutron paar dat slechts met een fractie van zijn restmassa gebonden is. Aan de andere kant van het spectrum spelen zich overal in de kosmos hoogenergetische reacties af, die men poogt na te bootsen in deeltjesversnellers. Dit alles kan verklaard worden aan de hand van de theorie van de sterke wisselwerking, kwantum-chromodynamica, en de bijbehorende elementaire velden, quarks en gluonen.

De sterke wisselwerking voldoet aan enkele opmerkelijke eigenschappen die ervoor zorgen dat het zich onderscheidt van de andere fundamentele krachten. De wisselwerking wordt kleiner naarmate interagerende deeltjes zich naar elkaar toe bewegen. Anderzijds neemt de kracht van de wisselwerking toe met toenemende afstand tussen de deeltjes. Dit contra-intuïtieve aspect geeft aanleiding tot *confinement*. Quarks worden nooit vrij waargenomen maar enkel gebonden in kleurloze objecten. De koppelingssterkte van de sterke wisselwerking variëert snel als functie van de lengte- en energieschaal, waardoor de relevante vrijheidsgraden constant wijzigen.

Het nucleon is de alomtegenwoordige manifestatie van de confinement van quarks. Door middel van diep-inelastische verstrooiingsexperimenten is een vrij compleet beeld opgebouwd van de intrigerende structuur van het nucleon. Gluonen staan in voor ongeveer de helft van de impuls van het proton en de vreemde quarks in de zee leveren een niet te verwaarlozen bijdrage tot de spin. Desalniettemin kan dit complexe systeem gemiddeld gezien beschreven worden als een gebonden toestand van drie valentie quarks. Dit vormt het uitgangspunt van constituente-quarkmodellen die ontegensprekelijk

hadronspectra, symmetrie-eigenschappen en elektromagnetische vormfactoren succesvol weten te beschrijven. Maar waar ligt de limiet van deze gemiddeld-veldbeschrijving? Vanaf welke energieën treedt de overgang naar partonische vrijheidsgraden op?

Nucleonspectroscopie

Het in kaart brengen van alle baryonen en hun aangeslagen toestanden speelt een cruciale rol binnen de hadronenfysica. De massa's, vervalbreedtes en transitie-vormfactoren van nucleonresonanties vormen namelijk de link met de modellen die trachten de structuur van baryonen te doorgronden. De stand van zaken op experimenteel gebied wordt tweejaarlijks gebundeld in de *Review of Particle Physics* (RPP). Die haalt zijn informatie vooral uit partiële-golfanalyses (*partial-wave analysis*, PWA) van pion-nucleon (πN) verstrooiingsdata. Deze experimentele gegevens kunnen echter ook verwerkt worden samen met data uit inelastische kanalen en fotongeïnduceerde reacties. De verschillende analyses slagen er niet in om een eenduidige interpretatie te geven, terwijl zij toch een vergelijkbare overeenkomst vinden met het experiment. Over de eerste paar aangeslagen toestanden van het nucleon is er eensgezindheid, maar reeds heel snel lopen de bevindingen over het aantal resonanties, hun massa's en de bijbehorende kwantumgetallen uiteen.

De overeenkomst tussen theoretische voorspellingen en de opgelijste resonanties in de RPP vertoont een gelijkaardig patroon. Onder de 1800 MeV-grens slagen constituente-quarkmodellen erin om een adequaat beeld te schetsen. Hogerop in het nucleonspectrum loopt het echter mis. Het aantal voorspelde toestanden is een veelvoud van hetgeen experimenteel is vastgesteld. In de literatuur wordt verwezen naar de ontbrekende (*missing*) resonanties. Dit kan erop wijzen dat constituente-quarkmodellen gebruik maken van de verkeerde vrijheidsgraden. Alternatieve modellen, die één paar quarks als gebonden beschouwen, voorspellen namelijk dat het nucleonspectrum veel minder rijk is. Een andere verklaring bestaat erin dat vele aangeslagen toestanden niet worden waargenomen, vanwege de dominantie van de πN data bij het opstellen van de RPP.

Vreemdheidsproductie aan het nucleon

Elektromagnetische (EM) vreemdheidsproductie biedt mogelijks een antwoord op deze situatie. De aanwezigheid van vreemde deeltjes als eindproduct van de reactie duidt erop dat een vreemd quark-antiquarkpaar in de zee van het nucleon wordt aangeslagen. De productie van kaonen is bijgevolg gevoelig voor nieuwe vrijheidsgraden in het nucleon. Dit kan ertoe leiden dat bepaalde (ontbrekende) resonanties niet vervallen naar een pion en een nucleon, maar naar een kaon en een hyperon. Dit intuïtieve beeld wordt bovendien bevestigd door berekeningen aan de hand van constituente-quarkmodellen.

De zoektocht naar ontbrekende resonanties heeft ertoe geleid dat EM vreemdheidsproductie een essentieel deel uitmaakt van de onderzoeksactiviteiten aan toonaangevende experimentele faciliteiten zoals ELSA en MAMI in Duitsland, ESFR in Frankrijk, Jefferson Lab in de VS en SPring-8 in Japan. In de afgelopen jaren zijn dan ook veel nieuwe experimentele resultaten verschenen. Aangezien het verval van het geproduceerde hyperon zelf-analyserend is, bekomt men de polarisatie van het uitgaande baryon zonder bijkomende apparatuur. Dit biedt de mogelijkheid om een *compleet* kaonproductie-experiment uit te voeren. Mits de bepaling van de ongepolariseerde differentiële werkzame doorsnede, aangevuld met zeven weloverwogen polarisatieobservabelen, kan de onderliggende reactieamplitude

namelijk ondubbelzinnig bepaald worden. Op deze manier kunnen heel stringente beperkingen opgelegd worden aan modellen die trachten de dynamica van de vreemdheidsproductiereactie te doorgronden. Bij dit alles dient echter een kanttekening geplaatst te worden. In de praktijk is ieder experiment uiteraard onderhevig aan fouten inherent aan het meetproces. Deze meetfouten doen teniet aan de volledigheid van een compleet experiment en in de praktijk zullen een hele resem observabelen vereist zijn om een eenduidig beeld te vormen van de reactiedynamica.

Vreemdheidsproductie aan het deuteron

Tot op heden gaat, zowel op experimenteel gebied als vanuit theoretisch standpunt, de meeste aandacht uit naar kaonproductie-experimenten aan het proton. De beschikbare database wordt namelijk gedomineerd door de $p(\gamma^{(*)}, K^+)\Lambda$- en $p(\gamma^{(*)}, K^+)\Sigma^0$-reacties. Een grondige studie van de vier overige kaonproductiekanalen biedt echter de mogelijkheid om vreemdheidsproductie beter te begrijpen aangezien deze reacties sterk complementair zijn. Een dergelijk initiatief vereist dat ook experimenten op het neutron uitgevoerd worden. Omdat dit deeltje onstabiel is, neemt men toevlucht tot deuterium als trefkern. Deze zwakgebonden toestand van een proton en een neutron is namelijk de ideale bron van neutronen. Vanuit dit oogpunt, wordt in dit doctoraat een model voor kaonproductie aan het deuteron ontwikkeld.

Het Regge-plus-resonantiemodel

Een betrouwbare beschrijving van kaonproductie aan het proton en neutron is uiteraard van cruciaal belang om vreemdheidsproductie aan het deuteron te modelleren. In eerste instantie wordt de productie van geladen kaonen aan het proton onder de loep genomen.

Het isobaar model

De EM productie van de verschillende pseudoscalaire mesonen vertoont vele gelijkenissen. Omdat het pion het lichtste meson is, werd pionproductie historisch als eerste bestudeerd. Bij lage energieën vertoont de werkzame doorsnede enkele markante pieken die een duidelijke manifestatie zijn van de vorming van aangeslagen nucleontoestanden. Een beschrijving aan de hand van hadronische vrijheidsgraden is dan ook aan de orde. Men spreekt over een hadrodynamisch raamwerk. Aangezien mesonen, baryonen en hun aangeslagen toestanden geen elementaire deeltjes zijn, beschikt men niet over een fundamentele theorie om hun interacties te begrijpen. Als alternatief wordt een effectieve-veldentheoretische formulering op poten gezet die steunt op fenomenologische interactie-Lagrangianen. Die laatste beschrijven de meest algemene interactie tussen hadronen en worden opgesteld op basis van symmetrieprincipes zodat aan de eigenschappen van de onderliggende elementaire veldentheorie voldaan is. De eindige extensie van de hadronen wordt in rekening gebracht met behulp van vormfactoren. Dit dient echter doordacht geïmplementeerd te worden omdat vormfactoren de ijkinvariantie van de interactie kunnen opheffen.

Binnen het isobaar model wordt de reactiedynamica beschreven aan de hand van laagste-orde (*tree-level*) Feynmandiagrammen die opgesteld worden op basis van effectieve interactie-Lagrangianen. Deze diagrammen worden op meerdere manieren geclassificeerd. Men maakt het onderscheid tussen

het s-, t- en u-kanaal al naargelang er een niet-vreemd baryon, een meson of een hyperon uitgewisseld wordt. Wanneer het deeltje in de intermediaire toestand geen resonantie is, spreekt men over een Borndiagram. Het laatste en belangrijkste onderscheid heeft te maken met de impulsoverdracht binnen het diagram. Doorgaans is het uitgewisselde deeltje virtueel. De kinematica van kaonproductie zijn dusdanig dat bij de uitwisseling van nucleon- en deltaresonanties de intermediaire toestand zich echter op zijn massaschaal (*on-shell*) kan bevinden. Hierdoor wordt de propagator singulier en vertoont de transitieamplitude een pool. Men spreekt over een resonant diagram. De voornaamste drijfveer voor mesonproductie-experimenten is het potentiëel om nucleonresonanties te ontdekken. Vanuit dit oogpunt worden alle niet-resonante diagrammen beschouwd als achtergrondprocessen die de bepaling van het nucleonspectrum in de weg staan.

Het isobaar model steunt op een hadrodynamische beschrijving en niet op een fundamentele theorie. Hierdoor zijn de sterktes van de verschillende bijdragen tot de wisselwerking niet gekend en dienen zij bepaald te worden door middel van een fit aan de experimentele gegevens. Omdat de parameters van de resonante en achtergronddiagrammen gelijktijdig geoptimaliseerd worden, zijn zij sterk gecorreleerd met elkaar. Een correcte inschatting van de belangrijkste achtergrondcontributies is dan ook elementair. Wanneer het isobaar model aangewend wordt voor de studie van vreemdheidsproductie geldt dit gegeven des te meer. De gemeten werkzame doorsnede heeft een egaal energieverloop en vertoont niet de markante kenmerken die duiden op de aanwezigheid van overheersende resonante structuren. Dit wijst erop dat de achtergrondprocessen domineren en bijgevolg is het cruciaal dat zij correct in rekening gebracht worden.

Binnen het isobaar model wordt de achtergrond van de vreemdheidsproductiereactie beschreven door middel van de uitwisseling van de drie Borndiagrammen. Deze termen divergeren echter waardoor hun aanwezigheid nefast is bij hogere energieën. Deze situatie kan gecorrigeerd worden door de uitwisseling van vectormesonen in het t-kanaal en eventueel hyperonresonanties in het u-kanaal te beschouwen. Op deze manier worden echter een groot aantal extra parameters in het model geïntroduceerd. Bovendien blijkt dat de afschatting van de resonantieparameters sterk afhangt van de techniek waarmee de achtergrond onder controle wordt gehouden. Dit vraagt om een alternatieve beschrijving van de achtergrondbijdragen.

De Regge-plus-resonantiestrategie

Bij hoge energieën zijn hadronische vrijheidsgraden niet langer aangewezen. De dynamica van het vreemdheidsproductieproces wordt niet langer bepaald door nucleonresoanties en dit uit zich in vloeiende, egale werkzame doorsnedes die uitsluitend bepaald worden door achtergrondcontributies. In principe is dit het domein van de partonische vrijheidsgraden. Door middel van Regge-fenomenologie hoeven we echter geen afstand te doen van de isobaar beschrijving. Regge theorie laat ons toe om op een efficiënte manier een ganse familie aan deeltjes, een trajectorie[1], uit te wisselen met behulp van één enkel diagram. De kaonproductiedata in het hoge-energiegebied kan succesvol beschreven worden met de uitwisseling van een $K(494)$- en een $K^*(892)$-trajectorie in het t-kanaal. Deze beschrijving omvat slechts drie parameters.

Alhoewel Regge theorie afgeleid wordt bij asymptotisch hoge energieën en in de limiet van voorwaartse verstrooiingshoeken, blijkt het Regge model ook in het resonantiegebied een bevredigende beschrijving te geven van de beschikbare data. Uiteraard slaagt dit zuivere achtergrondmodel er niet in om

[1] een Regge-trajectorie wordt aangeduid met de naam van het lichtste hadron dat er deel van uitmaakt.

de subtiele structuren in de gemeten observabelen die het gevolg zijn van resonante bijdragen te beschrijven. Dit kan echter opgelost worden door resonante bijdragen toe te voegen.

De Regge-plus-resonantiestrategie (*Regge-plus-resonance*, RPR) bestaat erin om een hybridisch model op te stellen dat enerzijds de resonante bijdragen bij lage energieën beschrijft en terzelfertijd over de correcte hoge-energielimiet beschikt. Dit wordt verwezenlijkt door in eerste instantie het Regge model te optimaliseren aan de hand van experimentele gegevens bij hoge energieën. Vervolgens doet dit model dienst als parametrisatie van de achtergrondprocessen in het resonantiegebied. Zonder de achtergrondparameters aan te passen, worden resonante diagrammen toegevoegd en hun koppelingssterktes gefit aan de data. Het resulterende model heeft beduidend minder vrije parameters in vergelijking met isobare modellen. Bovendien slaagt men er op deze manier in om de bepaling van de sterktes van de resonante en niet-resonante diagrammen te ontkoppelen.

Het model

In het kader van het doctoraat van T. Corthals is een RPR-model ontwikkeld aan de hand van de destijds gepubliceerde data voor $p(\gamma^{(*)}, K^+)\Lambda$- en $p(\gamma^{(*)}, K^+)\Sigma^0$-productie. Dit model vormt het onderwerp van hoofdstuk 2. Aan de hand van hoge-energiedata stelt men het Regge model op. Dit achtergrondmodel wordt vervolgens aangerijkt met resonante contributies.

In het Λ-productiekanaal bekomt men een RPR-amplitude die erin slaagt de beschikbare data correct te beschrijven. De resonante bijdragen worden geleverd door de $S_{11}(1650)$, $P_{11}(1710)$, $P_{13}(1720)$, $P_{13}(1900)$ en $D_{13}(1900)$ nucleonresonanties. Over het bestaan van de eerste drie bestaat weinig twijfel aangezien ze ook een belangrijke rol spelen in andere reacties. De noodzaak om twee resonanties met een massa van 1900 MeV in te voeren is echter interessant. De $P_{13}(1900)$-resonantie werd reeds in enkele eerdere analyses geïntroduceerd en maakt deel uit van het door constituente-quarkmodellen voorspelde nucleonsprectrum. Er is echter geen plaats voor binnen het quark-diquark beeld. Het is dus een kandidaat om de controverse tussen beide op te lossen en de meest aangewezen vrijheidsgraden voor de beschrijving van nucleonstructuur vast te stellen. De $D_{13}(1900)$-resonantie tenslotte is in de RPR-analyse essentieel om de data te beschrijven, maar staat niet in de RPP. We hebben hier dus te maken met een mogelijke ontbrekende resonantie.

De beschrijving van het Σ-productiekanaal is minder éénduidig. De hoge-energiedata laten niet toe om een uniek Regge model te bepalen. Het teken van de tensorkoppeling van de $K^*(892)$-trajectorie blijft in het ongewisse. De twee bekomen modelvarianten worden Regge-3 en Regge-4 gedoopt. In het resonantiegebied is dezelfde set resonanties als in het Λ-kanaal van toepassing met uitzondering van de $D_{13}(1900)$-resonantie. Bovendien spelen in dit reactiekanaal ook Δ-resonanties een rol. De $D_{33}(1700)$-, $S_{31}(1900)$-, $P_{31}(1910)$- en $P_{33}(1920)$-resonanties maken deel uit van het RPR-model. De beschrijving van Σ-productie wijst dus ook in de richting van de $P_{13}(1900)$-resonantie. Er zijn echter geen aanwijzingen voor ontbrekende resonanties.

Sinds de publicatie van het RPR-model werden een groot aantal nieuwe experimentele resultaten gepubliceerd. Enerzijds werden reeds gekende grootheden met een veel hogere precisie gemeten en anderzijds kwamen ook enkele voorheen onbepaalde observabelen ter beschikking. De nieuwe data maken het mogelijk om het RPR-model kritisch tegen het licht te houden. De enkele conceptuele tekortkomingen van het huidige RPR-model werden weggewerkt in het kader van de doctoraten van L. De Cruz en T. Vrancx. Op basis van dit verbeterde RPR-model is momenteel een heranalyse van

de experimentele gegevens aan de gang.

Niettegenstaande de enkele imperfecties, blijkt uit de confrontatie van de RPR-modelberekeningen met de nieuwe data de sterke voorspellende kracht van het formalisme. Dit is vooral treffend wanneer vergeleken wordt met dubbele-polarisatieasymmetrieën. Deze worden adequaat beschrijven over een ruim energiegebied en dit zowel bij voorwaartse als achterwaartse hoeken. Bovendien is ook de extrapolatie naar reacties met virtuele fotonen uiterst betrouwbaar. De RPR-modelvoorspellingen voor electrongeïnduceerde vreemdheidsproductie zijn zondermeer impressionant te noemen, gegeven het feit dat geen nieuwe vrije parameters ingevoerd werden.

Uitbreiding van het RPR-formalisme

Het RPR-model werd geoptimaliseerd voor de beschrijving van de $K^+\Lambda$- en $K^+\Sigma^0$-productiekanalen. Om betrouwbare berekeningen uit te voeren voor vreemdheidsproductie aan het deuteron is het echter noodzakelijk om ook de resterende kanalen correct te karakteriseren. Dit wordt bemoeilijkt door de relatief kleine experimentele database. Om het gefitte RPR-model te kunnen gebruiken, dienen transformatieregels opgesteld te worden voor de koppelingsconstanten van de relevante diagrammen. Concreet zijn dit de t-kanaaldiagrammen van het $K(494)$- en $K^*(892)$-meson en de resonante diagrammen waarbij een resonantie uitgewisseld wordt in het s-kanaal. Dit onderwerp wordt uitvoerig behandeld in hoofdstuk 3.

Vreemdheidsproductie aan het neutron

In eerste instantie wordt de productie van kaonen aan een vrij neutron onderzocht. De conversie van de koppelingsconstanten in de sterke-interactievertices steunt op SU(2)-isospinsymmetrie. De transformatie in de EM vertices heeft meer voeten in de aarde. De verhouding van EM koppelingssterktes voor de resonante diagrammen kan uitgedrukt worden in termen van heliciteitsamplitudes. Deze amplitudes dienen experimenteel bepaald te worden in andere productiereacties zoals photongeïnduceerde pionproductie. De heliciteitsamplitudes die opgelijst staan in de RPP, hebben echter relatief grote foutenvlaggen. Bovendien zijn de heliciteitsamplitudes voor de $P_{13}(1900)$- en $D_{13}(1900)$-resonanties onbepaald.

De kwaliteit van de RPR-modelverspellingen aan het neutron wordt nagegaan aan de hand van experimentele gegevens voor het $n(\gamma, K^+)\Sigma^-$ kanaal. Deze data laten toe om een onderscheid te maken tussen de twee evenwaardige RPR-modellen in het Σ-productiekanaal. Vergelijkingen met de data laten duidelijk zien dat het Regge-4 model de werkzame doorsnede niet correct beschrijft. Het Regge-3 model daarentegen geeft wel een bevredigend resultaat. Wanneer ook de resonante bijdragen beschouwd worden, verbetert de overeenkomst met het experiment nog verder. De foutenvlaggen op de experimenteel bepaalde heliciteitsamplitudes spelen echter een belangrijke rol. De onzekerheden propageren naar het eindresultaat en geven aanleiding tot grote fluctuaties bij de berekening van werkzame doorsnedes. Enerzijds zet dit een limiet op de voorspellende kracht van het RPR-formalisme. Anderzijds zullen bijkomende metingen op het neutron ook toelaten om de heliciteitsamplitudes nauwkeuriger te bepalen.

Productie van neutrale kaonen

Ook bij de transformatie van de RPR-amplitudes naar reactiekanalen met een neutraal kaon in de finale toestand kunnen we steunen op isospinsymmetrie in de sterke-interactievertex. Dit is de enige vereiste aanpassing voor de resonante diagrammen. Het kaonuitwisselingsdiagram daarentegen is exact nul en de EM koppelingsconstantes van de $K^*(892)$-trajectorie moeten getransformeerd worden op basis van gegevens over het EM verval van dit meson.

Wanneer voorspellingen op basis van deze naïeve aanpak vergeleken worden met de beschikbare data in het $K^0\Sigma^-$-productiekanaal, blijkt de predictie de meetresultaten ruimschoots te overtreffen. Meerdere methodes worden onderzocht om dit problematische gedrag te corrigeren. Uiteindelijk wordt er gekozen voor een pragmatische aanpak waarbij de EM koppelingssterkte artificieel kleiner gemaakt wordt door hem te fitten aan de beschikbare data. Op deze manier wordt een behoorlijke beschrijving van de data gerealiseerd.

Radiatieve kaonvangst

Vooraleer het formalisme voor vreemdheidsproductie aan het deuteron geïntroduceerd wordt, is er een klein intermezzo in hoofstuk 4. De kruissymmetrische partner van photongeïnduceerde kaonproductie wordt er besproken. De radiatieve kaonvangstreactie geeft complementaire informatie vanwege zijn gevoeligheid voor hyperonresonanties. Net als het nucleonsprectrum is ook het bepalen van de aangeslagen toestanden van vreemde baryonen een belangrijk ijkpunt voor baryonstructuurmodellen.

Door de kruissymmetrie wordt de rol van de s- en u-kanaal in de transitieamplitude omgekeerd. Bij radiatieve kaonvangst zijn het dus de u-kanaaldiagrammen met hyperonresonanties in de intermediaire toestand die voor de resonante bijdragen zorgen. Aangezien de t-kanaalcontributie dezelfde blijft, kan het Regge-model uit hoofdstuk 2 opnieuw als parametrisatie van de achtergrond gebruikt worden.

De resultaten van het Regge-model worden vergeleken met de allereerste experimentele gegevens voor de differentiële werkzame doorsnede. In het $p(K^-,\gamma)\Lambda$-kanaal geeft de Regge-voorspelling reeds een goede beschrijving van de data. Het $p(K^-,\gamma)\Sigma^0$-resultaat daarentegen wijst op een belangrijke rol voor resonante bijdragen. Bij wijze van verkende analyse wordt getracht de beschrijving van de data te optimaliseren door één voor één enkele gekende hyperonresonaties uit de RPP aan de Regge-amplitude toe te voegen. De data laten niet toe om meerdere resonanties gelijktijdig te overwegen en er kunnen geen sluitende conclusies getrokken worden. De analyse wijst op een belangrijke rol voor hyperonresonanties in het 1550 (1700) MeV massagebied in het $\gamma\Lambda$ ($\gamma\Sigma^0$)-productiekanaal.

Vreemdheidsproductie aan het deuteron

Nu het RPR-formalisme geïntroduceerd is en er een efficiënt model voor de beschrijving van EM vreemdheidsproductie aan het vrije nucleon op punt staat, kan de stap gezet worden naar het deuteron.

Theoretisch raamwerk

Behalve de elementaire productieamplitude is ook de beschrijving van de structuur van de trefkern een essentieel ingrediënt om tot een correcte beschrijving te komen van kaonproductie aan het deuteron. Binnen een covariant formalisme wordt de transitievertex van een deuteron dat overgaat naar twee ongebonden nucleonen beschreven aan de hand van vier vormfactoren. Deze vormfactoren zijn op hun beurt gedefiniëerd in functie van de golffuncties van het deuteron. Op basis van niet-relativistische *realistische* nucleon-nucleon potentialen kunnen de deuterongolffuncties berekend worden. Er zijn ook relativistische resultaten beschikbaar die steunen op een parametrisatie van de nucleon-nucleon interactie op basis van een één-bosonuitwisselingspotentiaal bekomen in de covariante spectatortheorie (*covariant spectator theory*, CST). Alle modelresultaten zijn onderling consistent zolang de relatieve impuls van de constituenten kleiner is dan 400 MeV. Bij die energieën is de waarschijnlijkheid om nog een nucleon in het deuteron aan te treffen echter reeds ettelijke grootteordes geslonken.

In hoofdstuk 5 wordt een covariant formalisme gepresenteerd voor de transitieamplitude van de kaonproductiereactie aan het deuteron op basis van de relativistische impulsbenadering. Deze benadering houdt in dat het inkomende foton interageert met slechts één enkel nucleon binnen het deuteron. Op die manier kan de complexe veeldeeltjestransitieoperator herleid worden tot een som van ééndeeltjestransitieoperatoren.

De belangrijkste bijdrage tot het reactiemechanisme wordt geleverd door de relativistische vlakke-golfimpulsbenadering (*relativistic plane-wave impulse approximation*, RPWIA). Dit diagram beschrijft de situatie waarbij de drie reactieproducten na de wisselwerking met het foton ongestoord de interactieregio verlaten. Hogere-orde effecten komen voor wanneer het kaon-hyperonpaar of het hyperon-nucleonpaar herverstrooien. In dit doctoraat wordt enkel de laatste mogelijkheid beschouwd. De bijdrage van de hyperon-nucleon herverstooiing (*hyperon-nucleon final-state interaction*, YN-FSI) wordt berekend in de veronderstelling dat het spectatornucleon altijd *on-shell* is. Het YN-FSI-diagram valt uiteen in een *on-shell* en een *off-shell* stuk. In het eerste geval zijn de inkomende en uitgaande deeltjes in de herverstrooiingsvertex op hun massaschaal. Bij de *off-shell*-contributie daarentegen is het intermediair hyperon virtueel. Dit maakt het mogelijk dat de $\Sigma N \to \Lambda N$ transitie reeds bijdragen levert vooraleer de fysische drempelenergie overschreden wordt.

Resultaten

Hoofdstuk 6 is gewijd aan de resultaten die bekomen werden aan de hand van het formalisme uit hoofdstuk 5. Het RPR-model uit hoofdstuk 2 wordt hierbij toegepast als elementaire kaonproductieoperator. Voor de berekening van reacties op het gebonden neutron en processen waarbij een neutraal kaon gevormd wordt, zijn de transformaties uit hoofdstuk 3 essentieel.

In eerste instantie wordt het belang van de verschillende modelingrediënten in de RPWIA onderzocht. De momentumdistributie van het deuteron blijkt de bepalende factor die de differentiële werkzame doorsnede vorm geeft. De momentumdistributie piekt wanneer het spectatornucleon een impuls van om en bij de 50 MeV heeft. De regio's in de faseruimte van de vreemdheidsproductiereactie waar dit geldt, dragen dan ook maximaal bij tot de werkzame doorsnede. De absolute sterkte van de reactie wordt bepaald door de onderliggende elementaire reactieamplitude. Aangezien het foton koppelt aan een gebonden deeltje is de elementaire amplitude altijd *off-shell*. Aan de hand van een *on-shell*-reductie van de RPWIA-amplitude wordt het belang en de bijdrage van deze

off-shell-extrapolatie nagegaan. Er is enkel een belangrijk effect wanneer het spectatornucleon een hoge impuls wegdraagt en de werkzame doorsnede dus klein is. In diezelfde kinematische situatie is ook de gevoeligheid aan de gebruikte deuteron golffunctie het grootst. De allergrootste bron van onzekerheden op de bekomen resultaten zijn echter de heliciteitsamplitudes die aangewend worden om de elementaire reactie op het neutron uit te rekenen.

Na de studie van de RPWIA wordt de aandacht gevestigd op het effect van het YN-FSI-diagram. Hierbij wordt gebruik gemaakt van amplitudes die berekend werden met de hyperon-nucleon potentiaal van het Jülich model. Bij lage impulsen van het uitgaande nucleon is het effect van YN-FSI verwaarloosbaar. Bij hoge impulsen daarentegen wordt de kenmerkende isotrope productie van het nucleon verstoord door de herverstrooiing. Zowel het *on-shell* als het *off-shell* stuk van het diagram versterken de emissie van nucleonen in de voortwaartse richting. Voor de semi-inclusive kaonproductiereactie vinden we een gelijkaardig effect. Het YN-FSI-diagram speelt vooral een rol wanner de impuls van het foton en het kaon op één lijn liggen. Over het algemeen kan men vaststellen dat de relatieve bijdrage van het YN-FSI-diagram enkel significant is daar waar het quasi-vrije reactieproces niet domineert en de werkzame doorsnede bijgevolg klein is. Dit heeft als gevolg dat het deuteron als een efficiënte bron van neutronen kan beschouwd worden.

De modelberekeningen worden tenslotte vergeleken met de beschikbare data. Aan het LNS werden werkzame doorsnedes gemeten bij fotonenergieën dicht bij de drempelenergie. Het effect van YN-FSI is verwaarloosbaar bij deze kinematieken. De RPWIA-voorspellingen voor de semi-inclusive neutrale-kaonproductiedata zijn bevredigend. De vorm van de werkzame doorsnedes wordt correct beschreven en op de laagste fotonenergie na wordt ook de sterkte van de reactie goed voorspeld. De resultaten voor semi-inclusive Λ-productie zijn van dezelfde kwaliteit. Op gebied van electrongeïnduceerde processen is de hoeveelheid beschikbare data eerder beperkt. In totaal zijn er twee gepubliceerde datapunten voor semi-inclusive geladen-kaonproductie bij voorwaartse hoeken. De RPWIA-voorspelling overschat de data met ruwweg een factor twee à drie. Metingen over een groter energie- en hoekbereik zouden het mogelijk maken om de discrepantie tussen model en experiment beter te begrijpen.

Vooruitblik

In dit werk werd vreemdheidsproductie aan het nucleon en het deuteron uitgebreid besproken in het kader van het RPR-raamwerk. De reactiemechanismen zijn goed begrepen en de overeenkomst tussen theorie en experiment is bevredigend. Er blijft echter ruimte om de beschrijving van kaonproductiereacties verder te ontwikkelingen en te verbeteren.

In de nabije toekomst zullen een reeks nieuwe polarisatiemetingen voor de $n(\gamma, K^0)\Lambda$ en $n(\gamma, K^0)\Sigma^0$ reacties via de CLAS collaboratie beschikbaar worden. Deze data zullen toelaten om de uitbreidingen van het RPR-model die in hoofdstuk 3 gepresenteerd werden te evalueren. De geplande uitbreiding van de infrastructuur aan Jefferson Lab biedt bovendien de mogelijkheid om EM vreemdheidsproductie te bestuderen bij hoge energieën. De experimentele bepaling van de werkzame doorsnede van kaonproductiereacties aan het neutron of met een ongeladen kaon in de finale toestand zou waardevolle informatie bevatten om het Regge formalisme verder te verbeteren. Zoals in hoofdstuk 3 duidelijk werd, wordt het opstellen van een volledig RPR-model momenteel enigszins beperkt door een gebrek aan data in het energiegebied waar resonante bijdragen geen rol meer spelen.

Het elementaire kaonproductiemodel speelt uiteraard een essentiële rol bij de beschrijving van

vreemdheidsproductie aan het deuteron. De resultaten die in dit werk gepresenteerd worden, maken gebruik van het RPR-2007 model uit hoofdstuk 2. Zoals vermeld, is een heranalyse van de kaonproductiedatabase op basis van het uitgebreide RPR-formalisme aan de gang. Dit vernieuwde model zal uiteraard een betere beschrijving geven van het reactiemechanisme en toelaten om meer betrouwbare berekeningen voor vreemdheidsproductie aan het deuteron te bekomen.

De studie van vreemdheidsproductie aan het deuteron wordt voornamelijk gemotiveerd door de mogelijkheid om het reactiemechanisme aan het neutron te onderzoeken. De resultaten in hoofdstuk 6 hebben aangetoond dat het deuteron inderdaad een goede potentiële neutronenbron is. Om deze vaststelling verder te bevestigen is het van belang om overige herverstrooiingsdiagrammen te beschouwen. Met name het tweestapsproces, waarbij in eerste instantie een pion geproduceerd wordt, kan mogelijk een belangrijke bijdrage leveren. De berekening van dit diagram verloopt analoog aan die van YN-FSI. In de literatuur zijn meerdere modellen beschikbaar die EM pionproductie adequaat beschrijven. Om het tweestapsdiagram te evalueren, dient men ook over een correcte beschrijving van de $N(\pi, K)Y$-reactie te beschikken. Voor dit proces zijn weinig experimentele gegevens beschikbaar en de betrouwbaarheid van de berekening van het tweestapsdiagram zal dan ook verder theoretisch werk vereisen.

List of publications

Part of the results presented in this dissertation have been published in the literature, or presented at international conferences.

Papers

- T. Corthals, T. Van Cauteren, P. Vancraeyveld, J. Ryckebusch, and D. G. Ireland, *Electroproduction of kaons from the proton in a Regge-plus-resonance approach*. *Phys.Lett.* **B656** (2007) 186, arXiv:0704.3691 [nucl-th]
- P. Vancraeyveld, L. De Cruz, J. Ryckebusch, and T. Van Cauteren, *Regge-plus-resonance predictions for kaon photoproduction from the neutron*. *Phys.Lett.* **B681** (2009) 428, arXiv:0908.0446 [nucl-th]
- S. Prakhov, P. Vancraeyveld, *et al.*, *Measurement of K^-p radiative capture to $\gamma\Lambda$ and $\gamma\Sigma^0$ for p_{K^-} between 514 and 750 MeV/c*. *Phys.Rev.* **C82** (2009) 015201, arXiv:0912.1653 [nucl-th]
- L. De Cruz, D. G. Ireland, P. Vancraeyveld, and J. Ryckebusch, *Bayesian model selection for electromagnetic kaon production on the nucleon*. *Phys.Lett.* **B694** (2010) 33, arXiv:1004.0353 [nucl-th]
- T. Vrancx, L. De Cruz, J. Ryckebusch, and P. Vancraeyveld, *Consistent interactions for high-spin fermion fields*. *Phys.Rev.* **C84** (2011) 045201, arXiv:1105.2688 [nucl-th]

Presentations

- P. Vancraeyveld, T. Corthals, J. Ryckebusch and T. Van Cauteren, *Electromagnetic production of kaons from the proton in the Regge-plus-resonance model*. Poster presented at JLab's Users Group Meeting, Newport News, VA, USA (June 16, 2008).
- P. Vancraeyveld, L. De Cruz, D. G. Ireland, J. Ryckebusch and T. Van Cauteren, *Kaon photo- and electroproduction in a Regge-plus-resonance approach*. Contributed talk at Spring meeting of the DPG Division Hadronic and Nuclear Physics and EPS European Nuclear Physics Conference, Bochum, Germany (March 18, 2009).

- P. Vancraeyveld, L. De Cruz, J. Ryckebusch, and T. Van Cauteren, *Regge-model predictions for $K^+\Sigma$ photoproduction from the nucleon.* *AIP Conf.Proc.* **1182** (2009) 619, arXiv:0906.5505 [nucl-th]. Contributed talk at 10$^{\text{th}}$ Conference on the Intersection of Particle and Nuclear Physics, San Diego, CA, USA (May 26, 2009).
- P. Vancraeyveld, L. De Cruz, J. Ryckebusch, and T. Van Cauteren, *Regge-plus-resonance predictions for charged-kaon photoproduction from the deuteron.* *EPJ Web Conf.* **3** (2010) 03013, arXiv:0912.2679 [nucl-th]. Contributed talk at 19$^{\text{th}}$ International IUPAP Conference on Few-Body Problems in Physics, Bonn, Germany (September 1, 2009).
- P. Vancraeyveld, L. De Cruz, and J. Ryckebusch, *Regge-plus-resonance predictions for neutral-kaon photoproduction from the deuteron.* *AIP Conf.Proc.* **1374** (2011) 335, arXiv:1010.0113 [nucl-th]. Contributed talk at 12$^{\text{th}}$ International Conference on Meson-Nucleon Physics and the Structure of the Nucleon, Williamsburg, VA, USA (June 2, 2010).
- P. Vancraeyveld, L. De Cruz and J. Ryckebusch, *Regge-plus-resonance predictions for kaon photoproduction from the deuteron.* Poster presented at Gordon Research Conference on Photonuclear Reactions, Tilton, NH, USA (August 3, 2010).

Bibliography

If you steal from one author, it's plagiarism;
if you steal from many, it's research.
— Wilson Mizner

[1] K. Nakamura *et al.*, *Review of particle physics*. *J.Phys.* **G37** (2010) 075021. Available from http://pdglive.lbl.gov. Page 2, 22, 23, 34, 35, 43, 44, 55, 56, 117, 200.

[2] G. Höhler, *Pion-nucleon scattering*, vol. I/9b2 of *Landolt-Börnstein*. Springer Verlag, 1983. Page 2.

[3] R. E. Cutkosky, C. P. Forsyth, R. E. Hendrick, and R. L. Kelly, *Pion-nucleon partial wave amplitudes*. *Phys.Rev.* **D20** (1979) 2839. Page 2.

[4] R. A. Arndt, W. J. Briscoe, I. I. Strakovsky, and R. L. Workman, *George-Washington (GW) Data Analysis Center (DAC) Scattering Analysis Interactive Dail-in (SAID)*. Available from http://gwdac.phys.gwu.edu. Page 2, 200.

[5] V. Shklyar, H. Lenske, and U. Mosel, *A coupled-channel analysis of $K\Lambda$ production in the nucleon resonance region*. *Phys.Rev.* **C72** (2005) 015210, arXiv:nucl-th/0505010 [nucl-th]. Page 2, 23, 24.

[6] *Excited Baryon Analysis Center (EBAC)*. Available from http://ebac-theory.jlab.org. Page 2.

[7] M. Döring, C. Hanhart, F. Huang, S. Krewald, and U.-G. Meissner, *Analytic properties of the scattering amplitude and resonances parameters in a meson exchange model*. *Nucl.Phys.* **A829** (2009) 170, arXiv:0903.4337 [nucl-th]. Page 2.

[8] *Bonn-Gatchina partial-wave analysis*. Available from http://pwa.hiskp.uni-bonn.de. Page 2.

[9] G. Y. Chen, S. Kamalov, S. N. Yang, D. Drechsel, and L. Tiator, *Nucleon resonances in πN scattering up to energies $\sqrt{s} \leq 2.0$ GeV*. *Phys.Rev.* **C76** (2007) 035206, arXiv:nucl-th/0703096 [nucl-th]. Page 2.

[10] A. Usov and O. Scholten, *$K\Lambda$ and $K\Sigma$ photoproduction in a coupled channels framework*. *Phys.Rev.* **C72** (2005) 025205, arXiv:nucl-th/0503013 [nucl-th]. Page 2, 5.

[11] E. Klempt and J.-M. Richard, *Baryon spectroscopy*. *Rev.Mod.Phys.* **82** (2010) 1095, arXiv:0901.2055 [hep-ph]. Page 2, 3, 23.

[12] M. Anselmino, E. Predazzi, S. Ekelin, S. Fredriksson, and D. Lichtenberg, *Diquarks*. *Rev.Mod.Phys.* **65** (1993) 1199. Page 2.

[13] R. Koniuk and N. Isgur, *Baryon decays in a quark model with chromodynamics*. *Phys.Rev.* **D21** (1980) 1868. Page 2.

[14] S. Capstick, *Photoproduction and electroproduction of nonstrange baryon resonances in the relativized quark model*. *Phys.Rev.* **D46** (1992) 2864. Page 2.

[15] S. Capstick and W. Roberts, *Strange decays of nonstrange baryons*. *Phys.Rev.* **D58** (1998) 074011, arXiv:nucl-th/9804070 [nucl-th]. Page 2.

[16] T. Kuo, *Low-energy photoproduction of Λ^0 and K^+ from protons*. *Phys.Rev.* **129** (1963) 2264. Page 2.

[17] H. Thom, *Phenomenological analysis of $K^+\Lambda$ photoproduction*. *Phys.Rev.* **151** (1966) 1322. Page 2, 8.

[18] F. Renard and Y. Renard, *Photoproduction of $K^+\Lambda$ and $K^+\Sigma^0$ and $g_{\Lambda KN}$, $g_{\Sigma KN}$ coupling constants*. *Nucl.Phys.* **B25** (1971) 490. Page 2.

[19] R. Adelseck, C. Bennhold, and L. Wright, *Kaon photoproduction operator for use in nuclear physics*. *Phys.Rev.* **C32** (1985) 1681. Page 2.

[20] R. A. Adelseck and B. Saghai, *Kaon photoproduction: data consistency, coupling constants, and polarization observables*. *Phys.Rev.* **C42** (1990) 108. Page 2, 15.

[21] R. Williams, C. Ji, and S. Cotanch, *Crossing and duality consistent study of Λ, Σ^0, and $\Lambda(1405)$ production by kaon photoproduction and radiative capture*. *Phys.Rev.* **C43** (1991) 452. Page 2, 56.

[22] J. David, C. Fayard, G. Lamot, and B. Saghai, *Electromagnetic production of associated strangeness*. *Phys.Rev.* **C53** (1996) 2613. Page 2, 8, 24, 27, 56.

[23] T. Mart, C. Bennhold, H. Haberzettl, and L. Tiator, *Kaon–MAID*. Available from http://www.kph.uni-mainz.de/MAID/kaon/kaonmaid.html. Page 2, 40, 41.

[24] B. S. Han, M. K. Cheoun, K. Kim, and I.-T. Cheon, *An isobaric model for kaon photoproduction*. *Nucl.Phys.* **A691** (2001) 713, arXiv:nucl-th/9912011 [nucl-th]. Page 2, 24.

[25] T. Mart and C. Bennhold, *Evidence for a missing nucleon resonance in kaon photoproduction*. *Phys.Rev.* **C61** (2000) 012201, arXiv:nucl-th/9906096 [nucl-th]. Page 2.

[26] S. Hsiao, D. Lu, and S. N. Yang, *Pseudovector versus pseudoscalar coupling in kaon photoproduction: revisited*. *Phys.Rev.* **C61** (2000) 068201, arXiv:nucl-th/0004007 [nucl-th]. Page 2.

[27] S. Janssen, J. Ryckebusch, D. Debruyne, and T. Van Cauteren, *Kaon photoproduction: background contributions, form factors and missing resonances*. *Phys.Rev.* **C65** (2002) 015201, arXiv:nucl-th/0107028. Page 2, 5.

[28] O. V. Maxwell, *Model dependence in the photoproduction of kaons from protons and deuterons*. *Phys.Rev.* **C70** (2004) 044612. Page 2, 8.

[29] A. de la Puente, O. V. Maxwell, and B. A. Raue, *New fits to the reaction $\gamma p \to K^+\Lambda$*. *Phys.Rev.* **C80** (2009) 065205, arXiv:0809.3805 [nucl-th]. Page 2, 24.

[30] T. Mart, *Electromagnetic production of kaon near threshold*. *Phys.Rev.* **C82** (2010) 025209, arXiv:1007.5366 [nucl-th]. Page 2.

[31] Z.-P. Li, *The kaon photoproduction of nucleons in the chiral quark model*. *Phys.Rev.* **C52** (1995) 1648, arXiv:hep-ph/9502218 [hep-ph]. Page 2.

[32] Z.-P. Li, W.-H. Ma, and L. Zhang, *Kaon production via $\gamma N \to K\Sigma$ in the chiral quark model*. *Phys.Rev.* **C54** (1996) 2171(R). Page 2.

[33] D.-H. Lu, R. Landau, and S. Phatak, *Kaon photoproduction in the color dielectric model*. *Phys.Rev.* **C52** (1995) 1662. Page 2.

[34] Z.-P. Li, H.-X. Ye, and M.-H. Lu, *An unified approach to pseudoscalar meson photoproductions off nucleons in the quark model*. *Phys.Rev.* **C56** (1997) 1099–1113, arXiv:nucl-th/9706010 [nucl-th]. Page 2.

[35] S. Ahlig, R. Alkofer, C. Fischer, M. Oettel, H. Reinhardt, *et al.*, *Production processes as a tool to study parameterizations of quark confinement*. *Phys.Rev.* **D64** (2001) 014004, arXiv:hep-ph/0012282 [hep-ph]. Page 2.

[36] R. Alkofer, S. Ahlig, C. Fischer, and M. Oettel, *Kaon photoproduction and form-factors in a covariant and confining diquark quark model*. *Nucl.Phys.* **A680** (2001) 70. Page 2.

[37] E. Henley and K. Pham, *A simple quark model for $\gamma p \to K^+\Lambda^0$*. *Nucl.Phys.* **A842** (2010) 72, arXiv:1003.3438 [nucl-th]. Page 2.

[38] M. Guidal, J. M. Laget, and M. Vanderhaeghen, *Pion and kaon photoproduction at high energies: forward and intermediate angles*. *Nucl.Phys.* **A627** (1997) 645. Page 2, 5, 6, 19, 20, 26, 33.

[39] T. Corthals, J. Ryckebusch, and T. Van Cauteren, *Forward-angle $K^+\Lambda$ photoproduction in a Regge-plus-resonance approach*. *Phys.Rev.* **C73** (2006) 045207, arXiv:nucl-th/0510056. Page 2, 6, 8, 11, 21, 22, 23, 24, 25, 26, 28, 91, 157, 161.

[40] T. Corthals, D. G. Ireland, T. Van Cauteren, and J. Ryckebusch, *Regge-plus-resonance treatment of the $p(\gamma, K^+)\Sigma^0$ and $p(\gamma, K^0)\Sigma^+$ reactions at forward kaon angles*. *Phys.Rev.* **C75** (2007) 045204, arXiv:nucl-th/0612085. Page 2, 6, 8, 11, 21, 22, 23, 24, 25, 26, 28, 39, 91, 157, 161.

[41] T. Mart and T. Wijaya, *Extending isobar model for kaon photoproduction up to 16 GeV*. *Acta Phys.Pol.* **B34** (2003) 2651. Page 2, 6.

[42] T. Mart and C. Bennhold, *Kaon photoproduction in the Feynman and Regge theories*. arXiv:nucl-th/0412097 [nucl-th]. Page 2, 6.

[43] W.-T. Chiang, F. Tabakin, T. Lee, and B. Saghai, *Coupled channel study of $\gamma p \to K^+\Lambda$.* *Phys.Lett.* **B517** (2001) 101, arXiv:nucl-th/0104052 [nucl-th]. Page 2.

[44] J. Caro Ramon, N. Kaiser, S. Wetzel, and W. Weise, *Chiral SU(3) dynamics with coupled channels: inclusion of p-wave multipoles.* *Nucl.Phys.* **A672** (2000) 249–269, arXiv:nucl-th/9912053 [nucl-th]. Page 2.

[45] B. Juliá-Díaz, B. Saghai, T.-S. Lee, and F. Tabakin, *Dynamical coupled-channel approach to hadronic and electromagnetic production of kaon-hyperon on the proton.* *Phys.Rev.* **C73** (2006) 055204, arXiv:nucl-th/0601053 [nucl-th]. Page 2, 23.

[46] A. Anisovich, V. Kleber, E. Klempt, V. Nikonov, A. Sarantsev, *et al.*, *Baryon resonances and polarization transfer in hyperon photoproduction.* *Eur.Phys.J.* **A34** (2007) 243, arXiv:0707.3596 [hep-ph]. Page 2.

[47] B. Borasoy, P. Bruns, U.-G. Meissner, and R. Nissler, *A Gauge invariant chiral unitary framework for kaon photo- and electroproduction on the proton.* *Eur.Phys.J.* **A34** (2007) 161, arXiv:0709.3181 [nucl-th]. Page 2.

[48] R. Shyam, O. Scholten, and H. Lenske, *The associated photoproduction of K^+ meson off proton within a coupled-channels K-matrix approach.* *Phys.Rev.* **C81** (2010) 015204, arXiv:0911.3351 [hep-ph]. Page 2.

[49] T. Mart and A. Sulaksono, *Kaon photoproduction in a multipole approach.* *Phys.Rev.* **C74** (2006) 055203, arXiv:nucl-th/0609077 [nucl-th]. Page 3, 23.

[50] R. L. Workman, *Multipole analysis of kaon photoproduction data.* arXiv:1105.2967 [nucl-th]. Page 3.

[51] A. Sandorfi, S. Hoblit, H. Kamano, and T.-S. Lee, *Determining pseudoscalar meson photo-production amplitudes from complete experiments.* *J.Phys.G* **38** (2011) 053001, arXiv:1010.4555 [nucl-th]. Page 3, 15.

[52] V. Burkert and T. Lee, *Electromagnetic meson production in the nucleon resonance region.* *Int.J.Mod.Phys.* **E13** (2004) 1035, arXiv:nucl-ex/0407020 [nucl-ex]. Page 3.

[53] I. S. Barker, A. Donnachie, and J. K. Storrow, *Complete experiments in pseudoscalar photoproduction.* *Nucl.Phys.* **B95** (1975) 347. Page 3, 15.

[54] W.-T. Chiang and F. Tabakin, *Completeness rules for spin observables in pseudoscalar meson photoproduction.* *Phys.Rev.* **C55** (1997) 2054. Page 3, 15.

[55] H. Haberzettl, *Gauge invariant theory of pion photoproduction with dressed hadrons.* *Phys.Rev.* **C56** (1997) 2041, arXiv:nucl-th/9704057 [nucl-th]. Page 4, 5.

[56] L. De Cruz, D. G. Ireland, P. Vancraeyveld, and J. Ryckebusch, *Bayesian model selection for electromagnetic kaon production on the nucleon.* *Phys.Lett.* **B694** (2010) 33, arXiv:1004.0353 [nucl-th]. Page 4, 11, 21, 23.

[57] S. Janssen, J. Ryckebusch, W. Van Nespen, D. Debruyne, and T. Van Cauteren, *The role of hyperon resonances in $p(\gamma, K^+)\Lambda$ processes.* *Eur.Phys.J.* **A11** (2001) 105, arXiv:nucl-th/0105008. Page 5.

[58] D. G. Ireland, S. Janssen, and J. Ryckebusch, *A genetic algorithm analysis of N^* resonances in $p(\gamma, K^+)\Lambda$ reactions*. *Nucl.Phys.* **A740** (2004) 147. Page 5.

[59] R. Davidson and R. Workman, *Form-factors and photoproduction amplitudes*. *Phys.Rev.* **C63** (2001) 025210, arXiv:nucl-th/0101066 [nucl-th]. Page 5.

[60] F. Gross and D. Riska, *Current conservation and interaction currents in relativistic meson theories*. *Phys.Rev.* **C36** (1987) 1928. Page 5.

[61] M. M. Kaskulov and U. Mosel, *Deep exclusive charged π electroproduction above the resonance region*. *Phys.Rev.* **C81** (2010) 045202, arXiv:1001.1952 [hep-ph]. Page 6.

[62] B. G. Yu, T. K. Choi, and W. Kim, *Regge phenomenology of pion photoproduction off the nucleon at forward angles*. *Phys.Rev.* **C83** (2011) 025208, arXiv:1103.1203 [nucl-th]. Page 6.

[63] W.-T. Chiang, S. N. Yang, L. Tiator, M. Vanderhaeghen, and D. Drechsel, *A Reggeized model for η and η' photoproduction*. *Phys.Rev.* **C68** (2003) 045202. Page 6, 22.

[64] J. He and B. Saghai, *η production off the proton in a Regge-plus-chiral quark approach*. *Phys.Rev.* **C82** (2010) 035206, arXiv:1005.2797 [nucl-th]. Page 6, 22.

[65] S. Ozaki, H. Nagahiro, and A. Hosaka, *Charged K^* photoproduction in a Regge model*. *Phys.Rev.* **C81** (2010) 035206, arXiv:0910.0384 [hep-ph]. Page 6.

[66] S.-i. Nam and C.-W. Kao, $\Lambda(1520)$ *photoproduciton off the proton target with Regge contributions*. *Phys.Rev.* **C81** (2010) 055206, arXiv:1003.0700 [hep-ph]. Page 6.

[67] M. Guidal, J. M. Laget, and M. Vanderhaeghen, *Exclusive electromagnetic production of strangeness on the nucleon: review of recent data in a Regge approach*. *Phys.Rev.* **C68** (2003) 058201. Page 6, 21.

[68] R. Schumacher and M. Sargsian, *Scaling and resonances in elementary $K^+\Lambda$ photoproduction*. *Phys.Rev.* **C83** (2011) 025207, arXiv:1012.2126 [hep-ph]. Page 6.

[69] T. Corthals, *Regge-plus-resonance approach to kaon production from the proton*. PhD thesis, Ghent University, 2007. Available from http://inwpent5.ugent.be/papers/phdtamara.pdf. Page 6, 7, 8, 11, 19, 22, 27, 47, 91, 157.

[70] R. Machleidt and I. Slaus, *The Nucleon-nucleon interaction*. *J.Phys.G* **G27** (2001) R69, arXiv:nucl-th/0101056 [nucl-th]. Page 6.

[71] R. A. Gilman and F. Gross, *Electromagnetic structure of the deuteron*. *J.Phys.* **G28** (2002) R37, arXiv:nucl-th/0111015 [nucl-th]. Page 6.

[72] M. Garçon and J. Van Orden, *The deuteron: structure and form-factors*. *Adv.Nucl.Phys.* **26** (2001) 293, arXiv:nucl-th/0102049 [nucl-th]. Page 6.

[73] R. A. Adelseck and L. E. Wright, *Lambda-neutron interaction in kaon photoproduction from the deuteron*. *Phys.Rev.* **C39** (1989) 580. Page 7, 8.

[74] B. F. Gibson and E. V. Hungerford, *A Survey of hypernuclear physics*. *Phys.Rept.* **257** (1995) 349. Page 7.

[75] E. Hungerford, *Electroproduction of strange nuclei*. *Nucl.Phys.* **A691** (2001) 21. Page 7.

[76] O. Hashimoto and H. Tamura, *Spectroscopy of Λ hypernuclei*. *Prog.Part.Nucl.Phys.* **57** (2006) 564. Page 7.

[77] F. M. Renard and Y. Renard, *Hyperon-nucleon interactions and associate production on the deuteron*. *Nucl.Phys.* **B1** (1967) 389. Page 8.

[78] F. M. Renard and Y. Renard, *Final state Λ-neutron interactions in* $\gamma + d \to K^+ + \Lambda + n$. *Phys.Lett.* **B24** (1967) 159. Page 8.

[79] X. Li and L. Wright, *Final-state Λn interaction in K photoproduction from the deuteron*. *J.Phys.G* **G17** (1991) 1127. Page 8.

[80] X. Li, L. Wright, and C. Bennhold, *Kaon photoproduction on the neutron using deuterium*. *Phys.Rev.* **C45** (1992) 2011. Page 8.

[81] H. Yamamura, K. Miyagawa, T. Mart, C. Bennhold, and W. Gloeckle, *Inclusive* K^+ *and exclusive* K^+Y *photoproduction on the deuteron: Λ- and Σ-threshold phenomena*. *Phys.Rev.* **C61** (2000) 014001, arXiv:nucl-th/9907029. Page 8.

[82] K. Miyagawa, T. Mart, C. Bennhold, and W. Glöckle, *Polarization observables in exclusive kaon photoproduction on the deuteron*. *Phys.Rev.* **C74** (2006) 034002, arXiv:nucl-th/0608052 [nucl-th]. Page 8.

[83] A. Salam and H. Arenhövel, *Interaction effects in* K^+ *photoproduction on the deuteron*. *Phys.Rev.* **C70** (2004) 044008, arXiv:nucl-th/0407098. Page 8.

[84] A. Salam, *Rescattering effects and two-step process in kaon photoproduction on the deuteron*. PhD thesis, Johannes-Gutenberg Universität Mainz, 2003. Page 8.

[85] A. Salam, K. Miyagawa, T. Mart, C. Bennhold, and W. Glöckle, K^0 *photoproduction on the deuteron and the extraction of the elementary amplitude*. *Phys.Rev.* **C74** (2006) 044004, arXiv:nucl-th/0608053 [nucl-th]. Page 8.

[86] A. Salam, T. Mart, and K. Miyagawa, *Neutral kaon photoproduction on the deuteron*. *Mod.Phys.Lett.* **A24** (2009) 968, arXiv:0906.0316 [nucl-th]. Page 8.

[87] B. O. Kerbikov, *Hyperon-nucleon final state interaction in kaon photoproduction of the deuteron*. *Phys.Atom.Nucl.* **64** (2001) 1835, arXiv:nucl-th/0009074. Page 8.

[88] O. V. Maxwell, *Rescattering contributions to the photoproduction of kaons from the deuteron*. *Phys.Rev.* **C69** (2004) 034605. Page 8.

[89] P. Bydzovsky, *Photo- and electroproduction of kaons*. *Int.J.Mod.Phys.* **E19** (2010) 2369, arXiv:0905.0999 [nucl-th]. Page 8.

[90] P. Bydzovsky and M. Sotona, *Strangeness electromagnetic production on nucleons and nuclei*. *Nucl.Phys.* **A835** (2010) 246, arXiv:0912.0415 [nucl-th]. Page 8.

[91] A. Gasparyan, J. Haidenbauer, C. Hanhart, and K. Miyagawa, *ΛN scattering length from the reaction* $\gamma d \to K^+\Lambda n$. *Eur.Phys.J.* **A32** (2007) 61, arXiv:nucl-th/0701090 [nucl-th]. Page 8.

[92] J.-M. Laget, *Rescattering in meson photoproduction from few body systems*. *Phys.Rev.* **C73** (2006) 044003. Page 8.

[93] J. Laget, *Pentaquark, cusp and rescattering in single kaon photoproduction off deuterium.* *Phys.Rev.* **C75** (2007) 014002, arXiv:nucl-th/0603009 [nucl-th]. Page 8.

[94] S. Hsiao and S. Cotanch, *Deuteron electrodisintegration with kaon production.* *Phys.Lett.* **B163** (1985) 300. Page 8.

[95] S. Cotanch and S. Hsiao, *Electromagnetic production of strangeness.* *Nucl.Phys.* **A450** (1986) 419c. Page 8.

[96] T. Lee, V. Stoks, B. Saghai, and C. Fayard, *Study of hyperon-nucleon interactions with $d(e, e'K)$ reactions.* *Nucl.Phys.* **A639** (1998) 247. Page 8.

[97] T. Corthals, T. Van Cauteren, P. Vancraeyveld, J. Ryckebusch, and D. G. Ireland, *Electroproduction of kaons from the proton in a Regge-plus-resonance approach.* *Phys.Lett.* **B656** (2007) 186, arXiv:0704.3691 [nucl-th]. Page 8, 11, 23, 26, 27, 39.

[98] L. De Cruz, *Bayesian model selection for electromagnetic kaon production in the Regge-plus-resonance framework.* PhD thesis, Ghent University, 2011. Available from http://inwpent5.ugent.be/papers/phdlesley.pdf. Page 11, 23, 24, 25, 26, 46.

[99] T. Vrancx, L. De Cruz, J. Ryckebusch, and P. Vancraeyveld, *Consistent interactions for high-spin fermion fields.* *Phys.Rev.* **C84** (2011) 045201, arXiv:1105.2688 [nucl-th]. Page 11, 23, 25.

[100] E. Leader, *Spin in particle physics.* *Camb. Monogr. Part. Phys. Nucl.Phys. Cosmol.* **15** (2001) 1. Page 14, 117, 128, 142, 169.

[101] E. Pasyuk, *CLAS+FROST: New generation of photoproduction experiments at Jefferson Lab.* *Chin.Phys.* **C33** (2009) 1205, arXiv:0906.4221 [hep-ex]. Page 15.

[102] K. Ardashev *et al.*, *JLab Hall-B experiment E-06-101.* Available from http://www.jlab.org/exp_prog/proposals/06/PR-06-101.pdf. Page 15.

[103] D. G. Ireland, *Information content of polarization measurements.* *Phys.Rev.* **C82** (2010) 025204, arXiv:1004.5250 [hep-ph]. Page 15.

[104] C. Fasano, F. Tabakin, and B. Saghai, *Spin observables at threshold for meson photoproduction.* *Phys.Rev.* **C46** (1992) 2430. Page 15.

[105] G. Knochlein, D. Drechsel, and L. Tiator, *Photoproduction and electroproduction of eta mesons.* *Z.Phys.* **A352** (1995) 327, arXiv:nucl-th/9506029 [nucl-th]. Page 15, 16, 17.

[106] X. Artru, M. Elchikh, J.-M. Richard, J. Soffer, and O. V. Teryaev, *Spin observables and spin structure functions: inequalities and dynamics.* *Phys.Rept.* **470** (2009) 1, arXiv:0802.0164 [hep-ph]. Page 15.

[107] B. Dey, M. E. McCracken, D. G. Ireland, and C. A. Meyer, *Polarization observables in the longitudinal basis for pseudo-scalar meson photoproduction using a density matrix approach.* *Phys.Rev.* **C83** (2010) 055208, arXiv:1010.4978 [hep-ph]. Page 15.

[108] T. Regge, *Introduction to complex orbital momenta.* *Nuovo Cim.* **14** (1959) 951. Page 18.

[109] P. Collins, *An Introduction to Regge Theory and High Energy Physics.* Cambridge Monographs on Mathematical Physics. Cambridge University Press, 2009. Page 19.

[110] S. Donnachie, *Pomeron physics and QCD*. Cambridge monographs on particle physics, nuclear physics, and cosmology. Cambridge University Press, 2002. Page 19.

[111] A. V. Anisovich, V. V. Anisovich, and A. V. Sarantsev, *Systematics of $q\bar{q}$ states in the (n, M^2) and (J, M^2) planes*. *Phys.Rev.* **D62** (2000) 051502. Page 19.

[112] M. Guidal, *Photoproduction de mésons sur le nucléon aux énergies intermédiaires*. PhD thesis, Université de Paris-Sud, U.F.R. Scientifique d'Orsay, 1997. Page 19, 26.

[113] A. M. Boyarski *et al.*, *Photoproduction of $K^+\Lambda$ and $K^+\Sigma^0$ from hydrogen from 5 to 16 GeV*. *Phys.Rev.Lett.* **22** (1969) 1131. Page 19, 20, 162, 163.

[114] D. J. Quinn *et al.*, *Study of charged-pseudoscalar-meson photoproduction from hydrogen and deuterium with 16 GeV linearly polarized photons*. *Phys.Rev.* **D20** (1979) 1553. Page 19, 20, 21, 162, 163.

[115] G. Vogel, H. Burfeindt, G. Buschhorn, P. Heide, U. Kötz, *et al.*, *Recoil polarization in $K^+\Lambda$ photoproduction at 5 GeV*. *Phys.Lett.* **B40** (1972) 513. Page 20, 21, 162.

[116] J. Storrow, *Exchange mechanisms of hadronic reactions*. *Rept.Prog.Phys.* **50** (1987) 1229. Page 21.

[117] H. Holvoet, *Study of the helicity dependence of double pion photoproduction on the proton*. PhD thesis, Ghent University, 2002. Page 22.

[118] M. Benmerrouche, R. M. Davidson, and N. C. Mukhopadhyay, *Problems of describing spin-$\frac{3}{2}$ baryon resonances in the effective Lagrangian theory*. *Phys.Rev.* **C39** (1989) 2339. Page 22.

[119] R. Bradford *et al.*, *Differential cross sections for $\gamma + p \to K^+ + Y$ for Λ and Σ^0 hyperons*. *Phys.Rev.* **C73** (2006) 035202, arXiv:nucl-ex/0509033. Page 22, 24, 25, 26, 46, 48, 162, 163.

[120] A. Llères *et al.*, *Polarization observable measurements for $\gamma p \to K^+\Lambda$ and $\gamma p \to K^+\Sigma^0$ for energies up to 1.5 GeV*. *Eur.Phys.J.* **A31** (2007) 79. Page 22, 26, 162, 163.

[121] J. W. C. McNabb *et al.*, *Hyperon photoproduction in the nucleon resonance region*. *Phys.Rev.* **C69** (2004) 042201(R), arXiv:nucl-ex/0305028. Page 22, 25, 26, 162, 163.

[122] R. G. T. Zegers *et al.*, *Beam-polarization asymmetries for the $p(\vec{\gamma}, K^+)\Lambda$ and $p(\vec{\gamma}, K^+)\Sigma^0$ reactions at $E_\gamma = 1.5\,GeV - 2.4\,GeV$*. *Phys.Rev.Lett* **91** (2003) 092001. Page 22, 26, 162, 163.

[123] M. McCracken *et al.*, *Differential cross section and recoil polarization measurements for the $\gamma p \to K^+\Lambda$ reaction using CLAS at Jefferson Lab*. *Phys.Rev.* **C81** (2010) 025201, arXiv:0912.4274 [nucl-ex]. Page 22, 23, 24, 26, 162.

[124] M. Q. Tran *et al.*, *Measurement of $\gamma p \to K^+\Lambda$ and $\gamma p \to K^+\Sigma^0$ at photon energies up to 2 GeV*. *Phys.Lett.* **B445** (1998) 20. Page 22, 162, 163.

[125] K. H. Glander *et al.*, *Measurement of $\gamma p \to K^+\Lambda$ and $\gamma p \to K^+\Sigma^0$ at photon energies up to 2.6 GeV*. *Eur.Phys.J.* **A19** (2004) 251, arXiv:nucl-ex/0308025. Page 22, 24, 25, 26, 46, 48, 162, 163.

[126] P. Bydzovsky and T. Mart, *Analysis of the data consistency on kaon photoproduction with Λ in the final state*. *Phys.Rev.* **C76** (2007) 065202, arXiv:nucl-th/0605014 [nucl-th]. Page 22.

[127] M. Dugger *et al.*, π^+ *photoproduction on the proton for photon energies from 0.725 to 2.875 GeV.* *Phys.Rev.* **C79** (2009) 065206, arXiv:0903.1110 [hep-ex]. Page 23, 35, 36, 39.

[128] A. Sarantsev, V. Nikonov, A. Anisovich, E. Klempt, and U. Thoma, *Decays of baryon resonances into* ΛK^+, $\Sigma^0 K^+$ *and* $\Sigma^+ K^0$. *Eur.Phys.J.* **A25** (2005) 441, arXiv:hep-ex/0506011 [hep-ex]. Page 23, 24.

[129] D. Merten, U. Löring, K. Kretzschmar, B. Metsch, and H. R. Petry, *Electroweak form factors of non-strange baryons.* *Eur.Phys.J.* **A14** (2002) 477, arXiv:hep-ph/0204024. Page 23, 34.

[130] B. Dey *et al.*, *Differential cross sections and recoil polarizations for the reaction* $\gamma p \to K^+\Sigma^0$. *Phys.Rev.* **C82** (2010) 025202, arXiv:1006.0374 [nucl-ex]. Page 23, 25, 26, 163.

[131] B. Dey and C. A. Meyer, *Normalization discrepancies in photoproduction reactions.* arXiv:1106.0479 [hep-ph]. Page 23, 26.

[132] K. Hicks *et al.*, *Measurement of the* $\vec{\gamma}p \to K^+\Lambda$ *reaction at backward angles.* *Phys.Rev.* **C76** (2007) 042201. Page 24, 26, 162.

[133] L. De Cruz, T. Vrancx, P. Vancraeyveld, and J. Ryckebusch, *Bayesian inference of the resonance content of* $p(\gamma, K^+)\Lambda$. arXiv:1111.6511 [nucl-th]. Page 24, 25, 26, 46.

[134] H. Kohri *et al.*, *Differential cross section and photon-beam asymmetry for the* $\vec{\gamma}n \to K^+\Sigma^-$ *reaction at* $E_\gamma = 1.5 - 2.4$ *GeV.* *Phys.Rev.Lett* **97** (2006) 082003, arXiv:hep-ex/0602015. Page 25, 26, 36, 37, 40, 42, 46, 48, 163, 164.

[135] M. Sumihama *et al.*, *The* $\vec{\gamma}p \to K^+\Lambda$ *and* $\vec{\gamma}p \to K^+\Sigma^0$ *reactions at forward angles with photon energies from* 1.5 *to* 2.4 *GeV.* *Phys.Rev.* **C73** (2006) 035214, arXiv:hep-ex/0512053. Page 25, 26, 46, 48, 162, 163.

[136] W. Rarita and J. Schwinger, *On a theory of particles with half integral spin.* *Phys.Rev.* **60** (1941) 61. Page 24.

[137] M. Benmerrouche, R. Davidson, and N. Mukhopadhyay, *Problems of describing spin-3/2 baryon resonances in the effective Lagrangian theory.* *Phys.Rev.* **C39** (1989) 2339. Page 24.

[138] T. Mizutani, C. Fayard, G. Lamot, and B. Saghai, *Off-shell effects in the electromagnetic production of strangeness.* *Phys.Rev.* **C58** (1998) 75, arXiv:nucl-th/9712037 [nucl-th]. Page 25.

[139] V. Pascalutsa, *Quantization of an interacting spin-3/2 field and the* Δ *isobar.* *Phys.Rev.* **D58** (1998) 096002, arXiv:hep-ph/9802288 [hep-ph]. Page 25.

[140] R. Bradford *et al.*, *First measurement of beam-recoil observables* C_x *and* C_z *in hyperon photoproduction.* *Phys.Rev.* **C75** (2007) 035205, arXiv:nucl-ex/0611034. Page 26, 27, 162, 163.

[141] A. Llères *et al.*, *Measurement of beam-recoil observables* O_x, O_z *and target asymmetry for the reaction* $\gamma p \to K^+\Lambda$. *Eur.Phys.J.* **A39** (2009) 149, arXiv:0807.3839 [nucl-ex]. Page 26, 28, 162.

[142] K. Althoff, M. Gies, H. Herr, E. Hilger, V. Kadansky, *et al.*, *Photoproduction of* $K^+\Lambda$ *on polarized protons.* *Nucl.Phys.* **B137** (1978) 269. Page 26, 162.

[143] M. Coman *et al.*, *Cross sections and Rosenbluth separations in* $^1H(e,e'K^+)\Lambda$ *up to* $Q^2 = 2.35\ GeV^2$. *Phys.Rev.* **C81** (2010) 052201(R), arXiv:0911.3943 [nucl-ex]. Page 27, 28, 29.

[144] M. Guidal, J. M. Laget, and M. Vanderhaeghen, *Electroproduction of strangeness above the resonance region*. *Phys.Rev.* **C61** (2000) 025204, arXiv:hep-ph/9904511 [hep-ph]. Page 27.

[145] R. Mohring *et al.*, *Separation of the longitudinal and transverse cross sections in the* $^1H(e,e'K^+)\Lambda$ *and* $^1H(e,e'K^+)\Sigma^0$ *reactions*. *Phys.Rev.* **C67** (2003) 055205, arXiv:nucl-ex/0211005 [nucl-ex]. Page 28.

[146] D. Carman *et al.*, *Beam-recoil polarization transfer in the nucleon resonance region in the exclusive* $\vec{e}p \to e'K^+\vec{\Lambda}$ *and* $\vec{e}p \to e'K^+\vec{\Sigma}^0$ *reactions at CLAS*. *Phys.Rev.* **C79** (2009) 065205, arXiv:0904.3246 [hep-ex]. Page 29.

[147] T. Feuster and U. Mosel, *Photon and meson induced reactions on the nucleon*. *Phys.Rev.* **C59** (1999) 460, arXiv:nucl-th/9803057 [nucl-th]. Page 34.

[148] S. Kreuzer, "Ein massenabhängiges Confinement-Potential für das Bethe-Salpeter-Modell," Master's thesis, HISKP, Universität Bonn, 2006. Page 35, 36.

[149] R. A. Arndt, I. I. Strakovsky, and R. L. Workman, *Updated resonance photo-decay amplitudes to 2 GeV*. *Phys.Rev.* **C53** (1996) 430, arXiv:nucl-th/9509005. Page 35, 36, 39.

[150] R. A. Arndt, W. J. Briscoe, I. I. Strakovsky, and R. L. Workman, *Extended partial-wave analysis of* πN *Scattering data*. *Phys.Rev.* **C74** (2006) 045205, arXiv:nucl-th/0605082. Page 35, 36.

[151] S. Anefalos Pereira *et al.*, *Differential cross section of* $\gamma n \to K^+\Sigma^-$ *on bound neutrons with incident photons from 1.1 to 3.6 GeV*. *Phys.Lett.* **B688** (2010) 289, arXiv:0912.4833 [nucl-ex]. Page 37, 38, 42, 104, 164.

[152] F. X. Lee, T. Mart, C. Bennhold, and L. E. Wright, *Quasifree kaon photoproduction on nuclei*. *Nucl.Phys.* **A695** (2001) 237. Page 41.

[153] N. Hassall, *Spin observables in kaon photoproduction from the bound neutron in a deuterium target with CLAS*. PhD thesis, University of Glasgow, 2010. Available from http://nuclear.gla.ac.uk/npe-theses/Hassall_thesis.pdf. Page 43, 104.

[154] R. Lawall *et al.*, *Measurement of the reaction* $\gamma p \to K^0\Sigma^+$ *at photon energies up to* 2.6 *GeV*. *Eur.Phys.J.* **A24** (2005) 275, arXiv:nucl-ex/0504014. Page 43, 44, 45, 46, 48, 50, 51, 52, 53, 163.

[155] R. Castelijns *et al.*, *Nucleon resonance decay by the* $K^0\Sigma^+$ *channel*. *Eur.Phys.J.* **A35** (2008) 39, arXiv:nucl-ex/0702033. Page 43, 44, 45, 51, 52, 53, 163.

[156] R. Castelijns, *Photoproduction of strange mesons and hyperons on the proton*. PhD thesis, Rijksuniversiteit Groningen, 2006. Available from http://irs.ub.rug.nl/ppn/291566405. Page 43, 44.

[157] B. Carnahan, *Strangeness photoproduction in the* $\gamma p \to K^0\Sigma^+$ *reaction*. PhD thesis, Catholic University of America, Washington, USA, 2003. Available from

http://www.jlab.org/Hall-B/general/thesis/carnahan_thesis.ps. Page 43, 44, 50, 163.

[158] S. Janssen, *Strangeness production on the nucleon*. PhD thesis, Ghent University, 2002. Available from http://inwpent5.ugent.be/papers/thesis_stijn.pdf. Additional technical notes available from http://inwpent5.ugent.be/papers/formalism.pdf. Page 43.

[159] P. Singer and G. A. Miller, *Radiative meson decay in the cloudy bag model*. *Phys.Rev.* **D33** (1986) 141. Page 44.

[160] T. Van Cauteren. Private communication. Page 44, 47.

[161] D. A. Whitehouse, *Radiative kaon capture at rest in hydrogen*. *Phys.Rev.Lett.* **63** (1989) 1352. Page 55.

[162] P. B. Siegel and B. Saghai, *Initial state interactions for K^--proton radiative capture*. *Phys.Rev.* **C52** (1995) 392, arXiv:nucl-th/9505019 [nucl-th]. Page 55.

[163] T. Van Cauteren, J. Ryckebusch, B. Metsch, and H.-R. Petry, *Helicity amplitudes and electromagnetic decays of hyperon resonances*. *Eur.Phys.J.* **A26** (2005) 339, arXiv:nucl-th/0509047 [nucl-th]. Page 56, 57.

[164] T. Van Cauteren, J. Ryckebusch, B. Metsch, and H. Petry, *Electromagnetic properties of strange baryons in a relativistic quark model*. *Eur.Phys.J.* **A31** (2007) 613. Page 56, 57.

[165] C.-R. Ji and S. R. Cotanch, *Crossing constraints for hyperon reactions*. *Phys.Rev.* **C38** (1988) 2691. Page 56.

[166] R. Williams, C. Ji, and S. Cotanch, *Crossing-consistent analysis of kaon photoproduction and radiative capture*. *Phys.Rev.* **D41** (1990) 1449. Page 56.

[167] T. Van Cauteren, P. Vancraeyveld, and J. Ryckebusch, *Hyperon resonances in radiative kaon capture*. *Acta Phys.Pol. B, Proc.Suppl.* **2** (2009) no. 2, 347. Available from http://hdl.handle.net/1854/LU-811997. Page 56.

[168] S. Prakhov, P. Vancraeyveld, *et al.*, *Measurement of K^-p radiative capture to $\gamma\Lambda$ and $\gamma\Sigma^0$ for p_{K^-} between 514 and 750 MeV/c*. *Phys.Rev.* **C82** (2009) 015201, arXiv:0912.1653 [nucl-th]. Page 57, 58, 59, 60.

[169] T. Stanislaus, V. Abaev, D. Allen, C. Allgower, J. Alyea, *et al.*, *Measurement of the total cross section of the reaction $K^-p \to \Sigma^0\gamma$ between 514 and 750 MeV/c*. *Phys.Rev.* **C79** (2009) 015203. Page 59, 60.

[170] N. Byers and C. N. Yang, *Physical regions in invariant variables for n particles and the phase-space volume element*. *Rev.Mod.Phys.* **36** (1964) 595. Page 64, 137.

[171] M. E. Peskin and D. V. Schroeder, *An introduction to quantum field theory*. Addison-Wesley, Reading, USA, 1995. Page 66, 117.

[172] H. Arenhövel and A. Fix, *Incoherent pion photoproduction on the deuteron with polarization observables. I: Formal expressions*. *Phys.Rev.* **C72** (2005) 064004, arXiv:nucl-th/0506015. Page 68, 71.

[173] V. Dmitrasinovic and F. Gross, *Polarization observables in deuteron photodisintegration and electrodisintegration*. *Phys.Rev.* **C40** (1989) 2479. Page 73, 74, 80.

[174] S. Nozawa and T. S. H. Lee, *Electroproduction of pions on the nucleon. II: Polarization observables*. *Nucl.Phys.* **A513** (1990) 543–556. Page 76.

[175] J. Carlson and R. Schiavilla, *Structure and dynamics of few-nucleon systems*. *Rev.Mod.Phys.* **70** (1998) 743. Page 76.

[176] E. Kessler *et al.*, *The deuteron binding energy and the neutron mass*. *Phys.Lett.* **A255** (1999) 221. Page 76.

[177] R. Blankenbecler and L. F. Cook, *Bound states and dispersion relations*. *Phys.Rev.* **119** (1960) 1745. Page 78.

[178] M. Lacombe *et al.*, *Parametrization of the Paris NN Potential*. *Phys.Rev.* **C21** (1980) 861. Page 79, 80, 97.

[179] R. Machleidt, *The high-precision, charge-dependent Bonn nucleon-nucleon potential (CD-Bonn)*. *Phys.Rev.* **C63** (2001) 024001. Page 79, 80, 97, 147, 148.

[180] V. G. J. Stoks, R. A. M. Klomp, C. P. F. Terheggen, and J. J. de Swart, *Construction of high quality NN potential models*. *Phys.Rev.* **C49** (1994) 2950, arXiv:nucl-th/9406039. Page 79, 80, 97.

[181] F. Gross, J. W. Van Orden, and K. Holinde, *Relativistic one boson exchange model for the nucleon-nucleon interaction*. *Phys.Rev.* **C45** (1992) 2094–2132. Page 79, 80, 81, 97, 149, 150.

[182] F. Gross and A. Stadler, *Covariant spectator theory of np scattering: effective range expansions and relativistic deuteron wave functions*. *Phys.Rev.* **C82** (2010) 034004, arXiv:1007.0778 [nucl-th]. Page 79, 81, 149, 151.

[183] F. Gross and A. Stadler, *Covariant spectator theory of np scattering: phase shifts obtained from precision fits to data below 350 MeV*. *Phys.Rev.* **C78** (2008) 014005, arXiv:0802.1552 [nucl-th]. Page 80, 81, 91, 92, 94, 97, 149, 151, 152.

[184] M. J. Zuilhof and J. A. Tjon, *Electromagnetic properties of the deuteron and the Bethe-Salpeter equation with one-boson exchange*. *Phys.Rev.* **C22** (1980) 2369. Page 80.

[185] J. Carbonell and V. A. Karmanov, *Relativistic deuteron wave function in the light front dynamics*. *Nucl.Phys.* **A581** (1995) 625. Page 80.

[186] F. Gross, *Relativistic treatment of loosely bound systems in scattering theory*. *Phys.Rev.* **140** (1965) B410. Page 80, 87.

[187] J. W. Van Orden, N. Devine, and F. Gross, *Elastic electron scattering from the deuteron using the Gross equation*. *Phys.Rev.Lett* **75** (1995) 4369. Page 81.

[188] W. Dickhoff and D. Van Neck, *Many-body theory exposed!* World Scientific Publishing Co. Pte. Ltd., 2008. Page 82.

[189] F. Gross, *Three-dimensional covariant integral equations for low-energy systems*. *Phys.Rev.* **186** (1969) 1448. Page 87.

[190] M. Galassi, J. Davies, J. Theiler, B. Gough, G. Jungman, M. Booth, and F. Rossi, *GNU scientific library: reference manual*. Network Theory Ltd., 2003. Available from http://www.gnu.org/software/gsl. Page 89, 199.

[191] J. Haidenbauer, U.-G. Meissner, A. Nogga, and H. Polinder, *The hyperon-nucleon interaction: conventional versus effective field theory approach*. *Lect.Notes Phys.* **724** (2007) 113, arXiv:nucl-th/0702015. Page 98, 100.

[192] M. M. Nagels, T. A. Rijken, and J. J. de Swart, *Baryon-baryon scattering in a one-boson-exchange-potential approach. II. Hyperon-nucleon scattering*. *Phys.Rev.* **D15** (1977) 2547. Page 99.

[193] B. Holzenkamp, K. Holinde, and J. Speth, *A meson exchange model for the hyperon-nucleon interaction*. *Nucl.Phys.* **A500** (1989) 485. Page 99, 170.

[194] B. Sechi-Zorn, B. Kehoe, J. Twitty, and R. A. Burnstein, *Low-energy Λ-proton elastic scattering*. *Phys.Rev.* **175** (1968) 1735. Page 99, 100.

[195] G. Alexander, U. Karshon, A. Shapira, G. Yekutieli, R. Engelmann, H. Filthuth, and W. Lughofer, *Study of the $\Lambda - N$ System in Low-Energy $\Lambda - p$ Elastic Scattering*. *Phys.Rev.* **173** (1968) 1452. Page 99, 100.

[196] J. A. Kadyk, G. Alexander, J. H. Chan, P. Gaposchkin, and G. H. Trilling, *Λp interactions in momentum range 300 to 1500 MeV/c*. *Nucl.Phys.* **B27** (1971) 13. Page 99, 100.

[197] F. Eisele, H. Filthuth, W. Foehlisch, V. Hepp, and G. Zech, *Elastic $\Sigma^{\pm} p$ scattering at low energies*. *Phys.Lett.* **B37** (1971) 204. Page 99, 100.

[198] R. Engelmann, H. Filthuth, V. Hepp, and E. Kluge, *Inelastic $\Sigma^{-} p$-interactions at low momenta*. *Phys.Lett.* **21** (1966) 587. Page 99, 100.

[199] J. Haidenbauer and U.-G. Meissner, *The Jülich hyperon-nucleon model revisited*. *Phys.Rev.* **C72** (2005) 044005, arXiv:nucl-th/0506019. Page 99, 100, 168.

[200] T. A. Rijken and Y. Yamamoto, *Extended-soft-core baryon-baryon model. II. Hyperon-nucleon interaction*. *Phys.Rev.* **C73** (2006) 044008. Page 99, 168.

[201] K. Tominaga and T. Ueda, *Effective one-boson-exchange potential for ΛN and ΣN systems and hypertriton*. *Nucl.Phys.* **A693** (2001) 731. Page 99, 168.

[202] H. Polinder, J. Haidenbauer, and U.-G. Meissner, *Hyperon nucleon interactions: a chiral effective field theory approach*. *Nucl.Phys.* **A779** (2006) 244, arXiv:nucl-th/0605050. Page 99, 100.

[203] J. Haidenbauer, *Baryon-baryon interactions in effective field theory*. *Nucl.Phys.* **A835** (2010) 168. Page 99.

[204] J. M. Hauptman, J. A. Kadyk, and G. H. Trilling, *Experimental study of Λp and $\Xi^0 p$ interactions in the range 1–10 GeV/c*. *Nucl.Phys.* **B125** (1977) 29. Page 100.

[205] T. A. Rijken, V. G. J. Stoks, and Y. Yamamoto, *Soft-core hyperon nucleon potentials*. *Phys.Rev.* **C59** (1999) 21, arXiv:nucl-th/9807082. Page 99, 100.

[206] P. Nadel-Turonski, B. Berman, Y. Ilieva, D. Ireland, and A. Tkabladze, *Photoproduction and rescattering of polarized hyperons in deuterium.* *Few Body Syst.* **43** (2008) 227. Page 101, 104.

[207] B. Mecking *et al.*, *JLab Hall-B experiment E-89-045.* Available from http://www.jlab.org/exp_prog/proposals/89/PR89-045.pdf. Page 104.

[208] P. Nadel-Turonski and B. Berman, *CLAS approved analysis CAA-HS06-01.* Page 104.

[209] P. Nadel-Turonski *et al.*, *JLab Hall-B experiment E-06-103.* Available from http://www.jlab.org/exp_prog/proposals/06/PR06-103.pdf. Page 104.

[210] J. Johnstone, *The photon beam asymmetry for KY production from the bound proton in deuterium.* PhD thesis, University of Glasgow, 2009. Available from http://nuclear.gla.ac.uk/npe-theses/Johnstone_thesis.pdf. Page 104.

[211] K. Tsukada *et al.*, *Photoproduction of neutral kaons on the liquid deuterium target in the threshold region.* *Phys.Rev.* **C78** (2008) 014001, arXiv:0712.0657 [nucl-ex]. Page 104, 106, 107, 109, 110.

[212] K. Tsukada *et al.*, *Erratum: Photoproduction of neutral kaons on a liquid deuterium target in the threshold region.* *Phys.Rev.* **C83** (2011) 039904. Page 104, 106, 107, 109, 110.

[213] M. Kaneta *et al.*, *Neutral kaon photoproduction at LNS, Tohoku University.* *Int.J.Mod.Phys.* **E19** (2010) 2355. Page 104.

[214] K. Futatsukawa, *An investigation of the elementary photoproduction of strangeness in the threshold region.* PhD thesis, Tohoku University, 2011. Available from http://lambda.phys.tohoku.ac.jp/~kenta-f/Dthesis_futatsukawa.pdf. Page 104.

[215] K. Futatsukawa and H. Kanda, *Preliminary data from NKS2 at LNS, Tohoku University.* Private communication. Page 104, 106, 107, 108, 109, 110.

[216] F. Dohrmann *et al.*, *Quasifree* Λ, Σ^0, *and* Σ^- *electroproduction from* $^{1,2}H$, $^{3,4}He$, *and Carbon.* *Phys.Rev.* **C76** (2007) 054004, arXiv:0707.3059 [nucl-ex]. Page 111, 112.

[217] J. Cha, *Measurements of kaon electroproduction on hydrogen and deuterium.* PhD thesis, Hampton University, 2000. Available from http://www1.jlab.org/Ul/publications/documents/jinseok.pdf. Page 112.

[218] F. Gross, *Relativistic quantum mechanics and field theory.* New York, USA: Wiley (1993) 629 p. Page 117, 167.

[219] D. A. Varshalovich, A. N. Moskalev, and V. K. Khersonsky, *Quantum theory of angular momentum.* World Scientific Publishing Co. Pte. Ltd., Singapore, 1988. Page 120.

[220] M. Jacob and G. C. Wick, *On the general theory of collisions for particles with spin.* *Ann.Phys.* **7** (1959) 404–428. Page 128.

[221] E. W. Weisstein, *Triangle Function.* Available from http://mathworld.wolfram.com/TriangleFunction.html. From MathWorld – A Wolfram Web Resource. Page 137.

[222] P. Nyborg, H. S. Song, W. Kernan, and R. H. Good, *Phase-space considerations for four-particle final states.* *Phys.Rev.* **140** (1965) B914. Page 138.

[223] R. H. Dalitz, *Decay of τ mesons of known charge*. *Phys.Rev.* **94** (1954) 1046. Page 138.

[224] G. F. Chew and F. E. Low, *Unstable particles as targets in scattering experiments*. *Phys.Rev.* **113** (1959) 1640. Page 138.

[225] G. G. Ohlsen, *Polarization transfer and spin correlation experiments in nuclear physics*. *Rep.Prog.Phys.* **35** (1972) 717. Page 141, 142, 143.

[226] B. A. Robson, *The theory of polarization phenomena*. Oxford, UK: Clarendon Press (1974) 119 p. Page 142, 144.

[227] H. Arenhövel and M. Sanzone, *Photodisintegration of the deuteron: a review of theory and experiment*. *Few Body Syst.Suppl.* **3** (1991) 1. Page 144, 145.

[228] Available from `http://nn-online.org`. Page 147.

[229] M. Lacombe *et al.*, *Parametrization of the deuteron wave function of the Paris N-N potential*. *Phys.Lett.* **B101** (1981) 139. Page 147, 148.

[230] W. W. Buck and F. Gross, *A family of relativistic deuteron wave functions*. *Phys.Rev.* **D20** (1979) 2361. Page 149.

[231] J. Van Orden. Private communication. Page 149.

[232] S. Goers *et al.*, *Measurement of $\gamma p \to K^0\Sigma^+$ at photon energies up to 1.55 GeV*. *Phys.Lett.* **B464** (1999) 331. Page 163.

[233] F. Coutinho, *Off-the-mass shell scattering amplitude in a two-particle potential model*. *Am.J.Phys.* **50** (1982) 41. Page 168.

[234] J. Haidenbauer. Private communication. Page 169.

[235] P. Vancraeyveld, L. De Cruz, J. Ryckebusch, and T. Van Cauteren, *Regge-plus-resonance predictions for kaon photoproduction from the neutron*. *Phys.Lett.* **B681** (2009) 428, `arXiv:0908.0446 [nucl-th]`. Page .

[236] P. Vancraeyveld, L. De Cruz, J. Ryckebusch, and T. Van Cauteren, *Regge-model predictions for $K^+\Sigma$ photoproduction from the nucleon*. *AIP Conf.Proc.* **1182** (2009) 619, `arXiv:0906.5505 [nucl-th]`. Page .

[237] P. Vancraeyveld, L. De Cruz, J. Ryckebusch, and T. Van Cauteren, *Regge-plus-resonance predictions for charged-kaon photoproduction from the deuteron*. *EPJ Web Conf.* **3** (2010) 03013, `arXiv:0912.2679 [nucl-th]`. Page .

[238] P. Vancraeyveld, L. De Cruz, and J. Ryckebusch, *Regge-plus-resonance predictions for neutral-kaon photoproduction from the deuteron*. *AIP Conf.Proc.* **1374** (2011) 335, `arXiv:1010.0113 [nucl-th]`. Page .

[239] CLAS collaboration. Available from `http://www.jlab.org/Hall-B/`. Page 199.

[240] A. Stadler and F. Gross, *Covariant spectator theory: foundations and applications*. *Few-Body Syst.* **49** (2011) 91. Page 199.

[241] LEPS collaboration. Available from `http://www.rcnp.osaka-u.ac.jp/Divisions/np1-b/`. Page 199.

[242] SAPHIR collaboration. Available from http://saphir.physik.uni-bonn.de/. Page 200.

Nomenclature

I strive to be brief, and I become obscure.
— Horace

List of acronyms

(23)-CM	Centre-of-Mass of particles labelled 2 and 3, see page 62.
Dnp	Deuteron-neutron-proton, see page 77.
CC	Coupled-Channels.
CLAS	CEBAF Large Acceptance Spectrometer, see Ref. [239].
CM	Centre-of-Mass (frame).
CQM	Constituent-Quark Model.
CST	Covariant Spectator Theory, see Ref. [240].
EFT	Effective-Field Theory.
EM	Electromagnetic.
FSI	Final-State Interaction, see page 83.
GSL	GNU Scientific Library, see Ref. [190].
KY-CM	Kaon-Hyperon Centre-of-Mass frame.
LAB	Laboratory (frame).
LEPS	Laser Electron Photon beamline at SPring-8, see Ref. [241].
NRPWIA	Non-Relativistic Plane-Wave Impulse Approximation, see page 84.
OPE	One-Photon Exchange.
PWA	Partial-Wave Analysis.
QCD	Quantum chromodynamics.

RIA	Relativistic Impulse Approximation, see page 82.
RPP	Review of Particle Physics, see Ref. [1].
RPR	Regge-plus-Resonance, see page 11.
RPWIA	Relativistic Plane-Wave Impulse Approximation, see page 84.
SAID	Scattering Analysis Interactive Dail-in, see Ref. [4].
SAPHIR	Spectrometer Arrangement for PHoton Induced Reactions, see Ref. [242].
YN-CM	Hyperon-Nucleon Centre-of-Mass frame.
YN-FSI	Hyperon-Nucleon Final-State Interaction, see page 86.

List of symbols

$\not{\boldsymbol{A}}$	Feynman-slash notation, see equation (A.32).
$\mathcal{C}$	Charge conjugation matrix, see equation (A.30).
e_i	Imaginary unit of the quaternion group $\mathbb{H}$, see equation (B.5).
ϵ_{ijk}	Levi-Civita tensor, see equation (A.24).
$\epsilon_{\alpha\beta\gamma\delta}$	Totally antisymmetric tensor, see equation (A.7).
Γ_{Dnp}	Covariant *Dnp*-vertex, see equation (5.82).
γ^μ	Dirac gamma matrices, see equation (A.27).
$G_i(\boldsymbol{p})$	Propagator for particle of spin-i, see equation (D.4).
$h(\vec{p})$	Helicity transformation, see equation (C.2).
$\hat{\mathcal{J}}^{\lambda_\gamma}$	Transition current for EM kaon-production from the deuteron, see page 83.
$\hat{J}^{\lambda_\gamma}$	Transition current for EM kaon-production from the nucleon, see page 13.
ξ	Rapidity of a Lorentz boost, see equation (A.15).
$\boldsymbol{\xi}^{\lambda_D}$	Deuteron polarisation vector, see equation (5.79).
$\lambda(x, y, z)$	Triangle function, see equation (E.2).
$\boldsymbol{p}_i$	Four-vector in the LAB frame, see equation (5.5).
$\boldsymbol{p}_i^*$	Four-vector in the (23)-CM frame, see equation (5.6).
$\dot{\boldsymbol{p}}_i^*$	Four-vector in the YN-CM frame, see equation (K.4).
Ψ^{++}	Positive-energy projected deuteron wave function, see equation (5.88).
Ψ^{-+}	Negative-energy projected deuteron wave function, see equation (5.92).
$r(\alpha, \beta, \gamma)$	Rotation defined by the Euler angles α, β and γ, see page 118.
$r(l, \vec{p})$	Wick helicity rotation, see equation (C.12).

$r(\vec{\omega})$	Rotation through the angle $\mid \vec{\omega} \mid$ about the unit axis $\hat{\vec{\omega}}$, see page 118.
σ_i	Pauli matrices, see equation (A.22).
$\mathcal{T}^{\lambda_\gamma}_{\lambda_N \lambda_Y}$	Hadronic transition matrix elements for $N(\gamma^{(*)}, K)Y$, see equation (2.10).
$\mathcal{T}^{\lambda_\gamma}_{\lambda_D \lambda_Y \lambda_N}$	Hadronic transition matrix elements for ${}^2\mathrm{H}(\gamma^{(*)}, KY)N$, see equation (5.27).
$u(\vec{p}, \lambda)$	Positive-energy helicity spinor, see equation (C.8).
$u(\vec{p}; m_s)$	Positive-energy Dirac spinor, see equation (A.34).
$v(\vec{p}, \lambda)$	Negative-energy helicity spinor, see equation (C.8).
$v(\vec{p}; m_s)$	Negative-energy Dirac spinor, see equation (A.34).